

---

# THESIS

Submitted in fulfillment of the requirements for the degree of

## DOCTOR OF PHILOSOPHY

in the

## UNIVERSITY OF PARIS-SEINE

**Specialty:** Chemistry of Polymers – Materials Science

Defended publicly on 18 March 2019 by:

**Kätlin ROHTLAID**

---

## **Fabrication, characterization and integration of microactuators and microsensors based on electronically conducting polymers**

---

In front of the jury composed of:

Dr. Christian BERGAUD	LAAS-CNRS, Toulouse, France	Reviewer
Dr. Edwin W. H. JAGER	Linköping University, Sweden	Reviewer
Pr. Alvo AABLOO	University of Tartu, Estonia	Examiner
Dr. Lise TROUILLET-FONTI	SOLVAY, France	Examiner
Pr. Eric CATTAN	IEMN-DOAE, Université Polytechnique des Hauts-de-France, France	Examiner
Pr. John D. W. MADDEN	University of British Columbia, Canada	Invited member
Pr. Frédéric VIDAL	LPPI, Université de Cergy-Pontoise, France	Director of thesis
Dr. Cédric PLESSE	LPPI, Université de Cergy-Pontoise, France	Co-director of thesis
Dr. Giao T. M. NGUYEN	LPPI, Université de Cergy-Pontoise, France	Co-supervisor of thesis

---

**Doctoral school:** Science and Engineering, University of Cergy-Pontoise

**Research unit:** LPPI, Laboratoire de Physicochimie des Polymères et des Interfaces, EA 2528



## Acknowledgments

Firstly, I would like to thank the European Union's Horizon 2020 research and innovation program and ITN MICACT project (No. 641822) for giving me the opportunity to carry out my PhD and for funding this thesis. I wish to thank all the committee members: Dr. Christian Bergaud, Dr. Edwin W. H. Jager, Pr. Alvo Aabloo, Dr. Lise Trouillet-Fonti, Pr. Eric Cattan and Pr. John D. W. Madden for accepting to report and judge my thesis.

I would like to express my deepest gratitude to Pr. Frédéric Vidal, Dr. Cédric Plesse and Dr. Giao T. M. Nguyen for accepting me for this position, for guiding me through this process and for their continuous support, incessant motivation and immense knowledge. I appreciate your availability and your presence, for always being here for me. You have inspired and motivated me during these 3 (and more) years every single day, to overcome the difficulties on the road which at one point may have seemed like a mission impossible. Thanks to you, I have stubbornly kept on working and never given up. I could not have asked for better supervisors!

I would also like to thank my two secondment supervisors, Pr. Eric Cattan and Pr. John D. W. Madden, without who, a large part of this work wouldn't have been possible. I appreciate all these valuable conversations, guidance and inspiration to find solutions on many difficulties and technical problems I faced.

Besides my supervisors, I would like to thank all the permanent members of LPPI who have accompanied and helped me during these 3 years on various questions and problems. Furthermore, the members of IEMN who have instructed me to gather the knowledge in microfabrication field.

I thank all my fellow labmates in LPPI for different discussions (scientific and not so scientific), for helping me, but also for all the fun times. I would also like to acknowledge all the fellow MICACT students for sharing the same path and making it more memorable. I am grateful for the opportunity to have worked in IEMN, UBC and in IMS lab and for all the help, discussions and guidance of the PhD students there.

Last but not least, I thank my family and friends, who have been encouraging and supporting me during these 3 years from distant and who have always been there for me!





# TABLE OF CONTENTS

<b>Abbreviations</b>	<b>9</b>
<b>General introduction</b>	<b>11</b>
<b>Chapter 1. Bibliography on ECP based microactuators</b>	<b>17</b>
1.1 Introduction	18
1.2 Electronically conducting polymers	19
1.2.1 History of electronically conducting polymers	19
1.2.2 Conductivity mechanism of electronically conducting polymers	19
1.3 Electronically conducting polymer actuators	22
1.3.1 Oxidation, reduction and the volume variation of conducting polymers	22
1.3.2 Synthesis of conducting polymers for actuator purpose	24
1.3.3 Conducting polymer actuators operating in liquid electrolyte	26
1.3.4 Conducting polymer actuators operating in open-air	27
1.4 Electronically conducting polymer microactuators	34
1.4.1 Microactuators operating in electrolytic solution	34
1.4.2 Microactuators operating in open air	37
1.5 Conclusion and problem statement	41
<b>Chapter 2. Optimization of PEDOT electrodes for layer stacking method via VPP</b>	<b>43</b>
2.1 Introduction	44
2.1.1 Vapor phase polymerization (VPP)	44
2.1.2 Vapor phase polymerization for microactuator fabrication	47
2.2 Improvement of PEDOT electrode electrical and electrochemical properties	49
2.2.1 Synthesis and characterization of PEDOT electrodes	49
2.2.2 Iron (III) tosylate content in butanol	52
2.2.3 EMImTFSI content	54
2.2.4 mPEG content	56
2.2.5 Polymerization time	58
2.2.6 Polymerization temperature	60
2.2.7 Rotation speed of spin-coating	61
2.2.8 Conclusion	63
2.3 Trilayer microactuators with optimized PEDOT electrodes using layer stacking method	63
2.4 Conclusion	65
<b>Chapter 3. PEDOT:PSS based microactuators and microsensors</b>	<b>67</b>
3.1 Introduction	68
3.2 Fabrication and characterization of PEDOT:PSS/PEO electrodes	70
3.3 PEDOT:PSS/PEO based microactuators	77
3.3.1 Fabrication of PEDOT:PSS/PEO microactuators with layer stacking method	77
3.3.2 Mechanical properties	79

3.3.3	Electrochemical properties	80
3.3.4	Actuation characterization	81
3.3.5	Blocking force characterization	83
3.3.6	Sensor characterization	84
3.4	Conclusions	88
<b>Chapter 4.</b>	<b>PEDOT:PSS based microactuators integrated into flexible microchips</b>	<b>89</b>
4.1	Introduction	90
4.2	Microfabrication process	91
4.3	Characterization of PEDOT:PSS based microsystems	98
4.3.1	Open-air characterization of the PEDOT:PSS-based microsystems	100
4.3.2	Discussion	103
4.3.3	Micro sensor characterization	107
4.4	Conclusion	110
<b>Chapter 5.</b>	<b>PEDOT:PSS linear actuators</b>	<b>111</b>
5.1	Introduction	112
5.1.1	Linear actuators operating in liquid electrolyte	112
5.1.2	Linear actuators operating in open-air	117
5.2	Electromechanical model to predict trilayer linear actuation	122
5.3	Fabrication and characterization of PEDOT:PSS composite electrodes	125
5.3.1	Fabrication of PEDOT:PSS electrodes	125
5.3.2	Mechanical characterization of the PEDOT:PSS/PEO based electrodes	126
5.3.3	Electrochemomechanical characterization of PEDOT:PSS composite electrodes	131
5.3.4	Conclusion	134
5.4	Semi-IPN with ionic liquid as a co-solvent	135
5.4.1	Synthesis of PEO-NBR semi-IPN's with EMImTFSI as a co-solvent	136
5.4.2	Rheology	137
5.4.3	Extractible content	138
5.4.4	Ionic conductivity	140
5.4.5	Mechanical properties	141
5.4.6	Thickness of spin-coated semi-IPNs	143
5.4.7	Conclusion	144
5.5	Trilayer linear actuators	145
5.5.1	Modeling: prediction of linear deformation	145
5.5.2	Fabrication of asymmetric trilayer linear actuators	150
5.5.3	Characterization of asymmetric trilayer linear actuators	151
5.6	Conclusion	163
	<b>Conclusions and perspectives</b>	<b>165</b>
	<b>References</b>	<b>173</b>

<b>Appendix</b>	<b>183</b>
Appendix 1.    Materials and experimental methods	184
A.1.1.    Materials	184
A.1.2.    Strain difference	184
A.1.3.    Photolithography steps and SU-8 photoresist	185
Appendix 2.    Additional results of chapter 3	188
A.2.1.    ATR-FT-IR	188
A.2.2.    PEDOT:PSS/PEO(40%) + different initiators (electrical and electrochemical properties)	189
A.2.3.    PH1000 + 40% PEO + different initiators	191
A.2.4.    Dimensional stability by water immersion	192
Appendix 3.    Additional results of chapter 5	194
A.3.1.    Model to predict the free strain of the electrodes based on bending deformations	194
A.3.2.    Rheology	196
A.3.3.    Ionic conductivity	196
A.3.4.    Thermomechanical properties	197
A.3.5.    Model to predict the blocking force	199
<b>Abstract</b>	<b>201</b>
<b>Résumé</b>	<b>203</b>



## Abbreviations

### *Materials*

APS	ammonium persulfate
BuOH	butanol
CDC	carbon-derived-carbon
EDOT	3,4-ethylenedioxythiophene
DCPD	dicyclohexyl peroxydicarbonate
EMImTFSI	1-ethyl-3-methylimidazolium bis(trifluoromethanesulfonyl)imide
Fe(OTs) <sub>3</sub>	iron (III) tosylate
FeCl <sub>3</sub>	iron (III) chloride
MeOH	methanol
mPEG	methacrylate poly(ethylene glycol)
NBR	nitrile butadiene rubber
PANI	polyaniline
PC	propylene carbonate
PEDOT	poly(3,4-ethylenedioxythiophene)
PEDOT:PSS	poly(3,4-ethylenedioxythiophene):poly(styrene sulfonate)
PEG	poly(ethylene glycol)
PEGDM	poly(ethylene glycol) dimethacrylate
PEGM	poly(ethylene glycol) methyl ether methacrylate
PEO	poly(ethylene oxide)
PPy	polypyrrole
PSS	polystyrene sulfonate
PVdF	poly(vinylidene fluoride)
Py	pyrrole

### *Fabrication and characterization*

AFM	atomic force microscopy
ATR	attenuated total reflection
CA	chronoamperometry
CV	cyclic voltammetry
DMA	dynamic mechanical analysis
FT-IR	Fourier-transform infrared
OCV	open circuit voltage
PEB	post exposure bake
RIE	reactive ion etching
SB	softbake
SEM	scanning electron microscopy
UV	ultraviolet
VPP	vapor phase polymerization
C.E	counter electrode
R.E	reference electrode
W.E	working electrode

$E$	Young's modulus (MPa)
$\sigma$	electronic conductivity ( $S.cm^{-1}$ )
$\rho$	volumetric charge density ( $C.m^{-3}$ )
$\varepsilon$	strain (%)
$\alpha$	strain-to-charge ratio ( $m^3.C^{-1}$ )
$\Delta E$	open circuit voltage variation (mV) for sensor measurements

### *Others*

C-IPN	conducting interpenetrating polymer network
CP	conducting polymer
EAP	electroactive polymer
ECP	electronically conducting polymer
IL	ionic liquid
IPMC	ionic polymer-metal composite
IPN	interpenetrating polymer network
MEMS	micro-electro-mechanical system
Semi-IPN	semi-interpenetrating polymer network

# General introduction

## General Introduction

The research activity of this thesis is carried out under MICACT (MICroACTuators) project, which has received funding from the European Union's Horizon 2020 research and innovation program under the Marie Skłodowska-Curie grant agreement No 641822. MICACT scientific program focuses on the research and development in the field of smart soft systems, made of electroactive polymer microactuators for advanced miniaturized devices. The network composed of 15 Early Stage Researchers (ESRs) who were divided into four main groups based on dielectric elastomers, ionic electroactive polymers (IEAPs), microfabrication and industrial applications, combining different tasks based on the development, modeling and characterization of different devices.

Micro-Electro-Mechanical Systems (MEMS) are multifunctional and intelligent integrated microscale systems combining different elements (electrical, mechanical, optical, magnetic, thermal, chemical, fluidic) which are fabricated with semiconductor processing techniques. Miniaturization and MEMS fabrication allows reducing the size and manufacturing costs and could possibly improve the performances of the microdevices. MEMS are usually classified into two main categories as actuators and sensors. Actuators are devices able to produce mechanical work from energy (electrical, chemical, mechanical, thermal, magnetic, etc) and sensors are devices able to convert specific variable (pressure, strain, flow, heat, chemicals, biological elements, etc) to a measurable signal. Microfabrication technology has advanced over the years and allowed the development of different MEMS, used in wide range of applications (aeronautics, satellites, automotive, computers, video game consoles, displays, printers, phones, medical devices, etc.) covered by most of scientific and technical fields (physics, chemistry, materials science, biology, medicine, electronics, mechanics, computer science, robotics, etc.).

Electroactive polymers (EAPs) are materials capable of changing their shape and/or size in response to electrical stimulation and based on their activation mechanism they are classified into two main categories: electronic EAPs and ionic EAPs. The focus of this thesis is on ionic EAPs, and more precisely on electronically conducting polymers (ECPs). The working mechanism of ECPs is driven by the ion diffusion inside/outside the polymer during a redox process in the presence of an electrolyte, resulting in volume variation of the materials. Additionally, they are also capable of generating electrical energy in response to mechanical



stimulation, i.e. behave as sensors. ECPs are flexible and lightweight materials, able to operate at low potentials (1-5 V) and offer the possibility of processability and miniaturization, making them attractive for the development of soft MEMS and move towards soft electronics (flexible substrates, soft robotics, biomedicine, microbiology, etc). However, there are still many limitations for further development in the ECP-MEMS field. First, the performances of the electroactive materials are still low and limiting their use in real applications, especially in open-air. The sensing ability of ECP based devices has been studied at macroscale but never demonstrated at microscale. Their complete fabrication with patterning and integration into microsystems has not been demonstrated yet in the case of air-operating microdevices. These issues and challenges will be addressed in the framework of this thesis to fabricate efficient ECP based microactuators and microsensors.

The main focus of this manuscript is the design, characterization and integration of microactuators and microsensors based on electronically conductive polymers. The research work of this manuscript has been performed in the Laboratoire de Physicochimie des Polymères et des Interfaces (LPPI) in collaboration with Institut d'Electronique, de Microélectronique et de Nanotechnologie (IEMN) and Electrical and Computer Engineering laboratory in the University of British Columbia (UBC). The first secondment (8 months) in the framework of MICACT ITN project was performed in IEMN related to the microsystem fabrication. The second secondment (2 weeks) was related on the characterization of the intrinsic properties of ECPs and was performed in UBC.

The manuscript is divided into 5 chapters, one chapter focusing on the state of the art and 4 on the experimental work, carried out during this PhD.

The first chapter of this manuscript will give a bibliographic overview on ECP based microactuators. The history of the conducting polymers, their structure and their conductivity mechanism are described. The second part is focusing on their synthesis and on their use as active layers for ionic actuators on macroscale. Finally, the last part is describing different ECP based microactuators and the possibility to integrate them into complex microsystems.

The second chapter is the starting point of the experimental work of this manuscript. The work in this chapter is focused on the optimization of previously described microactuators, fabricated using layer stacking method. More specifically, the optimization of vapor phase polymerization (VPP) of poly(3,4-ethylenedioxythiophene) (PEDOT) was carried out to

enhance the electrical and electrochemical properties of the resulting electrodes. This study allowed the fabrication of microactuators with improved performances compared to the previous microactuators fabricated with layer stacking method. The results of this chapter are published in collaboration with Tan. N. Nguyen (ESR in MICACTION project, IEMN) as a joint publication in *Electrochimica Acta*.

The third chapter of this manuscript describes the fabrication of microactuators using commercial poly(3,4-ethylenedioxythiophene):poly(styrene sulfonate) (PEDOT:PSS) dispersion in order to develop more simple and reproducible layer stacking method. Polar reactive additives based on poly(ethylene oxide) (PEO) were incorporated to the PEDOT:PSS commercial dispersion and the effect on the electrical and electrochemical properties of the resulting composite electrodes were studied. The optimized electrodes were used to fabricate PEDOT:PSS/PEO based trilayer microactuators using layer stacking method and laser patterning. These microactuators demonstrated improved performances and more importantly, mechanical sensing behavior at microscale was demonstrated for the first time. The work of this chapter was carried out in LPPI and in IEMN and the results are submitted for a publication.

The fourth chapter of this manuscript is the continuation of the work described in chapter 3 to integrate these microactuators into microsystems. The microfabrication process was developed to fabricate microactuators with top and bottom electrical contacts directly on a flexible substrate without any manual handling during the process. The process allows the design of different configurations, for example, the fabrication of actuator-sensor microsystem with four electrical contacts. The work in this chapter was carried out in IEMN and another publication is under preparation.

The fifth and last chapter will describe the development of linear actuators. First, the electromechanical properties of the PEDOT:PSS based electrodes were studied as a function of the redox level. Then, an electromechanical model was used to fabricate trilayer linear actuators, combining PEDOT:PSS electrodes with different mechanical and electrochemical properties. These trilayer linear actuators were successfully characterized and additionally, linear strain sensing of these materials was demonstrated, making them attractive for the development of multifiber artificial muscles. The work of this chapter was carried out in UBC and in LPPI and will be the focus of another publication.

Finally, a conclusion will summarize the main points of this PhD with the main prospects for the future work.



Chapter 1. Bibliography on ECP  
based microactuators

## 1.1 Introduction

Artificial muscle is a general term for a group of materials or devices that are intended to mimic the functionality of natural muscles. Electroactive polymers (EAPs) have been intensively investigated for this purpose, since they are soft, lightweight, easily processed and manufactured. The main functionality of these materials is that through external electric stimulus they are able to generate reversible contraction and expansion, which leads to changing their shape or size similarly to the natural muscles. Based on their activation mechanism, EAPs are classified into two main categories: electronic EAPs and ionic EAPs.

The electronic EAPs are driven by the electric field<sup>[1,2]</sup> and this group includes dielectric elastomers, ferroelectric polymers, also called piezoelectric polymers, and electrostrictive polymers.<sup>[3-6]</sup> In an example of dielectric elastomer actuators, the actuation mechanism is caused by the electrostatic forces between two electrodes, which apply Maxwell pressure to a soft dielectric elastomer and result in plane expansion of the device. Electronic EAPs are known to produce relatively large actuation forces, respond rapidly (order of a millisecond) and to operate in open-air for a long time. A perceived drawback with these types of actuators is their need of high voltage (up to  $150 \text{ MV.m}^{-1}$ ) which may be disadvantageous for many applications, could be close to the electrical breakdown level and even dangerous if not handled carefully.

The ionic EAPs are driven by the electrical potential which induces mobility or diffusion of ions between their two electrodes. This group of materials include electronically conducting polymers (ECPs), ionic polymer-metal composites (IPMC), carbon nanotubes (CNTs), carbide derive carbon (CDC) and ionic polymer gels (IPGs).<sup>2,7-17</sup> Compared to the electronic EAPs, the main advantage of the ionic EAPs is their low operating voltages (1-5V).

The focus of this thesis is on ionic EAPs and more specifically on ECP based actuators. The bibliography chapter is divided into three main sections. The first part is describing the history of electronically conducting polymers (ECPs) focusing on their structure and on their conductivity mechanism. The second part is focused on the working principle of ECPs, on their synthesis and on their use as active layers for the purpose of ionic actuators. Finally, the last part of this chapter is describing different ECP based microactuators in a perspective of the development of microsystems.

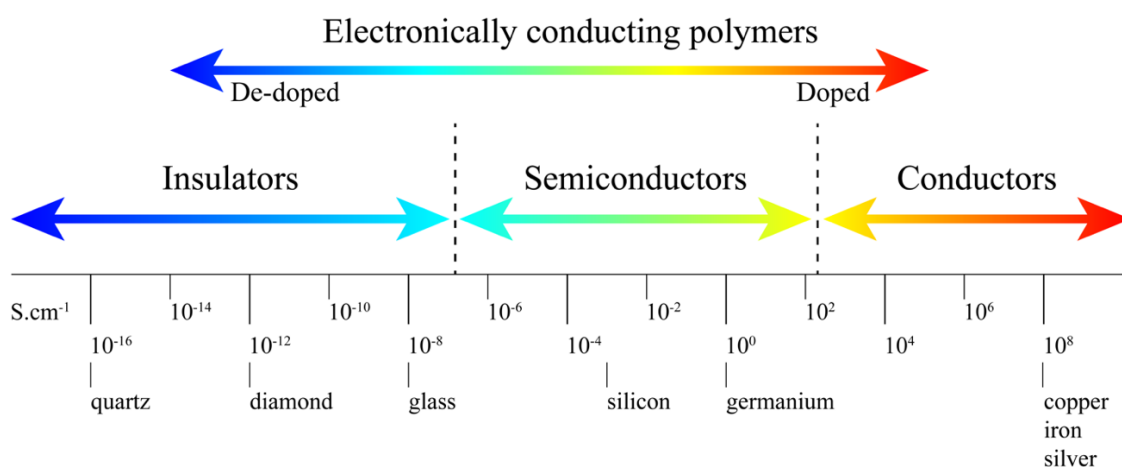
## 1.2 Electronically conducting polymers

### 1.2.1 History of electronically conducting polymers

Conducting polymers were discovered in 1977 from a mistake of a PhD student in Shirakawa's group, who applied a thousand times higher amount of Ziegler-Natta catalyst into acetylene. The accelerated reaction rate resulted in the formation of silvery film on the walls of the reaction vessel.<sup>[18]</sup> This obtained metallic looking material was then additionally investigated by MacDiarmid and Shirakawa. It was discovered that the material is conductive because of the conjugated double bonds and the obtained iodine-doped polyacetylene resulted in electronic conductivity of  $10^3 \text{ S.cm}^{-1}$ . Shortly after this discovery, a series of conducting polymers, like polypyrrole (PPy), polyaniline (PAn) and polythiophene (PTh) were reported and promoted the research of conducting polymers. In 2000, Heeger, MacDiarmid and Shirakawa shared the Nobel prize "for the discovery and development of conducting polymers" (polyacetylene).<sup>[19]</sup>

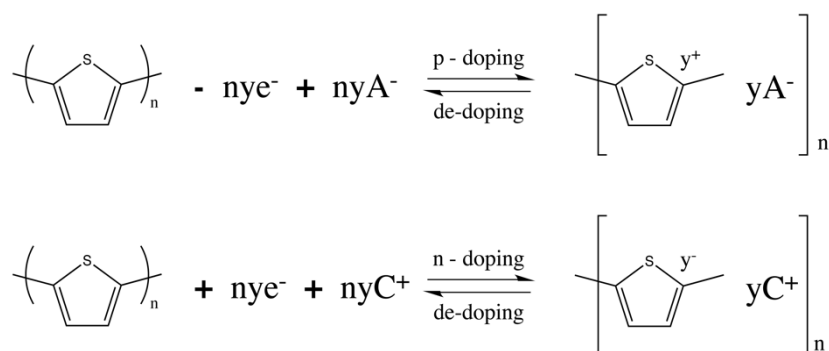
### 1.2.2 Conductivity mechanism of electronically conducting polymers

The electronically conducting polymers (ECPs) or  $\pi$ -conjugated polymers have a bonding pattern consisting of alternating single ( $\sigma$ -bonds) and double ( $\pi$ -bonds) carbon bonds along the backbone of the polymer chain. Such conjugation leads to a structure with continuous overlapping  $\pi$ -molecular orbitals along the polymer backbone. In their neutral form, ECPs are insulators or poorly conducting semiconductors since they do not have intrinsic charge carriers.



**Figure 1.** The conductivity range of electronically conducting polymers.

The conductivity is obtained by partial addition (n-doping) or removal (p-doping) of electrons to or from the neutral and insulating polymer chains which provides charge carriers able to move along the orbital system. Depending on their doping level, the conductivity values of ECPs can range between insulators and conductors (**Figure 1**).<sup>[20]</sup> Doping is generally a reversible oxidation-reduction reaction by chemical or electrochemical means and results in positive or negative charges on the polymer chain. Most commonly, p-doping is used because it is more stable compared to n-doping and will be the focus of the subsequent discussion. During p-doping,  $\pi$ -electrons are removed from the polymer chains. As a consequence, surrounding anions are incorporated within the polymer chains to maintain the charge neutrality of the system. The de-doping reaction corresponds to a return to the neutral state of ECPs (**Figure 2**).

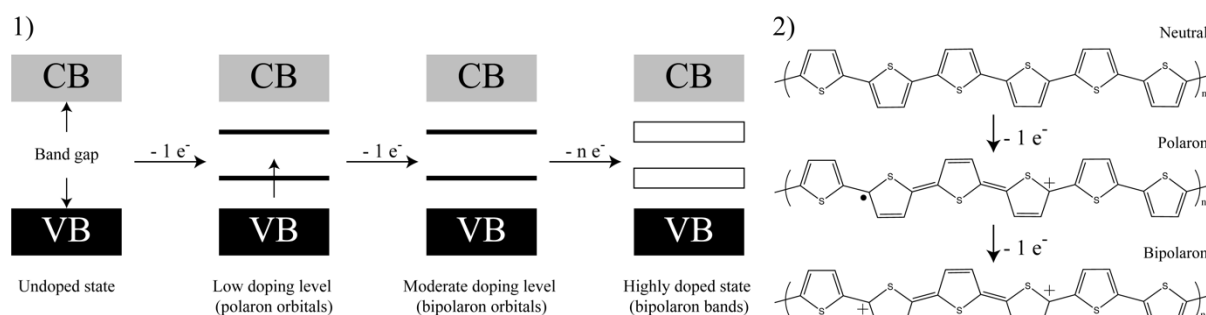


**Figure 2.** Reversible p- and n-doping mechanisms of polythiophene.

Several types of charge carriers may appear during p-doping and for ECPs they are typically referred as polarons, bipolarons or charged solitons.<sup>[21,22]</sup> According to the band theory, the electrical properties of these materials are determined by their electronic structure and the electrons move within discrete energy states, called bands. The highest occupied molecular orbital (HOMO) corresponds to the valence band (VB), usually described for inorganic semiconductors and the lowest unoccupied molecular orbital (LUMO) to the conduction band (CB). The energy difference between them is called the band gap (**Figure 3**). The bands should be partially filled, in order to obtain the electrical conductivity of the materials. Metals have high conductivities, due to their partially filled conduction bands. On the contrary, semiconductors have completely full VB and completely empty CB and need to be doped to change their band structures and to become conductors. In the example of ECPs and p-doping, the polarons are created when one electron is removed from top of the VB. The removal of the second electron on a chain results in the formation of a bipolaron through dimerization of two polarons. The number of polarons and bipolarons increases with the



doping level. High doping levels lead to new energy bands through which electrons can flow and metal-type conductivity can be achieved.<sup>[23]</sup>



**Figure 3.** Schematic representation of a: 1) band structure as a function of doping level; 2) p-doping of polythiophene.

Therefore, the appearance of the charge carriers along the macromolecular chains results in drastic changes in the electrical properties of the polymers. Depending on the state of the polymer (neutral or doped) and the type of doping, the electronic properties of ECPs can be very different. Some conjugated polymers with their chemical structures, doping nature and conductivities are presented in **Table 1**. Different conjugated polymers are used for many applications, but the common feature amongst them is the presence of conjugation.

**Table 1.** Doping nature (n or p), conductivities and structures for some electronically conducting polymers.

Polymer	Doping nature	Conductivity (S.cm <sup>-1</sup> )	Structure
Polyacetylene (PA)	n, p	10 <sup>5</sup> [24]	
Polyaniline (PANI)	n, p	10 <sup>2</sup> [25]	
Polypyrrole (PPy)	p	10 <sup>3</sup> [26]	
Polythiophene (PT)	p	10 <sup>3</sup> [27]	
Poly(3,4-ethylenedioxythiophene) (PEDOT)	n, p	10 <sup>3</sup> [28]	

The reversible redox process i.e. the ability to switch between the two states (neutral and oxidized/reduced) is then a property of conducting polymers. In addition to changing the conductivity, several other properties are dependent on the redox level, which allows their use in different applications such as supercapacitors, electrochromic devices and actuators. This work and the next sections will be focused on actuator related applications.

### 1.3 Electronically conducting polymer actuators

Electronically conducting polymer actuators are electromechanically active devices that are able to change their shape or size in response to the electrical stimulus. They are the most recent entry in the class of direct drive actuators but have attracted lots of interest due to their low operating voltages, relatively large forces and biocompatibility.<sup>[10]</sup> The next subsections will describe first the working principle of ECPs and different synthesis methods used in actuators field. Moreover, an overview of the ECP actuators will be given based on their operation environment (in solution and in open-air).

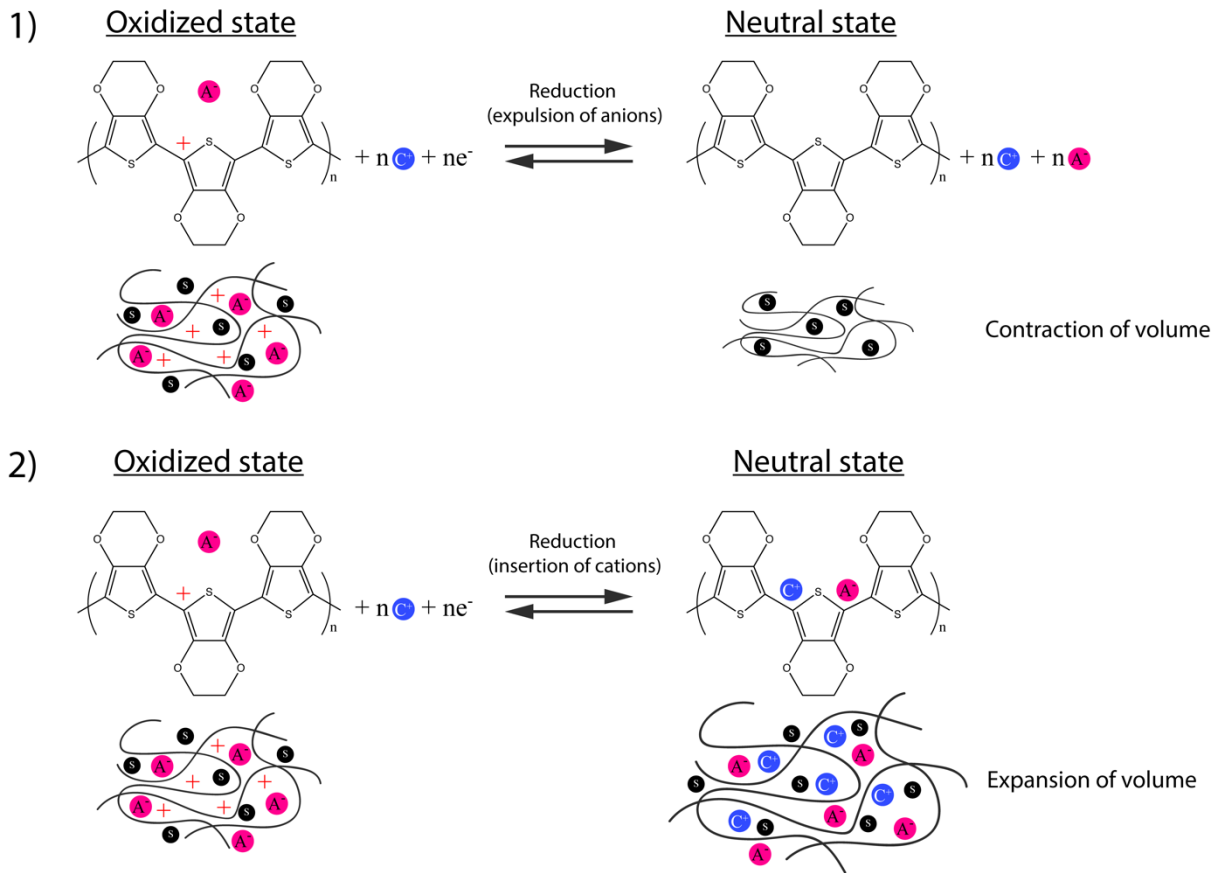
#### 1.3.1 Oxidation, reduction and the volume variation of conducting polymers

The working principle of ECP actuators is based on the electrochemically driven insertion or expulsion of ions, occurring during their reversible redox process. During the oxidation-reduction process, positive charges are created (p-doping) or removed (de-doping) from the polymer backbone. As a consequence of this charge modification, ions from a surrounding electrolyte are being inserted in or expelled from the polymer chains in order to maintain the charge neutrality. Consequently, this ion exchange mechanism induces the expansion or contraction of the polymer, leading to a volume variation of the ECPs.<sup>[29–31]</sup>

The switching between oxidized and reduced state can be achieved either by 1) expulsion of anions or 2) insertion of cations:

- 1) During oxidation of the conducting polymer, the electrochemically generated positive charges will be compensated by the insertion of anions (and accompanying solvent molecules) within the material, leading to a volume expansion. During reduction (de-doping), positive charges are removed and anions are expelled, leading to a volume contraction.<sup>[32,33]</sup>
- 2) If the polymer is doped during the synthesis with large and immobile anions, or if the mobility of anions is low compared to the one of cations, the opposite mechanism takes place. During oxidation, cations will be expelled from the material in order to maintain the electroneutrality, resulting in volume contraction. During reduction, cations are inserted among the polymer chains and a volume expansion can be observed.<sup>[34,35]</sup>

**Figure 4** illustrates these two reversible mechanisms during redox reaction with poly(3,4-ethylenedioxythiophene) (PEDOT) chosen as an example.



**Figure 4.** Volume variation mechanism of conducting polymers on an example of PEDOT.

In some cases, when both ions have comparable size and/or mobility, the two redox mechanisms can take place concomitantly or consecutively. This results in opposite volume variations and can lead to a decrease in final expansion/contraction.<sup>[36]</sup> In addition to the size and mobility of ions, then also the nature of the solvent and conformational changes in the polymer can affect the redox process and consequently also the volume changes.<sup>[37–39]</sup> In general, ion exchange mechanism is the main factor concerning the redox process and volume variation of ECPs. This unique volume changing characteristic of ECPs can be used for actuator applications.

The volume variation of electronically conducting polymers, i.e. the strain  $\varepsilon$ , depends on the injected volumetric charge density  $\rho$  ( $\text{C}\cdot\text{m}^{-3}$ ) of the ECP and on an empirical electromechanical coupling coefficient, so-called strain-to-charge ratio  $\alpha$  ( $\text{m}^3\cdot\text{C}^{-1}$ ), by the relationship:  $\varepsilon = \alpha\rho$ .<sup>[40]</sup> Therefore, high volume variation requires high electrochemical charge density, i.e. high number of expelled/inserted ions, and high elementary volume variation for each exchanged charge. The sign of  $\alpha$  depends on the involved mechanism. A positive value of  $\alpha$  corresponds to an anion mechanism, since during oxidation ( $\rho > 0$ ), the

insertion of the negatively charged ions in the ECP promotes an expansion and therefore a positive volume variation ( $\varepsilon > 0$ ). On the opposite, negative value of  $\alpha$  corresponds to a cation mechanism since during oxidation ( $\rho > 0$ ), the expulsion of the positively charged ions from the ECP promotes a contraction, resulting in a negative volume variation ( $\varepsilon < 0$ ).

### 1.3.2 Synthesis of conducting polymers for actuator purpose

There are several possibilities to synthesize conducting polymers, but the most commonly used and described methods in the literature for ECP actuators are the chemical and electrochemical oxidative polymerizations. Both of these methods lead to p-doped conducting polymers, i.e. in their oxidized state after synthesis. The choice of the method (chemical or electrochemical) has an effect on the resulting polymer's morphology, crystallinity, doping level, conductivity and molecular weight. Most commonly used and described ECPs for actuator applications are PANI, PPy and PEDOT.

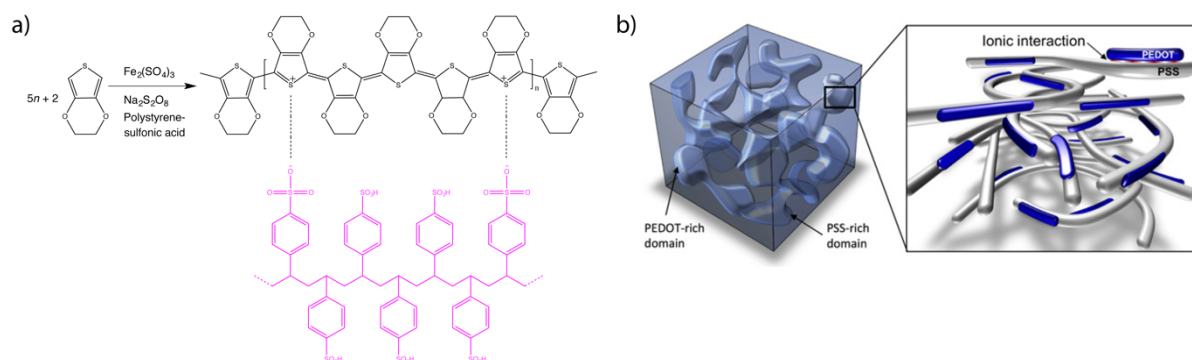
The electrochemical synthesis of ECPs is usually carried out employing the galvanostatic or potentiostatic method or by cyclic voltammetry. This synthesis method allows the control of wide range parameters, such as the nature of counter-ions, usually chosen according to the solubility in the chosen solvent, the polymerization temperature and the potential or current.<sup>[41]</sup> It is an effective process which allows reproducibility and more precise control on electropolymerization kinetics, morphology and the thickness of the resulting ECP layers. However, the process is limited to the synthesis on conducting substrates and large deposition areas can suffer from the lack of film uniformity. Usually thin metal layers are used in order to deposit the ECP layers. Recently, Temmer *et al.* proposed a different method for ECP actuators by replacing the metal layer with chemically oxidized PEDOT where afterwards PPy was electrochemically deposited.<sup>[36,42]</sup>

The chemical oxidative polymerization method is realized in the presence of a monomer (pyrrole, EDOT, etc.) and an oxidant. Most commonly used oxidants for chemical oxidation are iron (III) chloride ( $\text{FeCl}_3$ ) and iron (III) tosylate ( $\text{Fe}(\text{OTs})_3$ ). Using  $\text{FeCl}_3$  as the oxidant for the chemical oxidation, directly mixed with the monomer, results in highly conductive, but brittle and insoluble powder, which is usually not applicable for self-standing film or actuator fabrication.<sup>[41]</sup> Host materials are most commonly used for ECP actuators in order to obtain the ECP as a film. In this case, the host material is swollen with the monomer, which is then immersed into the oxidant solution and allows the formation of ECP film directly at

the interface of the host material.<sup>[43]</sup> Generally, the chemical oxidation is a cheap and facile method and the polymerization can be obtained on non-conductive substrates, which is not possible with electrochemical polymerization. On the contrary, it is hard to control and, in most routes, also hard to obtain homogeneous thin films.

Vapor phase polymerization (VPP) is another route of chemical oxidation, which is usually carried out by introducing the monomer vapor to the oxidant covered substrate. This polymerization method was first described by Mohammadi *et al.* in 1986 and allows the formation of thin and uniform ECP layers.<sup>[44]</sup> More detailed overview on vapor phase polymerized ECP layers and on different influencing parameters will be presented in the beginning of Chapter 2.

ECPs are also commercially available in the form of poly(3,4-ethylenedioxythiophene):poly(styrene sulfonate) (PEDOT:PSS) dispersion. This ink-type conducting polymer dispersion was first commercialized under the trade name of Baytron® and is currently manufactured by Heraeus under the trade name of Clevios™.<sup>[45]</sup> It is the most successful commercialized conducting polymer ink in terms of practical applications (conductive coatings, antistatic coatings, electroluminescent devices, capacitors, etc.). A deep blue PEDOT:PSS micro dispersion can be obtained through aqueous oxidative polymerization of the hydrophobic EDOT monomer in the presence of polystyrene sulfonic acid (PSS) (**Figure 5a**). The resulting aqueous mixture is a colloidal dispersion of PEDOT:PSS particles with hydrophobic and positively charged (doped) PEDOT core surrounded by hydrophilic and negatively charged PSS shell (**Figure 5b**).<sup>[46]</sup> The PSS has two functions in the PEDOT:PSS complex: i) it serves as the charge-balancing counter-ion for the doped PEDOT, and ii) it disperses and stabilizes the PEDOT particles in the water and other solvents.<sup>[41,47]</sup> The ink-type nature of PEDOT:PSS dispersion has the advantage of easy processing through various methods, such as drop casting, spray coating, spin coating and ink-printing techniques.<sup>[48–57]</sup> It possesses many unique properties, such as flexibility, intrinsic conductivity, biocompatibility and high chemical stability.<sup>[41]</sup> The electrical conductivity of PEDOT:PSS is influenced by different synthetic conditions, processing additives or post treatment techniques.<sup>[58–65]</sup>



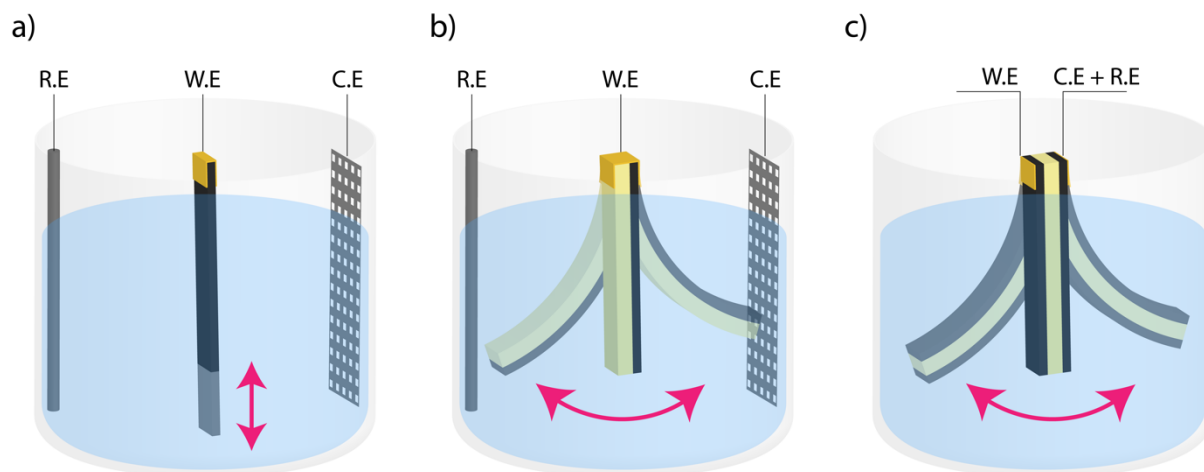
**Figure 5.** a) Oxidative polymerization of EDOT monomer in the presence of PSS and a primary structure of PEDOT:PSS.<sup>[66]</sup> b) scheme representing the morphology of PEDOT:PSS.<sup>[46]</sup>

### 1.3.3 Conducting polymer actuators operating in liquid electrolyte

The use of conducting polymers as actuators was first demonstrated by Baughman in 1990s (**Figure 6b**).<sup>[7,10,67]</sup> This actuator was constructed to operate in electrolytic solution in bending mode. Ever since, great advances and improvements in this field have been made and reported. Conducting polymer actuators can be divided into different categories based on: active ECP material, operating environment (in solution, open-air), number of layers (freestanding, bilayers, trilayers), motion type (linear or bending) and dimensions (nano-, micro-, macroscale). The overview of ECP actuators in these sections is based on their operating environment and will be discussed subsequently.

Conducting polymer actuators operating in liquid electrolyte can be constructed as freestanding films, bilayer actuators or trilayer actuators. The freestanding films (**Figure 6a**) were initially used in their most basic form to understand the fundamental performances of conducting polymers. The volume change of the ECP is isotropic, but if the configuration of the polymer is anisotropic as a film, a linear deformation can be obtained.<sup>[68,69]</sup> Different studies on linear actuation of ECPs will be detailed in the beginning of Chapter 5.

Bilayer actuators are usually two-layer structures consisting of a passive layer (constant volume) and an ECP layer (**Figure 6b**). The fabrication of a bilayer actuator is usually obtained by the electrochemical synthesis of conducting polymer layer directly on a substrate with a thin layer of sputtered metal.<sup>[11,70–72]</sup> The substrate, i.e. the passive materials can be a plastic or a piece of paper.<sup>[10,73–76]</sup> Another possibility to realize bilayer actuators is to fabricate both layers (passive and conductive) separately and later manually attaching them.<sup>[77,78]</sup>



**Figure 6.** Schematic view of different actuators operating in liquid electrolyte in three-electrode configuration: a) freestanding linear actuator, b) bilayer bending actuator and c) trilayer bending actuator.

The actuation of these freestanding and bilayer devices has to be performed in three-electrode configuration when immersed in liquid electrolyte. The ECP layer acts as a working electrode (W.E). Metal grids or wires (platinum, gold, silver, stainless steel) are usually being used as a counter electrode (C.E) and classical reference electrode (R.E) is added to control the potential of the system. The electrochemical oxidation/reduction of the W.E when applying potential difference or current results in reversible volume variation of the ECP layer and consequently leads to a linear (freestanding film) or bending (bilayer actuator) movement.<sup>[34,69,79–82]</sup>

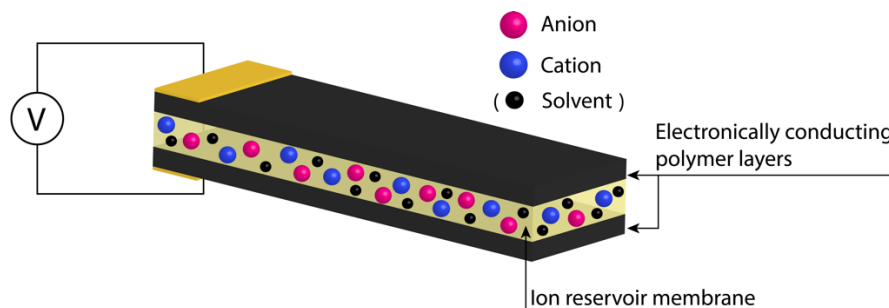
Two-electrode configuration can be used if the device is elaborated with a trilayer configuration. In this case, a second ECP electrode is deposited on the other side of the passive film (**Figure 6c**). One ECP layer is then connected to the W.E and the second ECP layer to the C.E + R.E. Electrical stimulation of the trilayer, still immersed in electrolyte, promotes opposite electrochemical reactions in the electrodes, one being oxidized (anode) while the second one (cathode) is concomitantly reduced. As a consequence, one layer expands while the other one contracts, leading to the bending movement of the actuator.<sup>[83,84]</sup> Trilayer configuration has the advantage of producing higher output forces compared to the bilayer actuator due to the presence of the two electrodes instead of one. However, the operation in liquid electrolyte may reduce their potential areas of applications.<sup>[78,85]</sup>

#### 1.3.4 Conducting polymer actuators operating in open-air

Air-operation of ECP actuators allows broadening their application field. Since these ionic actuators require an ion source in order to operate, the strategy was to replace the previously



described passive film for trilayer configuration with an ionically conducting film, behaving as an ion reservoir. In other words, the necessary ions are incorporated directly in the self-standing trilayer device. (**Figure 7**).



**Figure 7.** Schematic view of a trilayer actuator for operating in open-air.

The redox process takes place in the same way as for the trilayers in the liquid electrolyte, except that the ion exchange occurs between the electrodes with the electrolyte directly included in the separator membrane. When applying a potential, the ions will be inserted into one ECP layer and expelled from the other ECP layer resulting in an open-air bending movement of the actuator. The ion reservoir membranes and the open-air trilayer actuators will be described in the following sections.

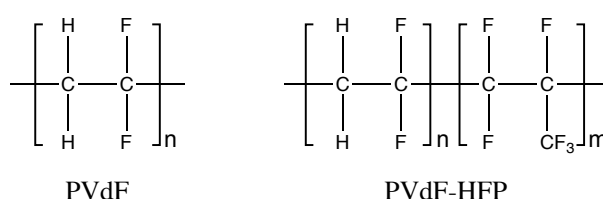
#### 1.3.4.1 Ionic membranes for conducting polymer actuators

Different ECPs (PPy, PEDOT, etc.) and different ion reservoir membranes (gel electrolyte, porous membrane filled with electrolyte, solid polymer electrolyte) have been used for actuator fabrication.<sup>[79,86–90]</sup> The ion reservoir membrane has an important role in the actuator configuration by providing the system with ionic conductivity and mechanical properties. Nowadays, most commonly used ion reservoir membranes for actuators are based on microporous poly(vinylidene fluoride) (PVdF) containing electrolyte, based on single networks or on interpenetrating polymer network (IPN) architecture swollen with electrolyte.

Poly(vinylidene fluoride) (PVdF) and its copolymers (**Figure 8**) are widely used as porous membranes mainly for filtration purposes.<sup>[91,92]</sup> For actuation applications, they are mostly used because of their commercial availability allowing fast and simple actuator fabrication and because of their porous nature allowing strong anchoring of the ECP layer to avoid delamination issues. PVdF is a semi-crystalline polymer with the repeat unit of  $-(\text{CH}_2\text{CF}_2)_n-$ , presenting high mechanical strength and stability, good chemical resistance and is often used as a commercial thermoplastic membrane (Millipore®).<sup>[93]</sup> This polymer presents good



compatibility with liquid electrolytes, which simply fill the porous structure without solvating the membrane. The porous copolymer poly(vinylidene fluoride)-*co*-hexafluoropropylene (PVdF-HFP) is often used for electrochemical applications due to good electrochemical stability.<sup>[94,95]</sup> PVdF-HFP has both, crystalline VdF and amorphous HFP units. The crystalline phase provides the structural properties to support a freestanding film and the amorphous phase is capable of trapping large amount of electrolyte which contributes to increasing the swelling rate of the polymer and then, provides with the ionic conductivity.



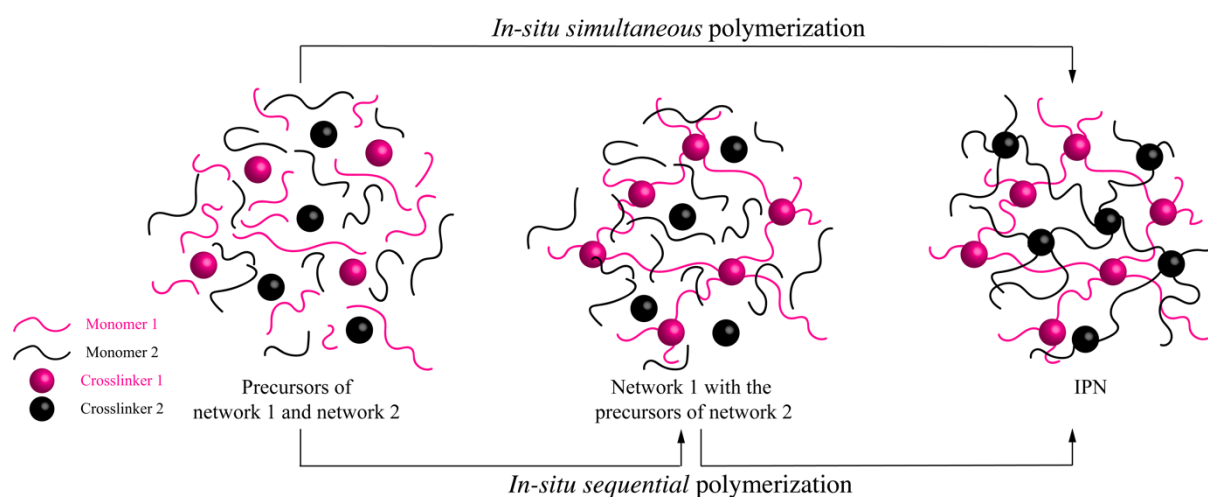
**Figure 8.** Chemical structures of poly(vinylidene fluoride) (PVdF) and poly(vinylidene fluoride)-*co*-hexafluoropropylene (PVdF-HFP).

The use of single networks for ion reservoir membranes has been demonstrated by different research groups. The first ion reservoir membrane for open-air actuators was developed by Sansiñena *et al.* and was based on poly(epichlorohydrin-*co*-ethylene oxide) [P(ECH-*co*-EO)] and lithium perchlorate (LiClO<sub>4</sub>).<sup>[86]</sup> The resulting gel-like membrane presented good ionic conductivity but relatively poor mechanical properties. Vidal *et al.* demonstrated the fabrication of dangled chain PEO network since it favors ionic mobility.<sup>[43]</sup> The single PEO network was obtained by free radical copolymerization of poly(ethylene glycol) dimethacrylate (PEGDM) and poly(ethylene glycol) methyl ether methacrylate (PEGM), later swollen in 0.1 M LiClO<sub>4</sub> aqueous solution. However, the resulting material presented poor mechanical properties due to the brittle nature of PEO and was not satisfying as an ionic reservoir membrane for actuator fabrication. Cho *et al.* proposed the use of high molecular weight nitrile butadiene rubber (NBR) network swollen in ionic liquid as an ionic membrane for actuator fabrication.<sup>[96,97]</sup> The presence of NBR could fulfill the mechanical requirements, but the membrane's ionic conductivity was not sufficient for the use as an ionic reservoir. The use of polyurethane (PU) containing Mg(ClO<sub>4</sub>)<sub>2</sub> as an ion reservoir membrane was demonstrated by Choi *et al.*<sup>[98]</sup>, however with poor ionic conductivity. The ionic conductivity of the similar PU system was further improved by the group of Okuzaki by using ionic liquid (IL) as an electrolyte to develop IL/PU gels suitable for the actuator fabrication.<sup>[99,100]</sup>

Another commonly used ionic membrane for actuators is based on interpenetrating polymer network (IPN) architecture containing an electrolyte. IPNs are defined as the combination of

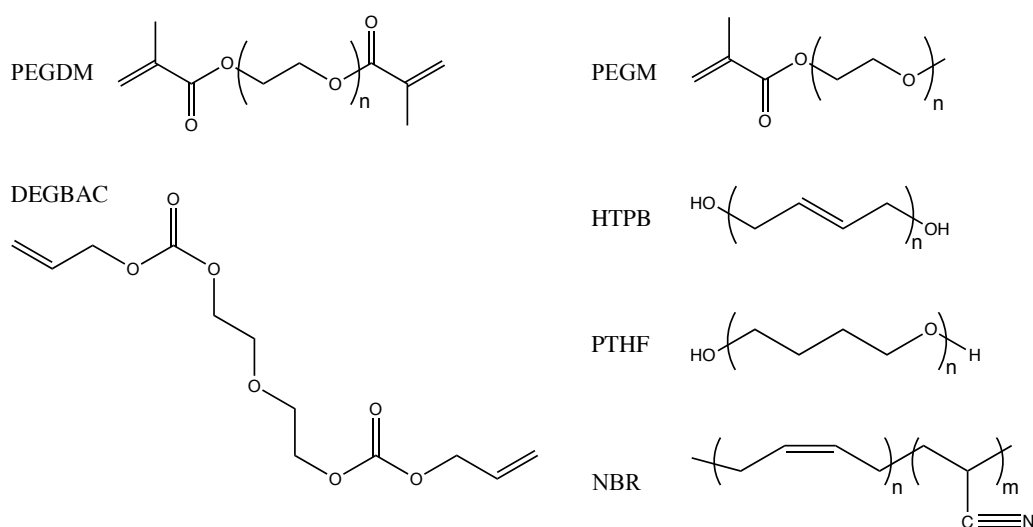
two or more crosslinked polymers, synthesized in the presence of each other.<sup>[101,102]</sup> It is the only way to combine crosslinked polymer networks and provide usually good dimensional and morphological stability. Depending on their synthesis pathway, the relative weight ratio of components and their relative crosslinking kinetics, different morphologies can be obtained. In order to combine the intrinsic properties of each polymer partners, co-continuous morphology across the material is usually desired. Semi-IPNs can also be obtained if one of the polymer partners is not crosslinked. In this case, it remains as linear macromolecules interpenetrated and trapped in the crosslinked structure of the second network.

There are many ways to synthesize IPNs. In the *sequential pathway*, the precursors of the second network (monomer 2, crosslinker, initiator) are introduced, usually by swelling, and subsequently polymerized in an already formed single network of the first partner. In the *in-situ pathway*, all the precursors, i.e. monomers, crosslinkers, initiators and/or catalysts, are mixed together, eventually with a solvent, and polymerized. Polymerization of both networks can be performed simultaneously or sequentially. When networks are polymerized simultaneously, it corresponds to the *in-situ simultaneous pathway*. It must be mentioned here that non-interfering polymerization mechanisms are used, like free-radical polymerization for one network and polycondensation for the other one. If networks are polymerized sequentially, it corresponds to the *in-situ sequential pathway*. In this case, polymerization mechanism can be similar but monomers have to present significantly different reactivity. (**Figure 9**).



**Figure 9.** Schematic view of the two polymerization routes to fabricate IPNs from the precursors of the network 1 and the network 2.

First IPN-based membrane for ionic reservoir in actuator application was elaborated as poly(ethylene oxide) (PEO)/polycarbonate (PC) IPN, obtained by *in-situ sequential* polymerization. From a reactive mixture containing all the network precursors, PEO network was obtained by free radical copolymerization of poly(ethylene glycol) dimethacrylate (PEGDM), poly(ethylene glycol) methyl ether methacrylate (PEGM) and PC network by free radical polymerization at higher temperature of the less reactive monomer di(ethylene glycol) bis(allyl carbonate) (DEGBAC).<sup>[90]</sup> Unfortunately this membrane was not suitable for long life operation of the actuator due to the brittle nature of PEO and PC and finally poor mechanical properties of the resulting IPNs after swelling with electrolyte. Optimized materials were proposed later by replacing the glassy PC network by those based on elastomers, such as polybutadiene (PB),<sup>[103,104]</sup> polytetrahydrofuran (PTHF)<sup>[105]</sup> and NBR<sup>[106]</sup>. When phase co-continuity is obtained, PEO phase can act as an efficient ionic conducting medium while elastomer phase acts as mechanical reinforcement due to its rubber properties. Upon swelling in an electrolyte, the resulting membrane can be used as ionic reservoir for actuators. Ionic conductivities up to  $10^{-3}$  S.cm<sup>-1</sup> and strain at break above 150% have been demonstrated. These results demonstrated the advantage of IPN architecture in the synthesis of highly ionically conductive and robust ion reservoir membranes by combining the intrinsic properties of each partner. All the chemical structures of these used polymers are brought in **Figure 10**.



**Figure 10.** Chemical structures of PEGDM, PEGM, DEGBAC, HTPB, PTHF and NBR.

### 1.3.4.2 Trilayer conducting polymer based bending actuators

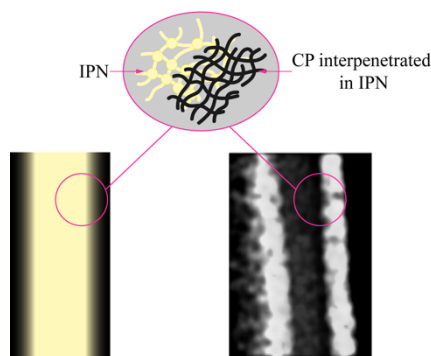
The first trilayer actuator, operating in open-air was described by MacDiarmid group in 1994.<sup>[107,108]</sup> This electrochemical actuator consisted of two PANI films which were affixed on both sides of double sided cellophane tape and wetted in hydrochloric acid aqueous solution. The deformation of the actuator at maximum bending was estimated to be approximately 1 % with an applied voltage of 4.0 V. Few years later, the wetted cellophane tape was replaced by gel-like membrane in order to fabricate all-polymer actuator.<sup>[86]</sup> The polymeric electrolyte solution was dropped on two electropolymerized PPy electrodes, which were affixed together after solvent evaporation. The actuator resulted in 90° angular bending and demonstrated an efficient fabrication of all polymer actuator.

The development of actuators has overcome different problems related to the mechanical properties or lifetime of the actuators. The gel electrolytes that were used as ion reservoir membranes for actuators were mostly insufficient due to poor mechanical properties. Another common problem was the use of electrolytic solutions (salt/organic solvent or salt/water) which were limiting the lifetime of the actuators due to the solvent evaporation. This issue can be solved if an ionic liquid is used as an electrolyte. Ionic liquids are salts in liquid state at ambient temperature.<sup>[109]</sup> They present large electrochemical windows, high ionic conductivity, do not require the use of any additional solvent, are non-volatile but also non-flammable.<sup>[110]</sup> They have been described for the first time in 2002 by Lu *et al.* as electrolytes for  $\pi$ -conjugated polymer electrochemical devices with enhanced lifetime (up to 1 million cycles).<sup>[88]</sup> In 2003, ionic liquids were used in actuator application for linear systems operating in solution<sup>[111]</sup> and for open-air bending trilayers.<sup>[89]</sup> Since then, many systems have been described and demonstrated high lifetime of the resulting actuators.<sup>[112]</sup>

The second issue was related to the delamination occurring at the interfaces of the layers due to the repeated electromechanical deformation of ECP electrodes. This problem has been solved thanks to several approaches at the same period than the introduction of ionic liquids. First, as mentioned earlier, the use of microporous PVdF membranes helped to improve the anchoring of the ECP layers on the central membrane.<sup>[89]</sup> For instance, Zhou *et al.* electropolymerized Py onto previously platinized commercial PVdF membrane.<sup>[89]</sup> Combined with the use of ionic liquids, the resulting PPy/PVdF/PPy trilayer actuators demonstrated 90° bending to either side and exceeded more than 3600 cycles without any obvious delamination between the electroactive PPy and the platinized PVdF layers. The use of commercially

available PVdF membranes with defined thickness and dimensions may limit the possibility of tuning the geometry and performances of the resulting actuators. To overcome these issues, Gaihre *et al.* demonstrated the possibility to control the porosity and final thickness of home-made PVdF membrane for actuator applications.<sup>[113]</sup>

Delamination problem of the layers was also solved according to another approach by the synthesis of conducting IPNs (C-IPNs).<sup>[43,103,112,114]</sup> Instead of depositing ECP layer on top of already fabricated membrane, ECP layers are interpenetrated within the membrane with their concentration decreasing from the surface to the central part of the film. Providing that no electrical connection occurs between the two electrodes, one-piece pseudo-trilayers are obtained, resolving *de facto* any delamination problem. This 3D interface, compared to the 2D interface of classical trilayer systems, may also improve the charge exchanges between the ECP electroactive layers and the ion reservoir membrane. Interpenetration of the electrodes was realized by chemical oxidative polymerization of EDOT with 1.5 M FeCl<sub>3</sub> aqueous solution in two steps. First, the EDOT monomers are introduced in the membrane by swelling and the resulting swollen membrane is immersed in oxidant solution. Due to opposite diffusion processes, i.e. desorption of the EDOT from the membrane and absorption of the oxidant in the membrane, polymerization occurs within the surface of the membrane, resulting in the expected pseudo-trilayer configuration. (**Figure 11**).



**Figure 11.** Conducting interpenetrating polymer network (C-IPN): schematic view of the configuration and EDX mapping of sulfur (white) corresponding to PEDOT.<sup>[105]</sup> In this example, the ion reservoir membrane displays an IPN macromolecular architecture.

The first C-IPN actuators, operating in open-air were introduced by the LPPI group in 2002, but low life time was reported due to the appearance of cracks during bending deformation.<sup>[90]</sup> In this case, the ion reservoir membrane was already an IPN combining PEO network and polycarbonate (PC) network, as mentioned earlier, the interpenetrated ECP electrodes were made of PEDOT and the electrolyte was LiClO<sub>4</sub>/H<sub>2</sub>O. Brittleness of these

first C-IPN actuators was solved by the synthesis of robust ionic membranes, and more specifically by replacing the vitreous PC network by short chain elastomer networks, such as PB<sup>[112,115]</sup>, PTHF<sup>[105]</sup> or PEO<sup>[116]</sup>. The synthesis of C-IPNs has also been described from single network of high molecular weight rubber, such as NBR<sup>[96,97]</sup> and by PEO/NBR IPNs<sup>[117]</sup>. With the use of ionic liquids, strains up to 2.4 % under  $\pm 2.0$  V, forces in the range of tens of mN (depending on device dimensions) and high life time (up to  $7 \times 10^6$  cycles at a frequency of 10 Hz) have been obtained. It is also interesting to mention that C-IPN architecture provides a control on the mechanical and electromechanical properties of the electrodes. Indeed, ECP chains are surrounded by other macromolecular chains in C-IPNs. As a consequence, a modification of ECP local concentration in the electrodes<sup>[118]</sup> or the introduction of another polymer partner<sup>[119]</sup> appears as a powerful tool for tuning the Young's modulus and the volumetric charge density of the electrodes, in order to control the final performances of the devices.

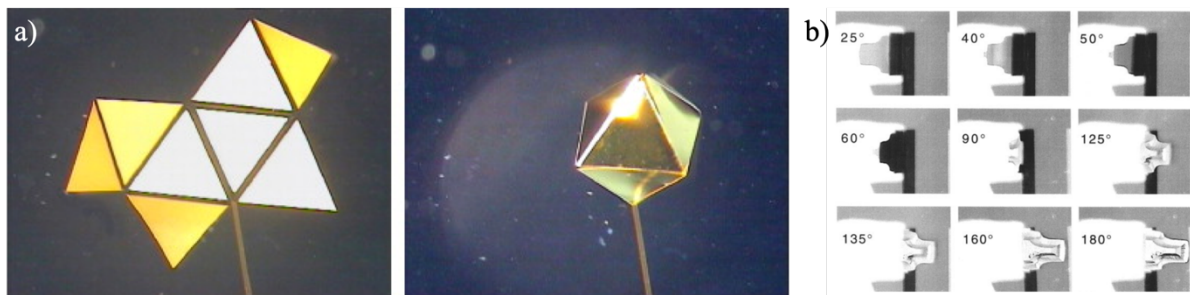
## 1.4 Electronically conducting polymer microactuators

Electronically conducting polymer based microactuators are promising candidates to enable broad range of applications for new generation of soft microsystems where large strains and forces are required. The concept and possible designs of micro electromechanical actuators based on ECPs was first described by Baughman in 1991.<sup>[120]</sup> He conceptually analyzed materials properties and device designs based on experimental verifications on a macroscale to propose different approaches for fabricating ECP microactuators. Then, the combination of different microfabrication technologies (photolithography, etching techniques, metal deposition methods and laser ablation) has allowed the design and fabrication of conducting polymer based microsystems with the variety of configurations for different purposes. The next subsections will give an overview of ECP microactuators based on their operation environment (in solution and in open-air).

### 1.4.1 Microactuators operating in electrolytic solution

The first microactuators were developed in bilayer configuration and operated in electrolytic solution. Smela *et al.* reported a work on bilayer strips of gold (Au) and dodecylbenzenesulfonate (DBS) doped polypyrrole (PPy) in 1993.<sup>[70]</sup> They used standard photolithography of positive photoresist S1828 to fabricate millimeter scale polymer fingers. After the dissolution of sacrificial layer, the polymer fingers were connected to the Si wafer

at one end but were free for the movement at the other. These fingers were stimulated in 0.1 M NaDBS aqueous solution and resulted in curling and uncurling with a response time of approximately 5 seconds. The same authors presented the possibility of more complex configuration by combining the same DBS doped PPy and Au bilayers with stiff parts.<sup>[81]</sup> The realization of these devices was done by combining standard photolithography, wet chemical etching and reactive ion etching (RIE). This work also demonstrated the differential adhesion method to release the bilayers by pulling themselves off from the substrate when the electrical stimulation was applied. These microactuators with rigid elements had a configuration of an unfolded box. During electrical stimulation in NaDBS solution, the bilayer hinges achieved 180° bending allowing the planar configuration microsystem to fold into an octahedron configuration (**Figure 12a**). Smela continued the research and demonstrated the fabrication of microsystems with a different release method.<sup>[121]</sup> The microactuator was fabricated using many different microfabrication technologies with the combination of standard photolithography, RIE, wet chemical etching, chemical vapor deposition (CVD) and metal evaporation. The novelty of this fabrication method was the release of the microsystems by finally etching through the Si wafer. These microsystems were electrically stimulated in NaDBS solution and the PPy/Au bilayer hinges were capable of lifting and positioning rigid Si and benzocyclobutene (BCB) plates (**Figure 12b**).

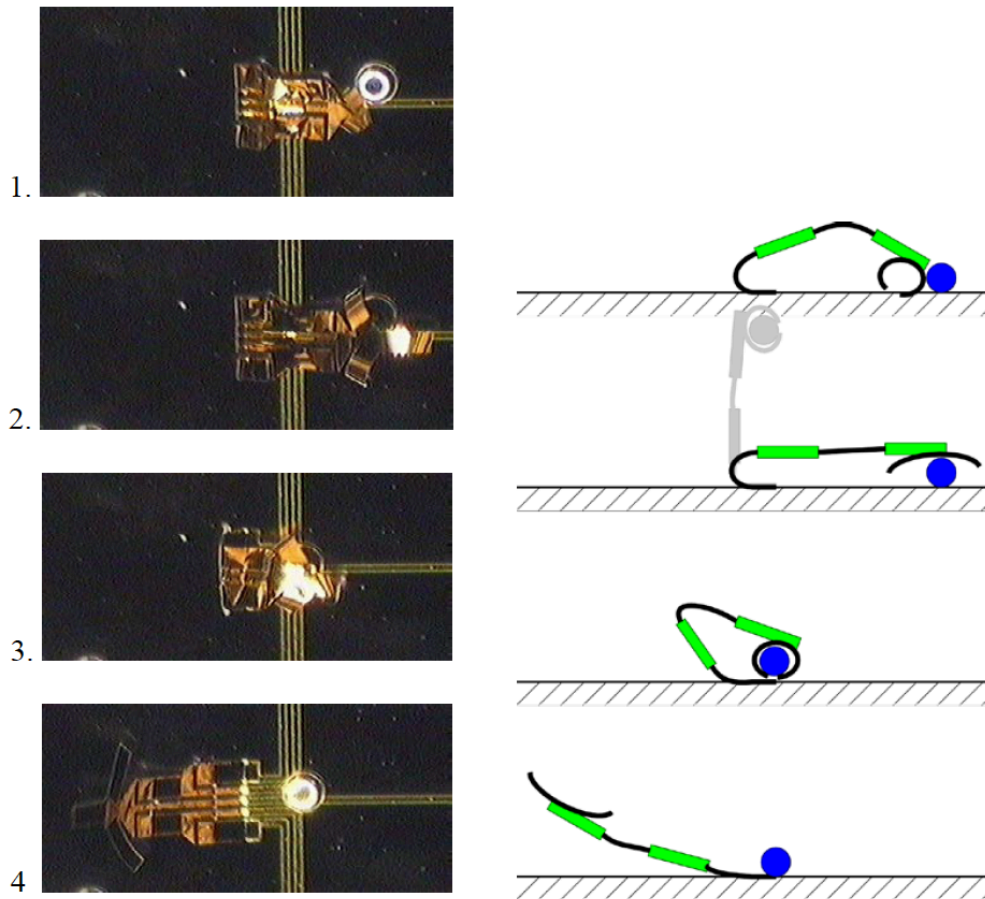


**Figure 12.** a) Octahedron of PPy/Au bilayer hinge microactuators with rigid elements by M. Krogh *et al.*, Micromuscle AB, inspired by Smela *et al.* <sup>[81]</sup> and b) rocket-shaped Si plate being positioned by PPy/Au hinges.<sup>[121]</sup>

Jager *et al.* demonstrated the fabrication of different microstructures for different purposes. They fabricated on-chip microsystems based on moveable PPy/Au bilayers with all the necessary electrodes (working, counter and reference) directly on a chip.<sup>[122]</sup> They found that the speed of the microactuators was the same compared to the usual device where macroscale electrodes were used. The next work proposed more complex design of micro robot arm, consisting of an elbow, a wrist and a hand with fingers.<sup>[71]</sup> The joint parts were made of PPy/Au bilayers that were connected to stiff elements of benzocyclobutene (BCB). Different



joints were stimulated separately, allowing the microarm to move, to grab and lift a 100  $\mu\text{m}$  glass bead and to move it over a distance of 200-250  $\mu\text{m}$  (**Figure 13**). The design and operation ability in different environments (salt solutions, blood plasma, urine and cell culture medium) makes them attractive for biomedical applications. Over the years they reported studies on different designs of microstructures as microfluidic system, cell clinic and microactuators for different biomedical applications.<sup>[11,123–125]</sup>



**Figure 13.** Microrobot arm grabbing and lifting 100  $\mu\text{m}$  glass bead: a) photos; b) schematic representation.<sup>[71]</sup>

Fairly simpler procedure of PEDOT:PSS based bilayer microactuator was proposed by Taccola *et al.*<sup>[126]</sup> The PEDOT:PSS/SU-8 bilayers with a final thickness of less than 600 nm were constructed by standard photolithography of SU-8 and wet chemical etching of PEDOT:PSS. The contacts were also included to the system but manually wiring, after the fabrication of the microstructures. The system consisted of many fingers, which were stimulated at the same time in NaDBS aqueous solution and resulted in displacement from 220 to 2090  $\mu\text{m}$ . The fabrication of all polymer PEDOT:PSS based microactuator presented the novelty of using spin-coating technique for the first time to deposit ECP layer.



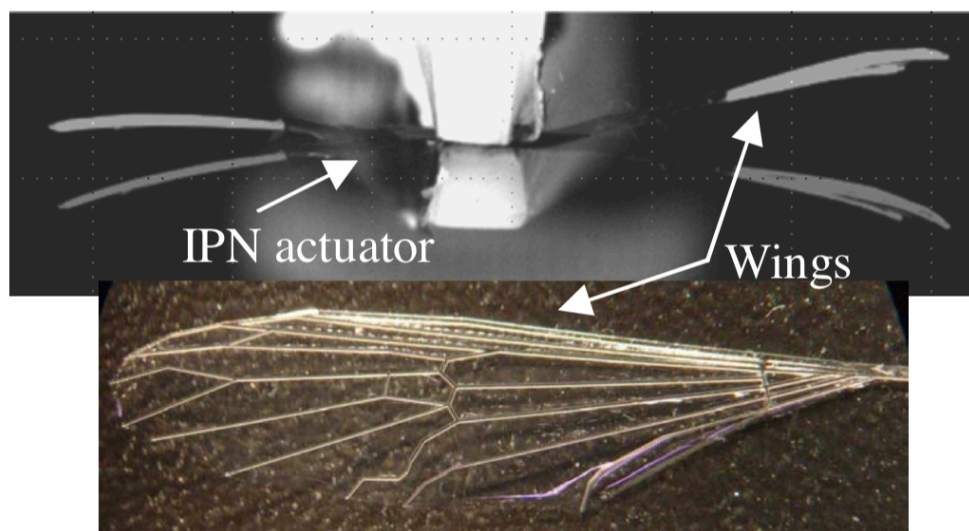
These bilayers have been integrated into complex microsystems for various applications during past few decades. The operation in liquid electrolyte, especially in salt solutions, blood plasma, urine and cell culture medium, is mostly advantageous for biological and biomedical applications. In order to broaden the application field, the microactuator needs to be able to operate in open-air. As mentioned before, for operation in open-air, the actuator needs to have a trilayer configuration with two electroactive electrodes sandwiching an ion storage membrane.

#### 1.4.2 Microactuators operating in open air

The first air-operating microactuator was demonstrated by Alici *et al.* in 2009.<sup>[127]</sup> The microactuator was fabricated as a conventional macroscale actuator using a commercial PVdF membrane with a thickness of 110  $\mu\text{m}$  and electropolymerizing PPy electrodes on both sides of the Au coated PVdF membrane. The downscaling of the device was performed using laser ablation technique, resulting in microactuators with dimensions 799 x 217 x 155  $\mu\text{m}$  (length x width x thickness). Gaihre *et al.* presented the synthesis of PVdF thin films in order to decrease the final thickness of these PPy microactuators to 54  $\mu\text{m}$ .<sup>[128]</sup> After synthesizing thinner PVdF films, they found that the actuator (850 x 250 x 54  $\mu\text{m}$ ) with PVdF membrane containing 0.05 M LiTFSI resulted in highest tip displacement of 0.253 mm.<sup>[113]</sup> They also demonstrated that miniaturization of the actuators resulted in higher strain energy per unit of mass or volume.<sup>[129]</sup> These trilayer microactuators were simple and obtained by laser ablation technique or by manually cutting, later operated in the same manner as macroscale actuators, manually connecting the PPy microactuators to the macroscopic measurement system.

Using similar PPy-Au-PVdF based trilayer actuators, Jager *et al.* proposed a method to fabricate individually controllable actuators on a commercial flexible printed circuit board (FPCB).<sup>[130]</sup> The fabrication of the millimeter scale actuators involved patterning of the Au on both faces of the PVdF membrane by flipping the substrate using wet chemical etching. Subsequently, the PPy electrodes were electropolymerized on the Au patterns simultaneously, resulting in trilayer actuators. The interface was fabricated separately and manually connected later with the resulting actuators. The actuators, 9 mm long and 2 mm wide, with FPCB interfacing resulted in 18 mm tip displacement when stimulated under 1.5 V.

Another actuator composition and microfabrication method was proposed by Khaldi *et al.*<sup>[131,132]</sup> The microactuator was fabricated as a C-IPN composed of PEO/PTHF IPN as the ion reservoir membrane and PEDOT interpenetrated electrodes. The low thickness of the resulting trilayer actuator (12  $\mu\text{m}$ ) allowed the use of RIE for patterning the actuators. The trilayer structure was manually placed on PVA sacrificial layer in order to maintain it fixed and planar during the etching process, using photoresist as a mask. RIE of the trilayer PEDOT/PEO/PTHF actuator was performed in 90/10  $\text{O}_2/\text{CF}_4$  plasma. After the etching, microbeams were swollen in ionic liquid EMImTFSI before the characterization. The microbeams with the dimensions of 900 x 300 x 17 $\mu\text{m}$  resulted in large displacement amplitude of 950  $\mu\text{m}$ , corresponding to the strain of 1.1%. The same author optimized the thickness of these actuators and glued SU-8 parts on the microbeams to mimic the wings of a crane fly (**Figure 14**).<sup>[133]</sup> This work demonstrated improvement of the actuation frequency of 50 Hz, compared to the previous 0.05 Hz.



**Figure 14.** Conducting IPN with SU-8 wings to mimic crane fly wings.<sup>[133]</sup>

Further decrease of the thickness was demonstrated by Maziz *et al.* by the fabrication of C-IPN based trilayer microactuators with an interpenetrating polymer networks of PEO and nitrile butadiene rubber (NBR).<sup>[134,135]</sup> The PEDOT electrodes were here also obtained through chemical oxidative polymerization on both sides of the PEO/NBR layer. The involvement of spin-coating step into the fabrication process allowed tuning the thickness of the membrane layer from 600 nm to 30  $\mu\text{m}$ . The actuators were patterned using standard photolithography and RIE, resulting in microactuators with final thicknesses of 6, 12 and 19  $\mu\text{m}$ . These microactuators demonstrated strain differences up to 0.9 % and output forces in

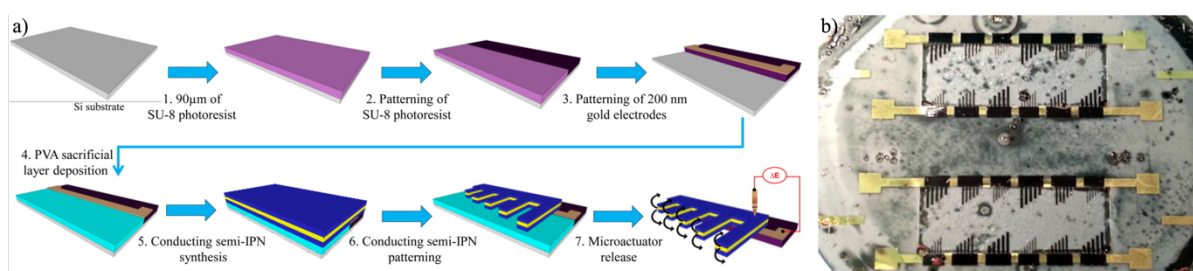
the range of  $\mu\text{N}$ . More importantly, reducing the final thickness of the microactuators allowed demonstrating actuation at high resonant frequency of 930 Hz.

Recently another interesting work was demonstrated by Khaldi *et al.* about patterning techniques for conducting polymers.<sup>[136]</sup> They presented two patterning methods: micro-Contact Printing ( $\mu\text{CP}$ ) and syringe-based printing. The PDMS stamp was used for  $\mu\text{CP}$ , where an oxidant solution layer was deposited through the stamp on PVdF membrane and followed by the vapor phase polymerization (VPP) of EDOT, resulting in well-defined micro-patterned electrodes. The PDMS stamp and  $\mu\text{CP}$  allow patterning of the device architecture in a single step with individually controllable actuators, wires and contact pads. Unfortunately, they did not succeed to use this technique on PEO-NBR membrane due to the insufficient affinity between the oxidant solution and the PEO-NBR membrane. Syringe-based printing requires different affinity and the PEO-NBR membrane was found to be suitable for this process. They fabricated the trilayer actuator based on layer stacking method. First, an oxidant solution was deposited in a desired shape using syringe-based printing followed by the EDOT VPP. The PEO-NBR network precursors were deposited through spin-coating, followed by a short curing and the second electrode was obtained in the same way as the first one. The final systems were cut out from the membrane using laser ablation and fabricated milli/micro hand actuator resulted in 2.2 % strain difference, stimulated at  $\pm 2.0$  V with a thickness of 70  $\mu\text{m}$ . This work proposed printing methods that have not been used so far for microactuator fabrication. Nonetheless, electrical connections were not integrated to the system requiring the use of macroscopic connections to electrically stimulate the resulting microactuators.

Except the work of Jager, then all the reported attempts on air-operated microactuators have been reported without the integration of electrical connections. As said before, in order to fabricate an efficient microsystem, electrical contacts have to be integrated in the system, and ideally directly during its fabrication, to connect the actuator with an electrical supply. For this purpose, Khaldi *et al.* proposed a bottom-up process to fabricate a system with an individual control of the system.<sup>[137,138]</sup> The process combined standard photolithography, wet chemical etching, evaporation and sputtering. The reported work proposed a fabrication of millimeter scale actuators, resulting in relatively low strain of 0.01 % at  $\pm 1.0$  V. Even though the fabrication process was successful and two electrical connections were incorporated, then

the final samples were manually cut out of the substrate which makes it harder to manipulate, if the sample dimensions will be decreased.

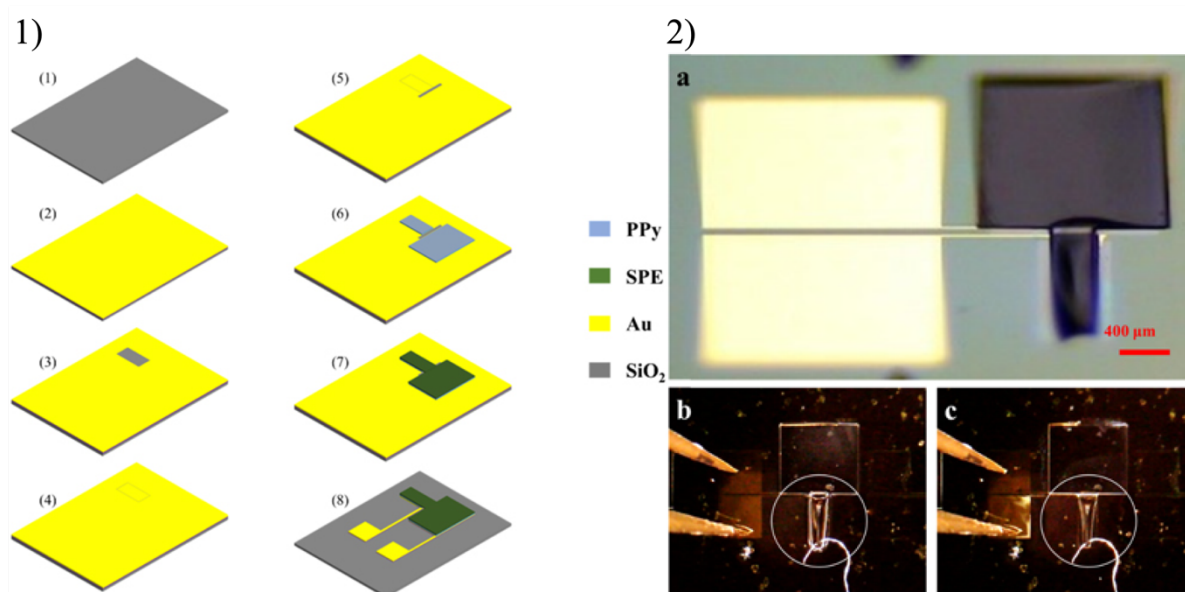
On the other hand, Maziz *et al.* reported a microactuator fabrication method on a flexible substrate, called top-down approach.<sup>[139]</sup> This process is the first one to integrate one electrical connection into open-air actuating microdevice without any kind of manual handling, using different microsystem technologies. The realization of the trilayer actuator was performed using layer stacking method, i.e. by sequentially stacking layers on top of the previous layers. Using spin-coating to deposit the layers allows precise control over the thickness of each layer and allow the fabrication without any manual handling during the synthesis. The PEDOT electrodes were obtained through EDOT vapor phase polymerization (VPP) and the membrane layer through radical polymerization of spin-coated PEO-NBR solution precursors. The PEDOT/PEO-NBR/PEDOT trilayer microactuators were fabricated on a SU-8 substrate with bottom electrical contact by combining standard photolithography, evaporation and RIE (**Figure 15**). The second contact was obtained by placing a micromechanical gold tip on top of the trilayer. The microactuator ( $650 \times 100 \times 10 \mu\text{m}$ ) was electrically stimulated in air ( $\pm 4.0 \text{ V}$ ) and resulted in the strain difference of 0.13% and an output force of  $0.75 \mu\text{N}$ . This work presented a great improvement compared to the previous works with full integration of bottom electrical contact and subsequent operation on a soft substrate without any manual handling and resulted in a functioning microactuator after all the microfabrication processing steps. The disadvantage of this method remains in the absence of the second electrical contact from the top of PEDOT electrode, requiring manual connection of this electrode for the characterization and relatively low performances.



**Figure 15.** a) overview of the fabrication steps and b) photograph of the microactuators fabricated with layer stacking method and with integrated bottom electrical contact.<sup>[139]</sup>

The most recent study in this field is demonstrated by Zhong *et al.*<sup>[140]</sup> He first demonstrated the fabrication of photopatternable ionic reservoir membrane composed of bisphenol A ethoxylate dimethacrylate (BEMA) and poly(ethylene glycol) methyl ether methacrylate

(PEGMA) networks with the necessary ions for the redox process directly incorporated before the photopolymerization. The microsystem was realized by locally electropolymerizing PPy electrodes in photoresist holes on a gold coated wafer. Subsequently, the membrane was micropatterned locally on top of the PPy layer using photolithography, resulting in bilayer microactuators. The final release was performed by wet chemical etching to form the device layout. After the etching, the working electrodes were movable but still attached to the wafer. The final microdevice was fabricated with parallel electrode configuration. In this case, the working and counter electrodes were placed parallel under the actuator, between which the ions were shuttled during the electrical stimulation (**Figure 16**). This novel method and the development of the photopatternable ionogel would be advantageous for microstructure fabrication. Although the novel fabrication method was reported, then the performances of the actuators were almost non-existent, probably due to the low ionic conductivity of the BEMA gel after all the processing steps.



**Figure 16.** Solid-state polypyrrole microactuator: 1) overview of the fabrication steps and 2) photographs of the microactuator a) as fabricated; b) and c) actuation results showing folding motion.<sup>[140]</sup>

## 1.5 Conclusion and problem statement

The bibliography chapter gave an overview of the basics for the following chapters of this thesis. First, the structure, synthesis and working mechanism of the ECPs was described and the possibility to use them as active layers for the actuator fabrication. The development of ECP based actuators is advanced over the years, where different configurations (freestanding films, bilayers, trilayers) in different operating environments (in solution and open-air) have

been reported. More interestingly in the framework of this thesis, their potential use as microactuators for different micro applications has been demonstrated.

The goal of this work is to fabricate efficient microactuators with simple elaboration process and their further integration into microsystems. The study on microactuators has improved a lot during the last few decades to fabricate complex devices for different applications with different microfabrication technologies, but there are still several possible improvements. The reported microactuators operating in open-air present still too low performances, preventing their use in practical applications. Moreover, until now there is no reported publications yet on fabricating functioning and individually controllable microactuators with two integrated electrical connections directly in contact with the top and bottom electrodes without any kind of manual handling during the fabrication process. Additionally, the sensing behavior has been demonstrated at macroscale but never investigated or demonstrated on microscale devices. For this purpose, the developed layer stacking method of Maziz is taken as the starting point of this thesis to elaborate more simple and efficient fabrication process with improved performances of the resulting microactuators and their further integration into microsystems. The challenges, possible solutions and results will be discussed in more details in the following chapters.

Chapter 2. Optimization of PEDOT  
electrodes for layer stacking  
method via VPP



**Foreword:** *Layer stacking method was developed in order to fabricate self-standing microactuators with one integrated electrical contact directly on a flexible substrate without any manual handling during the process. The process included the fabrication of electroactive poly(3,4-ethylenedioxythiophene) (PEDOT) layers using vapor phase polymerization (VPP) in order to obtain thin electrodes. However, the resulting microactuators presented low performances, limiting their use in practical applications. For that reason, the previously described layer stacking method has been taken as a starting point of the experimental work of this manuscript. The goal of this chapter is to study the influence of different parameters on PEDOT VPP electrodes in order to improve the performances of the final microactuators.*

## 2.1. Introduction

Over the past few decades, vapor phase polymerization (VPP) has attracted the attention of the researchers to fabricate thin conducting polymer layers for different applications, like organic light emitting diodes (OLEDs)<sup>[141,142]</sup>, piezoelectric devices<sup>[143]</sup>, solar cells<sup>[144,145]</sup>, supercapacitors<sup>[146,147]</sup>, electrochromic devices<sup>[148,149]</sup>, sensors<sup>[150]</sup> and also biomedical applications<sup>[151,152]</sup>. The main advantage of the VPP compared to the electrochemical and chemical bulk polymerizations is the formation of thin and uniform electronically conducting polymer (ECP) layers. Other advantage is the synthesis on different substrates, also non-conductive, which is not possible with electrochemical polymerization. The morphological and electrical properties of the resulting ECPs are highly dependent on the polymerization parameters, such as the choice of the oxidant and the monomer, the use of different dopants and additives, concentration of the oxidant solution, polymerization time and temperature. These different parameters have been studied during many years for the purpose of different applications and are shortly overviewed in the next section.

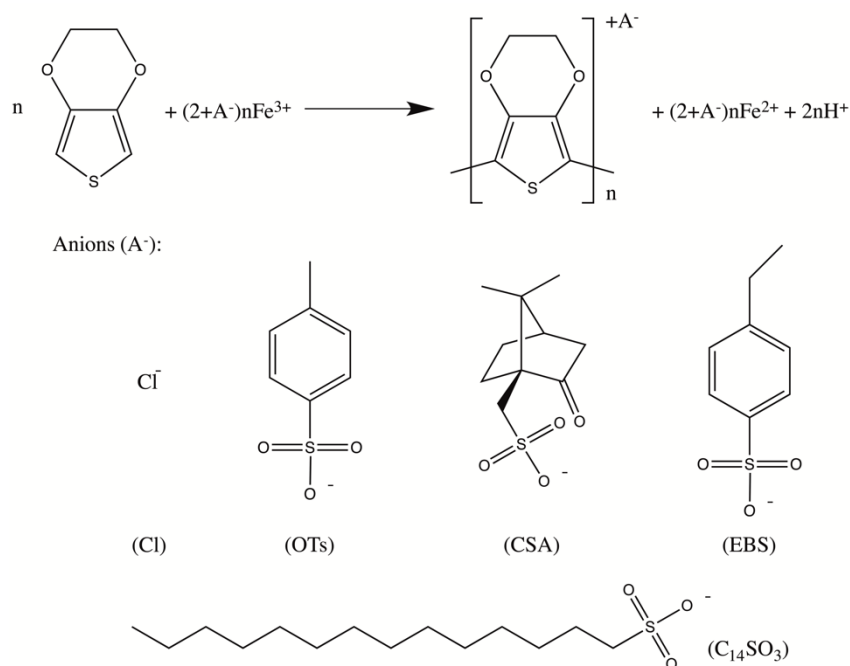
### 2.1.1 Vapor phase polymerization (VPP)

The vapor phase polymerization (VPP) is a type of chemical polymerization which is carried out in a polymerization chamber, where the monomer vapor is usually introduced to the oxidant covered substrate. This type of polymerization was first studied by Mohammadi *et al.* in 1986.<sup>[44]</sup> In this work, they reported a fabrication of polypyrrole (PPy) thin films using iron chloride (FeCl<sub>3</sub>) as an oxidant on different substrates, such as Ti, Ni, Mo, Au coated glass and thin wafers of ITO. The next year, the same author reported the work on PPy prepared by



VPP using hydrogen peroxide ( $\text{H}_2\text{O}_2$ ) as an oxidant and hydrochloric acid ( $\text{HCl}$ ).<sup>[153]</sup> For all the studied systems, Mohammadi *et al.* claimed that the resulting VPP PPy exhibited similar properties with electrochemically polymerized PPy layers. These works on VPP were a starting point of a fabrication of ECP thin films and helped to overcome the problems of insolubility and also solvent/substrate compatibility.

The most commonly used oxidizing agent is  $\text{Fe}^{3+}$  which is usually paired with chloride or tosylate anions or different sulphonates.<sup>[28,154–160]</sup> While the standard polymerization potential for the  $\text{Fe}^{3+}$  is constant (0.77 V), the change of anion leads to a change in the polymerization rate.  $\text{Fe}(\text{OTs})_3$  is known to have a slower polymerization rate but results in topographically smoother and electronically more conductive polymer layers which allows their utilization in optoelectronic devices compared with  $\text{FeCl}_3$ .<sup>[145,161]</sup> The reaction scheme of the 3,4-ethylenedioxythiophene (EDOT) VPP in the presence of  $\text{Fe}^{3+}$  and different anions is brought in **Figure 17**.



**Figure 17.** Vapor phase polymerization scheme for EDOT in the presence of  $\text{Fe}^{3+}$  and different anions.

Winther-Jensen *et al.* investigated the properties of poly(3,4-ethylenedioxythiophene) (PEDOT) layers obtained through VPP using different  $\text{Fe}^{3+}$  salts.<sup>[162]</sup> The studied anions were camphor-sulfonate (CSA), chloride (Cl), 4-ethylbenzenesulfonate (EBS), tetradecylsulfonate ( $\text{C}_{14}\text{SO}_3$ ) and para-toluenesulfonate (OTs) (**Figure 17**). In this process, the substrates were covered with  $\text{Fe}(\text{III})$  salts and then exposed to a monomer vapor. The PEDOT layers resulted in the electronic conductivity of  $19 \text{ S}\cdot\text{cm}^{-1}$  fabricated with  $\text{FeCl}_3$  and  $933 \text{ S}\cdot\text{cm}^{-1}$  fabricated

with  $\text{Fe}(\text{OTs})_3$ . They also investigated the conductivity after ion-exchange and found that the resulting material had almost the same electronic conductivity i.e. the film prepared with  $\text{FeCl}_3$  did not improve the electronic conductivity after ion exchange with OTs and the OTs prepared layers did not lose the electronic conductivity after ion exchange with Cl. They concluded that the formed structure during the VPP is the determining factor of the resulting PEDOT films.

The study on oxidant concentration and vapor phase polymerization time on PEDOT electrodes was performed by Ali *et al.*<sup>[163,164]</sup> In the first work, the PEDOT films were obtained from the VPP on  $\text{FeCl}_3$  covered substrate. It was found that the thickness and the electronic conductivity of the PEDOT layers are dependent on the concentration of the oxidant. The thickness of the PEDOT films increased linearly when the  $\text{FeCl}_3$  concentration in ethanol was increased from 1 wt% to 7 wt%. They also found that the electronic conductivity and the smoothness of the PEDOT layers was increasing from the concentration of 1 wt% - 3 wt%, resulting in the increase of electronic conductivity from  $110 \text{ S.cm}^{-1}$  to  $392 \text{ S.cm}^{-1}$ . On the contrary, the increase of the  $\text{FeCl}_3$  concentration above 3 wt% resulted in decrease of the electronic conductivity ( $85 \text{ S.cm}^{-1}$ ) and forming holes in the PEDOT layers, which consequently is the reason for the decreased electrical properties. The second work of Ali *et al.* investigated the effect of oxidant concentration and time on VPP PEDOT layers fabricated with  $\text{Fe}(\text{OTs})_3$ . They found that the thickness of the resulting PEDOT films was increasing as a function of the VPP time and the concentration of the oxidant solution. The electronic conductivity increased until 10 min of VPP time ( $680 \text{ S.cm}^{-1}$ ) when the PEDOT had grew to a final thickness and continuous smooth PEDOT film was formed. After that, the conductivity remained almost constant (until 20 min of VPP).

In most cases, the VPP is carried out in a way where the oxidant is in a liquid form. Chelawat *et al.* demonstrated a different approach, using bromine as an oxidant during the polymerization step, resulting in completely dry VPP process.<sup>[165]</sup> Bromine was used as an oxidant and a dopant which was delivered as a vapor in the process. The resulting bromine PEDOT films were compared to the conventional  $\text{FeCl}_3$  fabricated PEDOT films. The use of bromine resulted in enhancement of electronic conductivity and stability compared to iron chloride PEDOT layers. The resulting electronic conductivities were  $380 \text{ S.cm}^{-1}$  and  $40 \text{ S.cm}^{-1}$  for the PEDOT layers with bromine and iron chloride, respectively. They also concluded that the use of bromine helped to retain longer electrical stability during aging experiments of

the PEDOT layers, because it is less volatile and has a lower oxidation potential compared to chloride.

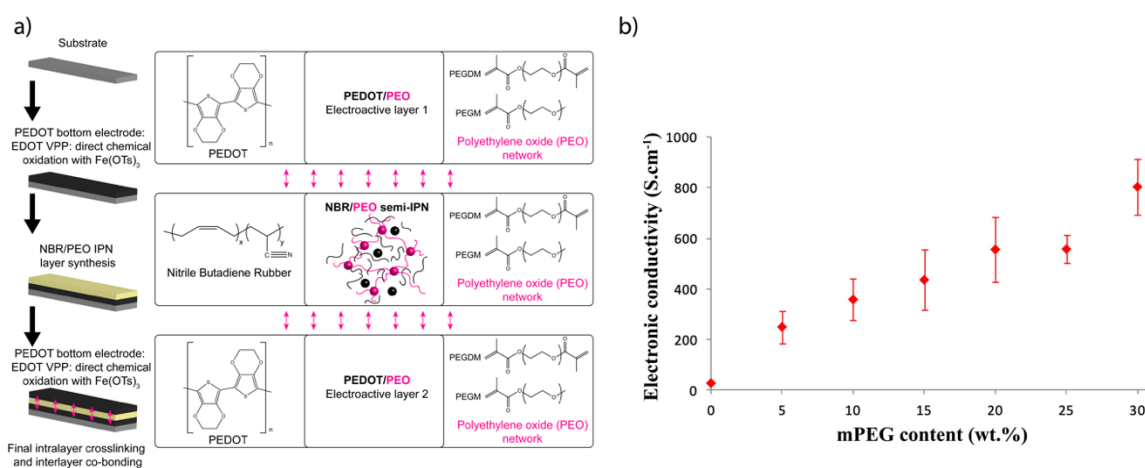
Winther-Jensen *et al.* performed further studies on EDOT VPP with base additives.<sup>[28]</sup> The release of acidic protons during the EDOT polymerization (**Figure 17**) initiated the study of this workgroup. The aim of the work was to find a synthesis route where the acidity can be controlled before and during the reaction in order to prevent any unwanted acidic side reactions. They tried three different bases (pyridine, pyrazine and quinoline) and found that pyridine has the best results as a base additive with a boiling point low enough to be removed easily from the mixture. Other work groups have also used base additives to fabricate PEDOT layers through VPP.<sup>[166,167]</sup> Truong *et al.* demonstrated the fabrication of PEDOT layers using VPP and pyridine as a base additive.<sup>[168]</sup> They also showed that by increasing the pyridine ratio, it was possible to increase the conductivity of the PEDOT layers from 30 S.cm<sup>-1</sup> to 300 S.cm<sup>-1</sup>. Another common additive for VPP of EDOT is poly(ethylene glycol) (PEG). The use of PEG as an additive in the EDOT VPP was first demonstrated by Fabretto.<sup>[169–171]</sup> It was demonstrated that the using poly(ethylene glycol-*ran*-propylene-glycol) (PEG-*ran*-PPG) surfactant in the oxidant solution suppresses the oxidant crystallization and helps to form defect free highly conductive PEDOT films.

The final properties of the ECP electrodes are drastically dependent on VPP conditions (polymerization time, oxidant nature and concentration) but also on the presence of additives. Depending on the final application, different approaches can be used to obtain smooth and thin CP layers with conductivities up to several hundreds of S.cm<sup>-1</sup>.

### 2.1.2 Vapor phase polymerization for microactuator fabrication

Even though VPP is a common polymerization method for thin ECP layers, it is not as described as classical oxidative polymerization or electrochemical polymerization for the synthesis of soft actuators. However, as soon as microactuators are considered, the conventional polymerization methods appear to be limited. Classical oxidative polymerization is not suitable for thin film fabrication. Secondly, electrochemical polymerization is limited by the synthesis on conductive substrates. While the electrochemical polymerization has been widely used for 2-layer devices, then elaboration of trilayers becomes tricky because it requires two conductive surfaces on each side of the ion reservoir polymer membrane.<sup>[172]</sup> VPP circumvents these problems and allows the synthesis

of thin, smooth and highly conductive ECP electrodes directly on non-conducting surfaces (substrate and/or polymeric membrane), resulting in trilayer configuration. Moreover, the obtainable low thicknesses can make these materials compatible with conventional microfabrication technologies like laser patterning, but also photolithography and etching techniques. The elaboration and the development of different microactuators has been carried out over the past few decades. The previous fabrication methods have usually been adapted from the macroscale processes and require manual handling of the device at one point of the process. The layer stacking method, including VPP, was developed by Maziz *et al.* in order to fabricate the microactuators without any manual handling during the synthesis, as described in Chapter 1.<sup>[139]</sup> The presence of poly(ethylene oxide) (PEO) reactive precursors (mPEG, methacrylic functionalized PEG) in each layer (PEDOT and membrane) is a key element in the described process, since it allows, after mPEG polymerization, the final co-bonding between all the layers and prevents any delamination problem (**Figure 18a**). Moreover, he reported the improvement of the electronic conductivity of PEDOT electrodes owing to the incorporation of mPEG as reactive additive (**Figure 18b**) during the EDOT VPP. By using custom-made SU-8 flexible substrate with integrated bottom electrical contact, Maziz demonstrated that it was possible to fully elaborate and directly operate the resulting microactuators without manual handling. However, the device presented a maximum strain of 0.13% and a maximum output force of 0.75  $\mu\text{N}$  under electrical stimulation of  $\pm 4.0$  V, which can appear limiting for practical applications.



**Figure 18.** Electronic conductivity of the PEDOT electrodes obtained via VPP as a function of mPEG content (before mPEG polymerization) from the thesis of Maziz.<sup>[173]</sup>

While the influence of VPP conditions on the resulting electronic conductivity of the ECP layers has been studied by many workgroups over the years, the performances of the actuators are not only dependent on the electronic conductivity but they are also strongly

related to the electrochemical properties of the ECP electrodes. The electroactivity of the electrodes ensures the ability to be electrochemically oxidized or reduced, which is a determining factor for actuation of the final device. However, the influence of VPP conditions on electrochemical properties of the ECP electrodes has not been performed so far. For this purpose, a thorough study on electrochemical properties as a function of EDOT VPP conditions is performed in this work.

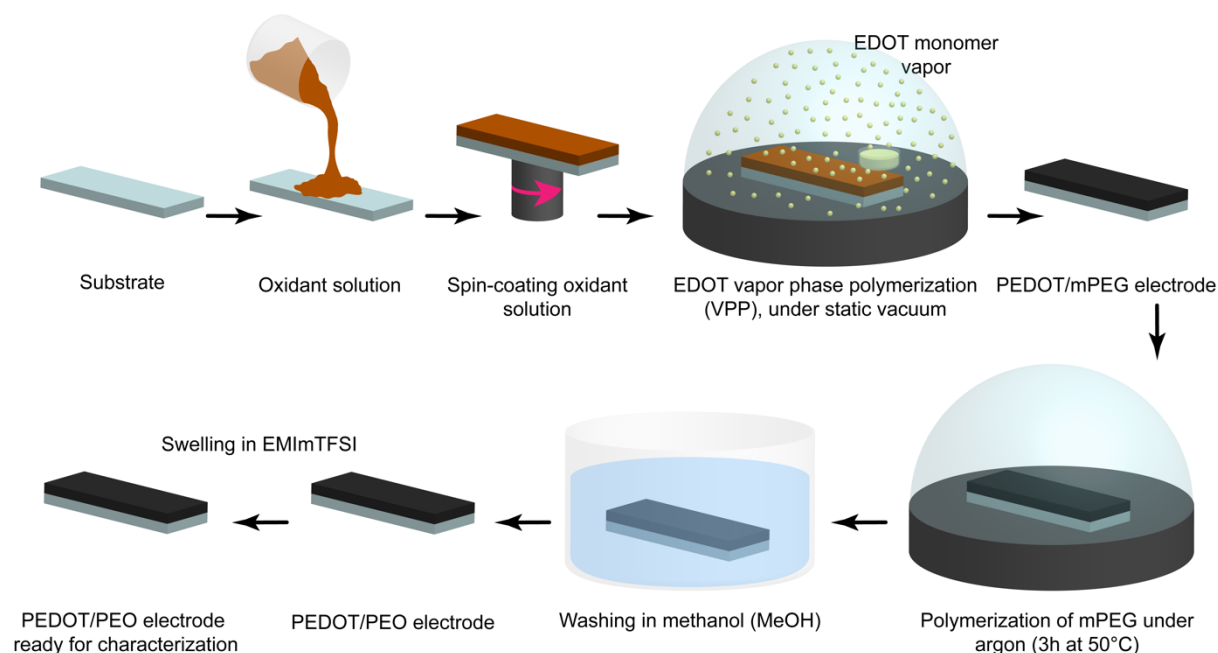
## 2.2 Improvement of PEDOT electrode electrical and electrochemical properties

High electronic conductivity and high electroactivity (volumetric charge density) are necessary properties in order to obtain efficient bending type trilayer actuator with large deformation. High electronic conductivity will be important to promote fast electronic charge transport along the length of the PEDOT electrodes and it will be involved in the curvature homogeneity of the final microbeam. As mentioned in Chapter 1, besides electronic conductivity, then also volumetric charge density ( $\rho$ ) is a critical parameter since the electrode strain ( $\varepsilon$ ) is directly proportional to the number of inserted/expelled ions and then to the exchanged electrochemical charge.<sup>[40]</sup> In other words, if the PEDOT chains are highly conductive but not accessible for insertion/expulsion of ions of the chosen electrolyte, the resulting deformation will be small. For this purpose, the volumetric charge density of each synthesized PEDOT electrode has also been minutely characterized and needs to be as high as possible.

### 2.2.1 Synthesis and characterization of PEDOT electrodes

The synthesis of the PEDOT electrodes was performed according to the layer stacking method, described in the work of Maziz *et al.* and is brought in **Figure 19**.<sup>[139]</sup> The PEDOT electrodes were obtained using EDOT VPP. Direct chemical oxidation of EDOT vapor was carried out in the presence iron (III) tosylate ( $\text{Fe}(\text{OTs})_3$ ). PEO precursors are added as reactive additives for improving the electrochemical properties of PEDOT electrodes. The PEO precursors (mPEG) are composed of 50 wt% poly(ethylene glycol) methacrylate (PEGM) and 50 wt% poly(ethylene glycol) dimethacrylate (PEGDM) as a monomer and a crosslinker, respectively. The mPEG was added to the commercial  $\text{Fe}(\text{OTs})_3$  solution (55 wt% in butanol) (Clevios CB55 V2, Heraeus Precious Metals GmbH & Co) and stirred to ensure the homogeneity of the solution. Finally, dicyclohexylperoxidicarbonate (DCPD, 3

wt% vs mPEG) as the radical initiator was introduced to the solution. The obtained solution was stirred until dissolution and degassed. The oxidant solution was then spin-coated onto a substrate and exposed to the EDOT monomer vapor for a fixed time at a fixed temperature. EDOT VPP was carried out under static vacuum (rotary pump) by heating liquid EDOT monomer that evaporates and polymerizes in contact with the substrate covered by the oxidant solution. The EDOT VPP was followed by a final heat treatment under argon during 3h at 50°C for mPEG polymerization. The obtained PEDOT/PEO electrodes were thoroughly washed in methanol (MeOH) to remove unreacted oxidant solution as well as unpolymerized EDOT or methacrylate monomers and dried at room temperature. The resulting PEDOT/PEO composite electrodes were immersed into ionic liquid 1-ethyl-3-methylimidazolium bis(trifluoromethanesulfonyl)imide (EMImTFSI) prior to the characterizations.



**Figure 19.** PEDOT electrode fabrication using vapor phase polymerization (VPP).

The study of the PEDOT electrodes was carried out as a function of oxidant solution composition (oxidant concentration, content of mPEG, content of EMImTFSI as an additive), rotation speed of the spin-coater for deposition of oxidant solution layer, EDOT VPP time and temperature. The initial synthesis conditions for oxidant solution composition were: commercial 55 wt% Fe(OTs)<sub>3</sub> in BuOH, 10 wt% mPEG in the oxidant solution (vs Fe(OTs)<sub>3</sub> in BuOH) and 0 wt% EMImTFSI as an additive. The spin-coating speed, acceleration and duration were 2500 rpm, 1000 rpm.s<sup>-1</sup> and 30 s, respectively. The EDOT VPP time of 30 min and temperature of 40°C were used. When one parameter was changed, the others remained

the same as in the initial parameters. The initial parameters and the range of changed values for each parameter are presented in **Table 2**.

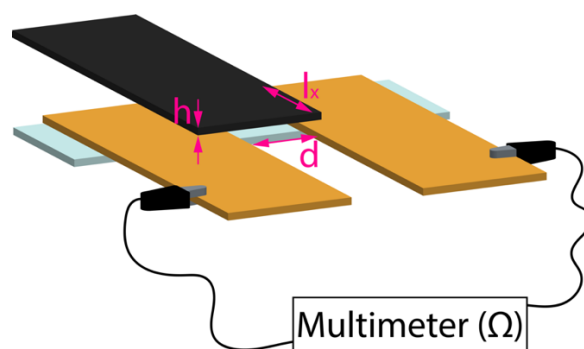
**Table 2.** Range of changed parameters for PEDOT electrode optimization.

Parameter	Initial parameters	Range of changed parameters
Fe(OTs) <sub>3</sub> in BuOH	55 wt%	40 wt% and 55 wt%
mPEG content vs Fe(OTs) <sub>3</sub>	10 wt%	0 – 30 wt%
EMImTFSI content vs Fe(OTs) <sub>3</sub>	0 wt%	0 – 40 wt%
Spin-coating speed	2500 rpm	1000 – 2500 rpm
EDOT VPP time	30 min	30 – 180 min
EDOT VPP temperature	40°C	30 – 80°C

The properties of the electrodes are determined by the means of thickness (in dry and swollen state), the electronic conductivity and electroactivity. The electronic conductivity ( $\sigma$ ) of the PEDOT electrodes was obtained by measuring the sheet resistance of the electrodes and is obtained from the relation between the resistivity and the conductance from the formula:

$$\sigma = \frac{d}{hl_x R} \quad (1)$$

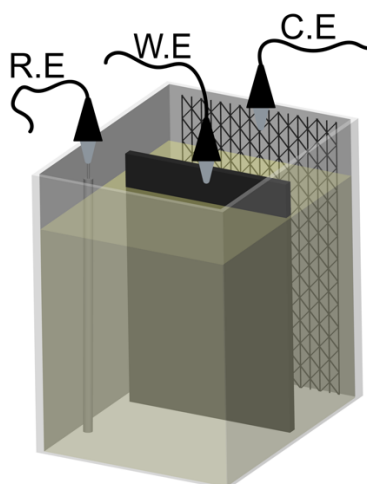
Where  $d$  is the distance between the gold plates,  $h$  is the thickness of the PEDOT electrode,  $l_x$  is the length of the electrode that is on the surface of the gold plates and  $R$  is the sheet resistance of the electrode from the multimeter (**Figure 20**).



**Figure 20.** Schematic representation of the electronic conductivity measurements.

The electrochemical properties of the electrodes were obtained from cyclic voltammetry measurements. The experimental setup of the cyclic voltammetry for PEDOT electrodes is illustrated in **Figure 21**. The PEDOT electrode was connected as a working electrode (W.E), stainless steel mesh was used as a counter electrode (C.E) and silver wire as a pseudo-reference electrode (R.E). The cyclic voltammetry was performed in neat EMImTFSI at a scan rate of 20 mV.s<sup>-1</sup> and a voltage window of ±1.0 V for all the PEDOT electrodes.





**Figure 21.** Schematic representation of cyclic voltammetry measurements.

The integration of the current from cyclic voltammetry gives the charge, which is divided by the volume of the electrode, providing volumetric charge density ( $\rho$  in  $\text{C}\cdot\text{m}^{-3}$ ) in order to describe the amount of electric charge per volume of the PEDOT electrodes. This value allows evaluating quantitatively the electroactivity of the PEDOT electrodes. The volumetric charge density ( $\rho$ ) was calculated according to the following equation:

$$\rho = \frac{\int_0^{t/2} i(t) dt}{lwh} \quad (2)$$

Where  $i(t)$  is the measured current,  $t$  is the duration of one cycle of applied voltage,  $l$ ,  $w$  and  $h$  are the length, width and thickness of the resulting PEDOT electrodes.

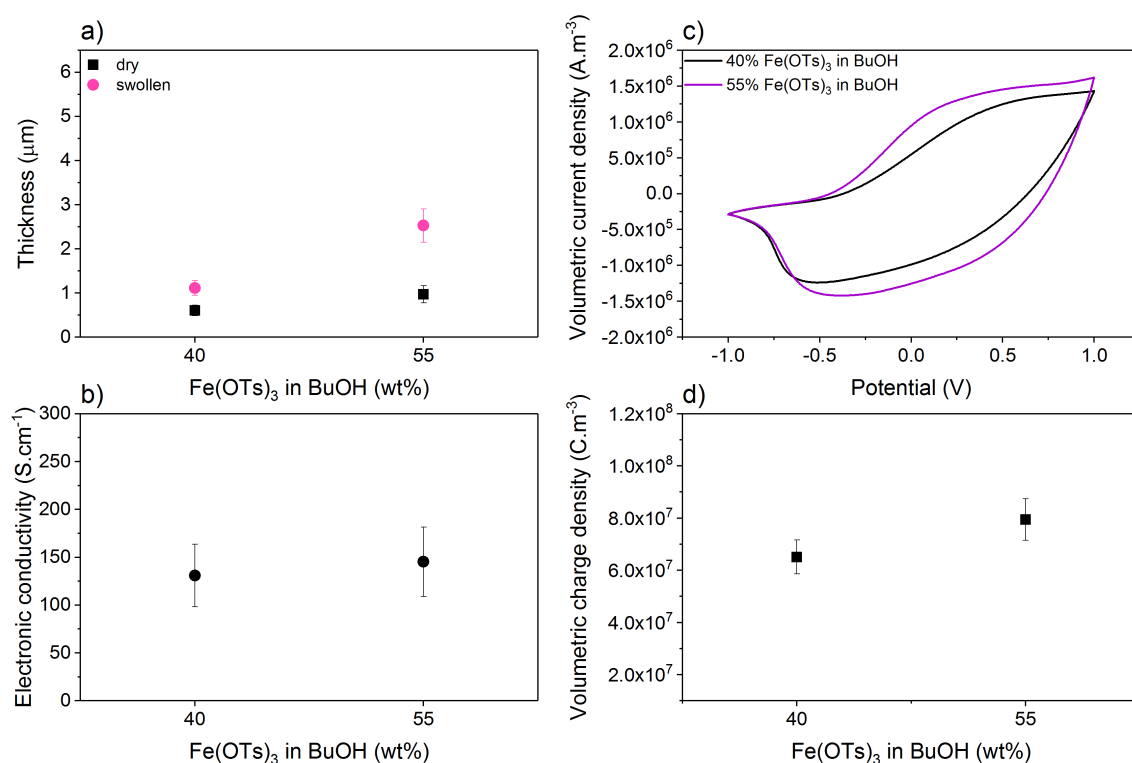
The next sub-sections are divided according to the changed parameters and in every sub-section one changed parameter will be discussed. All the following results have been obtained by the average of 3 measurements (1 measurement on 3 different samples).

### 2.2.2 Iron (III) tosylate content in butanol

Two different  $\text{Fe}(\text{OTs})_3$  solutions in butanol were compared: a commercial solution containing 55 wt%  $\text{Fe}(\text{OTs})_3$  in BuOH and a solution containing 40 wt%  $\text{Fe}(\text{OTs})_3$  in BuOH (obtained by diluting the commercial solution with BuOH). First, the thickness of the obtained PEDOT layers as a function of the oxidant concentration was studied in a dry state but also after swelling in EMImTFSI (**Figure 22a**). The thicknesses of the PEDOT electrodes in a dry state were  $0.61 \mu\text{m}$  (with 40 wt%  $\text{Fe}(\text{OTs})_3$  in BuOH) and  $0.97 \mu\text{m}$  (with 55 wt%  $\text{Fe}(\text{OTs})_3$  in BuOH). In the swollen state, the resulting thicknesses are always higher due to the incorporation of ionic liquid (EMImTFSI) and the corresponding thickness values are 1.1



$\mu\text{m}$  and  $2.5 \mu\text{m}$  with 40 wt% and 55 wt%  $\text{Fe}(\text{OTs})_3$ . The difference in thickness versus oxidant concentration in the dry state is small, but becomes more obvious in the swollen state. Higher thickness of the PEDOT electrode with 55 wt%  $\text{Fe}(\text{OTs})_3$  in BuOH can be related to higher amount of PEDOT chains due to the higher amount of available oxidant per substrate area. As a second parameter, the electronic conductivity of these PEDOT electrodes is studied in the swollen state (EMImTFSI) and demonstrates almost no difference (**Figure 22b**). The PEDOT electrode fabricated with 55 wt%  $\text{Fe}(\text{OTs})_3$  has a slightly higher electronic conductivity of  $145 \text{ S}\cdot\text{cm}^{-1}$  compared to the  $131 \text{ S}\cdot\text{cm}^{-1}$  of the 40 wt%  $\text{Fe}(\text{OTs})_3$  electrode.



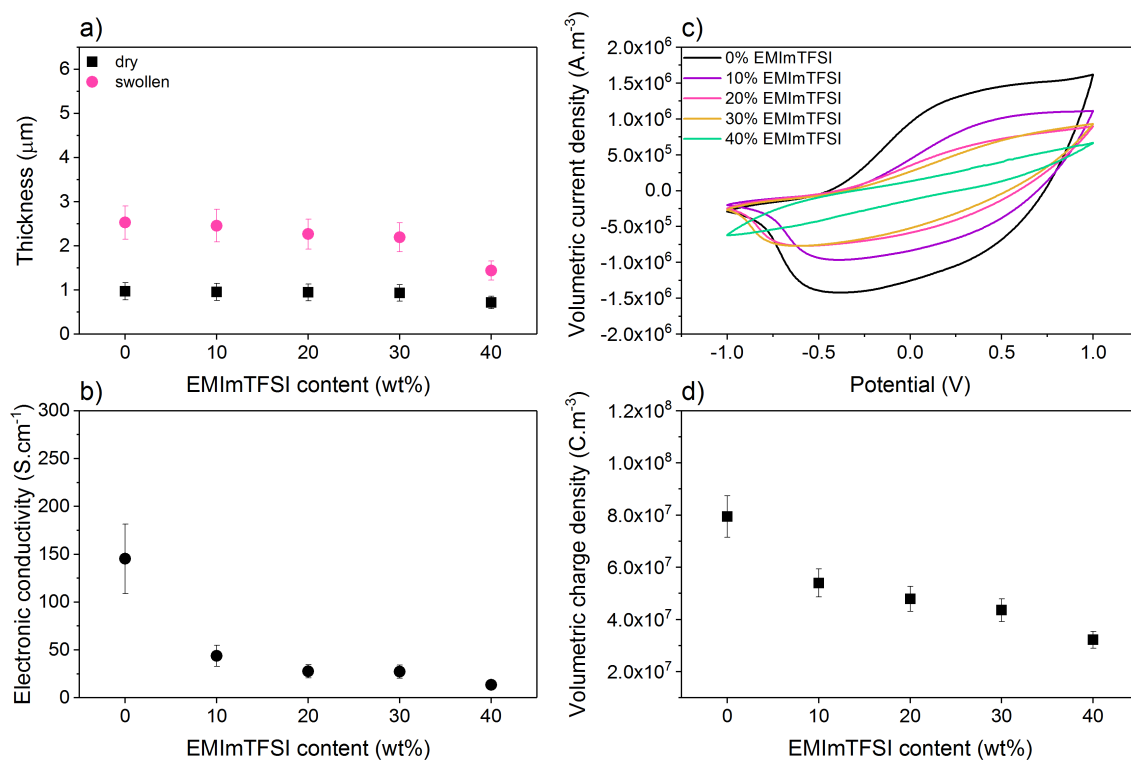
**Figure 22.** Results of PEDOT electrodes dependent on the oxidant concentration in butanol: a) thickness in dry and swollen (EMImTFSI) state, b) electronic conductivity, c) cyclic voltammograms and d) volumetric charge density. For c) and d): scan rate of  $20 \text{ mV}\cdot\text{s}^{-1}$  and a voltage window of  $\pm 1.0 \text{ V}$  in EMImTFSI. Content of mPEG: 10 wt%; spin-coating speed-acceleration-duration:  $2500 \text{ rpm} - 1000 \text{ rpm}\cdot\text{s}^{-1} - 30 \text{ s}$ ; EDOT VPP time: 30 min and EDOT VPP temperature:  $40^\circ\text{C}$ .

The cyclic voltammetry (CV, normalized as a function of the electrode volume) in **Figure 22c** demonstrates higher electroactivity of the PEDOT electrode fabricated from more concentrated solution of  $\text{Fe}(\text{OTs})_3$ . The cyclic voltammogram presents clearly defined oxidation and reduction peaks, indicating that effective redox process takes place. **Figure 22d** presents the resulting values of  $\rho$  and demonstrates that the PEDOT electrode with higher content of oxidant in the solution (55 wt%) presents slightly higher volumetric charge density ( $7.95 \times 10^7 \text{ C}\cdot\text{m}^{-3}$ ) compared to the 40 wt% electrode ( $6.51 \times 10^7 \text{ C}\cdot\text{m}^{-3}$ ). The values

of both electrodes are in the same range ( $10^7 \text{ C.m}^{-3}$ ) as reported for PPy electrodes.<sup>[174]</sup> Overall, it can be said that the electrodes fabricated with 55 wt%  $\text{Fe}(\text{OTs})_3$  solution resulted in slightly higher electrical and electrochemical properties. This is probably due to the higher oxidant content in the solution, resulting in higher amount of interconnected PEDOT chains, which are consequently more electrically conductive and electroactive. For the subsequent experiments, the commercially available 55 wt%  $\text{Fe}(\text{OTs})_3$  solution was thus chosen.

### 2.2.3 EMImTFSI content

Ionic liquid is not really common additive during VPP, but it has been already used to improve the electronic conductivity of the PEDOT:PSS electrodes.<sup>[175–177]</sup> Nonetheless, it can be mentioned that 1-butyl-3-methylimidazolium tetrafluoroborate ( $\text{BMImBF}_4$ ) was first used successfully as an additive and a post-treatment solvent for VPP in order to improve the thermoelectrical properties of the PEDOT electrodes.<sup>[178]</sup> However, no study has been reported on the influence of ionic liquid on the electroactivity of PEDOT electrodes obtained via VPP. As a consequence, a study on PEDOT electrodes was performed in this work as a function of EMImTFSI content in the oxidant solution (vs  $\text{Fe}(\text{OTs})_3$  in BuOH). **Figure 23a** presents the thickness of the PEDOT electrodes with increased content of EMImTFSI in the oxidant solution. In both cases, in dry and in swollen state, the change in thickness is almost meaningless, decreasing slightly when higher content of ionic liquid is added. The thickness is decreasing from  $0.97 \mu\text{m}$  to  $0.72 \mu\text{m}$  in the dry state and from  $2.53 \mu\text{m}$  to  $1.44 \mu\text{m}$  in the swollen state, when 40 wt% EMImTFSI is added into the oxidant solution. The decrease in thickness can be explained by the concentration of the final oxidant solution. When higher content of ionic liquid is incorporated, the resulting oxidant concentration is decreasing, resulting in thinner PEDOT layers. **Figure 23b** demonstrates the decrease in the electronic conductivity when EMImTFSI is incorporated to the oxidant solution. Drastic decrease in electronic conductivity (from  $145 \text{ S.cm}^{-1}$  to  $14 \text{ S.cm}^{-1}$ ) is observed when EMImTFSI is introduced to the oxidant solution (from 0 to 40 wt% respectively). Since the difference in the thickness of PEDOT layers is not significant, the large decrease in the electronic conductivity is indicating that in the formed PEDOT electrodes, the conducting particles are more separated, preventing an efficient charge transport along the length of the PEDOT electrodes.



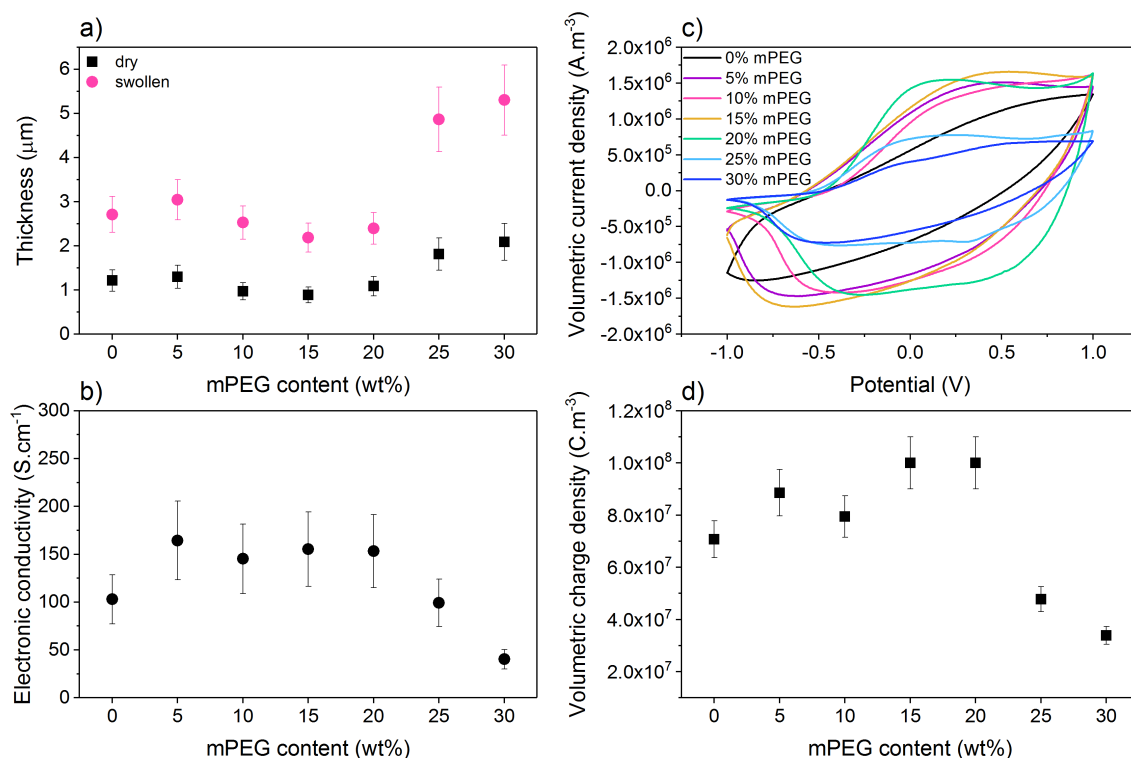
**Figure 23.** Effect of EMImTFSI addition to the PEDOT electrodes: a) thickness in dry and swollen (EMImTFSI) state, b) electronic conductivity, c) cyclic voltammograms and d) volumetric charge density at a scan rate of 20 mV.s<sup>-1</sup> and a voltage window of  $\pm 1.0$ V in EMImTFSI. Content of mPEG: 10 wt%; spin-coating speed-acceleration-duration: 2500rpm – 1000rpm.s<sup>-1</sup> – 30s; EDOT VPP time: 30 min and EDOT VPP temperature: 40°C.

Electroactivity results of the PEDOT electrodes with EMImTFSI as an additive are brought in **Figure 23c** and **d**. The cyclic voltammetry is demonstrating a progressive decrease in current when higher content of EMImTFSI is incorporated. The PEDOT electrode synthesized without EMImTFSI additive presents the highest current density with defined oxidation and reduction peaks, indicating that the redox process is occurring. The PEDOT electrode with 40 wt% EMImTFSI demonstrates really resistive behavior without any definition of oxidation and reduction peaks, preventing the redox process to take place efficiently. Volumetric charge density in **Figure 23d** confirms the decrease in the electrochemical properties when EMImTFSI is incorporated as an additive during the VPP of the PEDOT electrodes. The initial value of  $7.95 \times 10^7$  C.m<sup>-3</sup> is decreasing to  $3.22 \times 10^7$  C.m<sup>-3</sup> with an incorporation of 40 wt% EMImTFSI into the oxidant solution. It can be concluded that while using ionic liquid as an additive had a positive effect for PEDOT thermoelectrical properties or for PEDOT:PSS electronic conductivity,<sup>[175–178]</sup> then using EMImTFSI has a negative impact on EDOT VPP and results in PEDOT electrodes with both, decreased electrical and electrochemical properties.

#### 2.2.4 mPEG content

The key element in the layer stacking method is the addition of PEO precursors (mPEG) since it promotes intralayer crosslinking and interlayer co-bonding. According to this, a study on PEDOT electrodes as a function of mPEG content (vs  $\text{Fe}(\text{OTs})_3$  in BuOH) was performed to evaluate the influence on the resulting electrode's electrical and electrochemical properties. The influence of mPEG content on electrode thickness in dry and swollen state is brought in **Figure 24a**. In dry state, the thickness is not changing significantly when mPEG content is increased from 0 to 20 wt%, varying between 0.89 and 1.30  $\mu\text{m}$ . The slight thickness variation in this content range may be due the increase of solid content (mPEG) in the oxidant solution and as a result, a progressive decrease of oxidant concentration. The thickness of the PEDOT electrodes with higher content of additive (20 – 30 wt%), is increasing up to 2.0  $\mu\text{m}$ . The thickness of the swollen electrodes remains quite constant (2.19 to 3.05  $\mu\text{m}$ ) in the range of 0 – 20 wt% of mPEG while a significant increase up to 5.30  $\mu\text{m}$  is observed when the content of mPEG is increased above 20 wt%.

Drastic increase in thickness (above 20 wt% mPEG) was observed for both, the electrodes in the dry and swollen states. This result can be possibly explained by the polymerization of mPEG already occurring within the oxidant solution. Indeed, it has been described that combination of peroxide based initiator and  $\text{Fe}^{3+}$  ions could promote hydroxyl-mediated chain mechanism.<sup>[179]</sup> We postulate here that  $\text{Fe}^{3+}$  ions and DCPD can behave in a similar manner. While non-significant for low mPEG and DCPD contents, this reaction could become faster when increasing the concentration of the initiator. This progressive mPEG polymerization may then lead to an increase of the solution's viscosity and consequently to an increase of the spin-coated oxidant layer thickness. This explanation is consistent with the increase of the standard deviation of the corresponding thicknesses, resulting from the poor control on this undesired phenomenon.



**Figure 24.** Results of mPEG content in the oxidant solution: a) thickness in dry and swollen (EMImTFSI) state, b) electronic conductivity, c) cyclic voltammograms and d) volumetric charge density at a scan rate of  $20 \text{ mV}\cdot\text{s}^{-1}$  and a voltage window of  $\pm 1.0 \text{ V}$  in EMImTFSI. Spin-coating speed-acceleration-duration:  $2500 \text{ rpm} - 1000 \text{ rpm}\cdot\text{s}^{-1} - 30 \text{ s}$ ; EDOT VPP time: 30 min and EDOT VPP temperature:  $40^\circ\text{C}$ .

The electrical and electrochemical properties of the electrodes as a function of mPEG content are presented in **Figure 24b, c** and **d**. Adding up to 20 wt% mPEG into the oxidant solution improved the electrical properties of the PEDOT electrodes. As soon as 5 wt% of mPEG is added to the oxidant solution, an increase in the electronic conductivity is observed, from  $103 \text{ S}\cdot\text{cm}^{-1}$  to  $164 \text{ S}\cdot\text{cm}^{-1}$ . This result is consistent with the literature where it was found that the doping level and the electronic conductivity of the VPP PEDOT electrodes were highest with 10 – 20 wt% glycol-based surfactants in the oxidant solution.<sup>[171]</sup> However, as in the case of thickness, the electronic conductivity doesn't significantly change and remains in the same range ( $145 - 164 \text{ S}\cdot\text{cm}^{-1}$ ) when 5 to 20 wt% mPEG is added into the oxidant solution. Increasing the mPEG content above 20 wt% significantly decreases the electronic conductivity of the resulting PEDOT electrodes ( $40 \text{ S}\cdot\text{cm}^{-1}$  with 30 wt% mPEG). This can be the result from the combination of significant increase in thickness (due to mPEG polymerization) and a decrease in PEDOT concentration (due to the dilution of oxidant solution).

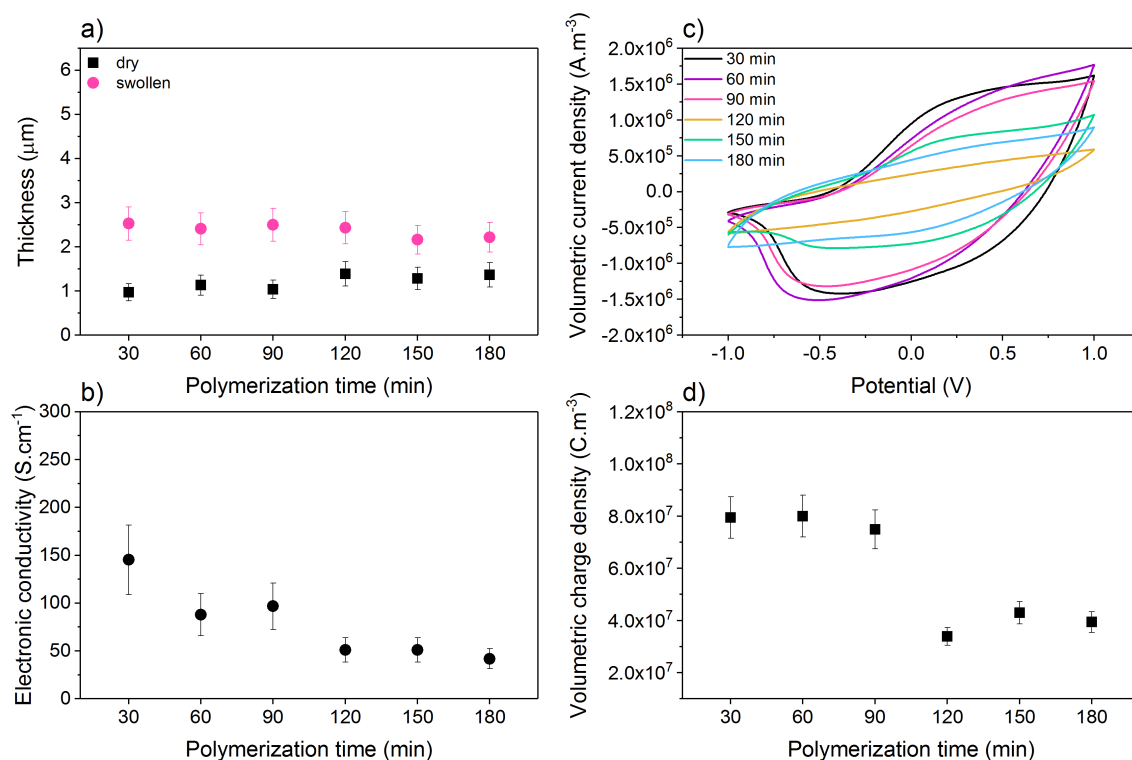
The electrochemical properties demonstrate the same trend. First, cyclic voltammogram (**Figure 24c**) of the PEDOT electrode without mPEG (0 wt%) presents resistive behavior

without any significant definition in oxidation and reduction peaks. It can be seen that adding 5 wt% mPEG into the oxidant solution increases the current of the resulting PEDOT electrode and demonstrates clearly defined oxidation and reduction peaks. The electrochemical behavior of the PEDOT electrodes with mPEG content between 5- 20 wt% remains quite in the same range but notably higher compared to the relatively resistive behavior of the PEDOT electrode without mPEG. It demonstrates that addition of mPEG into the oxidant solution not only improves the electronic conductivity, but is also beneficial for the electroactivity of the PEDOT electrodes. However, in a same way as for the electronic conductivity, increasing mPEG content above 20 wt% tends to decrease the electrochemical properties. Indeed, at 25 wt% mPEG, a decrease of current is observed as well as a loss of definition in oxidation and reduction peaks. This result is even more pronounced with 30 wt% mPEG, presenting more resistive behavior. The volumetric charge density  $\rho$  presents quantitatively the electrochemical changes of the PEDOT electrodes as a function of mPEG content (**Figure 24d**). The  $\rho$  is increasing from  $7.07 \times 10^7$  to  $1.00 \times 10^8$  C.m<sup>-3</sup> when increasing the content of mPEG from 0 to 20 wt% and then drops to  $3.39 \times 10^7$  C.m<sup>-3</sup> when 30 wt% mPEG is added. It can be summarized that adding mPEG into the oxidant solution helps to increase the electrical and electrochemical properties of the PEDOT electrodes. It is also important not to increase the concentration above 20 wt% in order to maintain high electrical and electrochemical properties.

### 2.2.5 Polymerization time

As a next parameter, the effect of EDOT VPP time on PEDOT electrode properties was studied. While increasing the polymerization time, it can be seen that the thickness (**Figure 25a**) of the dry electrodes is slightly increasing from 0.97  $\mu\text{m}$  to 1.37  $\mu\text{m}$ , indicating that the amount of PEDOT increases with longer polymerization time. After swelling in EMImTFSI, the trend is however the opposite: increasing the polymerization time leads to the decrease in the final thickness of the swollen PEDOT electrodes (from 2.53  $\mu\text{m}$  to 2.22  $\mu\text{m}$ ). In other words, the thicker electrodes in dry state, obtained from longer VPP time present also a lower swelling ability. This highlights the fact that the compactness of the electrodes is possibly also increasing with longer VPP time, resulting in stiffer PEDOT layers and therefore lower swelling ability. For the same time range, the electronic conductivity is decreasing almost gradually from 145 S.cm<sup>-1</sup> (30 min) to 42 S.cm<sup>-1</sup> (180 min) (**Figure 25b**). This can be explained by longer EDOT polymerization time leading to higher structural disorder or

randomly orientated molecule chains in the polymer. The electronic conductivity of the conducting polymers is dependent on the molecular structure of the polymer. If the PEDOT layer is formed with chaotic molecular structure and/or randomly orientated chains, then the charge transport is disturbed, resulting in reduced electrical properties.<sup>[180,181]</sup>



**Figure 25.** Evolution of PEDOT electrode's properties as a function of the polymerization time: a) thickness in dry and swollen (EMImTFSI) state, b) electronic conductivity, c) cyclic voltammograms and d) volumetric charge density at a scan rate of  $20 \text{ mV}\cdot\text{s}^{-1}$  and a voltage window of  $\pm 1.0\text{V}$  in EMImTFSI. Content of mPEG: 10 wt%; spin-coating speed-acceleration-duration:  $2500\text{rpm} - 1000\text{rpm}\cdot\text{s}^{-1} - 30\text{s}$  and EDOT VPP temperature:  $40^\circ\text{C}$ .

The cyclic voltammograms show the electrochemical properties of the PEDOT electrodes with increased VPP time (**Figure 25c**). The PEDOT electrodes with a polymerization time until 90 min present almost constant current with defined oxidation and reduction peaks. An obvious drop in electrochemical behavior is observed for the electrodes with polymerization times higher than 90 min, presenting lower current with relatively resistive electrochemical behavior. The volumetric charge density in **Figure 25d** ranges between  $7.49 \times 10^7 - 8.00 \times 10^7 \text{ C}\cdot\text{m}^{-3}$  up to the polymerization time of 90 min. When the polymerization time is increased above 90 min, a large drop is observed, resulting in 2 times lower volumetric charge density between  $3.39 \times 10^7 - 4.30 \times 10^7 \text{ C}\cdot\text{m}^{-3}$ . Longer polymerization time leads to more compact PEDOT electrodes with decreased swelling ability and therefore lower electrical and electrochemical properties. It can be summarized on the effect of EDOT VPP



time that in order to fabricate highly conductive and electroactive electrodes, the polymerization time should stay below 90 min.

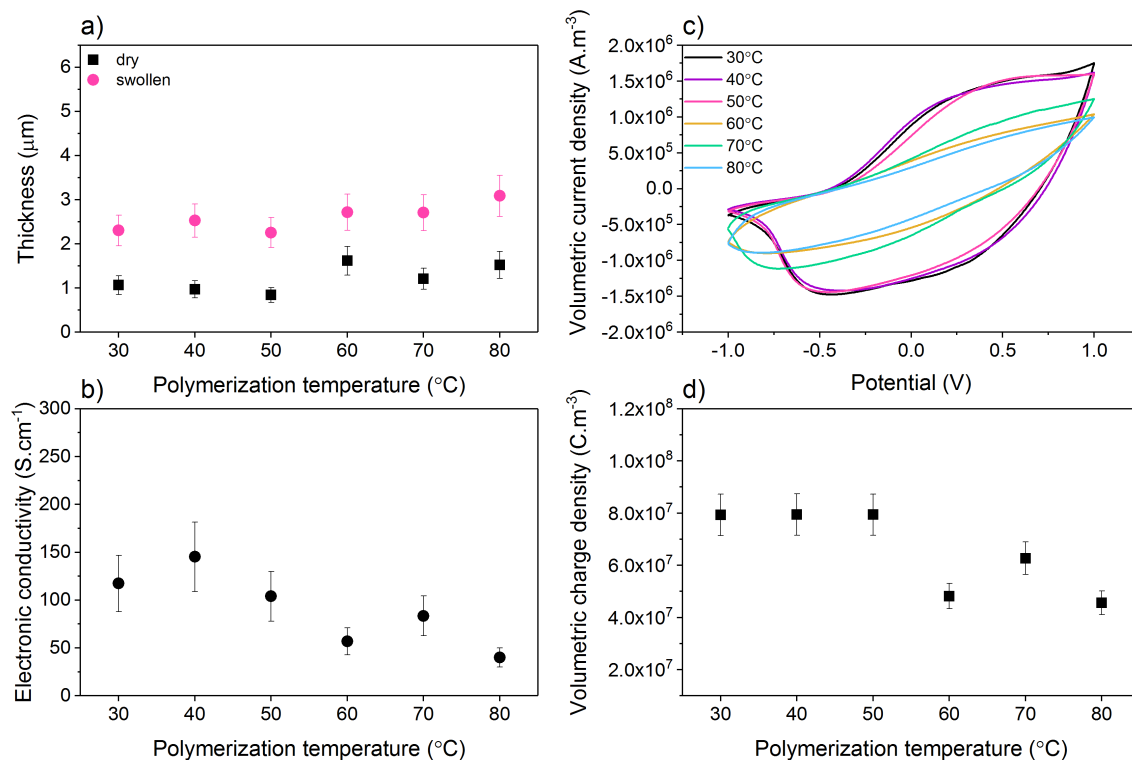
### 2.2.6 Polymerization temperature

The effect of EDOT VPP temperature on the properties of PEDOT electrodes is brought in **Figure 26**. The thickness of the PEDOT electrodes (**Figure 26a**) as a function of the EDOT VPP temperature, ranging from 30°C to 80°C, is varying between 0.84  $\mu\text{m}$  to 1.62  $\mu\text{m}$  in the dry state and between 2.26  $\mu\text{m}$  to 3.09  $\mu\text{m}$  in the swollen state. A small increase in thickness is observed in both, in dry and swollen state. Higher thickness of the PEDOT electrodes at higher temperatures can be explained by higher concentration of the EDOT vapor and the kinetics of the reaction at higher temperatures, leading to thicker PEDOT electrodes. The electronic conductivity of the PEDOT electrodes as a function of the polymerization temperature is brought in **Figure 26b**. The electronic conductivity of the PEDOT electrodes synthesized between 30°C - 50°C remains higher ( $>100 \text{ S}\cdot\text{cm}^{-1}$ ) compared to the electrodes synthesized at higher temperatures ( $40 \text{ S}\cdot\text{cm}^{-1}$  at 80°C). Wu *et al.* reported that EDOT VPP temperature has a great influence on the crystal structure and the morphology of the PEDOT electrodes.<sup>[182]</sup> They also demonstrated that the optimal VPP temperature is  $46 \pm 1^\circ\text{C}$ , above which the electronic conductivity of the PEDOT layers decreased because the lattice structure of the PEDOT electrodes had almost no orientation. The decrease in electronic conductivity above 50°C can be explained by faster polymerization rate due to the more concentrated EDOT vapor and consequently forming PEDOT electrodes with structural disorder.

The electrochemical properties in **Figure 26c** and **d** demonstrate similar behavior as the electrical properties. Cyclic voltammograms present high electroactivity with almost no change in current and redox process for the PEDOT electrodes synthesized with a temperature until 50°C. The PEDOT electrodes synthesized above 50°C present a large drop in current and more resistive behavior without any significant oxidation or reduction process compared to the electrodes synthesized until 50°C. At lower polymerization temperatures (30°C - 50°C) the volumetric charge density is almost constant, between  $7.93 \times 10^7$  -  $7.95 \times 10^7 \text{ C}\cdot\text{m}^{-3}$ . Above 50°C, the volumetric charge density is decreasing drastically and resulting in  $4.56 \times 10^7 \text{ C}\cdot\text{m}^{-3}$  at 80°C. The decrease in electrochemical properties can also be explained by the morphological and structural disorder when the PEDOT synthesis is performed at higher temperatures. When the PEDOT electrodes are synthesized with defective structure, then the charge transport in the sample is disturbed and preventing an efficient redox process



to occur, leading to the decrease in the electrochemical properties of the resulting PEDOT electrodes. The polymerization temperature of the EDOT VPP should stay between 30°C - 50°C in order to obtain highly conductive and electroactive PEDOT electrodes.

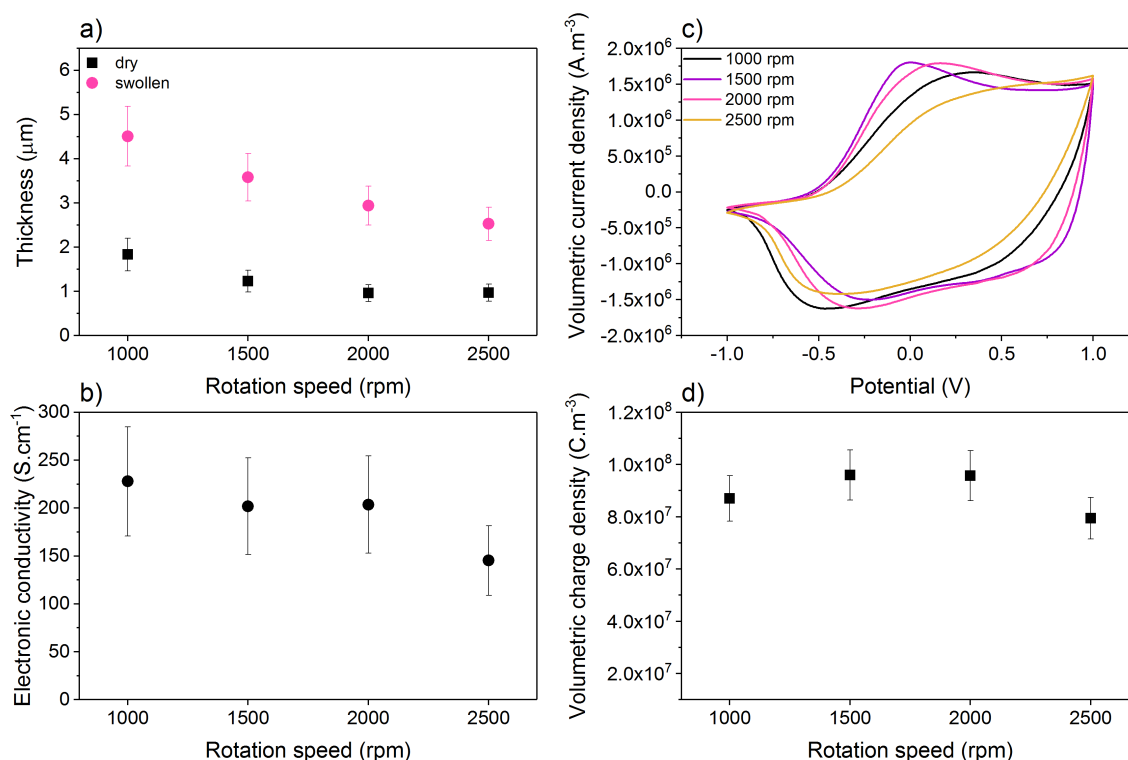


**Figure 26.** Influence of EDOT VPP temperature on PEDOT electrode's properties: a) thickness in dry and swollen (EMImTFSI) state, b) electronic conductivity, c) cyclic voltammograms and d) volumetric charge density at a scan rate of 20  $\text{mV}\cdot\text{s}^{-1}$  and a voltage window of  $\pm 1.0\text{V}$  in EMImTFSI. Content of mPEG: 10 wt%; spin-coating speed-acceleration-duration: 2500rpm – 1000rpm. $\cdot\text{s}^{-1}$  – 30s and EDOT VPP time: 30 min.

### 2.2.7 Rotation speed of spin-coating

As a last parameter, then the influence of the rotation speed of the spin-coater allowing to deposit oxidant solution was studied. The spin-coating acceleration and duration were 1000  $\text{rpm}\cdot\text{s}^{-1}$  and 30 s, respectively and the only changed parameter was the rotation speed. Decreasing the rotation speed of the spin-coater led to thicker oxidant solution layer on the substrate and resulted therefore in thicker PEDOT electrode layers (**Figure 27a**). The thickness of the dry PEDOT electrodes is decreasing from 1.83  $\mu\text{m}$  to 0.96  $\mu\text{m}$  and of the ionic liquid swollen PEDOT electrodes from 4.51  $\mu\text{m}$  to 2.53  $\mu\text{m}$  when the rotation speed of the spin-coater is increased to 2500 rpm. The electronic conductivity of the PEDOT electrodes is almost constant ( $>200$   $\text{S}\cdot\text{cm}^{-1}$ ) between 1000 – 2000 rpm and is decreasing to 145  $\text{S}\cdot\text{cm}^{-1}$  with a rotation speed of 2500 rpm. (**Figure 27b**). Even if small drop in electronic

conductivity is observed at 2500 rpm, all the resulting values present high electronic conductivity of the PEDOT electrodes.



**Figure 27.** Properties of PEDOT electrodes as a function of spin-coater's rotation speed: a) thickness in dry and swollen (EMImTFSI) state, b) electronic conductivity, c) cyclic voltammograms and d) volumetric charge density at a scan rate of  $20 \text{ mV}\cdot\text{s}^{-1}$  and a voltage window of  $\pm 1.0 \text{ V}$  in EMImTFSI. Content of mPEG: 10 wt%; spin-coating acceleration-duration:  $1000 \text{ rpm}\cdot\text{s}^{-1} - 30 \text{ s}$ ; EDOT VPP time: 30 min and EDOT VPP temperature:  $40^\circ\text{C}$ .

Changing the rotation speed did not have a tremendous effect on the electrochemical properties of the PEDOT electrodes, which remain high at all rotation speeds. Cyclic voltammetry presents high current with clearly defined oxidation and reduction peaks for all the resulting PEDOT electrodes (**Figure 27c**). The quantitative representation of the electrochemical changes demonstrates the same trend:  $\rho$  remains high at all rotation speeds (1000-2500 rpm) between  $7.95 \times 10^7 \text{ C}\cdot\text{m}^{-3}$  and  $9.60 \times 10^7 \text{ C}\cdot\text{m}^{-3}$  (**Figure 27d**). It can be concluded that depending on the desired electrode thickness, any rotation speed can be chosen while maintaining the same synthesis conditions (10 wt% mPEG, 55%  $\text{Fe}(\text{OTs})_3$  in BuOH), EDOT VPP during 30 min at  $40^\circ$ ) to obtain highly conductive PEDOT electrodes with high electroactivity.

### 2.2.8 Conclusion

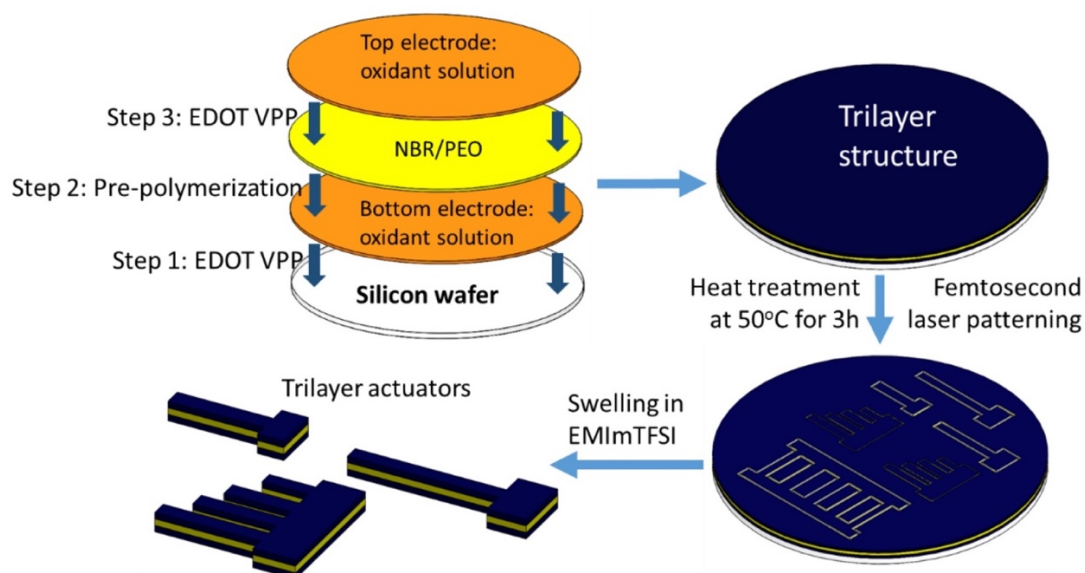
This study was carried out in order to fabricate highly conductive and electroactive PEDOT electrodes for layer stacking method to obtain efficient bending type trilayer actuators. It can be concluded that the ratio between the oxidant and the solvent and the rotation speed of the spin-coater did not have a tremendous effect on the electrical and electrochemical properties of the PEDOT electrodes. These parameters can be chosen according to the desired thickness of the PEDOT electrodes. It was found that it is important to add mPEG into the oxidant solution in order to increase the electrical and the electrochemical properties of the PEDOT electrodes, while not increasing the concentration above 20 wt%. The ionic liquid EMImTFSI did not influence the EDOT VPP positively, therefore the use of EMImTFSI as an additive is not recommended if high electronic conductivity and electroactivity are expected. In addition, the EDOT VPP time and temperature must not exceed 90 min and 50°C, respectively, in order to maintain high electrical and electrochemical properties. The optimized properties resulted in high electronic conductivities (up to 228 S.cm<sup>-1</sup>), high volumetric charge density (1.0 x 10<sup>8</sup> C.m<sup>-3</sup>) and the thickness of the swollen electrodes can be tuned between 1.1 and 5.3 μm.

This study has been published as a joint publication with MICTACT PhD student Tan N. Nguyen (IEMN) who worked on the fabrication and characterization of the microactuators, based on optimized PEDOT electrodes.<sup>[183]</sup>

### 2.3 Trilayer microactuators with optimized PEDOT electrodes using layer stacking method

The fabrication and characterization of the laser patterned trilayer PEDOT microactuators were performed by T. N. Nguyen in IEMN according to the optimized conditions of PEDOT electrodes: commercial 55 wt% Fe(OTs)<sub>3</sub> in BuOH, 10% mPEG in the oxidant solution (vs Fe(OTs)<sub>3</sub> in BuOH), the spin-coating speed, acceleration and duration were 1500 rpm, 1000 rpm.s<sup>-1</sup> and 30 s, the EDOT VPP time and temperature 50 min at 40°C. The fabrication of the trilayer actuators is illustrated in **Figure 28**. The trilayer actuators were fabricated with layer stacking method as described previously by Maziz.<sup>[139]</sup> The bottom and top PEDOT electrodes were obtained from EDOT VPP and the middle PEO-NBR layer from radical pre-polymerization of spin-coated mPEG/NBR mixture. The final trilayer configuration was obtained after heat treatment at 50°C during 3h in order to complete the polymerization of

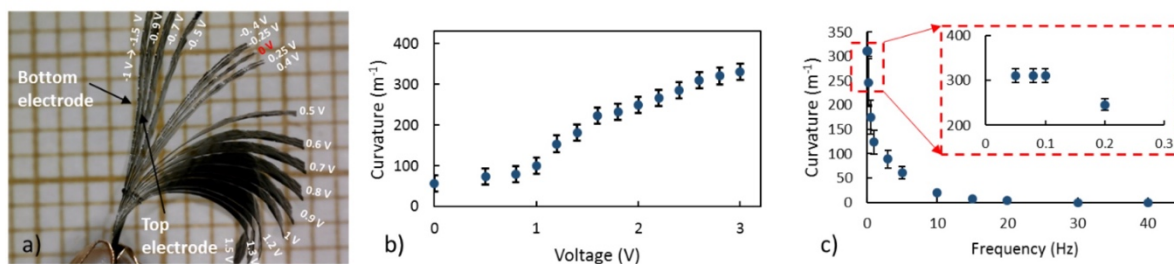
mPEG in the middle layers and to form co-bonding between all the layers via methacrylate functions of mPEG. Micropatterning was carried out using laser ablation to obtain trilayer microactuators. As a final step, the microactuators were swollen in ionic liquid (EMImTFSI) before further characterization.



**Figure 28.** Microactuator fabrication process according to layer stacking method.<sup>[183]</sup>

The thickness of the resulting microactuator was 11.2  $\mu\text{m}$  in dry state and 18.3  $\mu\text{m}$  in the swollen state. The length and the width of the microactuators were 6 mm and 1 mm, respectively. The microactuator was connected to voltage source and the displacement was recorded with a micro-camera. **Figure 29** illustrates the curvature of the resulting microactuator as a function of applied voltage and frequency. It was found that the curvature of the beam, thus the strain was increasing, when the applied voltage was increased (at 0.1 Hz) (**Figure 29a** and **b**). The maximum value of  $330 \pm 31 \text{ m}^{-1}$  was obtained with electrical stimulation  $\pm 1.5 \text{ V}$ , corresponding to the strain difference ( $\varepsilon\%$ ) of  $0.50 \pm 0.05 \%$ <sup>1</sup>. The strain difference calculation is described in Appendix 1 (A.1.2). As for many actuators, the strain is decreasing when the frequency is increased (**Figure 29c**).<sup>[134,184]</sup> The effect of the frequency on strain will be discussed in Chapter 5. The maximum force 11  $\mu\text{N}$  was obtained at the tip of the microactuator with an applied voltage of  $\pm 1.65 \text{ V}$ .

<sup>1</sup>  $\varepsilon\% = Kh$ , where K is the curvature and h is the thickness of the actuator.



**Figure 29.** PEDOT trilayer microactuator elaborated with the optimized synthesis parameters: a) illustration of the curvature as a function of applied voltage; b) curvature as a function of applied voltage (at 0.1 Hz); c) curvature as a function of frequency (at  $\pm 1.5$  V).<sup>[183]</sup>

The optimization of the electrical and electrochemical properties of the PEDOT electrodes allowed the fabrication of more efficient PEDOT trilayer microactuators. In comparison to the previous Maziz's layer stacking method, the only modified parameters are the PEDOT electrodes synthesis conditions. These microactuators resulted in improved strain difference (0.5 %) and generated forces (11  $\mu\text{N}$ ) compared to previous 0.13 % and 0.75  $\mu\text{N}$ .

## 2.4 Conclusion

The optimization of the PEDOT electrodes was performed in order to improve the electrical and electrochemical properties of the PEDOT electrodes, to integrate them into trilayer microactuators with layer stacking method and to improve the performances of these type of microactuators.

It was found that the oxidant concentration did not have a huge impact and can be chosen according to the desired thickness of the PEDOT electrodes. Addition of EMImTFSI affected the EDOT VPP negatively and is not recommended to use if high electrical and electrochemical properties are expected. Adding mPEG into the oxidant solution helps to improve both, the electronic conductivity and the electrochemical properties of the PEDOT electrodes but it is important not to increase the concentration above 20%. The EDOT VPP time and temperature must not exceed 90 min and 50°C, respectively, in order to maintain high electrical and electrochemical properties.

These optimized parameters helped to fabricate efficient microactuator, resulting in 0.5% strain difference and maximum force of 11  $\mu\text{N}$ . The resulting properties demonstrate an improvement compared to the previous layer stacked fabricated microactuator of Maziz and prove the impact of the electrode optimization to develop more efficient microactuators for microsystems.



# Chapter 3. PEDOT:PSS based microactuators and microsensors

**Foreword:** *The goal of this chapter is to simplify previously developed layer stacking method and to fabricate reproducible microactuators and microsensors based on poly(3,4-ethylenedioxythiophene):poly(styrenesulfonate) (PEDOT:PSS).*

### 3.1 Introduction

Poly(3,4-ethylenedioxythiophene):poly(styrene sulfonate) (PEDOT:PSS) is a commercially available conducting polymer dispersion. This aqueous dispersion has the advantage of easy processing through various methods, such as drop casting, spray coating, spin coating and ink-printing techniques.<sup>[45,49–57]</sup> Although PEDOT:PSS is known as a promising candidate for many applications due to its remarkable properties, it also has shortcomings when it comes to electrical and electrochemical, but also mechanical properties. Indeed, pristine PEDOT:PSS layers are brittle and present usually low electronic conductivity (below 1 S.cm<sup>-1</sup>) and poor redox electroactivity.<sup>[185]</sup> Due to the extensive research in the field of organic electronics, many groups around the world have focused on the enhancement of the electronic conductivity of PEDOT:PSS by thermal, light, acid, organic solvent, ionic liquid and surfactant treatments.<sup>[58–65]</sup> This conductivity increase is usually attributed to the phase separation between PEDOT-rich and PSS-rich domains, leading to a percolated fibrillary morphology. In addition to electronic conductivity, it has been demonstrated that incorporation of additives (xylitol, bis(trifluoromethane) sulfonimide lithium salt (LiTFSI), 4-(3-butyl-1-imidazolium)-1-butananesulfonic acid triflate) has allowed tuning also the mechanical properties of the PEDOT:PSS and the fabrication of stretchable electrodes.<sup>[46,99]</sup> However, very few studies are focused on the improvement of the electrochemical properties of PEDOT:PSS. Among them, the inclusion of additives (lithium salts) or the increase of the operating temperature have been demonstrated to improve the electrochemical properties for Li-Ion batteries or energy storage devices.<sup>[186,187]</sup> Concerning electroactive soft actuators, the use of PEDOT:PSS as an electrode material has tremendously increased in recent years due to its commercial availability and high thermal and chemical stability. For such applications, electrical, electrochemical and mechanical properties are critical. Different research groups have reported the fabrication of PEDOT:PSS-based actuators with different additives, such as ionic liquid, poly(ethylene oxide) (PEO), ethylene glycol (EG), single-walled carbon nanotubes (SWCNTs) and multi-walled carbon nanotubes (MWCNTs) to improve the performances of the resulting actuators.<sup>[55,56,100,188–193]</sup> In most cases, these actuators are realized by casting the PEDOT:PSS dispersion either on both faces of the polymer membrane



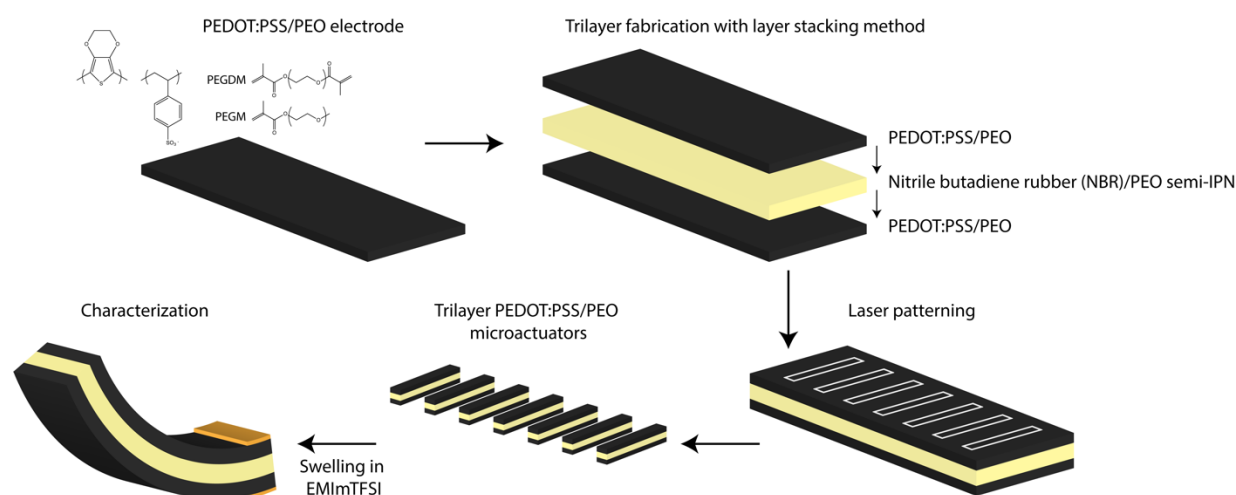
or by hot-pressing all three layers in order to obtain trilayer actuators.<sup>[100,188,190–192]</sup> Less common is the use of ink-jet printing or spray-coating to deposit the PEDOT:PSS electrodes on both sides of the polymer membrane, requiring special interactions between the conducting polymer solution and the membrane to obtain good adhesion.<sup>[56,193]</sup> However, only a minor research has been reported for PEDOT:PSS microactuators. Taccola *et al.* demonstrated the fabrication of PEDOT:PSS/SU-8 bilayer fingers but the limiting factor of this work was the operation in liquid electrolyte.<sup>[126]</sup> Põldsalu *et al.* reported the fabrication of ink-jet printed PEDOT:PSS microactuators where bending actuation was demonstrated in air.<sup>[57]</sup> Unfortunately, the process appears insufficient for microactuator fabrication, requiring flipping the substrate to obtain the PEDOT:PSS electrodes on both faces of the ionic membrane.

To minimize any manual handling, layer stacking method was recently developed by Maziz *et al.* by fabricating and operating trilayer microactuators directly on a substrate, as described in the bibliography section.<sup>[139]</sup> It was found in the previous chapter that the electroactivity of the PEDOT electrodes was greatly improved by incorporating glycol-based monomers (mPEG) during the VPP.<sup>[183]</sup> These PEDOT electrodes were then used to fabricate microactuators with layer stacking method and resulted in the improvement of the microactuator's performances with maximum strain of 0.5 % and maximum output force of 11  $\mu$ N. However, this process requires washing step in order to remove the oxidant and the residuals of the EDOT monomer after VPP synthesized electrodes, which is poorly compatible with microsystem process and susceptible to promote lift-off from the substrate, arising problems during the fabrication process.

In this chapter, a simple and effective fabrication method is proposed to fabricate microactuators with layer stacking method. For this purpose, commercially available PEDOT:PSS dispersion (Clevios PH1000) was chosen as an electrode material for this study because it allows to replace EDOT VPP, to avoid washing step and ensures ease of processing and scalability. Polyethylene glycol methacrylate derivatives (mPEG) are incorporated into the PEDOT:PSS dispersion for several reasons. First, as previously described, PEO based additives should provide enhancement of electronic conductivity due to the morphological modifications of the conducting polymer layer. The ionic conducting properties of incorporated PEO phase should also facilitate ion transport and exchange between the electroactive PEDOT domains and the electrolyte. As a result, an enhancement

of the electroactivity of the electrodes is expected and should be an advantage for an electrochemical actuator application. Finally, the reactive nature of mPEG additives, via the methacrylate functions is expected to enhance (i) the mechanical properties of the PEDOT:PSS electrodes due to the formation of a semi-interpenetrated PEO network and (ii) to enhance the adhesion between the electrodes and the ionic conducting membrane because of covalent co-bonding.

The work developed in this chapter is first focused on the synthesis and characterization of electrodes elaborated from commercial PEDOT:PSS solution with mPEG reactive additives. Afterwards, these PEDOT:PSS/PEO composite electrodes are used to fabricate trilayer actuators with layer stacking method, which are patterned using laser ablation to obtain microactuators. Finally, the electrochemical and mechanical properties of the corresponding PEDOT:PSS/PEO microactuators are characterized. Additionally, this work provides also the first demonstration that mechanical strain sensing behavior, extensively studied at macroscale, still occurs at microscale for these trilayer systems and highlights that the output signal is significantly enhanced by downsizing the devices compared to similar macroscale samples. (**Figure 30**).

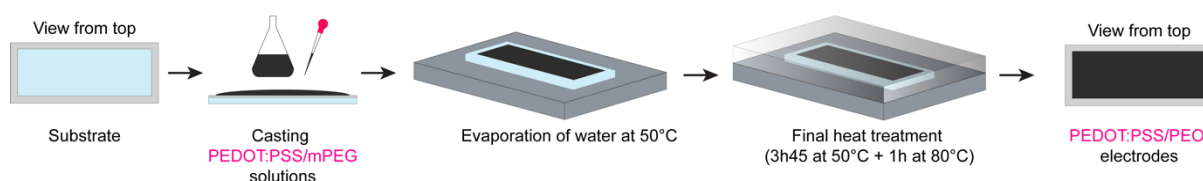


**Figure 30.** PEDOT:PSS/PEO microactuator fabrication with layer stacking method.

### 3.2 Fabrication and characterization of PEDOT:PSS/PEO electrodes

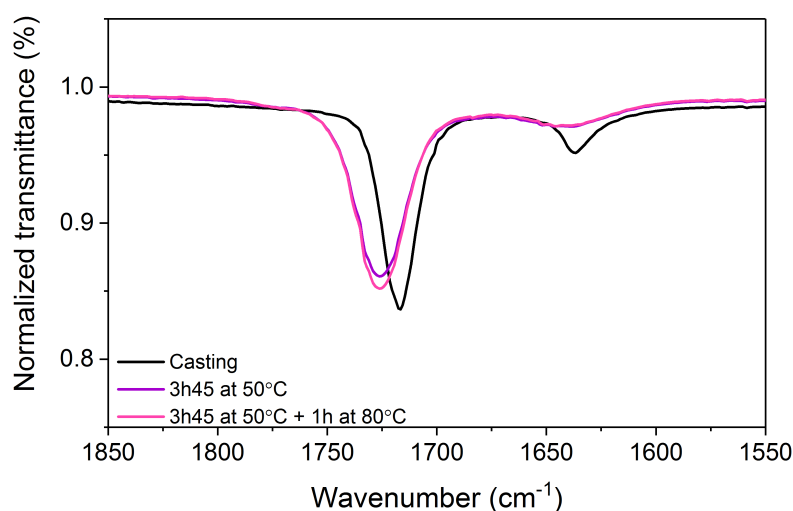
The fabrication of the PEDOT:PSS electrodes was performed as following. First, the commercial PEDOT:PSS aqueous dispersion (Clevios PH1000) was modified by the introduction of water soluble PEO precursors (mPEG). These reactive additives contain 50/50 wt% mixture of poly(ethylene glycol) methyl ether methacrylate (PEGM) as a monomer and poly(ethylene glycol) dimethacrylate (PEGDM) as a crosslinker. The content

of additives was calculated to represent 0 – 60 wt% of PEO in the final mass of the casted electrodes, knowing that the PEDOT:PSS solid content in the commercial PH1000 dispersion is given on average 1.15 wt%. In order to initiate the formation of PEO network in the PEDOT:PSS electrodes, a water soluble radical initiator is also required. Ammonium persulfate (APS) as a water-soluble radical initiator was chosen and then introduced to the PEDOT:PSS/mPEG mixture (3 wt% vs mPEG). The PEDOT:PSS/mPEG/APS mixture was stirred until dissolution of all additives and degassed. Casting molds were prepared by covering the microscope slide edges with adhesive tape. The modified PEDOT:PSS dispersion was casted<sup>[53,54]</sup> ( $0.08 \text{ ml.cm}^{-2}$ ) into the molds and the substrates were then placed in open-air on a heating plate at  $50^\circ\text{C}$  to let the water evaporate and to form free-standing PEDOT:PSS/mPEG electrodes. The final heat treatment was carried out under argon during 3h 45min at  $50^\circ\text{C}$  and 1h at  $80^\circ\text{C}$  to promote the free radical polymerization of mPEG within the PEDOT:PSS electrodes. The fabrication process of the PEDOT:PSS/PEO composite electrodes is illustrated in **Figure 31**.



**Figure 31.** Fabrication process of PEDOT:PSS electrodes using casting method.

In order to evidence the conversion of methacrylate functions in this system, the polymerization kinetics of mPEG initiated by APS was followed by attenuated total reflection (ATR) infrared spectroscopy (FT-IR). This study was not performed in PEDOT:PSS modified solution but in degassed deionized water, i.e. in the absence of PEDOT:PSS, due to the strong absorbance of PEDOT:PSS in the IR range, covering up most characteristic signals. Nevertheless the concentration of mPEG in the water (0.77 wt% in water) was set to be similar to the one used for the fabrication of the PEDOT:PSS/PEO 60/40 electrode (0.77 wt% mPEG and 1.15 wt% PEDOT:PSS in water). The solution was then casted into previously prepared molds and followed by the heat treatment during 3h 45 min at  $50^\circ\text{C}$  and 1 h at  $80^\circ\text{C}$ . The infrared spectra were obtained after each three steps in the fabrication process (casting and drying at  $50^\circ\text{C}$ , heat treatment at  $50^\circ\text{C}$  and heat treatment at  $80^\circ\text{C}$ ) and the spectra are brought in **Figure 32**. Actually, the final sample is composed of just PEO, since the water is evaporated during the casting process.



**Figure 32.** Normalized transmittance of ATR-FT-IR spectrums of the mixture of PEO precursors and APS after different steps in the fabrication process.

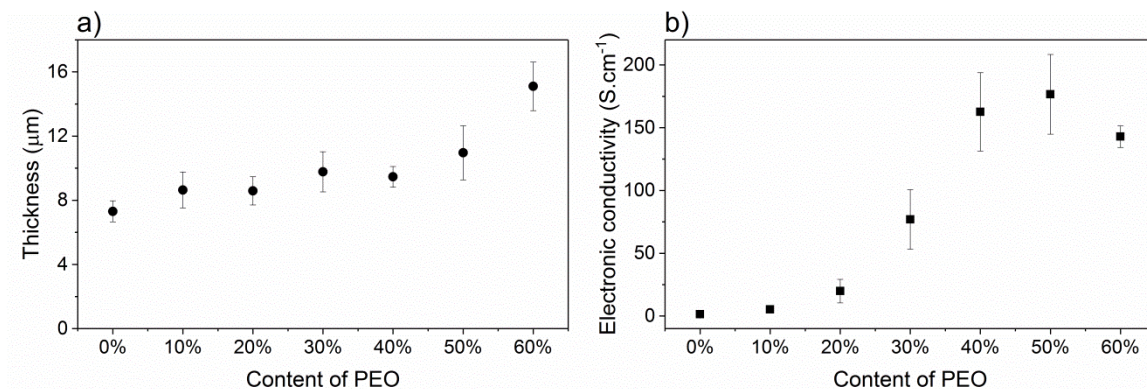
The IR spectrum after casting and drying presents two peaks in the 1850-1550  $\text{cm}^{-1}$  range. The absorbance band at 1637  $\text{cm}^{-1}$  is assigned to the stretching vibrations of methacrylate C=C double bonds. The absorbance band at 1717  $\text{cm}^{-1}$  is attributed to  $\alpha,\beta$ -unsaturated aliphatic esters, thus methacrylate C=O stretching vibrations. After 3h 45 min at 50°C, the absorption band at 1637  $\text{cm}^{-1}$  is disappearing, indicating that the polymerization of methacrylate takes place efficiently, even before the final step at 80°C. At the same time, the absorption band at 1717  $\text{cm}^{-1}$  is shifted to 1726  $\text{cm}^{-1}$ , corresponding to C=O stretching vibrations of the saturated aliphatic esters, proving also the polymerization of PEO precursors. As a consequence, APS was confirmed as efficient radical initiator for the PEO network formation and chosen as initiator for the fabrication of PEDOT:PSS/PEO electrodes. Different initiators (peroxide-based and azo initiators) were also studied and the results are presented in Appendix 2, section A.2.1.

PEDOT:PSS/PEO electrodes were then fabricated according to the procedure described above. Then, these obtained PEDOT:PSS/PEO composite electrodes were immersed into ionic liquid (EMImTFSI) prior to the characterizations.

High electronic conductivity ( $\sigma$ ) and high volumetric charge density ( $\rho$ ) are important for obtaining fast and homogeneous bending along the length of the actuator and to ensure the accessibility of ions during the redox process as described in the previous chapter. For this purpose, the study on electrical and electrochemical properties of the PEDOT:PSS electrodes is carried out as a function of the PEO content (0 – 60 wt%). Thickness, electronic

conductivity and electroactivity of each electrode are characterized when swollen by electrolyte (EMImTFSI). The electronic conductivity and volumetric charge density of the electrodes were calculated in the same way as brought in Chapter 2 section 2.2.1.

**Figure 33a** presents the thickness of the resulting electrodes as a function of PEO content. The thickness is increasing from 7.3  $\mu\text{m}$  (0% PEO) to 15.1  $\mu\text{m}$  (60% PEO), due to the increase in solid content of the casting solution. The effect of PEO content on the electronic conductivity is depicted on **Figure 33b**. The electronic conductivity of the pristine PEDOT:PSS electrode is only 1  $\text{S}\cdot\text{cm}^{-1}$  and reaches a maximum value of 163  $\text{S}\cdot\text{cm}^{-1}$  at a concentration of 40% PEO in the electrode. Even though the electrode containing 50% PEO presents slightly higher electronic conductivity, then some phase separation occurred, leading to partly wet and non-homogeneous surface. As a consequence, the electrode composition with 40% PEO in the electrodes was considered as the maximum content to fabricate reproducible electrodes. Although insulating PEO phase is diluting the conductive part of the PEDOT:PSS/PEO electrode, the electronic conductivity is increased by two orders of magnitude, demonstrating the beneficial effect of this additive.<sup>[194,195]</sup>

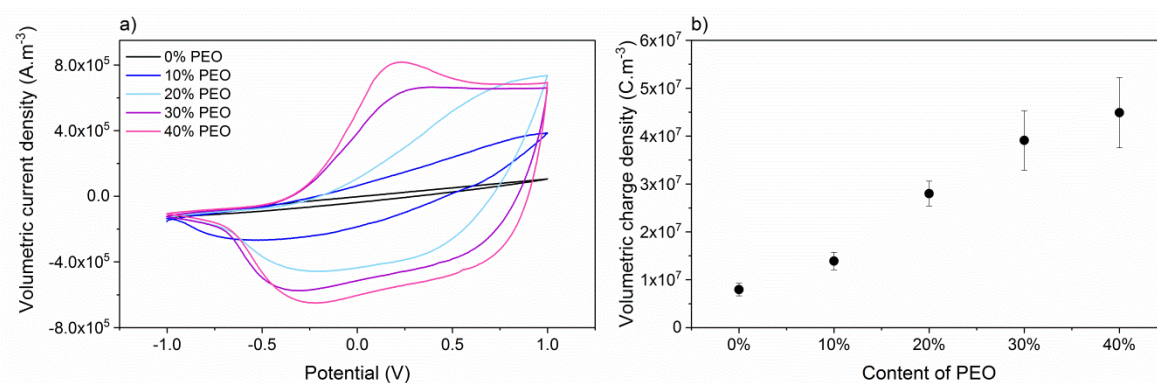


**Figure 33.** a) Thickness and b) electronic conductivity of PEDOT:PSS electrodes in swollen state (EMImTFSI) as a function of the PEO content

As another important parameter for efficient bending type actuator, the influence of the PEO content on electrochemical properties of the PEDOT:PSS/PEO composite electrodes was studied. **Figure 34a** depicts the cyclic voltammograms of the electrodes and demonstrates a progressive increase in current when higher content of PEO is incorporated to the electrodes. The PEDOT:PSS electrode with 40% PEO presents high current density with clearly defined oxidation and reduction peaks. As expected, the presence of PEO as an additive allows the redox process to take place more efficiently within the PEDOT:PSS electrodes probably due to the good ion transport properties of the PEO. The same behavior was observed in the case

of VPP PEDOT electrodes in the previous chapter, where incorporation of PEO improved both, the electrical and electrochemical properties.<sup>[183]</sup> The increased electroactivity can be related to the increased ionic and electronic conductivity, which allows faster charging of the electrodes when the content of PEO is added. Higher current and electrochemical behavior of the electrodes with lower content of PEO can be expected when lowering the scan rate during cycling.

The volumetric charge density  $\rho$  allows to evaluate quantitatively the electroactivity of the PEDOT:PSS electrodes. **Figure 34b** confirms the increase in electrochemical properties when PEO is incorporated as an additive into the PEDOT:PSS solution:  $\rho$  increases from  $8.0 \times 10^6 \text{ C.m}^{-3}$  to  $4.5 \times 10^7 \text{ C.m}^{-3}$  when 40% PEO is incorporated into the electrodes, demonstrating a 6-fold increase compared to the pristine PEDOT:PSS electrode.

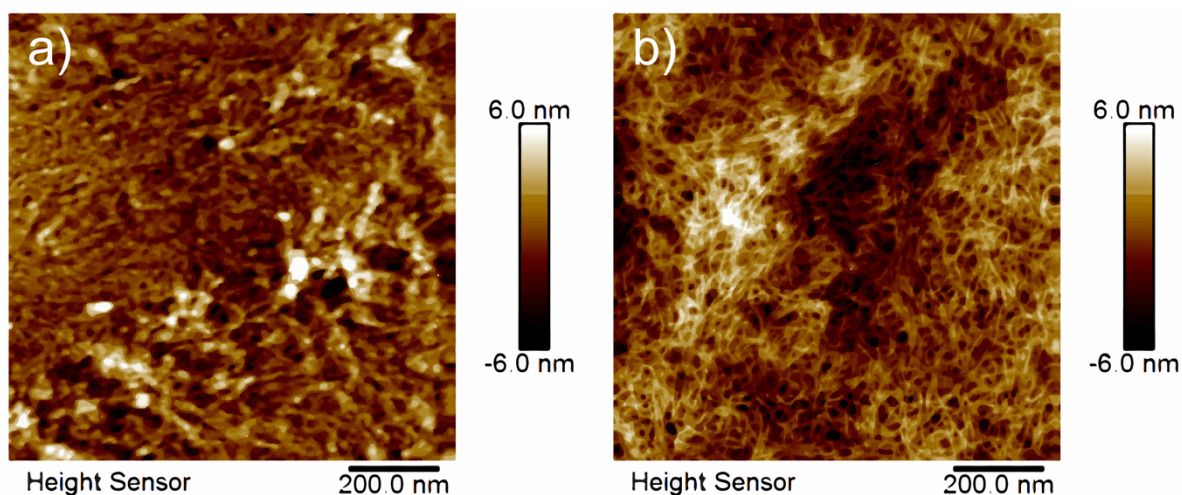


**Figure 34.** a) Cyclic voltammetry and b) volumetric charge density of PEDOT:PSS electrodes as a function of PEO content at a scan rate of  $20 \text{ mV.s}^{-1}$  and a voltage window of  $\pm 1.0 \text{ V}$  in EMImTFSI.

PEDOT:PSS electrodes were characterized using Atomic Force Microscopy (AFM) in order to understand the effect of the additives on the morphology of the electrodes. The pristine PEDOT:PSS electrode and the PEDOT:PSS electrode with 40% PEO were analyzed as fabricated. The surface of the PEDOT:PSS film is modified from granular to fibrous structure by the addition of PEO network (**Figure 35a-b**) as described elsewhere for other additives which is also known to improve the conductivity of the PEDOT:PSS.<sup>[185,195,196]</sup> Indeed, the presence of polar additive, such as PEO, can induce phase separation between the hydrophobic PEDOT and the hydrophilic PSS, creating a better connected fibrous network between PEDOT particles and allowing an improved electronic charge transport along the electrode. Moreover, the resulting fibrous and interconnected morphology is also most likely the reason for improved electrochemical properties of the PEDOT:PSS electrodes. Additionally to the presence of PEO, which should improve significantly the ionic

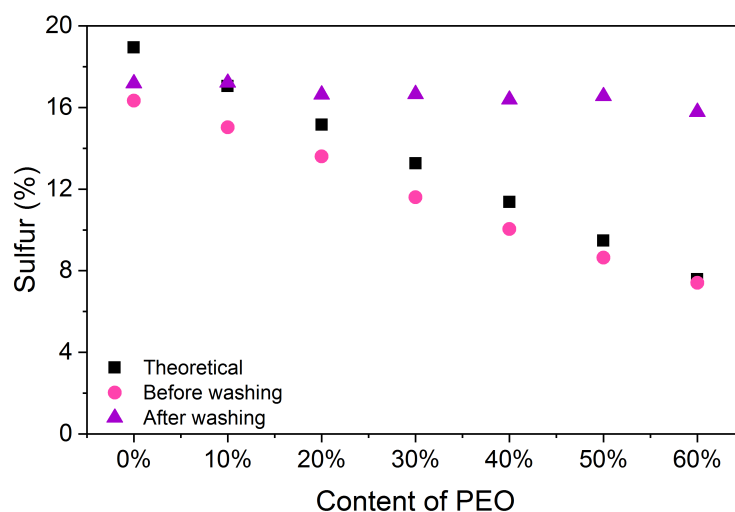


conductivity within the PEDOT:PSS layer due to its good ionic transport, [197] such morphology is possibly providing higher accessibility of PEDOT domains to ionic species.



**Figure 35.** AFM images of a) pristine PEDOT:PSS and b) PEDOT:PSS with 40% PEO films.

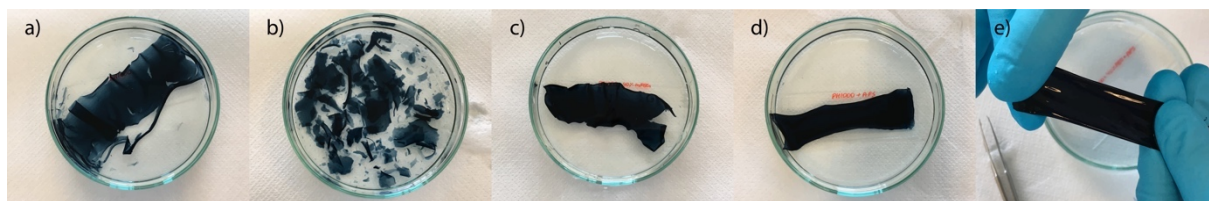
In order to evaluate the PEO polymer network formation within the composite electrodes, quantitative elemental analyses of sulfur were carried out on electrodes with 0 – 60% of incorporated PEO. Composite electrodes were fabricated in duplicate, one for analysis as fabricated; the other for analysis after washing in methanol (MeOH) and drying under vacuum in order to verify if the PEO network is crosslinked. **Figure 36** represents the results of elemental analysis as a function of content of PEO in the PEDOT:PSS/PEO electrodes. The theoretical value of sulfur was calculated by considering the weight ratio between PEDOT and PSS 1:2.5 as given in Clevios PH1000 commercial solution. The theoretical values are close to the experimental values for as fabricated samples, as expected. These values demonstrate that the expected content of PEO is present in the fabricated PEDOT:PSS electrodes. Increasing the content of PEO decreases the PEDOT:PSS part and therefore the sulfur content is decreasing. Contrarily, the results after washing in MeOH reveal that all the expected PEO network is washed out and the sulfur content is coming back to the pristine PEDOT:PSS level for all the electrodes. This result is surprising since PEO is expected to be polymerized and crosslinked. However, it appears from previous experiments that single PEO network becomes particularly brittle when swelling in polar solvent like methanol due to its high swelling rate. Assuming that the present PEO in the final material is in the form of more or less percolated microgels, washing in MeOH may extract the formed PEO microgels and be the reason of the constant value of the sulfur content.[198]



**Figure 36.** Elemental analysis of PEDOT:PSS electrodes as a function of PEO content.

The crosslinking effect of the mPEG/APS system in PEDOT:PSS can also be evaluated by the study on the film integrity and dimensional stability in the water. Indeed, it has been demonstrated by different authors that the crosslinking is considered to occur if the PEDOT:PSS films are stable in the water.<sup>[199–202]</sup> For that reason, the dimensional stability of the PEDOT:PSS based electrodes was studied by their immersion into the water. The effect of each precursor or initiator (mPEG or APS) on PEDOT:PSS electrodes was studied separately. The results with different initiators, as mentioned earlier, are presented in Appendix 2, section A.2.4. Pristine PEDOT:PSS film, PEDOT:PSS film with 40% mPEG and PEDOT:PSS film with APS lose their integrity or dimensions directly when immersed into the water (**Figure 37 a-d**). Pristine PEDOT:PSS film broke down into small pieces after 10 minutes. The PEDOT:PSS films with 40% mPEG or with APS deformed more slowly but it was not possible to handle them as films. This slight enhancement of mechanical properties has not been studied but could be attributed to the morphological modifications (granular to fibrous) in the case of only mPEG and to possible grafting in the case of only APS (peroxide-based initiator). On the other hand, the PEDOT:PSS electrode with 40% mPEG and APS was stable and remained as a strong film even when removing from the water. It was still possible to handle and to stretch the electrode without breaking it into pieces (**Figure 37e**). These results demonstrate the beneficial effect of reactive additives to fabricate PEDOT:PSS electrodes with improved electrical but also electrochemical and mechanical properties, which is an asset for the elaboration of robust and efficient electromechanical microdevices.





**Figure 37.** PEDOT:PSS films after water immersion during 10 minutes. a) PH1000 (directly when immersed into water); b) PH1000; c) PH1000 + 40% mPEG; d) PH1000 + APS; e) PH1000 + 40% mPEG + APS.

For the next sections of this work, the PEDOT:PSS electrode containing 40% PEO, which presented both, maximum electronic conductivity and electroactivity, was chosen as the composite electrode for the elaboration of microactuators and is assigned as PEDOT:PSS/PEO electrode.

### 3.3 PEDOT:PSS/PEO based microactuators

This section describes first the fabrication of PEDOT:PSS-based trilayer microactuators. Microactuators with pristine PEDOT:PSS and PEDOT:PSS/PEO composite electrodes were fabricated in order to evaluate the effect of PEO on the performances of the resulting PEDOT:PSS microactuators. The mechanical and electrochemical properties will be discussed. Moreover, the mechanical strain sensing of these microactuators will be demonstrated.

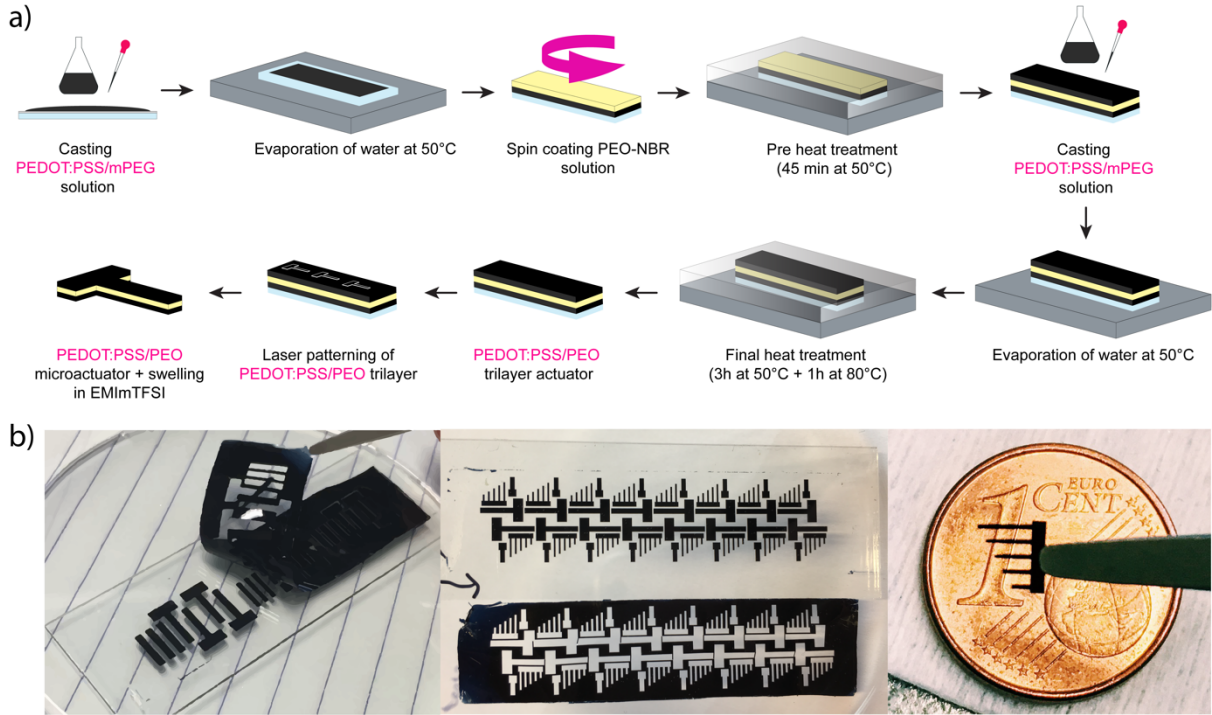
#### 3.3.1 Fabrication of PEDOT:PSS/PEO microactuators with layer stacking method

The synthesis of the trilayer actuators was performed according to layer stacking method.<sup>[139]</sup> This process was tailored to be compatible with PEDOT:PSS as the new electrode material (**Figure 38**) which does not require washing step. The PEDOT:PSS casting solutions were obtained by mixing Clevis PH1000 commercial solution, PEO precursors (0 wt% and 40 wt%) and APS (3 wt% vs PEO precursors), as described in the previous section for electrode fabrication. The solutions were casted ( $0.08 \text{ ml.cm}^{-2}$ ) into previously prepared microscope slide molds and the substrates were placed on a heating plate at  $50^\circ\text{C}$ , to evaporate the water and to form self-standing electrodes.

The polymeric membrane, as an ion storage membrane and an electronic insulator between two electrodes, is based on the semi-interpenetrating polymer network (semi-IPN) structure. The semi-IPN layer is polymerized *in situ* and is composed of a PEO network and a linear nitrile butadiene rubber (NBR), where the former promotes the membrane's ionic conductivity (when introduced to the electrolyte) and the latter ensures the mechanical

properties. First, the NBR solution was prepared by dissolving NBR (20 wt%) in cyclohexanone and stirred until complete dissolution. The PEO precursors (100 wt% vs NBR), consisting of PEGDM (25 wt% vs PEO network) and PEGM (75 wt% vs PEO network) were added to the NBR solution and stirred during 30 min. The radical initiator dicyclohexyl peroxydicarbonate (DCPD) (3 wt% vs PEO network) was then introduced to the solution and the final solution was stirred until complete homogenization and degassed. During the next step, the reactive mixture was spin coated (the spin coating speed, acceleration and duration were 1500 rpm, 1000 rpm.s<sup>-1</sup> and 30 s, respectively) onto the first PEDOT:PSS electrode layer and pre-polymerized in a sealed chamber under argon during 45 min at 50°C to initiate the formation of PEO network.

The second PEDOT:PSS electrode was fabricated on top of the PEDOT:PSS/semi-IPN bilayer in the same way as the first electrode: solutions were prepared, casted and solidified at 50°C by evaporating the water. Resulting trilayer actuators were then placed to a sealed chamber for the final heat treatment during 3h at 50°C and 1h at 80°C under argon for intralayer cross-linking and interlayer co-bonding. Finally, the fabrication process includes micropatterning of the trilayer structures into microbeams, using laser cutting (Oxford Lasers). The obtained microactuators are then immersed in ionic liquid (EMImTFSI, 72h) to incorporate the ions, necessary for the redox process. The length and the width of the characterized microbeams were 6.8 mm and 1.2 mm, respectively. The thicknesses were 29.7 and 34.6 μm for the pristine PEDOT:PSS and PEDOT:PSS/PEO microactuators, respectively.



**Figure 38.** a) Microactuator fabrication process based on layer stacking method (PEDOT:PSS with 0% and 40% PEO) and b) photographs of the laser patterned PEDOT:PSS based microactuators.

### 3.3.2 Mechanical properties

Stiffness of the beams was measured during mechanical bending experiments. The stiffness is calculated from the relationship between the applied displacement and the resulting forces, allowing to determine the Young's modulus of the microbeams. The experiments were carried out with the microrobotic system FT-RS1002 (Femtotools) and a microforce sensing probe FT-S1000 (Femtotools). The tip of the sensing probe was in contact with the microactuator at the distance of 3 mm. The displacement was applied and the resulting force was recorded. The Young's modulus was obtained from the relation between the displacement and the force of the microactuators and is calculated following the formula below:

$$E = \frac{4kL^3}{wh^3} \quad (3)$$

where  $k$  is the slope of the recorded force and the displacement curve,  $L$  is the distance between the clamped end of the microactuator and the tip of the force sensor,  $w$  and  $h$  are the width and thickness of the microactuator, respectively.

The PEDOT:PSS microactuator has relatively high Young's modulus (2.8 GPa) compared to the PEDOT:PSS/PEO microactuator (0.9 GPa) (**Table 3**). This trend has also been reported in the literature, suggesting that incorporating additives dilutes the casting solution and helps to form more fibrous PEDOT:PSS with less dense structure and therefore lower Young's modulus.<sup>[185]</sup> The equation below is then used to derive Young's modulus of the electrodes separately:

$$E_{electrode} = \frac{(E_{trilayer} h_{trilayer}^3) - (E_{PEO-NBR} h_{PEO-NBR}^3)}{h_{trilayer}^3 - h_{PEO-NBR}^3} \quad (4)$$

Where  $E_x$  and  $h_x$  are the Young's modulus (MPa) and the thickness ( $\mu\text{m}$ ) of the corresponding layers. The thicknesses of the PEDOT:PSS layers are obtained from the electrode study. The Young's modulus of the PEO-NBR membrane is approximately 0.3 MPa and the thickness 15  $\mu\text{m}$  (both in the presence of EMImTFSI). The derived results for the electrodes are brought in **Table 3**. The pristine PEDOT:PSS electrode presents higher Young's modulus (3.3 GPa), which is also slightly higher compared to the values reported in the literature for PEDOT:PSS films ( $\sim 2.5$  GPa) but quite in the same range.<sup>[203,204]</sup> The derived modulus of the PEDOT:PSS/PEO electrode is 1.0 GPa. Overall, these results demonstrate softening of microactuators and electrodes when PEO is incorporated to the PEDOT:PSS layers.

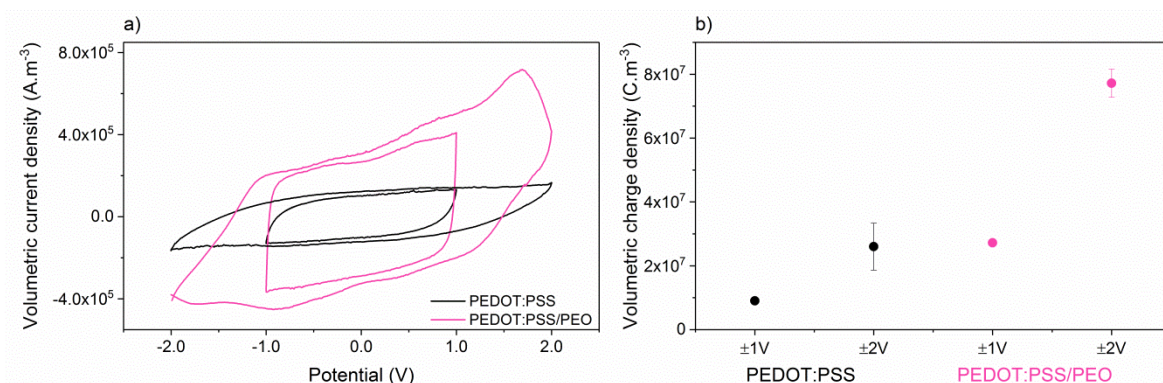
**Table 3.** The Young's modulus values of PEDOT:PSS microactuators and the calculated Young's modulus values of corresponding PEDOT:PSS electrodes.

	$E_{trilayer}$ (GPa)	$h_{electrode}$ ( $\mu\text{m}$ )	$E_{electrode}$ (GPa)
PEDOT:PSS	2.8	7.3	3.3
PEDOT:PSS/PEO	0.9	9.2	1.0

### 3.3.3 Electrochemical properties

The electrochemical properties of the PEDOT:PSS microactuators were determined using cyclic voltammetry ( $\pm 1.0$  V,  $\pm 2.0$  V, 20  $\text{mV}\cdot\text{s}^{-1}$ ). Cyclic voltammetry (CV) of the microactuators was performed using VMP Multipotentiostat (Biologic SA) in two-electrode configuration. One PEDOT:PSS electrode of the trilayer configuration was connected to the working electrode and the second PEDOT:PSS electrode to the reference and counter electrodes. The volumetric charge density was calculated according to the formula 2 in Chapter 2, section 2.2.1, considering the volume of one entire PEDOT:PSS electrode.

**Figure 39a** illustrates the cyclic voltammetry of the microactuators. Both microactuators present double-layer capacitor-like behavior at a potential window of  $\pm 1.0$  V. The curve of the PEDOT:PSS microactuator remains similar also at wider potential window ( $\pm 2.0$  V), indicating that the resistive behavior of pristine PEDOT:PSS electrodes prevents efficient redox process to take place. The PEDOT:PSS/PEO microactuator shows a redox process occurring at higher potential range ( $\pm 2.0$  V). These results are consistent with the work of Okuzaki *et al.* where it was found that actuators based on PEDOT:PSS, ionic liquid and polyurethane membrane as an ion reservoir present capacitor behavior at lower voltages and a redox behavior at voltages higher than 1.5 V.<sup>[100]</sup> The volumetric charge densities (**Figure 39b**) confirm the increasing trend of electroactivity at higher potentials and even further when PEO is incorporated to the PEDOT:PSS electrodes. The resulting values of  $\rho$  for PEDOT:PSS microactuator are  $9.0 \times 10^6$  C.m<sup>-3</sup> and  $2.6 \times 10^7$  C.m<sup>-3</sup> at voltage windows of  $\pm 1.0$  V and  $\pm 2.0$  V, respectively. The corresponding values for PEDOT:PSS/PEO microactuator are  $2.7 \times 10^7$  C.m<sup>-3</sup> and  $7.7 \times 10^7$  C.m<sup>-3</sup> at voltage windows of  $\pm 1.0$  V and  $\pm 2.0$  V. The volumetric charge density of the PEDOT:PSS/PEO microactuator is 3 times higher at both voltage windows compared to the pristine PEDOT:PSS microactuator. Higher electrochemical performances of the PEDOT:PSS/PEO microactuators can be related, as for electrode study, to the fibrous structure of the PEDOT:PSS electrode and the presence of PEO (AFM image, **Figure 35**), promoting good ion transport in the PEDOT phase and improving therefore the charge transport in the electrodes.

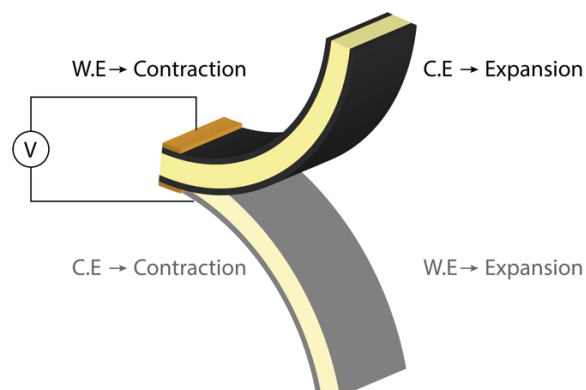


**Figure 39.** a) Cyclic voltammetry and b) volumetric charge density of PEDOT:PSS and PEDOT:PSS/PEO microactuators at a scan rate of  $20 \text{ mV}\cdot\text{s}^{-1}$  and a voltage windows of  $\pm 1.0$  V and  $\pm 2.0$  V.

### 3.3.4 Actuation characterization

The actuation characterizations of the microactuators were performed as a function of square wave potential between  $\pm 0.4$  and  $\pm 2.2$  V at a frequency of 0.1 Hz. The upper layer of the

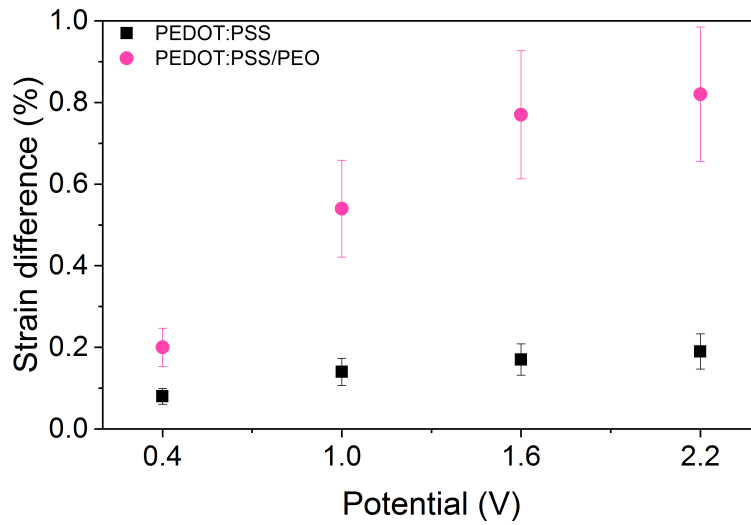
device was connected to the working electrode and the experimental setup is illustrated in **Figure 40**. The strain difference  $\varepsilon$  was calculated according to Sugino (Appendix 1, section A.1.2).<sup>[14]</sup>



**Figure 40.** Schematic view of the experimental setup for actuation characterization.

It can be seen from **Figure 41**, that applied potential has an effect on the strain difference of both microactuators. For both samples, the strain difference is increasing with the voltage and seems to reach a plateau beyond 1.6 V, indicating that the maximum deformation of the device is reached. Regardless of the applied potential, the strain difference is notably higher in the presence of PEO. The pristine PEDOT:PSS microactuator reached the maximum value of 0.19 % at the highest applied potential of 2.2 V. This value is relatively low and can be explained by both, low electronic conductivity and low volumetric charge density of the pristine PEDOT:PSS electrodes. The PEDOT:PSS/PEO microactuator reached the maximum value of 0.82 % also at 2.2 V. It confirms that the incorporation of PEO is also beneficial for the strain performances, most likely related to higher volumetric charge density and therefore a better charge transport in the composite electrodes, but also to the lower Young's modulus which facilitates their bending. Finally, it should be mentioned here that the bending direction during oxidation of the working electrode correspond to a volume contraction. In other words, during oxidation the  $\text{EMI}^+$  cations are expelled from the oxidized PEDOT electrodes (Chapter 1), which is consistent with the cation mobile mechanism previously reported for PEDOT macroactuators using EMITFSI as electrolyte.<sup>[106]</sup>





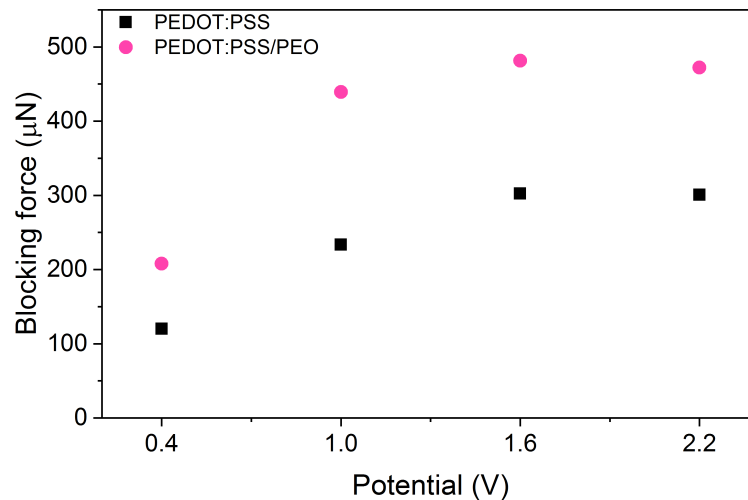
**Figure 41.** Strain difference (%) as a function of applied potential at a frequency of 0.1 Hz of the PEDOT:PSS and PEDOT:PSS/PEO microactuators.

### 3.3.5 Blocking force characterization

The blocking force measurements were carried out as a function of applied potential between  $\pm 0.4$  and  $\pm 2.2$  V at a frequency of 0.1 Hz. The microactuator was clamped and connected to the voltage source. The tip of the sensing probe was in contact with the microactuator at the distance of 3 mm. When potential was applied, the bending movement was then counteracted by the tip of the sensing probe and the resulting data was recorded.

At low potential (0.4 V), the generated forces for pristine PEDOT:PSS and PEDOT:PSS/PEO microactuators are 120  $\mu\text{N}$  and 208  $\mu\text{N}$ , respectively (**Figure 42**). As observed previously for strain, the output force is increasing with the increase of the potential for both microactuators until 1.6 V before reaching a plateau. The maximum values at 1.6 V for the PEDOT:PSS and PEDOT:PSS/PEO microactuators are 301  $\mu\text{N}$  and 472  $\mu\text{N}$ , respectively. This indicates that the output force is only improved by a factor 1.5 between pristine PEDOT:PSS and PEDOT:PSS/PEO microactuators, while a 4-fold increase was measured for strain values. This result can appear surprising taken into account the enhanced electrical and electrochemical properties, but can be explained by an electromechanical model proposed by Alici *et al.* showing that the output force is directly proportional to the Young's modulus of the electrodes.<sup>[205]</sup> The values of Young's modulus (**Table 3**) demonstrated the electrodes softening when PEO was incorporated, which consequently may decrease the generated forces of the final microbeam. Supposedly it can be a trade-off between electronic conductivity, electroactivity and Young's modulus where the first two improve the overall

performances of the PEDOT:PSS/PEO microactuator but softening of the electrodes limit the output force. Nevertheless, output forces in the range of hundreds of  $\mu\text{N}$  can be obtained which is considerably higher compared to previously described VPP PEDOT microactuators, where the maximum force was  $11 \mu\text{N}$ .<sup>[183]</sup> This large improvement can be of course attributed to the geometry factor (2-times thicker and 2-times shorter measurement distance in the present study) but also to the difference in Young's modulus between PEDOT obtained through VPP and PEDOT:PSS/PEO electrodes, around  $20 \text{ MPa}$ <sup>[206]</sup> and  $1.0 \text{ GPa}$  respectively.



**Figure 42.** Blocking force (at 3.0 mm from clamping) as a function of applied potential of the PEDOT:PSS and PEDOT:PSS/PEO microactuators. The length and the width of the microbeams are 6.8 mm and 1.2 mm, respectively

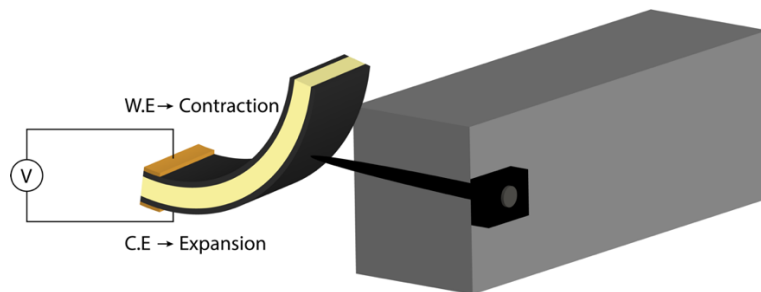
### 3.3.6 Sensor characterization

Depending on external stimuli (electrical or mechanical stimulation), ECP based devices are known to act as both, as actuators or as strain sensors. The mechanism behind the voltage generation in sensor mode is not fully defined yet, but there are several proposed mechanisms with experimental characterizations to understand better this voltage generation. Wu *et al.* introduced the “Deformation Induced Ion Flux” model to estimate the magnitude and the polarity of the sensor response.<sup>[174]</sup> This model is based on circumstances where the mechanical stress is changing the volume of the conducting polymer and consequently affects the internal ion concentration. This leads to an imbalance of ion concentration between the conducting polymer and the electrolyte and results in voltage generation. Aforementioned model postulates that the sensor response and the polarity are directly linked to the difference in ion mobility. Another study, reported by Shoa *et al.* have shown that applying force to



polypyrrole based device generates a proportional change in the voltage. The authors proposed also a model, indicating that the external application of stress alters the internal stress of ions, helping to insert or remove charge and as a consequence, to change the voltage.<sup>[207]</sup> More recently, the “piezoionic effect” has been introduced to explain the voltage generation through inhomogeneous ionic distribution, based on the Donnan potential.<sup>[208]</sup> All these ECP sensors were only described at macroscale, with variation of open circuit voltages usually in the range of mV or lower. However, there is no prediction based on theoretical model and no experimental demonstration to know if such behavior still occurs for microsized samples and which voltage amplitude can be generated.

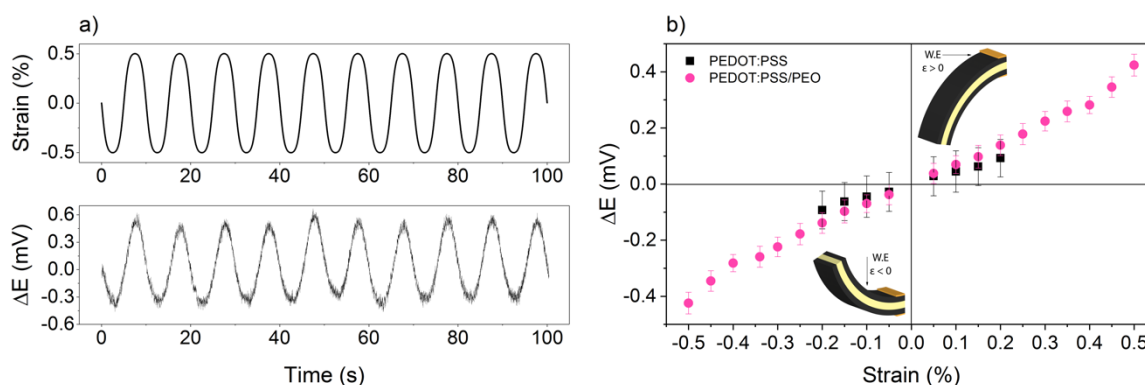
In this work, mechanical bending is applied to the microactuators and open circuit voltage (OCV) is recorded. The Dual Mode Lever System (Aurora Scientific, 300C) was used to apply mechanical stimulation and the resulting OCV was recorded with the potentiostat (VMP Multipotentiostat, Biologic SA). The upper layer of the device was connected to the working electrode and during upward bending displacement the top electrode was then compressed (**Figure 43**). The length and the width of the characterized microbeams were 6.8 mm and 1.2 mm, respectively.



**Figure 43.** Schematic view of the experimental setup for sensor characterization.

**Figure 44a** presents the sinusoidal mechanical stimulation (strain amplitude  $\pm 0.5\%$ ) applied to the PEDOT:PSS/PEO microbeam as a function of time with the corresponding OCV variation. It demonstrates a good correlation between strain and electrical response indicating that the detection of mechanical stimulation at microscale is possible. The signal is corresponding to an *in-phase* response, i.e. a positive strain of the working electrode corresponding to an increase of the OCV. The sign of the voltage variation is consistent with previously reported results on PEDOT macro-samples in the case of EMImTFSI, where it was demonstrated that the more mobile ionic species are the cations.<sup>[106]</sup> During compression/expansion of the working electrode, the mechanically induced ion flux is promoting dominant motion of cations from or towards the electrodes, respectively. In other

words, we demonstrate here that the ion motion mechanism taking place in macro-samples is the same in the microsized ones.

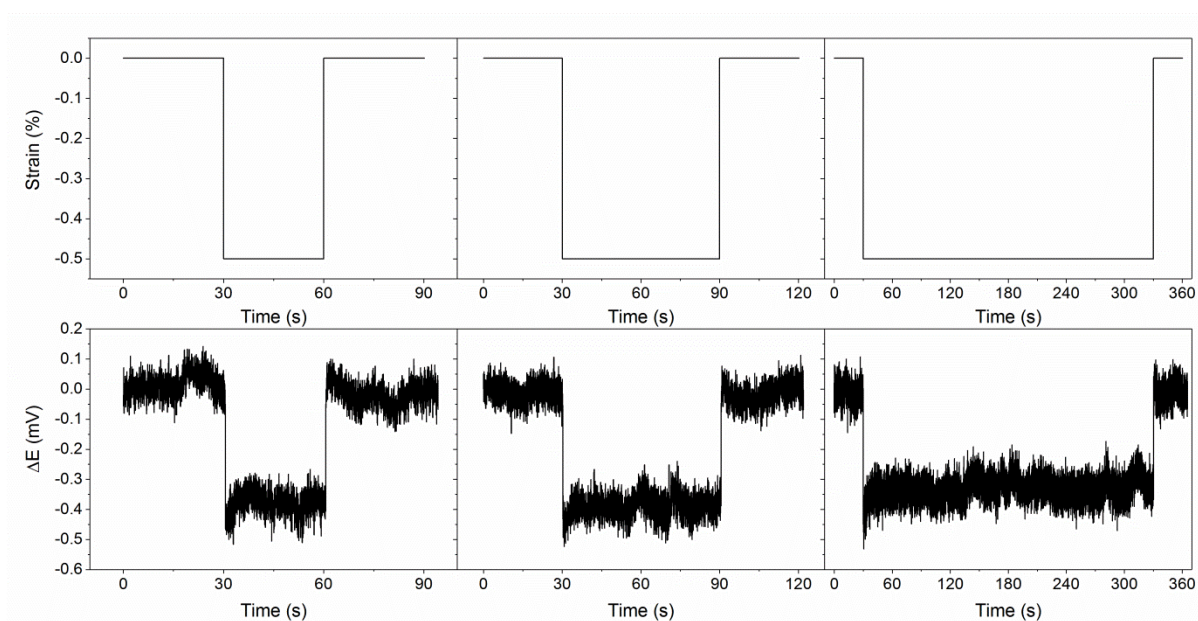


**Figure 44.** a) Open circuit voltage ( $\Delta E$ ) response of PEDOT:PSS/PEO microsensor to the sinusoidal mechanical stimulation at a strain of 0.5 %; b) Open circuit voltage ( $\Delta E$ ) response to the sinusoidal mechanical stimulation as a function of applied strain at a frequency of 0.1 Hz of the PEDOT:PSS and PEDOT:PSS/PEO microsensors

**Figure 44b** presents the amplitude of OCV variation measured during mechanical stimulation of the microbeams for applied strain ranging between -0.5 and 0.5 % at a frequency of 0.1 Hz. It can be observed that OCV depends on the mechanical stimulation and the variation increases linearly with the amplitude of the mechanical stimulation with a sensitivity close to  $0.74 \text{ mV}\cdot\%^{-1}$ . These results demonstrate that conducting polymer based microbeams are effectively behaving as strain microsensors, able to detect but also to quantify a mechanical deformation. The pristine PEDOT:PSS microsensor reaches a maximum value of 0.09 mV at a strain of 0.2 %. It must be mentioned here that applying higher strain tends to break the samples, probably because of stiffer electrodes and consequently more brittle devices. The PEDOT:PSS/PEO microbeam presents almost identical response but can be stimulated up to 0.5 %. For this amplitude, the OCV variation is equal to 0.42 mV. This result at a strain of 0.5 % is approximately 10 times higher compared to the values reported in previous work on thick trilayer macrodevices (0.04 mV at 0.5% strain).<sup>[106]</sup> Therefore, downsizing such devices not only allows to still detect mechanical stimulation, but it also provides higher sensitivity. Considering that ion flux is driven by stress gradient across the thickness of the device, a decrease of the device's thickness for the same applied strain tends to proportionally increase the stress gradient and then can be the main factor of the observed sensitivity enhancement.

**Figure 45** interprets the applied step displacement of -0.5 % strain, i.e. bending leading to the contraction of the working electrode, and the open circuit voltage variation ( $\Delta E$ ) for PEDOT:PSS/PEO microsensor. The responses during 30 s, 1 min and 5 min follow the same

trend and a negative output voltage signal of approximately -0.4 mV was produced during the compression of the working electrode. However, the electrical signal evolution over time is different compared to other reported ECP based trilayer sensors. Indeed, in the reported cases, an electrical signal relaxation is observed when maintaining constant strain, ultimately going back to initial value.<sup>[106]</sup> This typical relaxation phenomenon can be explained by the piezoionic effect introduced by Sarwar *et al.*<sup>[208]</sup> When applying mechanical stimulation, the mechanically induced cation flux from the compressed electrode is creating disequilibrium of ions and generating the OCV variation. However, since both cations and anions are mobile in classical electrolytes or ionic liquids, the less mobile anions are diffusing also over time, to progressively compensate this concentration difference. As a consequence, the OCV variation is progressively going back to 0 mV. This behavior can be considered as a drawback since it allows detecting dynamic stimulation but prevents any direct relationship between the position of the device and the OCV value. Interestingly, in the case of the PEDOT:PSS/PEO electrodes, the high concentration of non-mobile PSS<sup>-</sup> anions within the electrodes may tend to limit the relaxation compared to classical ECP electrodes. This situation seems to be similar to the behavior of IPMCs where only one type of mobile ions exist (cations), since anions are attached to the perfluorosulfonic membranes. In this case, no relaxation is also observed.<sup>[209]</sup> However, a specific study would be required to really explain the origin of this behavior. Nevertheless, this result is especially interesting since it allows sensing not only dynamical mechanical perturbation but also relating the OCV value directly to the steady position of the microsensor, facilitating their further use in practical microsystems.



**Figure 45.** PEDOT:PSS/PEO microsensor output voltage in response to the square wave mechanical stimulation with an applied strain of 0.5 % during 30 s, 1 min and 5 min.

### 3.4 Conclusions

The PEDOT:PSS based electrodes were fabricated counting PEO as a beneficial additive to improve the electrical, electrochemical and mechanical properties of the electrodes. The incorporation of the PEO into the PEDOT:PSS electrodes resulted in high electronic conductivity ( $163 \text{ S.cm}^{-1}$ ) and high volumetric charge density ( $4.5 \times 10^7 \text{ C.m}^{-3}$ ). The PEDOT:PSS based actuators were fabricated with tailored layer stacking method and micropatterned using laser ablation technique. Two types of microactuators with different electrode compositions (PEDOT:PSS and PEDOT:PSS/PEO) were fabricated in order to evaluate the effect of PEO on microactuators performances. The PEDOT:PSS/PEO microactuators resulted in improvement of all the studied parameters compared to the pristine PEDOT:PSS microactuators and presented large strains (0.82 %) and high output forces (472  $\mu\text{N}$ ). It was also demonstrated for the first time that such microdevices are able to present sensing properties and that their sensitivity is even higher to that of their thick macroscopic counterparts. The absence of electrical signal relaxation was observed in comparison with other reported ECP based sensors, which is more similar to IPMC based sensors probably due to the high concentration of non-mobile  $\text{PSS}^-$  anions. These results are opening promising perspectives in the fabrication of complex actuating/sensing microsystems where these easily processed electroactive materials could be combined together and interfaced with integrated electricals contacts. This integration will be the focus of the next chapter of this manuscript.

Chapter 4. PEDOT:PSS based  
microactuators integrated into  
flexible microchips

**Foreword:** *This chapter describes full microfabrication process to integrate the PEDOT:PSS based microactuators, developed in the previous chapter, into microsystems with two integrated electrical connections directly on a flexible substrate.*

## 4.1 Introduction

Microfabrication of electronically conducting polymer (ECP) based actuators has been successfully demonstrated and more interestingly their integration into complex devices for different applications as overviewed in Chapter 1. However, there are still several obstacles in the field of microfabrication: technologies for micro-integration, performance properties, efficiency, durability and lifetime that need to be improved in order to fabricate efficient microsystems. Most of the reported work on microfabrication of ECP actuators requires manual handling during some step of the process, making it harder to manipulate the devices and could lead to possible damage. Moreover, important progress in integration of electrical connections has to be made to use these materials as microsystems for microfluidic and microrobotic applications. Microactuators are small, thin and fragile, and the use of macroscopic connections makes it relatively hard to obtain and establish a sufficient connection between the microactuator and a power supply. In other words, macroscopic connections can damage the microactuator and/or cause short circuits. For that reason, integrated micro electrical connections are required on top and bottom of each trilayer, to have an individual control of each microactuator. Relying on the scientific field that orientates electronics towards soft electronics, the integration of the microactuators and its connections directly into flexible structures is favored. Until now, there is no reported work yet on fabrication of microactuators with two integrated electrical connections and efficiently operating in air.

The previous chapter described the fabrication of PEDOT:PSS based microactuators and their improvement of performances compared to the previous PEDOT based microactuators which makes them more attractive for the development of microsystems. The realization of a microsystem has two distinct steps: the optimization of the materials and the fabrication of the resulting device. The optimization of the materials was performed in the previous chapter and exhibit good improvement with the incorporation of PEO into the PEDOT:PSS electrodes. Designing a microsystem requires knowledge of the used materials in order to choose the best processing steps to fabricate microsystems without damaging the optimized

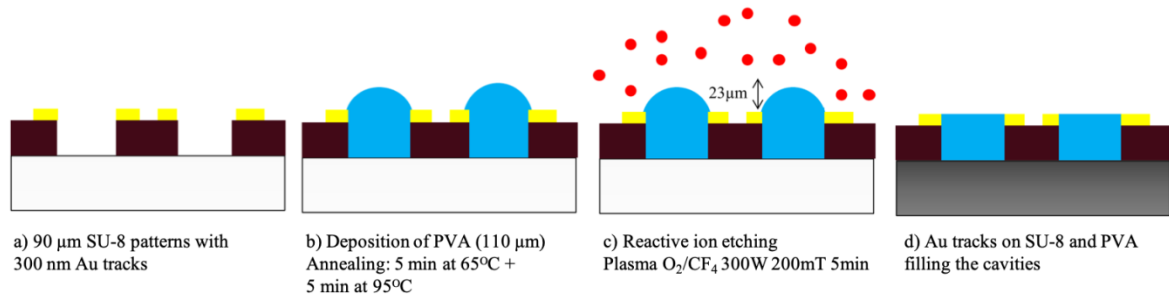
materials. While PEDOT:PSS makes the elaboration of microactuators easier compared to the vapor phase polymerization (VPP), the presence of hydrophilic polymer (PSS) makes the integration much more difficult. The realization of PEDOT:PSS based microsystems remains still challenging because it can be damaged in the water and its morphological and electrical properties can be disadvantageously influenced during different processes of the integration.

In this chapter, a microfabrication process will be described to fabricate PEDOT:PSS microactuators with two integrated gold electrical contacts on a self-standing flexible structure, using different microfabrication technologies. Moreover, this process has considered the hygroscopicity of the PEDOT:PSS, which means that after the fabrication of trilayer any water-based medium cannot be used. In particular, all the photoresist developers that contain water have been eliminated from the process, leaving negative SU-8 photoresist as the only usable photoresist after the fabrication of the PEDOT:PSS trilayer. More detailed description about SU-8 photoresist and photolithography steps with positive and negative photoresists is brought in Appendix 1, section A.1.3.

All the fabrication and characterizations in this chapter were carried out in collaboration with Pr. E. Cattan in the Institut d'Electronique, de Microélectronique et de Nanotechnologie (IEMN), in Université Polytechnique des Hauts-de-France (UPHF, France) during the first secondment of the MICACT ITN project.

## 4.2 Microfabrication process

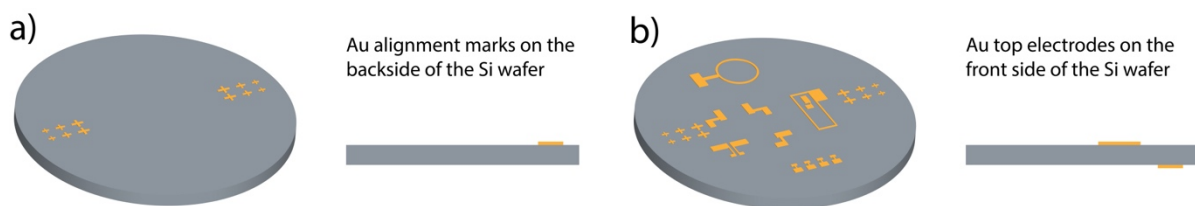
In the microfabrication process based on the previous work,<sup>[139]</sup> the SU-8 flexible structure was realized first and the actuators were obtained on top of it later. The proposed fabrication process included the use of sacrificial PVA layer beneath the trilayer actuator for filling the cavities due to thick SU-8 patterns (90  $\mu\text{m}$ ) (**Figure 46**). As a consequence, the boundary between the SU-8 and PVA was difficult to control and flatness in surface hard to obtain, creating high stresses in the trilayer microbeams which were obtained on top of these surfaces. The process described in this chapter will be carried out by fabricating the microsystems by reversing the steps, i.e. the microactuators with electrical connections are obtained first (on smooth Si wafer) and finally encapsulated using SU-8 layer, to obtain a flexible structure.



**Figure 46.** The microfabrication process of Maziz with PVA fillings for cavities between SU-8 patterns.<sup>[173]</sup>

The microchips are built on a 2-inch double side polished silicon (Si) wafer with a thickness of 150  $\mu\text{m}$ . The release of the microchips is obtained by etching through the wafer, therefore the lower is the thickness of the wafer, the shorter is the final etching time. Some processes have been realized with Si wafers with lower thicknesses (100  $\mu\text{m}$  or 50  $\mu\text{m}$ ) but risky handling and possible deformation of the substrate during different steps of layer depositions remain challenging. The thickness of 150  $\mu\text{m}$  allows easy manipulation of the wafer during the process and not being too thick for the final etching step. The full microfabrication process has been developed using eight high resolution photomasks and backside alignment due to the opacity of the PEDOT:PSS.

As a first step, to fabricate alignment marks on the backside of the wafer, a positive photoresist S1828 is spin-coated (3000rpm-1000rpm. $\text{s}^{-1}$ -10s) onto the Si wafer and baked 2 min at 110°C. Subsequently, the photoresist covered substrate is exposed to the UV at 365 nm with an exposure dose of 120  $\text{mJ}\cdot\text{cm}^{-2}$  through a photomask. The exposed areas are developed in MF-319 to form patterns for alignment marks. In the next step, first a titanium (Ti, 20 nm) and then a gold (Au, 300 nm) layers are deposited on the patterned photoresist by evaporation. Ti layer is used to improve the adhesion between the Si substrate and the Au layer. The alignment mark patterns are created by lift-off process in acetone (at room temperature), leaving only the designed Au patterns on the Si wafer (**Figure 47a**). The top electrodes are fabricated in the same way on the front side of the wafer, using another photomask to create patterns with desired shapes (**Figure 47b**).

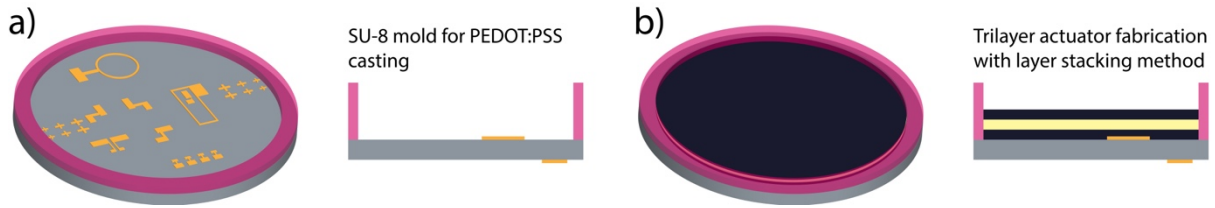


**Figure 47.** Schematic representation in 3D and 2D view: a) Si wafer with Au alignment marks on the backside of the wafer; b) Au top electrodes on the front side of the Si wafer.



In the third step of the process, SU-8 mold is prepared on the edge of the wafer to avoid the overflow of PEDOT:PSS during the casting process. For that, SU-8 2035 is spin-coated onto the Si wafer (1<sup>st</sup> segment: 500rpm-100rpm.s<sup>-1</sup>-10s with an open lid and 2<sup>nd</sup> segment: 2000rpm-400rpm.s<sup>-1</sup>-30s with a closed lid). The first segment is carried out with an open-lid at low speed to well cover the substrate with SU-8 and let the solvent evaporate as recommended by its manufacturer. The substrate is then placed on a hot-plate and soft baked (SB) during 3 min at 65°C and 6 min at 95°C. In the next step, the negative photoresist is exposed to an UV source (365 nm) at 170 mJ.cm<sup>-2</sup> and the post exposure bake (PEB) is carried out at the same temperature with the same duration as SB. The unexposed areas are then developed in the SU-8 developer during 6 min to create the SU-8 mold with a thickness of 60 µm for the following casting process (**Figure 48a**). From this step, SU-8 is used as an only photoresist and to simplify the reading of the process recipe, the SU-8 step with technical parameters (spin-coating, SB, PEB and development) will be separately sectioned as “process”.

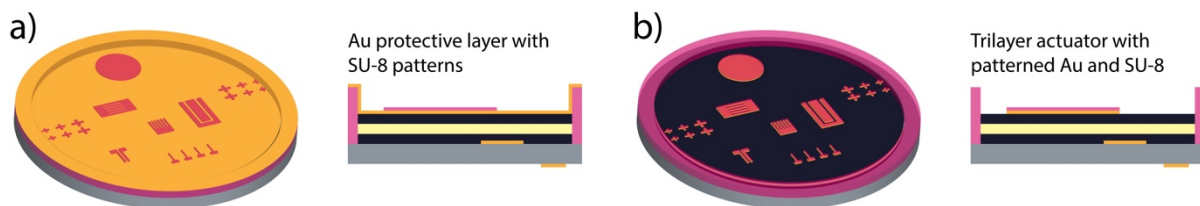
Subsequently, the trilayer actuator is fabricated according to the layer stacking method, described in detail in Chapter 3, section 3.3.1. First, the PEDOT:PSS solution with 40% mPEG and APS is casted (0.05 ml.cm<sup>-2</sup>) into the SU-8 mold, the substrate is then placed on a hot plate to evaporate the water at 50°C to form the PEDOT:PSS/PEO composite electrode. Then, the PEO-NBR solution is spin-coated (3000rpm-1000rpm.s<sup>-1</sup>-30s) on top of the PEDOT:PSS electrode and pre-treated at 50°C during 45 min under continuous nitrogen flow. The overflow of the PEO-NBR solution above the SU-8 mold of is not interfering the next steps of the process. The second PEDOT:PSS/PEO electrode is fabricated in the same way as the first one, on top of the PEO-NBR layer. Depending on the casting volume of PEDOT:PSS solution and the spin-coating speed of PEO-NBR mixture, the thickness of the actuator can be tuned according to the desired final thickness of the actuator. Lower casting volume and higher rotation speed compared to previous chapter were chosen in order to obtain thinner actuators for the actuator etching step. Finally, the substrate is placed into a closed annealing chamber and the final heat treatment is carried out at 50°C during 3h and post-cured at 80°C during 1h under continuous nitrogen flow (**Figure 48b**).



**Figure 48.** Schematic representation in 3D and 2D view: a) SU-8 mold for PEDOT:PSS casting; b) PEDOT:PSS/PEO-PEO/NBR-PEDOT:PSS/PEO trilayer actuator.

In order to pattern the trilayer actuator, a mask with desired patterns has to be used to protect the wanted shapes. Patterning of the trilayer actuator is carried out in  $O_2/CF_4$  plasma, in which an Au layer is known to be insensitive, whereas the standard photoresist mask is very sensitive. Therefore, to create the mask for actuator patterning, an Au layer (300 nm) is evaporated on top of the trilayer actuator. A negative photoresist SU-8 is used as a mask to pattern the desired Au shapes on top of the trilayer (**Figure 49a**). The thickness of the SU-8 layer was chosen to be completely etched during the reactive ion etching of the trilayer actuator. It also allows to obtain vertical wall during the trilayer etching and to limit under etching (etching in multiple directions) of the trilayer.

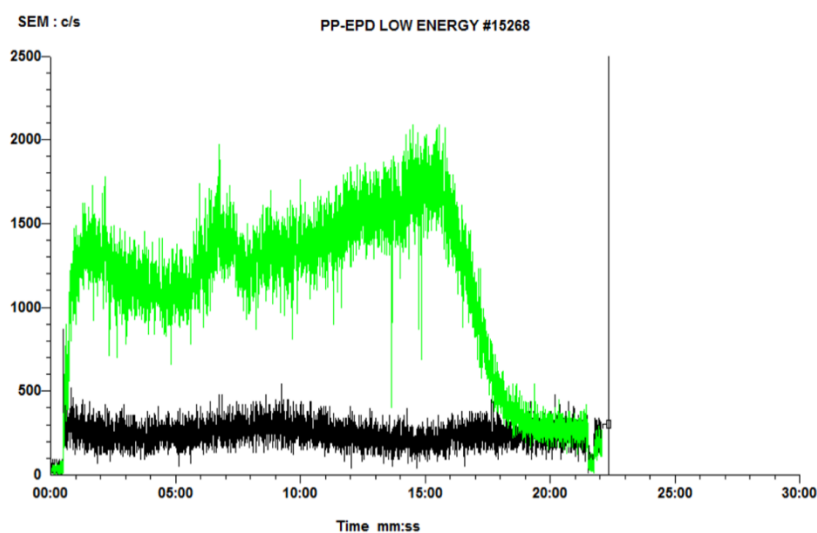
*Process: The SU-8 2010 layer is spin-coated on top of the Au layer at  $500rpm-100rpm.s^{-1}-10s$  with an open lid and at  $800rpm-400rpm.s^{-1}-30s$  with a closed lid, resulting in a layer with a thickness of  $24\ \mu m$ . The photoresist is then soft baked during 3 min at  $65\ ^\circ C$  and 6 min at  $95\ ^\circ C$ , followed by the UV exposure (365 nm) with an exposure dose of  $145\ mJ.cm^{-2}$  and PEB during 3 min at  $65\ ^\circ C$  and 6 min at  $95\ ^\circ C$ . The substrate is then immersed into SU-8 developer for 2 min to develop the unexposed areas.*



**Figure 49.** Schematic representation in 3D and 2D view: a) Au layer deposition with SU-8 patterns for IBE of Au; b) trilayer actuator with etched Au and SU-8 mask.

The next step involves etching of the exposed Au layer around the SU-8 patterns using ion beam etching (IBE) (**Figure 49b**). The SU-8 layer is not affected by the etching in IBE system, leaving a protective layer on the Au patterns. This step had to be optimized because wet chemical etching or lift-off is mostly preferred for metal layer removal. Using plasma can also increase the temperature of the substrate and cause destruction of the obtained actuator at this step of the process. The used IBE system has multiple clamping points and an efficient

cooling system, providing the best contact between the holder and the substrate and keeping the temperature of the system suitable. The argon (Ar) ion beam operates at a gas pressure of  $5 \times 10^{-4}$  mbar where an ion current density of  $300 \mu\text{A}\cdot\text{cm}^{-2}$  is obtained at a beam voltage of 700 V and a power of 300 W. A 15 sccm (standard cubic centimeters per minute) ion beam sputter and an 8 sccm plasma bridge neutralizer flow rates were used. The etch rate of the gold is  $15 \text{ nm}\cdot\text{min}^{-1}$ , i.e. the etching is finalized after 20 min, to create the masks for actuators etching. The end of the etching is determined using secondary ion mass spectroscopy (SIMS), which detects the remaining Au atoms on the sample surface. The etching is finished when the SIMS is not able to detect any Au atoms (**Figure 50**).



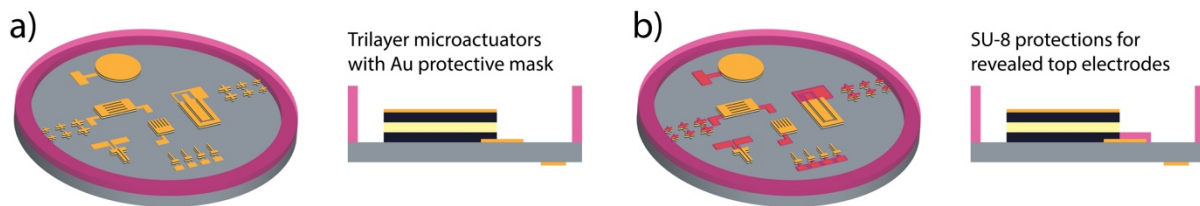
**Figure 50.** Secondary ion mass spectroscopy (SIMS) detecting the remaining Au atoms on the surface of the sample. Green is corresponding to Au atoms and black to Ti atoms.

The etching of the trilayer is performed with a reactive ion etching (RIE) in the gas mixture of  $\text{O}_2/\text{CF}_4$  (90/10) with a power of 300 W and a pressure of 200 mTorr during 35 min ( $\sim 0.65 \mu\text{m}\cdot\text{min}^{-1}$ ). These parameters have been optimized for PEDOT based actuators in the work of Khaldi *et al.* and later used in the integration process of Maziz *et al.* ( $1.75 \mu\text{m}\cdot\text{min}^{-1}$  for PEO/NBR/PEDOT IPN).<sup>[131,139,210]</sup> It was also found that the etching speed of NBR and/or PEDOT layers was not measurable, but also that the presence of interpenetrated and sensitive PEO allows the synergetic etching of these devices with reasonable time. PEO is improving the electrical and electrochemical properties of the PEDOT:PSS electrodes, consequently the performances of the microactuators and is necessary for the etching step, demonstrating an important role in the whole process. During the RIE step, also the SU-8 layer from Au patterns is being etched due to the polymer nature of the SU-8 and therefore being sensitive

to the O<sub>2</sub>/CF<sub>4</sub> gas mixture. The SU-8 patterns (24 μm) are fully etched after 12 min (**Figure 51a**).

After this step, microactuators with desired shapes are obtained, also revealing the top electrodes from beneath. In order to continue the process, the Au top electrodes must be protected to be able to remove the Au layer from the surface of the microactuators. Therefore, a negative photoresist SU-8 2010 is used to create the protections for Au top electrodes (**Figure 51b**).

*Process: SU-8 2010 is spin-coated at 500rpm-100rpm.s<sup>-1</sup>-10s with an open lid and at 3500rpm-400rpm.s<sup>-1</sup>-30s with a closed lid to form the protections for the top electrodes. The subsequent steps involve SB during 3 min at 65 °C and 6 min at 95 °C, exposure to the UV (365 nm) through a photomask with a dose of 125 mJ.cm<sup>-2</sup>, PEB 3 min at 65 °C and 6 min at 95 °C and finally the development in the SU-8 developer during 3 min to obtain SU-8 patterns with a thickness of 10 μm*

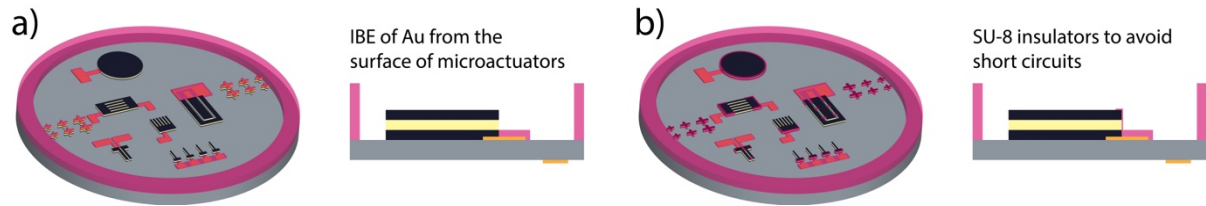


**Figure 51.** Schematic representation in 3D and 2D view: a) etched PEDOT:PSS/PEO microactuators with Au protective mask; b) SU-8 protections for revealed top electrodes.

When the protective parts are obtained for the top electrodes, then Au etching is carried out with an IBE in the same way as described previously, to remove the remaining layer from the surface of the microactuators (**Figure 52a**). Before continuing the process and in order to avoid short circuits between the top and the bottom PEDOT:PSS electrodes, an insulator layer is formed on the electrical contacts part of the microactuators. Moreover, some designs, requiring connections between different beams are also formed during this step. The negative photoresist SU-8 2002 is used to form a thin layer (2 μm) of insulators and connectors (**Figure 52b**).

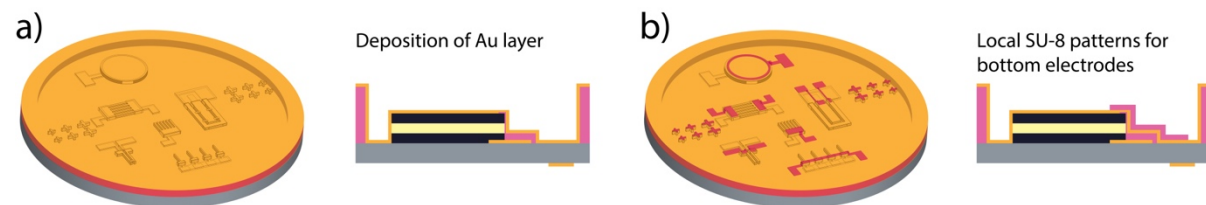
*Process: SU-8 2002 is spin-coated at 500rpm-100rpm.s<sup>-1</sup>-10s with an open lid and at 1000rpm-300rpm.s<sup>-1</sup>-30s with a closed lid, followed by the SB during 3 min at 65 °C and 6 min at 95 °C. The substrate is then exposed to the UV (365 nm) through a photomask with an*

exposure dose of  $80 \text{ mJ.cm}^{-2}$  and PEB is carried out at the same temperatures with the same duration as SB and finally developed in the SU-8 developer during 1 min.



**Figure 52.** Schematic representation in 3D and 2D view: a) IBE of Au from the surface of the PEDOT:PSS/PEO microactuators; b) SU-8 insulators to avoid short circuits between top and bottom electrical contacts.

In the next step, a 300 nm Au layer is evaporated on all-over the structure to create the surface for bottom electrodes (**Figure 53a**). Next, the SU-8 2010 photoresist is used to create the patterns for bottom electrodes directly on the Au layer (**Figure 53b**). The processing steps for SU-8 2010 are carried out in the same way as for the protections of top electrodes (illustrated in Figure 51b).

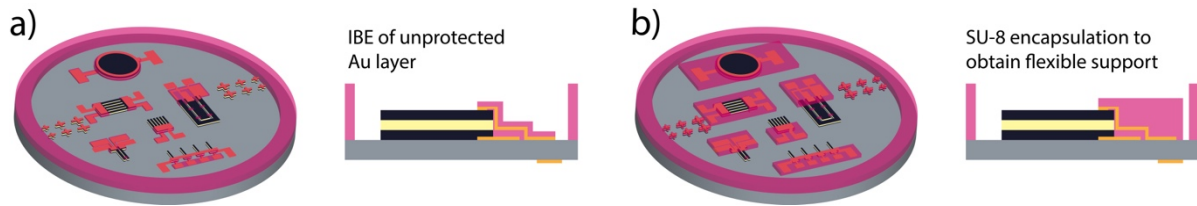


**Figure 53.** Schematic representation in 3D and 2D view: a) deposition of Au layer; b) local patterns of SU-8 to obtain bottom electrical contacts.

As a next step, IBE is used to remove the unprotected Au layer and to form SU-8 covered bottom electrodes on the PEDOT:PSS/PEO trilayer microactuators (**Figure 54a**). The Au etching with IBE is carried out as described previously. Subsequently, SU-8 encapsulation is used in order to manipulate the microchips individually and to obtain them on a flexible support. (**Figure 54b**).

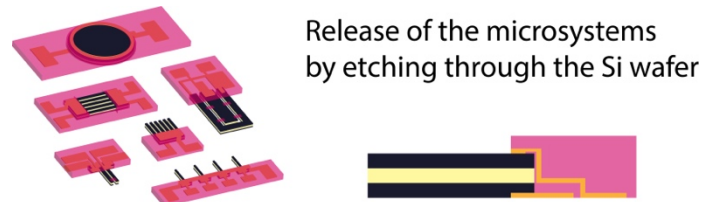
*Process: SU-8 2075 is spin-coated at  $500\text{rpm}-100\text{rpm.s}^{-1}-10\text{s}$  with an open lid and at  $4000\text{rpm}-300\text{rpm.s}^{-1}-30\text{s}$  with a closed lid to obtain a layer with a thickness of  $60 \mu\text{m}$ . The process is then followed by SB during 3 min at  $65^\circ\text{C}$  and 6 min at  $95^\circ\text{C}$ , exposure to the UV ( $365 \text{ nm}$ ) through a photomask with an expose dose of  $160 \text{ mJ.cm}^{-2}$ , PEB during 3 min at  $65^\circ\text{C}$  and 6 min at  $95^\circ\text{C}$  and the development of the unexposed areas in the SU-8 developer during 6 min.*

The stiffness of the final microsystem can be adjusted by tuning the thickness of the SU-8 layer (spin-coating parameters or different formulations of SU-8 with different viscosities).



**Figure 54.** Schematic representation in 3D and 2D view: a) IBE of unprotected Au layer; b) SU-8 encapsulation to obtain PEDOT:PSS/PEO microactuators on a flexible support.

The final step of the process involves the release of the microchips. For that, the Si wafer is thoroughly etched using a vapor phase etching of  $\text{XeF}_2$ . The wafer is placed in a chamber under a 1.0 Torr pressure and the etching gas  $\text{XeF}_2$  is introduced with a 4.0 Torr pressure. The etching is carried out during 600 cycles with a speed of  $20 \text{ cycles} \cdot \text{s}^{-1}$  (**Figure 55**).



**Figure 55.** Schematic representation in 3D and 2D view of the microsystem release by etching through the Si wafer.

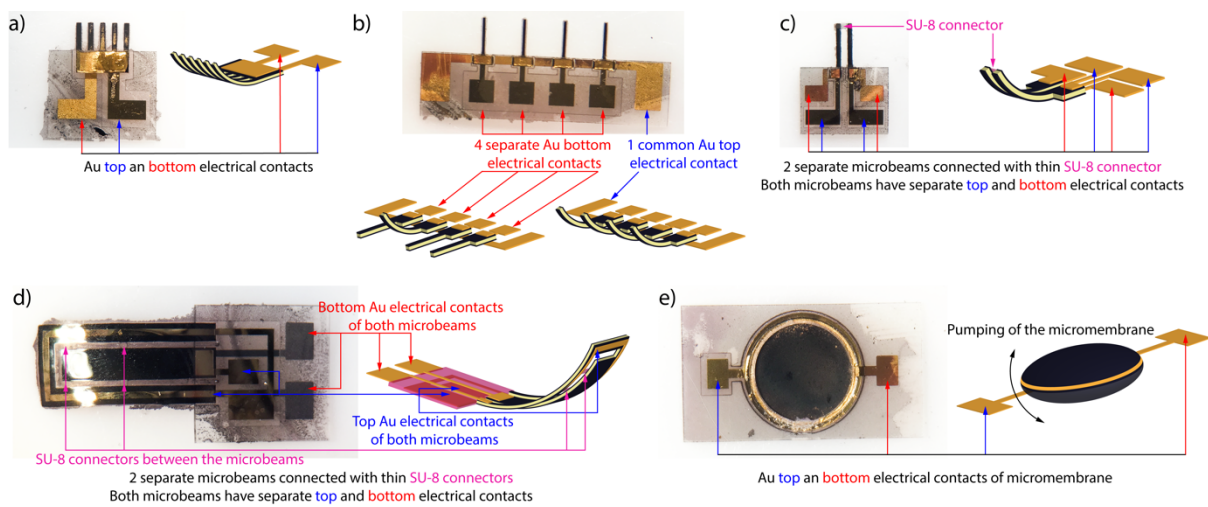
At the end of this step, all the microactuators with two electrical contacts and on the flexible support of SU-8 are being released. Both electrical contacts are accessible from one side of the encapsulation (the surface that was in contact with the Si wafer). The beams of the microactuators are subsequently swollen in ionic liquid (EMImTFSI, 72h) before further characterization.

### 4.3 Characterization of PEDOT:PSS based microsystems

The microfabrication process allows the design of different configurations of microactuators. **Figure 56** illustrates some of the fabricated designs to demonstrate the advantages of this fabrication method. **Figure 56a** represents the configuration of a microcomb where all the microbeams are connected with top and bottom electrical contact and electrical stimulation leads to their simultaneous bending. Another microsystem configuration in **Figure 56b** is realized with 4 independent bottom electrical contacts and one common top electrical contact to actuate the microbeams separately or all of them together. Microsystem in **Figure 56c** represents the possibility of realizing microactuator + microsensor configuration. The device



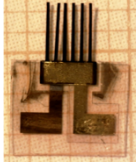

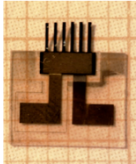
is composed of 2 separate microbeams which are physically connected using small and thin SU-8 connector. Both microbeams have separate top and bottom electrical contacts. When one beam is electrically stimulated, the second one is physically connected and mechanical strain sensing of the second beam could be measured. **Figure 56d** illustrates another configuration of microactuator + microsensors system, both with independent electrical contacts and physically connected with thin SU-8 layers. Different configuration in **Figure 56e** represents the micromembrane. The trilayer microactuator is patterned in a circular shape and integrated with top and bottom electrical contacts. Electrical stimulation of this configuration could result in pumping of the micromembrane.



**Figure 56.** Real images of the microdevices and 3D illustrations under electrical stimulation of different configurations of PEDOT:PSS-based microsystems with integrated electrical connections: a) microcomb with 2 electrical contacts; b) 4 microbeams with independent bottom electrical contacts and mutual top electrical contact; c) 2 microbeams connected with small and thin SU-8 layer with 2 pairs of electrical contacts; d) another configuration of 2 microbeams connected with SU-8 layers with 2 pairs of electrical contacts; e) micromembrane with 2 electrical contacts.

The properties of the microsystems were characterized by the means of the actuation, electroactivity and blocking force based on microcomb configuration in **Figure 56a**. Moreover, the sensing ability of the microsystems was tested and also the “self-sensing properties” of the microsystem with microactuator + microsensors configuration (**Figure 56c**). The characterized microbeams with the sample specifications and the beam dimensions based on configuration of a microcomb are summarized in **Table 4**.

**Table 4.** Summarized parameters of the characterized samples.

Sample	Picture of the sample	Length x width x thickness of the characterized beam	Measurement distance from the clamping
1.		2900 x 200 x 23 $\mu\text{m}$	2 mm
2.		2900 x 250 x 23 $\mu\text{m}$	2 mm
3.		1500 x 200 x 23 $\mu\text{m}$	1 mm

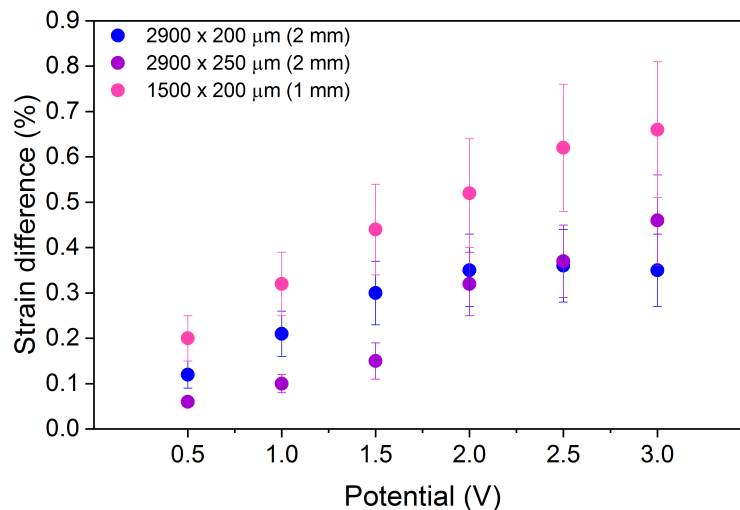
The microsystems were placed between two glass plates, covered with copper lines in order to connect them with the measurement system. The experiments were followed with two Dino Lite AM7000/AD7000 micro cameras from top and side views. During the actuation and blocking force measurements, the microsystems were connected to the voltage source (NF Electronic Instruments 1930) and an in-house amplifier to apply a square wave potential (0.5 – 3.0 V). The actuation displacement was recorded with the LKG 32 Keyence displacement sensor and the blocking force of the microsystems was determined with a microforce sensing probe FT-S1000 (Femtotools) combined with a high-precision three-axis nanomanipulation unit (FT-RS1002 Femtotools). The cyclic voltammetry was performed with Gamry Potentiostat/Galvanostat ZRA 600+ to evaluate the electroactivity of the microsystems.

#### 4.3.1 Open-air characterization of the PEDOT:PSS-based microsystems

The open-air characterizations of the PEDOT:PSS based flexible microchips were performed on few microbeams which are presented subsequently. The realized measurements are clearly not enough to conclude on observed results. These results are given to demonstrate that the microactuators are functioning after all the microfabrication processing steps. More in-depth studies are needed in order to conclude the observations. The discussion based on the microsystem results (strain difference and blocking force) is presented in this section and the comparison with already published works in the field and the results from the previous chapter are presented in the discussion section.



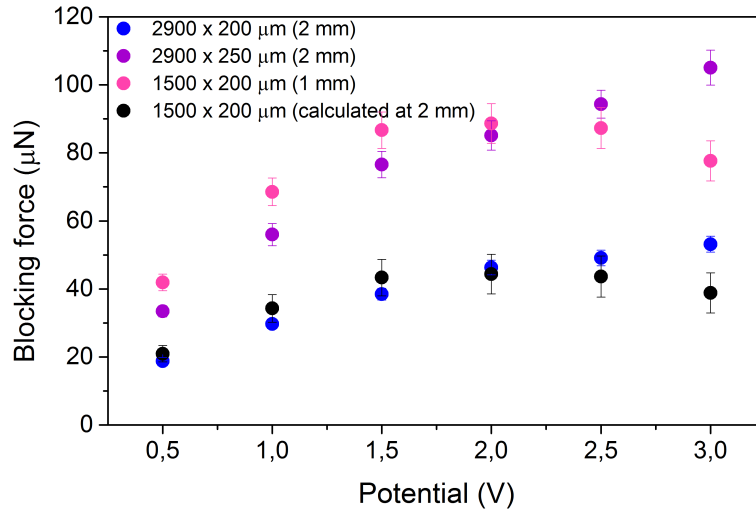
The actuation measurements of different PEDOT:PSS-based prototype beams were carried out as a function of applied voltage at a frequency of 0.1 Hz. The strain difference was calculated according to Sugino and the results are presented in **Figure 57**.<sup>[14]</sup> The applied potential has an effect on the strain difference of the PEDOT:PSS-based prototype beams, presenting common behavior which was also observed in the previous chapter. The microbeam with the dimensions of 2900 x 200  $\mu\text{m}$  presents relatively smooth increase in the strain difference, reaching the maximum value of 0.36 % at an applied potential of 2.0 V. The same length microbeam with a beam width of 250  $\mu\text{m}$  demonstrates really low strain difference values at low potential, before an increase at 2.0 V. The maximum strain difference 0.46 % of this microbeam is obtained at the maximum applied potential of 3.0 V. Both of these microbeams present similar behavior, indicating that the width (in this range) does not have obvious impact on the resulting strain. The microbeam with the dimensions of 1500 x 200  $\mu\text{m}$  presents the highest strain difference value of 0.66 % also at the highest applied potential of 3.0 V. In this last case, the measurements were performed at a distance of 1 mm (2mm for the two other samples), demonstrating higher strain but could also indicate to non-homogeneous curvature along the length of the microbeam. In other words, the actuation process is taking place more efficiently closer to the electrical contacts.



**Figure 57.** Strain difference as a function of the applied potential at a frequency of 0.1 Hz for different microbeams. Measurement distances are given in the brackets.

As another important parameter, then the blocking force of the microbeams was measured at a frequency of 0.1 Hz as a function of applied potential and the results are presented in **Figure 58**. It can be seen that the microbeams present increasing trend in blocking force

when the applied potential is increased, as observed in the previous chapter. The microbeam with the dimensions of 2900 x 200  $\mu\text{m}$  presents maximum value of 53  $\mu\text{N}$  at the highest applied potential of 3.0 V. The maximum output force of the microbeam with the dimensions of 2900 x 250  $\mu\text{m}$  is 105  $\mu\text{N}$  and two times higher due to wider and therefore stiffer microbeam, being able to produce more output force. Slightly different trend is observed for the microbeam with the dimensions of 1500 x 200  $\mu\text{m}$ . The blocking force is increasing until 1.5 V, which seems to be a saturation point for a plateau. The maximum output force of 89  $\mu\text{N}$  is obtained at the applied potential of 2.0 V. Higher force of this beam (1500 x 200  $\mu\text{m}$ ) compared to the same width but different length microbeam (2900 x 200  $\mu\text{m}$ ) can be explained by the difference in length, where the shorter beam is stiffer and consequently able to produce more force. On the other hand, the resulting 89  $\mu\text{N}$  (1500 x 200  $\mu\text{m}$ ) is lower compared to the 105  $\mu\text{N}$  (2900 x 250  $\mu\text{m}$ ) due to the lower width of the corresponding microbeam.



**Figure 58.** Blocking force as a function of the applied potential at a frequency of 0.1 Hz for different microbeams. Measurement distances are given in the brackets.

Since the measurements of the microbeam with dimensions 1500 x 200  $\mu\text{m}$  are performed at 1.0 mm, they cannot be directly compared to other beams due to smaller measurement distance. Therefore, the corresponding values at a distance of 2.0 mm were calculated according to the equation below and are also presented in **Figure 58**.<sup>[211]</sup>

$$F = \frac{E_{PPSS}\alpha\rho}{L} w \left( \frac{h_{SIPN}}{2} \right)^2 \left[ \left( 1 + \frac{2h_{PPSS}}{h_{SIPN}} \right)^2 - 1 \right] \quad (5)$$

where  $E_{PPSS}$ ,  $\alpha$ ,  $\rho$  and  $h_{PPSS}$  are the Young's modulus, strain-to-charge ratio, volumetric charge density and thickness of one PEDOT:PSS layer, respectively,  $h_{SIPN}$  thickness of the PEO-NBR layer,  $w$  width of the actuator and  $L$  is the distance between the clamped end of the microactuator (microbeam starting point after SU-8 support) and the tip of the force sensor.

The maximum output force of the microbeam with the dimensions of 1500 x 200  $\mu\text{m}$  at a distance of 2 mm would be 44  $\mu\text{N}$  at a potential of 2.0 V. It can be seen that the calculated values present similar behavior with the same width microbeam (2900 x 200), indicating good correlation and that the microbeams with the same width at the same measurement distance present comparable values. Overall, these characterizations of strain and blocking force demonstrate that different processing steps do not have a severe impact on the performances of the microbeams, resulting in functioning microsystems.

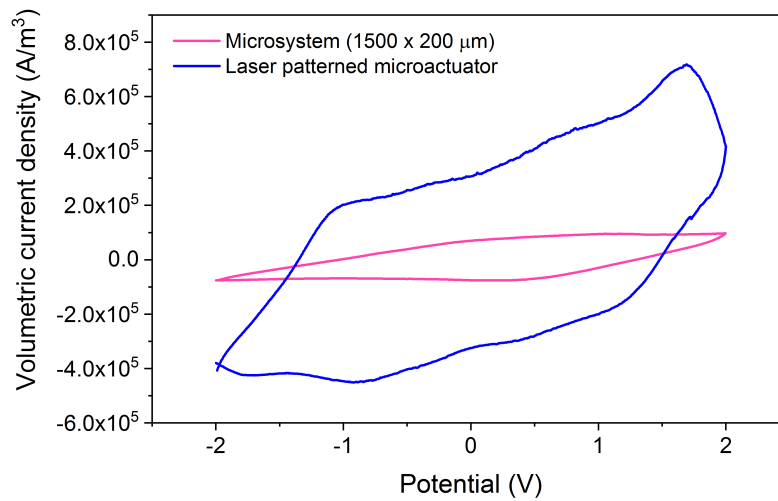
#### 4.3.2 Discussion

All the above characterized parameters presented common behavior of conducting polymer based actuators i.e. the strain and the blocking force were increasing with increased applied potential. The relative evolution of the measurements is not discussed here because the repetition was not performed. More measurements are needed in order to verify, validate and understand why the smallest beam has, for example, the largest strain and decreasing force after 2 V.

The results obtained in this chapter present great improvement compared to the PEDOT based microactuators of Maziz.<sup>[139]</sup> The highest obtained strain difference 0.66 % ( $\pm 3.0$  V) with beam dimensions of 1500 x 200 x 23  $\mu\text{m}$  is 5 times higher compared to the PEDOT based microactuator (0.13 %,  $\pm 4.0$  V) with beam dimensions of 650 x 100 x 10  $\mu\text{m}$ . Even higher improvement in blocking force is obtained, where the maximum measured output force 105  $\mu\text{N}$  is 140 times higher compared to the PEDOT-based microactuator (0.75  $\mu\text{N}$ ). Higher force of the PEDOT:PSS-based microsystems can be explained by higher thickness and larger dimensions of the microbeams, being able to produce larger output force, however geometric aspects alone are not enough to explain this improvement. Additionally, the used conducting polymer (PEDOT/PEO vs PEDOT:PSS/PEO) can have impact on the resulting performances of the microbeams due to the big difference in Young's modulus of the electrodes (20 MPa for PEDOT/PEO<sup>[206]</sup> and 1.0 GPa for PEDOT:PSS/PEO electrodes).

Another important difference comes from the fabrication process, while it cannot be said which one has higher influence on the properties of the microbeams. In the work of Maziz *et al.*, PVA and SU-8 patterns were used as a support to fabricate the actuator, creating stress in the final trilayer microactuators which might be one of the reasons for lower characterization results. Although the fabrication process described in this chapter has more processing steps, improvement in the fabrication process (microactuators are well protected during all the integration and second electrical contact is also integrated) and in the performances of the final PEDOT:PSS-based microbeams were obtained.

Even though great improvement compared to the aforementioned work of Maziz was obtained, the PEDOT:PSS/PEO-based microchips present lower results compared to the laser patterned PEDOT:PSS/PEO microactuators in Chapter 3 (beam dimensions: 6800 x 1200 x 35  $\mu\text{m}$ ). The electroactivity of the PEDOT:PSS-based microchips was evaluated using cyclic voltammetry and by calculating the volumetric charge density. The cyclic voltammetry was performed with a scan rate of 20  $\text{mV}\cdot\text{s}^{-1}$  at a potential window of  $\pm 2.0$  V. The volumetric charge density was calculated according to the formula in Chapter 2, section 2.2.1, considering the volume of one entire PEDOT:PSS/PEO electrode. The cyclic voltammogram of the PEDOT:PSS/PEO-based microsystem with highest actuation strain (sample 3 with dimensions of 1500 x 200  $\mu\text{m}$ ) is brought in **Figure 59** with the comparison of the PEDOT:PSS/PEO laser patterned microactuator from Chapter 3. The PEDOT:PSS/PEO microsystem presents resistive behavior with slightly defined oxidation and reduction peaks, indicating that some redox process is occurring but not effective, especially when compared to the laser patterned microactuator with clearly defined oxidation and reduction peaks. In comparison with the laser patterned sample, it can be also seen that the microsystem presents loss of the symmetry in the cyclic voltammogram pointing to different properties of the PEDOT:PSS/PEO electrodes. The calculated volumetric charge density of this PEDOT:PSS-based prototype is  $1.2 \times 10^7 \text{ C}\cdot\text{m}^{-3}$ , which is notably lower compared to the laser patterned microactuator ( $7.7 \times 10^7 \text{ C}\cdot\text{m}^{-3}$ , from Chapter 3).



**Figure 59.** Cyclic voltammograms of the PEDOT:PSS/PEO microsystem (sample 3) with beam dimensions of 1500 x 200  $\mu\text{m}$  and the laser patterned PEDOT:PSS/PEO microactuator with beam dimensions of 6800 x 1200  $\mu\text{m}$  (from Chapter 3) at a scan rate of 20  $\text{mV}\cdot\text{s}^{-1}$  and a voltage window of  $\pm 2.0$  V.

These lower electrochemical properties of the microsystem can be attributed to several possible reasons related to the fabrication process. First, the RIE can damage the edges of the microbeams and produce some under etching, resulting in minor damage of the microbeams. On the other hand, the removal of Au layer with IBE from the surface of the microactuators can have impact on the PEDOT:PSS electrodes. This can possibly be the reason of non-symmetric electrochemical response of the microdevice, when one PEDOT:PSS electrode is more damaged due to the Au removal. Another reason for lower performances can be the different processing steps and the use of SU-8 developer. SU-8 developer (1-Methoxy-2-propyl acetate) is a polar organic solvent and can partially wash out PEO from the PEDOT:PSS electrodes, as observed in elemental analysis (Chapter 3). Therefore, the PEDOT:PSS/PEO electrodes can be damaged during different developing steps and consequently result in decreased electrical and electrochemical properties of the resulting microbeams. Additionally, the microbeams are fixed from one end with SU-8 encapsulation, which might create some stress during the swelling of the microbeam. Different probable reasons can be related to the deposition of the bottom electrical contacts, which are fabricated close to the end of the process. By this point of the process, the substrate has been processed through many steps and some small layer of residuals (photoresists or not well etched PEDOT:PSS) might be on the Si wafer, creating an insulating layer for the gold bottom electrical contacts. In other words, the insulating layer might exist on the Si wafer before the deposition of bottom electrical contacts. On the other hand, if the microsystem release in  $\text{XeF}_2$  etching is not well finished, then residual layer can exist on both gold electrical

contacts. Since the electrical contacts are accessible from the Si wafer side after the encapsulation, the small residual layers might affect the electrical conductivity of the gold connections and consequently decrease the performances of the microchips. All these possible reasons might affect the performances of the final PEDOT:PSS microbeams and be responsible for lower electrochemical behavior.

As a consequence of the lower electroactivity, mentioned above, the PEDOT:PSS/PEO flexible microchips present also lower performances in strain difference compared to the laser patterned PEDOT:PSS/PEO microactuators. The maximum obtained strain difference of the PEDOT:PSS/PEO laser patterned microactuator is 0.82 % (beam dimensions: 6800 x 1200 x 35  $\mu\text{m}$ ), which is slightly higher compared to the PEDOT:PSS/PEO flexible microchip (0.66 %) (**Table 5**). These lower results can be attributed to the lower electrochemical properties of the microdevice, presenting more resistive behavior probably due to the different possible reasons related to the fabrication process, discussed previously.

The blocking force results of the PEDOT:PSS/PEO microsystem beams are also lower compared to the laser patterned PEDOT:PSS/PEO microactuators. The maximum experimental force value 105  $\mu\text{N}$  of the microdevice beam with dimensions of 2900 x 250 x 23  $\mu\text{m}$  is notably lower compared to the experimental force value of laser patterned beam (472  $\mu\text{N}$ ) with dimensions of 6800 x 1200 x 35  $\mu\text{m}$ . In order to really compare the blocking force results of the microsystem beam to the laser patterned microactuator, the calculations have to be done considering the same dimensions of the devices. The calculations are performed according to the equation (5) for the laser patterned sample, considering the sample dimensions and measurement length as for the microdevice. The electrochemical parameters ( $\rho$  and  $\alpha$ ) are used as correct values measured in Chapter 3, in order to evaluate the fabrication process effects on the resulting blocking force. The experimental values of the microdevice and the used parameters for the re-calculated experimental force of laser patterned microactuator are listed in **Table 5**.

**Table 5.** Experimental values of the PEDOT:PSS/PEO microsystem and experimental calculated force for PEDOT:PSS/PEO laser patterned microbeam.

Parameter	Unit	PEDOT:PSS/PEO microsystem (experimental)	PEDOT:PSS/PEO laser patterned (experimental calculated)
$E_{PPSS}^*$	Pa	$1.5 \times 10^9$ Pa	
$\varepsilon$	%	0.66	0.82 *
$\rho$	C.m <sup>-3</sup>	$1.2 \times 10^7$	$7.7 \times 10^7$ *
$\alpha$	m <sup>3</sup> .C <sup>-1</sup>	$5.4 \times 10^{-10}$	$1.1 \times 10^{-10}$ *
$L$	m	$2.0 \times 10^{-3}$	
$w$	m	$2.5 \times 10^{-4}$	
$h_{SPE}$	m	$9.6 \times 10^{-6}$	
$h_{PPSS}$	m	$6.7 \times 10^{-6}$	
<b>F</b>	μN	<b>105</b>	<b>107</b>

\*Values from Chapter 3.

The experimental output force of the microsystem is almost the same (105 μN) compared to the experimental calculated force of the laser patterned samples (107 μN) considering the same dimensions as for the microsystem but keeping the correct experimental electrochemical properties.

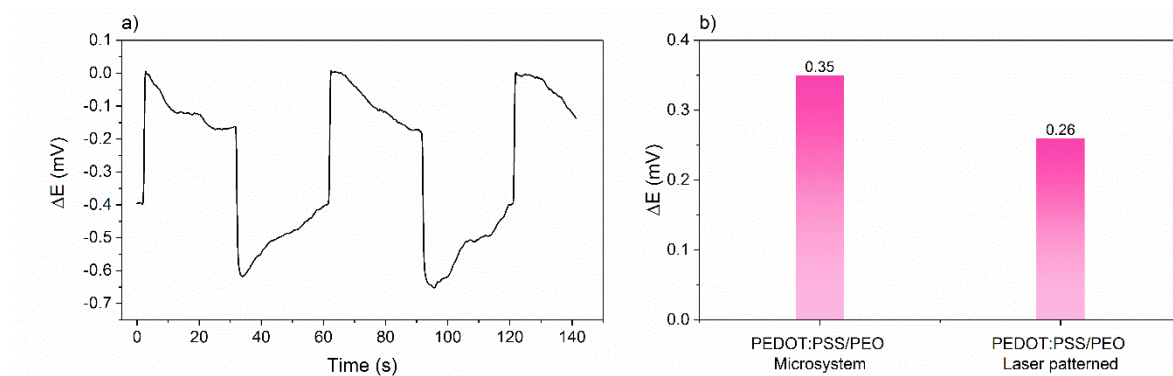
The characterization of actuation and blocking force demonstrated that the microdevices are able to produce actuation strain and output force close to the range of laser patterned microactuators. These results prove that the microfabrication process does not damage the resulting microbeams extensively and the lower strain performances are related to lower electrochemical properties.

### 4.3.3 Micro sensor characterization

The Dual Mode Lever System (Aurora Scientific, 300C) which was used to characterize the sensing ability of the laser patterned microactuators was not suitable for the characterization of the microbeams due to their small size. The FT-RS1002 (Femtools) microrobotic system was used in order to apply precise displacement in x axis direction. Pin was added to the arm of the system to have precise control over the applied displacement on the microbeam. The sensing was evaluated on one type of sample (microcomb configuration, **Figure 56a**), where the width and the distance between the microbeams allowed the pin to approach one beam, without being in contact with the other ones. The microsystem with the beam dimensions of 2900 x 300 x 23 μm, was mechanically stimulated by applying a step displacement of 300 μm and the corresponding open circuit voltage (OCV) was recorded (**Figure 60a**). The 300 μm step displacement corresponds to 0.34 % strain difference (measured at 2.0 mm), which



resulted in generated potential on average of 0.35 mV. However, the electrical signal response is different compared to the laser patterned PEDOT:PSS/PEO microactuators in Chapter 3. The laser patterned PEDOT:PSS/PEO microactuators demonstrated no relaxation most likely due to the high concentration of PSS<sup>-</sup> anions. In the present case, it can be just speculated that the microfabrication process with many SU-8 development steps might decrease the concentration of PSS<sup>-</sup> anions in the electrodes and therefore present relaxation in the electrical signal response. The obtained 0.35 mV is slightly higher, but quite in the same range as found in Chapter 3, for PEDOT:PSS/PEO laser patterned microbeam (0.26 mV at 0.35 % strain) (**Figure 60b**). These results demonstrate that the integrated microdevices are capable of detecting mechanical stimulation and to behave as microsensors. Even though the pin is small, it was still too large for most of the samples, where by mechanically stimulating one beam resulted also in the movement of the adjacent beams. Therefore, an improvement of the measurement setup or device configuration needs to be done in order to characterize such small microsystems and to carry out more in-depth study on mechanical strain sensing of these microdevices.

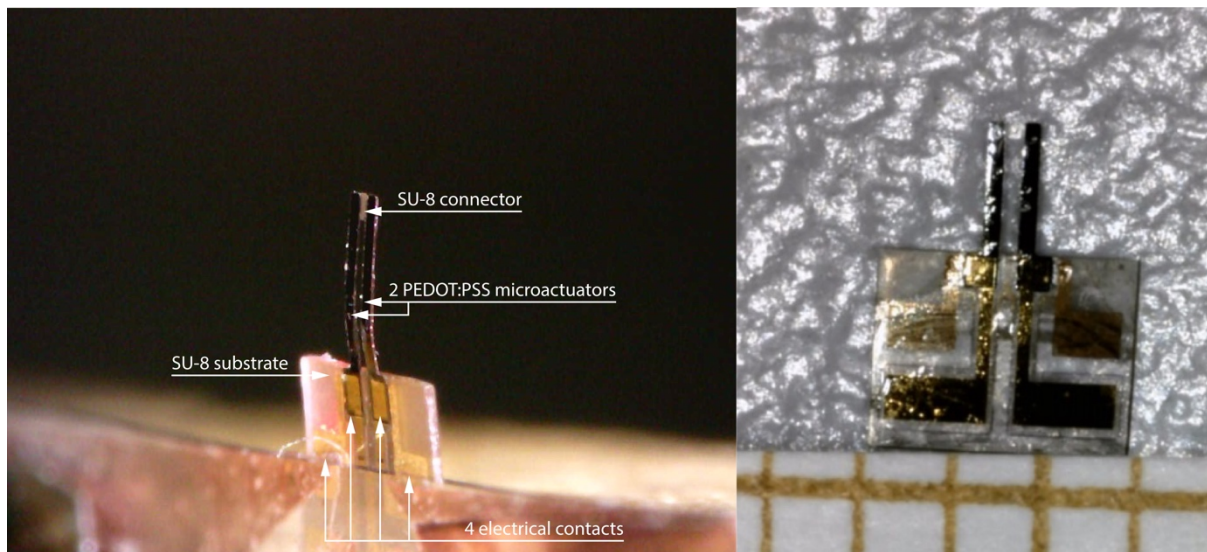


**Figure 60.** a) OCV response as a function of time of the PEDOT:PSS/PEO microsystem with the beam dimensions of 2900 x 300 x 23  $\mu\text{m}$  with an applied mechanical strain of 0.34 %; b) histogram with OCV values of PEDOT:PSS/PEO microsystem (applied strain 0.34 %) and laser patterned microactuator (applied strain 0.35 %).

Since the integration of efficient microsensors was demonstrated and in order to go further in the development of microsystem devices, a combination of actuation and simultaneous sensing has been explored. This so called “proprioception”, i.e. actuation and simultaneous self-sensing of the device’s own position is especially desirable for fully integrated and controllable microsystems. In this configuration, the microdevice is composed of one actuating microbeam which is mechanically connected using SU-8 connector to a second sensing microbeam (**Figure 56c** and **Figure 61**). Both microbeams have two electrical contacts, making them electrically independent, encapsulated on one flexible SU-8 substrate.



Each microbeam has dimensions of  $1500 \times 200 \times 23 \mu\text{m}$ , which are the smallest ones fabricated in this work. The purpose of this design was to actuate one microbeam using an applied potential, i.e. producing bending movement, while the second beam is physically connected to the first one (electrically insulated). During bending deformation of the device, the sensing microbeam will be mechanically stimulated and therefore OCV variation could be measured. This design would allow actuating the microsystem and at the same time to characterize the mechanical sensing of the same microsystem.



**Figure 61.** PEDOT:PSS microsystem: actuator + sensor configuration tested at  $\pm 2.0 \text{ V}$ . Dimensions of each beam are  $1500 \times 200 \times 23 \mu\text{m}$ .

The first characterization of the self-sensing microsystem did not give the expected results probably due to some electrical interference of the actuation input to the sensing signal. More specifically, the measured OCV variation appeared three orders of magnitude higher and the sign of the OCV variation was consistent with the sign of actuation voltage and opposite to the expected sign coming from mechanically induced cation motion. Therefore, the detected signal was not related to the actual sensor signal. Even though the two PEDOT:PSS microbeams were electrically separated and the electrical contacts were as far as possible from each other, then probably due to the SU-8 connector and the size of the microsystem some disturbance between the two functions was detected. Additional development of proprioceptive devices<sup>[212,213]</sup> is required to optimize the geometry, but also to include some shielding or electrical ground connection between the two microbeams in order to conclude the ability of proprioception of these microdevices.

## 4.4 Conclusion

The work in this chapter demonstrated for the first time successful microfabrication process to fully elaborate, integrate and air-operate conducting polymer-based microactuators on flexible microchips with two integrated gold electrical contacts. The integrated gold connections are in contact with PEDOT:PSS/PEO top and bottom electrodes and facilitate the electromechanical characterizations of the microstructures. The process combined different microfabrication technologies which allow batch fabrication of the microsystems on one Si substrate without any manual handling during the process. The work demonstrated the fabrication of actuator-sensor microsystem with four electrical contacts, but depending on the photomask design, more complex devices with more numerous electrical contacts can be designed. The microsystems were successfully characterized by the means of actuation, electroactivity and blocking force and it was demonstrated that it is possible to detect and quantify mechanical stimulation on these microdevices. The first PEDOT:PSS microsystem prototypes demonstrated good improvement compared to the previous air-operated PEDOT microsystems with only one integrated electrical contact on a SU-8 support, resulting here in the maximum strain of 0.66 % and the maximum output force of 105  $\mu$ N. Indeed, the performances of the microdevices were slightly lower compared to the laser patterned microactuators, but only few samples were tested, requiring further investigations. Moreover, the sensing test was performed, resulting in the output voltage of 0.35 mV when mechanical strain of 0.34 % was applied, which has never been performed on such small microactuators and more importantly on microsystems with integrated electrical contacts. The flexibility of the microchips with different freestanding microactuator shapes (beams, bridges, membranes etc.), can be tuned by modifying the thickness of the SU-8 photoresist. These microchips can fit and therefore be used in any other flexible or non-flexible microsystem, such as microfluidic channels, one part of a microrobot, optoelectronic components etc. Given the small number of fabricated and tested microchips during this PhD, these results are promising and encouraging for further investigations and future developments.

## Chapter 5. PEDOT:PSS linear actuators

**Foreword:** *The last chapter is devoted to the development of PEDOT:PSS based linear actuators. The electromechanical properties of the PEDOT:PSS/PEO composite electrodes will be studied in order to use the electromechanical model for the development of linear actuators. Trilayer linear actuators will be fabricated with layer stacking method by combining two PEDOT:PSS/PEO electrodes with different mechanical and electrochemical properties.*

## 5.1 Introduction

Mimicking the functionality of biological muscles and behaving as artificial muscles requires linear deformation of the actuators. In addition to large linear displacements, fast response speed, large forces, high stability and long lifetime, sensing is also an important feature which is inherent in biological muscles. Majority of studies on electronically conducting polymers (ECPs) are focused on bending deformation of the actuators, but in more recent years, linear actuation has been studied more extensively.

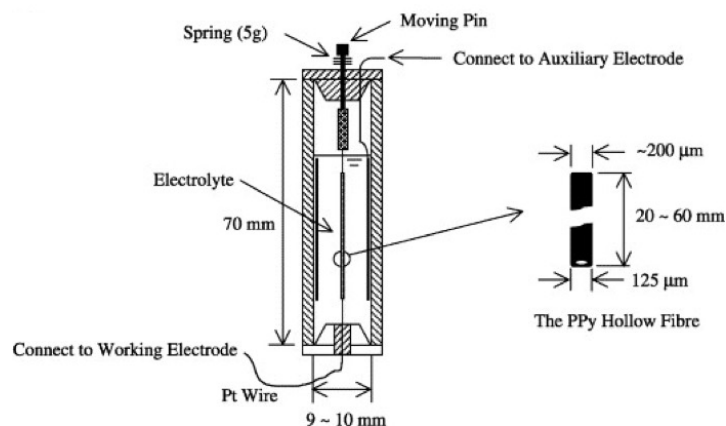
### 5.1.1 Linear actuators operating in liquid electrolyte

The ECP free-standing film alone presents a linear deformation when stimulated electrically in electrolytic solution.<sup>[214]</sup> The first works on linear deformation of free-standing films were reported by the workgroup of Kaneto in 1995.<sup>[215]</sup> A polyaniline (PANI) film was operated in 1 M HCl aqueous solution and the expansion ratio was found to be proportional to the oxidation degree and resulted in 2% of linear strain. Another study from the same research group investigated the properties of the PANI films with different acids in aqueous solutions (HCl, HI, HBF<sub>4</sub>, HPF<sub>6</sub>, HClO<sub>4</sub>, H<sub>2</sub>SO<sub>4</sub> and benzenesulfonic acid).<sup>[69]</sup> The results indicated that the elongation ratio of the PANI films is commonly larger for anions with larger molecular weight, resulting in elongation ratios between 2-3 %, depending on the surrounding media. In 1997, Mazzoldi *et al.* reported the work on polypyrrole (PPy) linear actuators. The PPy was obtained through electrochemical doping with benzenesulfonate anions (BS<sup>-</sup>) and stimulated in 0.1 M sodium benzenesulfonate in a mixture of acetonitrile and de-ionized water. The actuator resulted in isotonic strain of 0.53 % and isometric stress of 3.25 MPa.<sup>[216,217]</sup>

In 2005, Smela *et al.* reported the fabrication of PANI films and fibers, doped with 2-acrylamido-2-methyl-propane-1-sulfonic acid (AMPS).<sup>[218]</sup> The electro-chemo-mechanical

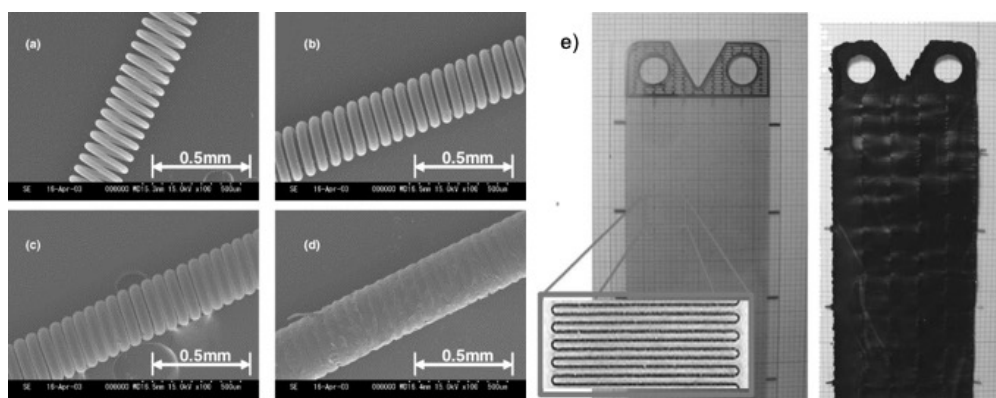
deformation measurements (ECMD) were carried out in 1M HCl and an intense study was carried out to allow better understanding of PANI actuators in terms of different properties. They found that the actuation strain is higher when the actuation period is longer, also that the elongation during oxidation reaction was faster compared to the contraction during reduction (3 s vs 30 s). They demonstrated that the fiber configuration presented faster reduction speed compared to the PANI(AMPS) film (10 s vs 30 s). The isotonic strain during reduction for a PANI(AMPS) fiber with 105  $\mu\text{m}$  diameter and 10 mm length was 0.92 % under 1.0 g of load. They also studied the effect of pH level and found that the current and charges dropped at higher pH, but the strain coefficient (strain per unit of charge density,  $\%/C.m^{-3}$ ) increased as a function of pH level.

An extensive amount of research in this field has been carried out on PPy based linear actuators with fiber configuration. Ding *et al.* demonstrated linear actuation on hollow PPy fibers with a helical wire interconnection (**Figure 62**).<sup>[219]</sup> First, a platinum wire was tightly wound helically around platinum core to have a conducting substrate for PPy electropolymerization. The platinum core is finally removed, resulting in PPy hollow tube actuator with thin helical platinum wire interconnection in the inner wall of the PPy. Two shorter platinum wires were used to have electrical connections at each end of the actuator which was electrically stimulated in tetrabutylammonium hexafluorophosphate (TBA PF<sub>6</sub>) in propylene carbonate (PC). They studied both, hollow tubes without and with helical wire interconnection and they found that for the same experimental conditions, the tube with helical interconnection outperformed the tube without helical wire by a factor 5. They claimed that the helix tube design allows more uniform potential distribution along the length of the actuator and results in improved performances. The new configuration provided up to 5 % strain, from which usable is slightly more than 1 %. The geometry improved the performances of the linear PPy actuators and allowed the utilization in electronic Braille display prototype.



**Figure 62.** Linear actuator with hollow PPy fiber and helical wire interconnection.<sup>[219]</sup>

PPy actuators have been realized also using metal coils as the core of fibular actuators.<sup>[220,221]</sup> One example was based on electrochemically deposited PPy on W micro-coil from methyl benzoate solution of tetra-*n*-butylammonium tetrafluoroborate (TBABF<sub>4</sub>) (**Figure 63 a-d**). The resulting actuators were operated in aqueous NaBF<sub>4</sub> solution and resulted in linear strain of 11.6 % and force of 0.2 N. They also demonstrated that the assembly of 10 bundled PPy deposited coils resulted in increase of the force by the proportion to the number of assembled coils (2.26 N) while keeping the same strain. The second work from the same author demonstrated PPy-zigzag metal wire composite film actuator (**Figure 63e**). This actuator was obtained from electrochemical polymerization of PPy from a methyl benzoate solution of tetrabutylammonium trifluoromethanesulfonate (TBACF<sub>3</sub>SO<sub>3</sub>) and resulted in even higher linear strain of 21.4% when actuated in aqueous NaPF<sub>6</sub> solution. The enhancement in the strain was explained by the configuration of the actuator. In general, ECPs expand and shrink three dimensionally, while in this zigzag metal wire structure, the width direction was restricted and converted into the axial deformation.



**Figure 63.** PPy linear actuators with W micro coil (a-d) and zigzag metal wire (e).<sup>[220,221]</sup>

Yamato *et al.* demonstrated the fabrication of tubular PPy linear actuators by electrochemically depositing PPy on the metal-coated acryl resin rod from dodecylbenzenesulfonic acid (DBS).<sup>[222]</sup> The central rod was dissolved by immersing the actuator in acetone. The resulting PPy tubular actuator with the metal layer inside of the PPy was actuated in 1 M NaCl solution. The maximum linear strain of 7 % was measured for a tube with a diameter of 2.0 mm. Even though these ECP-metal composite actuators exhibit large deformations, then irreversible processes between conducting polymer and metal interface may significantly degrade the material and result in decreased responses and shorter lifetime of the actuators.<sup>[223]</sup> Furthermore, and depending on the application, the rigid nature of the metals can be problematic compared to the soft polymer membranes.

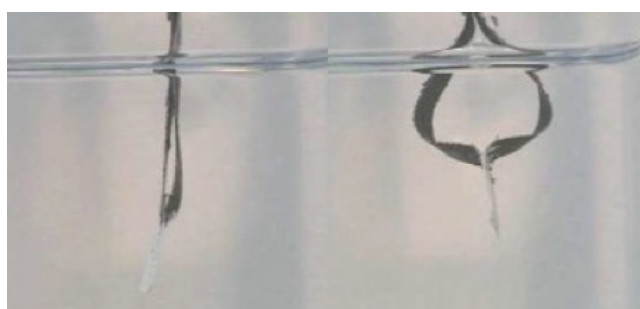
Fabrication of trilayer linear actuators based on carbide-derived-carbon (CDC) and PPy was reported by Kiefer *et al.*<sup>[224]</sup> The aim was to compare the actuation properties of CDC, CDC–PPy and PPy linear actuators. For CDC-PPy actuators, the PPy electrodes were electrochemically deposited on both sides of the CDC film, forming a trilayer actuator. In this case, CDC acted as an active interlayer and PPy electrodes helped to improve the actuation compared to the CDC layer. Different actuators with configurations of pristine CDC actuator, CDC-PPy trilayer actuator and freestanding PPy film were operated in 0.2 M NaDBS aqueous solution. The resulting strain of the CDC-PPy actuator was in the range of 1.2 % and almost double compared to the pristine CDC linear actuator (0.5 %). Overall, using stiff CDC as an active layer is decreasing the final linear deformation, because the linear strain of a single PPy layer was found to be in the range of 2 %.

Zondaka *et al.* reported recently the work on CDC and poly(3,4-ethylenedioxythiophene) (PEDOT) trilayer linear actuators.<sup>[225]</sup> First, a solution containing PVdF(HFP) and 1-ethyl-3-methylimidazolium trifluoromethanesulfonate (EMImTFS) in PC: 4-methyl-2-pentanone (1:10) was brushed on the glass-fiber fabric to fabricate the membrane for the actuator. The CDC layers were deposited on both sides of the fiber-glass, on which the PEDOT electrodes were electrochemically polymerized. The ECMD measurements for freestanding PEDOT layer, CDC trilayer and CDC-PEDOT trilayer were performed in 0.2 M LiTFSI in PC solution. The PEDOT freestanding film exhibited a large linear strain of 5 % with an expansion at oxidation. The CDC trilayer resulted in linear strain of 0.28 % with main expansion during reduction. Interestingly, the CDC-PEDOT trilayer demonstrated the linear strain of 0.26 % upon reduction, related to CDC in the trilayer configuration and much larger



additional strain of 0.6 % upon oxidation, related to PEDOT. They found that these two electroactive materials appeared to maintain their original actuation behavior (expansion during oxidation or reduction), even in the combined configuration.

Another way of realizing linear actuators is assembling different bending structures, bending in opposite directions, i.e. converting bending deformation into linear deformation. Otero *et al.* described first the construction of 4 PPy bilayer actuators, connected by hinges, forming a rhombus.<sup>[226]</sup> The device was operated in 1 M LiClO<sub>4</sub> aqueous solution and during the redox process, two of the bilayers acted as an anode and two other bilayers as a cathode, demonstrating a longitudinal movement. The next work by the same authors demonstrated the linear movement by assembling two bending type trilayer actuators (**Figure 64**).<sup>[227]</sup> The trilayer actuators are formed by first electropolymerizing the PPy layers and then manually placing them on both sides of the double-sided plastic tape. The system was electrically stimulated in 1 M LiClO<sub>4</sub> aqueous solution and the facing trilayers provided longitudinal movements. Although these systems performed longitudinal movements, it is not really an intrinsic linear deformation of the actuator which can result in the loss of energy and performances of the device. This study also highlights the problem of the opposite volume variation when using bi- or trilayers, leading necessarily to bending deformation, when both electrodes are not connected to the working electrode (W.E, in the case of trilayers). In order to fabricate an actuator with an intrinsic linear deformation, different configurations or approaches are required.



**Figure 64.** Photographs of linear actuator obtained by combining two bending trilayers.<sup>[227]</sup>

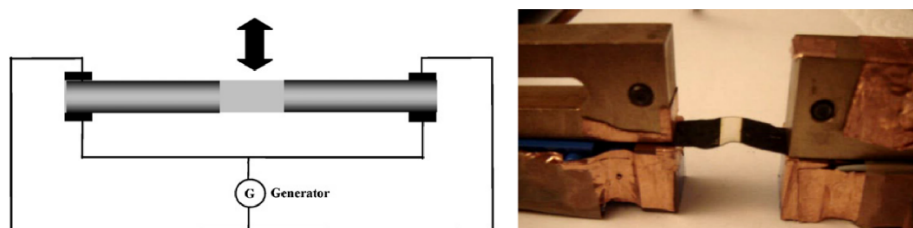
Even though all the above described different linear actuators demonstrated impressive results, then integration of linear actuators into practical devices is limited by their operation in liquid electrolyte. In order to broaden the application field, the linear actuator must operate in open-air, containing the electrolyte directly in the device. The next subsection will give an overview of the works done in the field of air-operating linear actuators.



### 5.1.2 Linear actuators operating in open-air

Intrinsic linear deformation of the actuators is not easy to obtain in open-air due to the working principle of ECP based actuators. Open-air actuation requires two electroactive electrodes which will undergo opposite electrochemical reactions during low voltage stimulation and consequently will present opposite volume variations. For trilayer actuator configuration, a bending movement is then necessarily obtained. There are two types of open-air linear actuators among the reported devices: (i) linear actuators from bending movements; and (ii) intrinsically linear actuators. Different research groups around the world have proposed different methods and configurations to obtain linear actuators operating in open-air, which will be overviewed in this subsection.

The LPPI group at UCP presented the fabrication of one-piece linear actuator by chemically synthesizing PEDOT electrodes locally on IPN by masking the central part of the actuator (**Figure 65**).<sup>[228]</sup> By this way, two conducting-IPN bending actuators were realized on one single IPN membrane. The resulting device was swollen in 1 M LiClO<sub>4</sub> in PC and actuated in open-air. By the conversion of bending deformation, a maximum obtained linear deformation of 0.87 mm was reported with an applied potential of 3.5 V. They also found that the displacement increased linearly with increased applied potential and the response time was roughly the same as for the bending configuration actuators.



**Figure 65.** Illustration and photograph of the linear actuator, developed by Vidal.<sup>[228]</sup>

Lewis *et al.* reported an interesting strategy to develop intrinsic linear open-air actuators by using a classical PPy based trilayer configuration.<sup>[87]</sup> The strategy relied on the electropolymerization of PPy electrodes in the presence of two different counterions. One PPy electrode was electropolymerized in the presence of sodium nitrate (with anion mechanism) and the other PPy electrode in the presence of sodium polystyrene sulfonate (with cation mechanism). In this way, the problem of opposite volume variations is solved since both electrodes result in the same volume variation direction during opposite electrochemical reactions. They demonstrated the development of the device and the

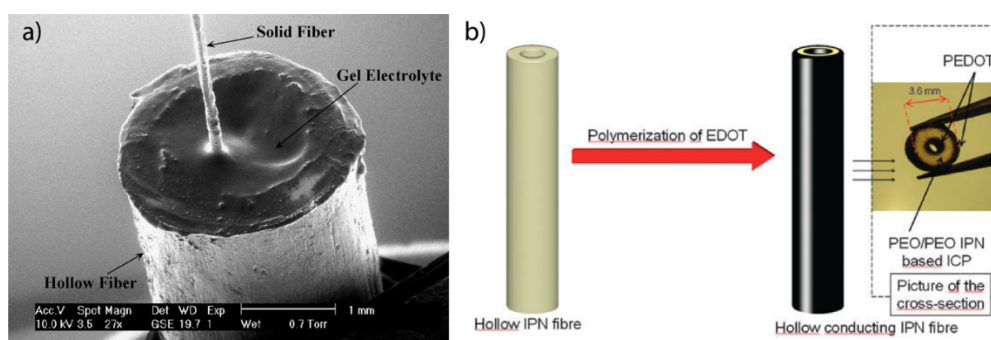
characterization by the means of cyclic voltammetry but no linear deformation value was reported. The drawbacks of this method are the polymerization of the ECP layers with limited choice of the electrolytes.

A multilayer device, based on PPy films and ionic liquid loaded separators was reported by Ikushima *et al.*<sup>[229]</sup> They developed a laminated structure of 9 active layers by alternating the sheets of PPy films and ionic liquid (EMImTFSI) soaked cellulose papers. The PPy layers form both, the working and the counter electrodes and the connections between the electrodes were made using platinum foil. The experimental linear strain was not measured for the laminated structure with 9 active layers, but for the freestanding PPy layer in the EMImTFSI bath (0.51 %) and for a trilayer device (one PPy film sandwiched between two ionic liquid-soaked papers) in open-air (0.24 %).

Mazzoldi *et al.* demonstrated the fabrication of a linear actuator based on fiber configuration.<sup>[230]</sup> They developed a polyaniline (PANI) fiber, doped in HClO<sub>4</sub> and embedded it into an ionic polymer membrane matrix by rolling, to obtain all polymer fiber actuator. A copper wire was directly incorporated by helically wrapping around the fiber, acting as a sacrificial counter electrode. The experiments were carried out in electrolytic solution (1 M HClO<sub>4</sub>) and in open-air, demonstrating that the isotonic strain was slightly higher in electrolytic compartment (0.55 %) compared to open-air stimulation (0.3 %). Another approach was demonstrated by Madden *et al.* in 1999.<sup>[231]</sup> The PPy was obtained through electrochemical polymerization and Agar gel was applied on both sides of the PPy film. A polyethylene film was sputter-coated with 400 nm thick Au layer in order to encapsulate the system and to form the counter-electrode. The obtained solid-state actuator resulted in linear strain just over 2% and the forces per cross-sectional area exceeded those of mammalian skeletal muscles by 50%. Unfortunately, the actuator's lifetime was still limited to few hours because of the gel drying. Another limitation for these two types of actuators could be the stiffness of metal layers which might lead to cracking during cycling of the devices.

Lu *et al.* presented the fabrication of linear actuators with another configuration.<sup>[232]</sup> In the first step, they fabricated solid and hollow PANI fibers. The solid-in-hollow actuator configuration was achieved by keeping the solid fiber centered in the hollow fiber, to avoid any electrical short circuits, and the gel electrolyte was inserted into the empty space between the two fibers (**Figure 66a**). These actuators resulted in isotonic strains of 0.9% but the main disadvantage remains in the matter of solvent evaporation, limiting the lifetime of the fiber

actuator. A different approach of realizing the hollow actuator configuration was demonstrated by Plesse.<sup>[116,233]</sup> The actuator was synthesized as a three component based IPN. First, an IPN as a membrane was synthesized with a hollow fiber configuration. The PEDOT electrodes were incorporated through chemical oxidation, resulting in different electrode areas in inner and outer part of the IPN (**Figure 66b**). The actuators were immersed in 0.1 M LiClO<sub>4</sub> in PC during one hour before the characterization. The hollow IPN actuator resulted in linear strain of 3 % for 2 mm long fibers but was decreasing to 1.2 % for 30 mm fibers due to ohmic drop. Forces above 300 mN were reported but the response time (120 s) was long due to the significant distance between the two PEDOT electrodes (1.25 mm).

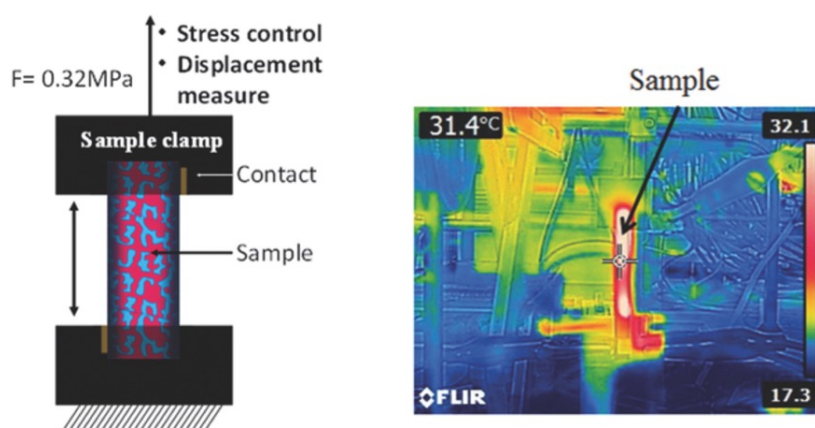


**Figure 66.** a) SEM image of PANI-CF<sub>3</sub>SO<sub>3</sub> solid-in-hollow fiber linear actuator <sup>[232]</sup> and b) schematic representation of the hollow IPN fibre actuator.<sup>[233]</sup>

Intrinsically linear actuators based on ECPs were also reported by using other working principles. For instance, Okuzaki demonstrated linear actuation in open-air on PEDOT:PSS films without any kind of electrolyte.<sup>[54,234]</sup> The PEDOT:PSS films were electrically stimulated and the contraction/expansion of the polymer film was caused by adsorption/desorption of the water vapor molecules. When the electric current passes through the polymer film, the temperature of the film is increasing due to the Joule heating, leading to the contraction of the PEDOT:PSS based film. The PEDOT:PSS film expanded linearly with an increase in relative humidity (RH). The maximum linear strain of 3.3 % was obtained at 90 % RH, but the film did not revert to its initial length when the RH was decreased back to the initial conditions. It was also found that the linear deformation is dependent on the content of PSS and the humidity on polymer film. The maximum contraction of the film was obtained with both, higher PSS content and higher RH. Maximum linear strain of 7 % was measured for the sample with 74 % extra PSS at 70 % RH. This strain of 7 % was 2times higher compared to the PEDOT:PSS film without extra PSS at 90 % RH. The first works on

linear deformations on free-standing films showed good results, but the RH is not the most convenient way to control the linear deformation and might restrict the use of these materials in real applications.

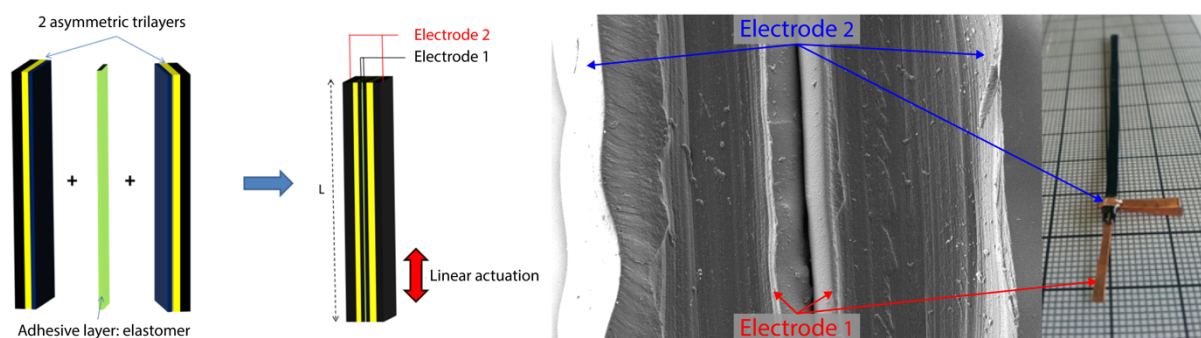
Another interesting work was presented by Khaldi *et al.* where the actuator was synthesized with a conducting IPN configuration presenting shape memory effect (SME).<sup>[235]</sup> The central membrane combined poly(ethylene oxide) (PEO) network swollen with an electrolyte as an ionically conducting polymer and polycaprolactone (PCL) network as a semi-crystalline polymer. Two PEDOT electrodes were interpenetrated on both faces of the PEO/PCL membrane and an ionic liquid (EMImTFSI) was incorporated through external swelling (**Figure 67**). In addition to classical bending actuation, the material demonstrated also reversible linear deformation in open-air via shape memory effect. Indeed, when stretched under constant load, orientation of PCL crystals leads to elongation of the actuator strip. When electrically cycled above the cut-off frequency (8V, 8Hz), the Joule heating is taking place in the ionic actuator phases (PEDOT/PEO/ionic liquid) and induces melting of PCL crystals which consequently leads to a linear contraction due to entropic elasticity. Contrarily, when the material is cooled down, then the oriented crystallization results in elongation of the trilayer actuator under constant load. The resulting open-air linear strain was 1.8 %, but the external applied stress and continuous heating/cooling cycling might be hindering for real applications.



**Figure 67.** Experimental setup and infrared image of PEO/PCL/PEDOT/EMImTFSI actuator where linear deformation is caused heating and cooling.<sup>[235]</sup>

A limited number of intrinsically linear actuators based on the redox process of ECPs has been developed with different designs and performances. Recently, a rational approach based on electrochemical model and experimental validation was proposed by Fannir *et al.*<sup>[118]</sup> The

model was elaborated to identify the critical parameters that would allow linear deformation of classical trilayers. It was demonstrated that linear deformation with classical trilayer actuators becomes possible when combining two electroactive electrodes with different mechanical and/or electromechanical properties, i.e. one soft and one stiff electrode, or one highly expanding electrode, and the other minimally deforming electrode. In this case, the electrodes are still presenting opposite deformations, but one electrode (stiffer) is dominating and leads to overall linear deformation. This electromechanical model will be detailed in the next section. In order to validate this model, linear actuators were fabricated by interpenetrating PEDOT electrodes on both face of a 250  $\mu\text{m}$  thick PEO/NBR membrane using a specific polymerization way for each electrode. Consequently, the PEDOT electrodes were obtained with different local concentrations in the host matrix, presenting different Young's modulus and different volumetric charge density. By combining two asymmetric trilayers (**Figure 68**) (electrode combination chosen according to the theoretical model), a linear strain of 0.55 %, close to the predicted value, was obtained in open-air but also under high vacuum due to the use of ionic liquids. Slow response time (due to relatively high thickness of the membrane), the laborious elaboration process (masking, synthesis time, manual assembling, long swelling duration in electrolyte) and the limited choice of electrode combinations (due to the synthesis pathway) are the main drawbacks of the resulting devices.

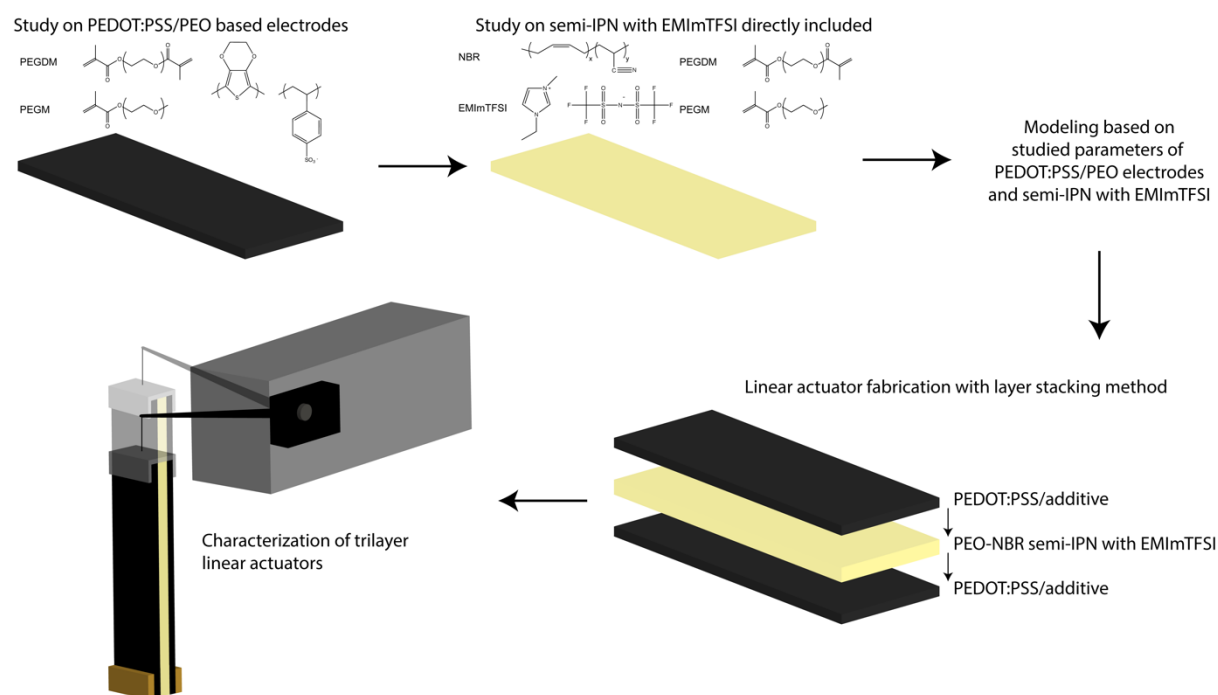


**Figure 68.** Schematic representation, SEM image of the cross-section and photograph of the linear actuator combining two asymmetric trilayers.<sup>[118]</sup>

The goal of this chapter is to validate and extend the approach of Fannir on PEDOT:PSS actuators, to develop a much simpler fabrication process to be compatible with microfabrication technologies and to improve the performances of the resulting linear actuators. First, the use of PEDOT:PSS based electrodes appears, as reported in Chapter 3, as a convenient way to tune the mechanical and electromechanical properties of the electroactive layers with the incorporation of PEO and then, can be an advantageous to extend the possibilities of electrode combinations. Moreover, the elaboration of trilayer

devices with layer stacking method may be also advantageous here to decrease drastically the thickness of the linear actuator, i.e. the thickness of the membrane and the electrodes, and then improve significantly the resulting response speed. It is also noteworthy to mention that PEDOT:PSS based electrodes can be elaborated without involving any final oxidant washing step of the actuator. Furthermore, and to improve the process, the ionic liquid as electrolyte could be introduced directly with the membrane precursors during the synthesis and to the PEDOT:PSS dispersion during the electrode elaboration. It would allow circumventing the usual time consuming and microsystem incompatible swelling step from the fabrication process as mentioned in Chapter 4.

The chapter is divided into five main parts: introduction of the electromechanical model, synthesis and characterization of PEDOT:PSS based electrodes with tuned properties, synthesis and characterization of the ion reservoir membrane in the presence of ionic liquid, selection of the best combination of materials based on the theoretical model and finally linear actuation and linear sensing performances (illustrated in **Figure 69**).



**Figure 69.** General scheme describing the study in the next sections of this chapter.

## 5.2 Electromechanical model to predict trilayer linear actuation

In order to develop linear actuators and predict the linear deformation, an electromechanical model has been developed during the thesis of Fannir, based on different models from Madden, Alici and Spinks.<sup>[118,236,237]</sup>



As mentioned previously, the free strain  $\varepsilon_0$  of the conducting polymer is empirically linked to the volumetric charge density  $\rho$  (C.m<sup>-3</sup>) and the strain-to-charge ratio  $\alpha$  (m<sup>3</sup>.C<sup>-1</sup>) of the ECP layer:<sup>[238]</sup>

$$\varepsilon_0 = \alpha\rho = \alpha \frac{q}{V} \quad (6)$$

Where  $q$  is the charge (C) that can be exchanged in a volume  $V$  (m<sup>3</sup>) of the ECP layer. The mechanical stress  $\sigma_x$  within a layer  $x$  of Young's modulus  $E_x$ , during the linear deformation  $\varepsilon$  of a multilayer device, is equal to the stress arising from Hooke's law:

$$\sigma_x = E_x \varepsilon \quad (7)$$

In the case of electrode, this stress is corrected by the stress induced by the redox strain from equations (1) and (7):

$$\sigma_x = \varepsilon E_x - \alpha_x \rho_x E_x \quad (8)$$

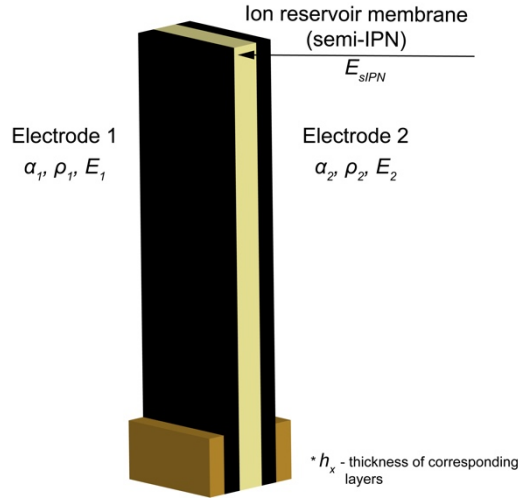
This means, if the redox process is causing the decrease in a volume (contraction) of the electrode, while the total length of the actuator is increasing, then the stress in the layer will increase. Contrarily, when the redox process is causing the increase in a volume (expansion) of the electrode with lengthening of the actuator, then the stress in the electrode layer will decrease. Then, the inner stresses of each layer in a trilayer actuator presenting hypothetical linear deformation  $\varepsilon$  can be defined according to the equations (9, 10 and 11). The schematic representation of the actuator configuration with all the corresponding layer parameters is brought in **Figure 70**.

$$\text{Electrode 1 layer: } \sigma_1 = \varepsilon E_1 - \alpha_1 \rho_1 E_1 = \varepsilon E_1 - \alpha_1 \frac{q_1}{V_1} E_1 \quad (9)$$

$$\text{Semi-IPN layer: } \sigma_{sIPN} = \varepsilon E_{sIPN} \quad (10)$$

$$\text{Electrode 2 layer: } \sigma_2 = \varepsilon E_2 - \alpha_2 \rho_2 E_2 = \varepsilon E_2 - \alpha_2 \frac{q_2}{V_2} E_2 \quad (11)$$

where  $\sigma_x$  ( $x=1, 2$  or sIPN) refers to the stress within the first ECP electrode layer, the second ECP electrode layer and the semi-IPN layer (ion reservoir membrane) of the trilayer actuator configuration. It is important to note here that  $q_1 = -q_2$  because exchanged charges in one electrode are compensated by the other one.



**Figure 70.** Schematic representation of the actuator configuration with all the corresponding layer parameters.

During hypothetical free linear actuation, without an external stress, the total output force at the equilibrium is equal to zero:

$$F_{total} = A_1\sigma_1 + A_{SIPN}\sigma_{SIPN} + A_2\sigma_2 = 0 \quad (12)$$

Where  $A_x$  is the cross-section area of each layer. Combining now equations (9, 10 and 11) into equation (12), and considering that  $q_1 = -q_2$ , the linear strain of the trilayer configuration is:

$$\varepsilon = \frac{A_1E_1\alpha_1\frac{q_1}{V_1} - A_2E_2\alpha_2\frac{q_1}{V_2}}{A_1E_1 + A_2E_2 + A_{SIPN}E_{SIPN}} \quad (13)$$

Knowing that  $V_x$ ,  $A_x$  and  $h_x$  are the volume, cross-section area and thickness of each layer ( $V_x = A_xL = h_xwL$ ) and considering that the length  $L$  and the width  $w$  are equal for all the layers, we obtain:

$$\varepsilon = \frac{q_1}{Lw} \frac{E_1\alpha_1 - E_2\alpha_2}{h_1E_1 + h_2E_2 + h_{SIPN}E_{SIPN}} = \rho_1 h_1 \frac{E_1\alpha_1 - E_2\alpha_2}{h_1E_1 + h_2E_2 + h_{SIPN}E_{SIPN}} \quad (14)$$

This theoretical electromechanical model (equation 14) shows that the combination of two identical ECP electrodes, with identical Young's modulus  $E_x$  and strain-to-charge ratios  $\alpha_x$ , would make the upper term of the equation equal to zero indicating that no linear actuation can occur. However, according to the theoretical model, two different electrodes with different Young's modulus and/or strain-to-charge ratios can make the strain value different from 0, predicting a possible linear deformation of the trilayer system. This result is the basis of the developments described in this chapter for designing linear actuators.



### 5.3 Fabrication and characterization of PEDOT:PSS composite electrodes

In this section elaboration and characterization of different PEDOT:PSS composite electrodes will be described. PEDOT:PSS will be modified by changing the nature and the content of additives in order to elaborate electrodes with different mechanical and electrochemical properties. Electromechanical and electrochemical properties of the composite electrodes will be described. All the characterizations in this section were carried out in collaboration with Pr. J. D. W. Madden in the Electrical and Computer Engineering laboratory, in University of British Columbia (UBC, Vancouver, Canada) during the second secondment of the MICACT ITN project. The measurements as a function of the redox level required specific equipment (Bose Electroforce<sup>®</sup> coupled with electrochemical cell) which is available in UBC.

The thickness ( $h$ ) of the PEDOT:PSS electrodes is measured with the profilometer Dektak 150 (Veeco). The Young's modulus ( $E$ ) is determined using Bose Electroforce<sup>®</sup> 3000 dynamic mechanical analyzer. The mechanical characterization using Bose Electroforce<sup>®</sup> 3000 dynamic mechanical analyzer coupled with electrochemical cell allow the determination of the volumetric charge density ( $\rho$ ), the free strain ( $\varepsilon$ ) and finally the strain-to-charge ratio ( $\alpha$ ).

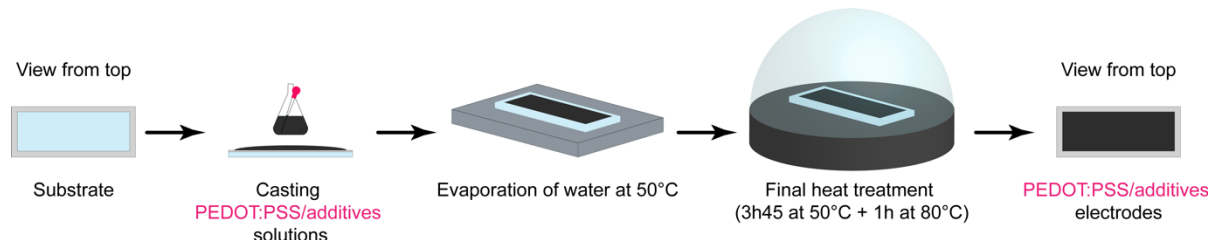
#### 5.3.1 Fabrication of PEDOT:PSS electrodes

Modifying the properties of PEDOT:PSS films is relatively easy using either different commercial PEDOT:PSS dispersions, different synthesis conditions, different additives or even post-treatments. In this work, only Clevios PH1000 commercial PEDOT:PSS dispersion was used, the synthesis conditions (time and temperature) were left the same but different additives were used in order to modify the properties of the resulting films. The poly(ethylene oxide) (PEO) precursors were considered as one type of additives for PEDOT:PSS electrodes. It was found in Chapter 3 that depending on the content of PEO precursors in the PEDOT:PSS electrodes, it is possible to modify the electrical, electrochemical and mechanical properties of these materials. The second choice of additive is 1-ethyl-3-methylimidazolium bis(trifluoromethanesulfonyl)imide (EMImTFSI) since ionic liquid was found to be an excellent additive to fabricate highly stretchable and highly conductive electrodes.<sup>[176]</sup> The fabrication of the PEDOT:PSS electrodes was carried out in the same way as described in Chapter 3, section 3.2 using casting method.<sup>[54,239]</sup> Different studied

compositions of PEDOT:PSS electrodes are listed below, from which the second composition is the new combination:

1. PEDOT:PSS (Clevios PH1000) + X% PEO (20%, 40% vs final mass of the electrode, i.e. PEDOT:PSS and PEO),
2. PEDOT:PSS (Clevios PH1000) + X% PEO (20%, 40% vs final mass of the electrode, i.e. PEDOT:PSS and PEO) + 45.5% EMImTFSI (vs solid content of Clevios PH1000, i.e. PEDOT:PSS).

The fabrication process of the electrodes is brought in **Figure 71**. Different PEDOT:PSS solutions (listed above) were casted (1 ml) into previously prepared microscope slide molds. The substrates were then placed on a heating plate at 50°C to evaporate the water and to form freestanding PEDOT:PSS based electrodes. The heat treatment was carried out under argon during 3h 45min at 50°C and 1h at 80°C. It is relevant to mention here that in the case of the second composition, EMImTFSI was used as a second additive in the fabrication process but finally all the resulting electrodes (first and second composition) were also externally swollen (72h) in ionic liquid (EMImTFSI) for further characterization.

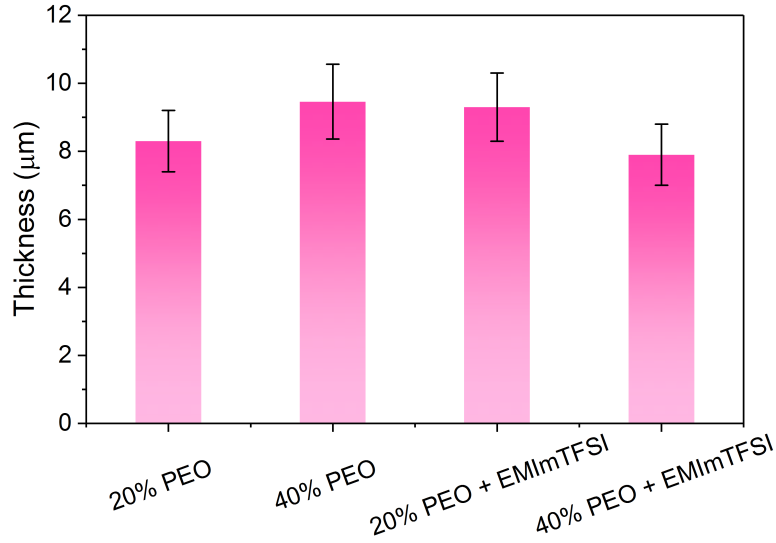


**Figure 71.** Fabrication process for PEDOT:PSS/additives electrodes.

## 5.3.2 Mechanical characterization of the PEDOT:PSS/PEO based electrodes

### 5.3.2.1 Thickness measurements

The thickness measurements of the PEDOT:PSS/PEO based electrodes after swelling in EMITFSI are presented in **Figure 72**. It can be seen that the thickness of all the electrodes is quite in the same range, between 8 – 10  $\mu\text{m}$ . Slight difference in thickness can be due to the different surface area of the microscope slide mold ( $6.8 \times 1.9 \text{ mm} \pm 0.7 \times 0.1 \text{ mm}$ ) for the same casting volume (1 ml), leading to some variation in thickness.



**Figure 72.** Thickness of different PEDOT:PSS electrodes swollen in electrolyte (EMImTFSI).

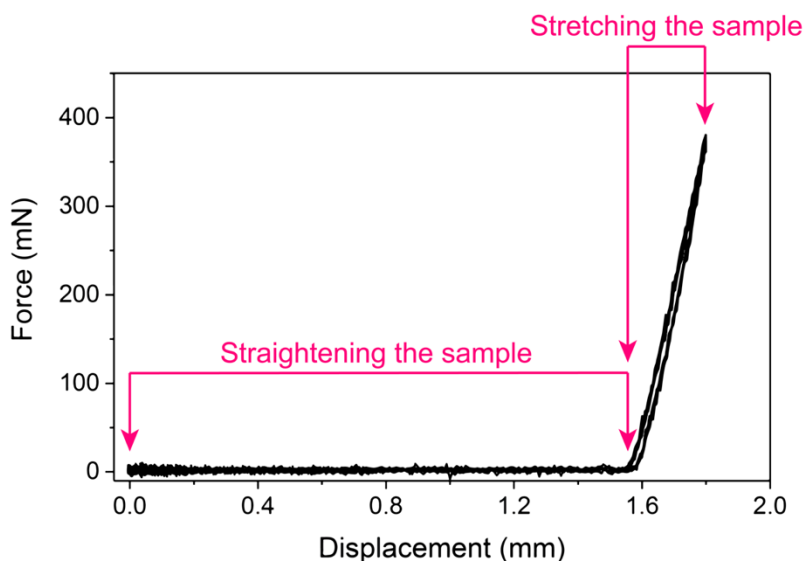
### 5.3.2.2 Young's modulus measurements in open-air

The Young's modulus of the different PEDOT:PSS/PEO electrodes in open-air (in swollen state) was measured in tensile mode directly connecting both ends of the freestanding PEDOT:PSS electrodes to the load cells. The width of the samples was 4 mm and the clamping distance 20 mm. A longitudinal displacement ( $0.04 \text{ mm}\cdot\text{s}^{-1}$ ) was applied and the corresponding force was recorded.

**Figure 73** demonstrates the raw data graph of the measurements. The sample is not perfectly stretched when connected and therefore the force is around zero in the beginning of the measurement. The values of Young's modulus are calculated from the linear relation between the force  $F$  and the displacement  $\Delta L$  when the sample is stretched according to the following equation:

$$E = \frac{F L_0}{A \Delta L} \quad (15)$$

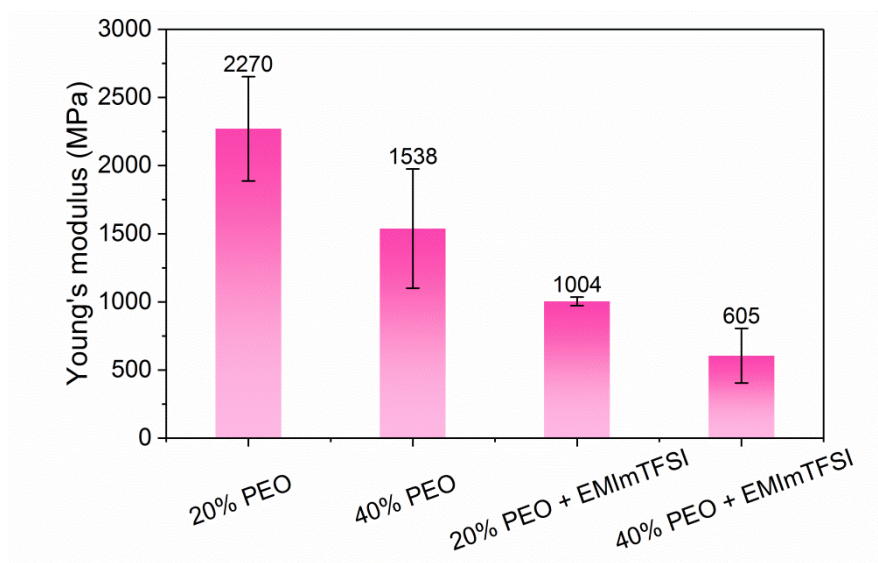
Where  $L_0$  is the distance between both ends of the clamps (when the sample is straightened) and  $A$  is the cross-section of the electrode.



**Figure 73.** Raw data curve of Young's modulus measurements.

The Young's modulus results in open-air for different PEDOT:PSS/PEO electrodes are brought in **Figure 74**. It can be seen that increasing PEO precursors in the PEDOT:PSS solution decreases the Young's modulus. By increasing the content of PEO from 20% to 40%, the Young's modulus is decreasing from 2270 MPa to 1538 MPa. As derived in Chapter 3 section 3.3.2, the Young's modulus of the pristine PEDOT:PSS electrode is 5770 MPa, demonstrating again the beneficial effect of softening the electrodes when PEO precursors are incorporated. More interestingly, incorporating EMImTFSI as an additional additive to the PEDOT:PSS/PEO solution helps to decrease the Young's modulus further, resulting in relatively soft electrodes. When comparing the PEDOT:PSS/PEO(20%) electrodes with and without EMImTFSI, it can be seen that the Young's modulus is decreasing from 2270 MPa to 1004 MPa when EMImTFSI is incorporated. The difference between the PEDOT:PSS/PEO(40%) electrodes with and without EMImTFSI is even higher (2.5 times) and the Young's modulus value of the PEDOT:PSS/PEO(40%)/EMImTFSI electrode is as low as 605 MPa. In general, it can be seen that increasing the content of polar additives led to softening of the resulting electrodes and even further, when EMImTFSI was incorporated as an additional additive. This tendency is also observed by other workgroups and can be explained by the brittle nature of the PEDOT:PSS. Incorporating additives to the synthesis process dilutes the solution and helps to form PEDOT:PSS with fibrous morphology, to fabricate electrodes with less dense structure and therefore lower Young's modulus.<sup>[185]</sup> As already shown in Chapter 3, these results demonstrate that it is possible to significantly tune the mechanical properties of the PEDOT:PSS electrodes to obtain robust electrodes with Young's modulus varying between 605 to 2270 MPa. The combination of

such electrodes could theoretically fulfill the requirements for the electromechanical model, described above.



**Figure 74.** Open-air experiments of Young's modulus for different PEDOT:PSS electrodes in swollen state (EMImTFSI).

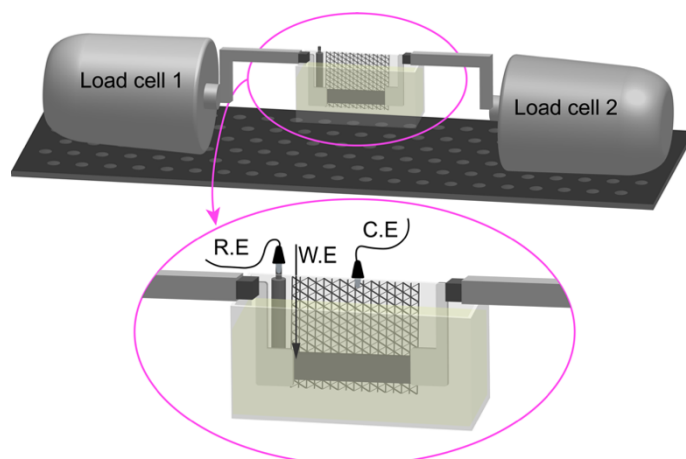
### 5.3.2.3 Young's modulus as a function of the redox level

Many research groups have observed the difference in Young's modulus dependent on the conducting polymer's redox level but also depending on the surrounding electrolyte.<sup>[218,240–244]</sup> During the actuation of the final device, the electrodes will be successively oxidized and reduced during the redox process, causing shrinking and swelling in ionic liquid. For this purpose, the measurements of Young's modulus for PEDOT:PSS/PEO composite electrodes are now performed as a function of the redox level and the results will be discussed subsequently.

The Young's modulus of the different PEDOT:PSS/PEO electrodes in oxidized and reduced state was determined using Bose Electroforce<sup>®</sup> 3000 dynamic mechanical analyzer coupled with an electrochemical cell. The experiments were carried out in neat EMImTFSI since it will be the electrolyte for open-air linear actuation measurements. The experimental setup is illustrated in **Figure 75**.

For these experiments, the samples were clamped between 3D printed plastic clamps from both ends in order to immerse the sample in ionic liquid EMImTFSI. One end of the sample was connected to a platinum sheet as a working electrode (W.E). Stainless steel mesh was used as a counter electrode (C.E) and silver wire as a pseudo-reference electrode (R.E). The

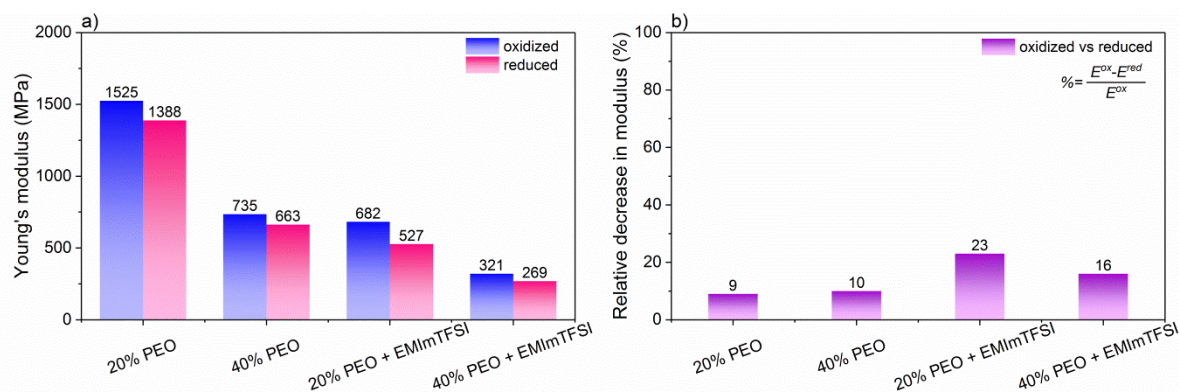
corresponding electrodes were oxidized or reduced by applying positive (+1.0 V) or negative (-1.0 V) potential (during 300 s) and the Young's modulus was then directly measured. The values were determined as in the case of open-air measurements from the linear relation between the force  $F$  and the displacement  $\Delta L$  (equation 15).



**Figure 75.** Young's modulus experiment setup for in solution measurements.

The results of Young's modulus for different PEDOT:PSS/PEO electrodes as a function of redox level are depicted in **Figure 76a**. The Young's modulus follows the same trend as for the open-air measurements, demonstrating softening of the electrodes, when higher amount of additives are incorporated to the PEDOT:PSS solution. It can be seen that the values in oxidized state are slightly higher than in the reduced state. In the case of the PEDOT:PSS/PEO(20%) electrode, the Young's modulus decreases from 1525 MPa to 1388 MPa when switching from oxidized to reduced state. The same trend can be observed for all the studied compositions of the electrodes and the variation ranges from 9 – 23 % (**Figure 76b**), depending on the electrode composition. The same trend has been observed by Bahrami-Samani and Fannir, both in neat EMImTFSI, but in one case for PPy and in the other case for PEDOT-interpenetrated polymer network (PEDOT-IPN).<sup>[118,245]</sup> It has been shown previously that in EMImTFSI a cation movement is dominating during the redox process.<sup>[246]</sup> In the oxidized state, expulsion of cations induces a volume shrinking and increase in ionic interactions between negatively charged TFSI<sup>-</sup> and positively charged PEDOT, which may explain stiffening of the electrodes. On the opposite, in the reduced state, the insertion of cations may lead to a plasticization due to the swelling but also due to the decrease of ionic interactions, resulting in lower Young's modulus. Consequently, by modifying the PEDOT:PSS/PEO electrode compositions and the redox state, it is possible to obtain electrodes with a Young's modulus between 321 – 1525 MPa in the oxidized state and

between 269 – 1388 MPa in the reduced state. These *in-situ* measurements exhibit also a large decrease in Young's modulus compared to the open-air measurements, where a difference between 36 – 55 % is obtained (not reported on the figure, values are summarized at the end of this section). This is probably due to the additional plasticization of the electrodes during the immersion and cycling in EMImTFSI.



**Figure 76.** a) Young's modulus values for different PEDOT:PSS electrodes as a function of redox level, immersed in EMImTFSI; b) relative decrease in Young's modulus in oxidized vs in reduced state.

These experiments demonstrated that redox level has a slight effect on the Young's modulus of the PEDOT:PSS composite electrodes. It was found that the modulus is higher in the oxidized state compared to the reduced state. Even though the difference is not large, it is still significant and should be taken into account in the electromechanical model.

### 5.3.3 Electrochemomechanical characterization of PEDOT:PSS composite electrodes

The electrochemomechanical characterizations are carried out simultaneously by coupling electrochemical stimulation of the electrodes in the EMImTFSI with deformation measurements using the Bose Electroforce<sup>®</sup> 3000 dynamic mechanical analyzer. Cyclic voltammetry (CV) allows the determination of the volumetric charge density ( $\rho$ ) and the resulting displacement provides the free strain ( $\varepsilon_0$ ). The electromechanical coupling parameter ( $\alpha$ ) will be determined according to the equation below:

$$\varepsilon_0 = \alpha \rho \rightarrow \alpha = \frac{\varepsilon_0}{\rho} \quad (16)$$

The experiments were carried out using the same experimental setup as brought in **Figure 75**. The free-standing PEDOT:PSS/PEO electrodes were connected to the potentiostat and to the Bose Electroforce<sup>®</sup> 3000 dynamic mechanical analyzer. A constant load of 2.5 g (0.7 MPa)

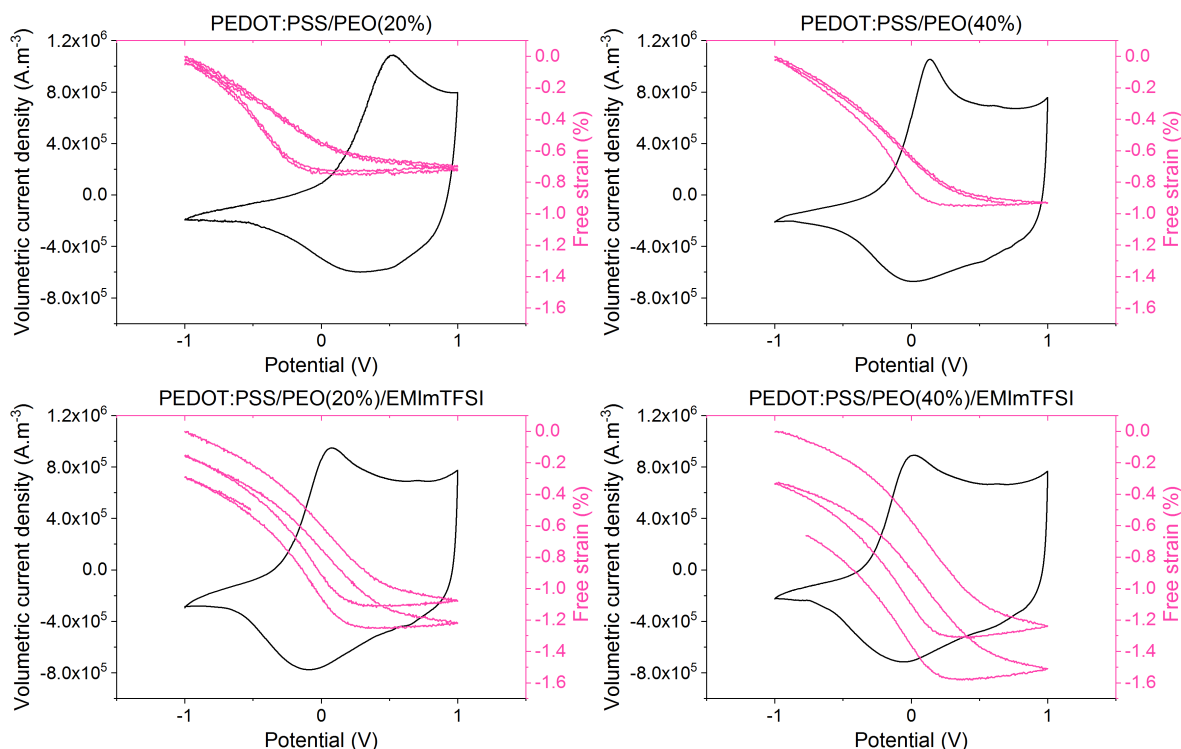


was applied to the electrodes to keep them straight while immersed in EMImTFSI. Cyclic voltammetry ( $\pm 1.0$  V,  $20 \text{ mV}\cdot\text{s}^{-1}$ ) was used to electrically stimulate the PEDOT:PSS/PEO electrodes and the Bose load cells were used to follow the linear deformation of the electrodes during the redox process. The free strain of the electrodes was calculated according to the equation below:

$$\varepsilon_0 = \frac{\Delta L}{L} \quad (17)$$

Where  $L$  is the initial length and  $\Delta L$  is the measured linear deformation of the electrode.

The results for the PEDOT:PSS/PEO electrodes with four different electrode compositions are presented in **Figure 77**. The PEDOT:PSS/PEO(20%) (**Figure 77a**) electrode presents slightly lower electroactivity with less defined oxidation and reduction peaks compared to the PEDOT:PSS/PEO(40%) electrode (**Figure 77b**). This trend is consistent with the results in Chapter 3, where it was found that increasing the PEO content is increasing the electronic conductivity and electroactivity of the PEDOT:PSS electrodes. More defined oxidation and reduction peaks compared to the Chapter 3 are probably due to the experimental setup and the distance between different electrodes being closer in this electrochemical cell (with Bose). The corresponding volumetric charge densities ( $\rho$ ) for the PEDOT:PSS electrodes with 20% and 40% PEO are  $3.62 \times 10^7$  and  $3.78 \times 10^7 \text{ C}\cdot\text{m}^{-3}$ , respectively. These values are slightly different than in Chapter 3 ( $2.8 \times 10^7 \text{ C}\cdot\text{m}^{-3}$  and  $4.5 \times 10^7 \text{ C}\cdot\text{m}^{-3}$ , for PEDOT:PSS electrodes with 20% and 40% PEO, respectively) but can be also explained by the difference in experimental setup. The volumetric charge density of the PEDOT:PSS/PEO electrodes is also in the same order of magnitude compared to the reported work on PPy electrodes.<sup>[174]</sup> **Figure 77c** and **d** present the results for the PEDOT:PSS electrodes with 20% and 40% PEO and EMImTFSI as a second additive. In both cases, the cyclic voltammograms present high electroactivity with reversible oxidation and reduction process and are similar to those without EMImTFSI as a second additive. The volumetric charge densities ( $\rho$ ) of the PEDOT:PSS/PEO electrodes with 20% and 40% PEO and EMImTFSI as a second additive are  $4.91 \times 10^7$  and  $4.85 \times 10^7 \text{ C}\cdot\text{m}^{-3}$ , remaining in the same order of magnitude compared to the electrodes without EMImTFSI.



**Figure 77.** Volumetric current density as a function of free strain: a) PEDOT:PSS/PEO(20%), b) PEDOT:PSS/PEO(40%), c) PEDOT:PSS/PEO(20%)/EMImTFSI and d) PEDOT:PSS/PEO(40%)/EMImTFSI.

The free strain ( $\varepsilon_0$ ) as a function of the potential is presented in the same figures for all the studied PEDOT:PSS composite electrodes. In all cases, the electrodes present contraction during oxidation and elongation during reduction, demonstrating cation motion during the redox process. Switching from -1 V to +1 V, the resulting free strain ( $\varepsilon_0$ ) of the PEDOT:PSS/PEO(20%) electrode is -0.73 % (**Figure 77a**). The PEDOT:PSS/PEO(40%) electrode with higher electroactivity and more clearly defined oxidation and reduction peaks presents also higher free strain value of -0.93 % (**Figure 77b**). For both PEDOT:PSS/PEO electrodes, the elongation and contraction of the electrodes were equal and no creep has been observed during cycling. Contrarily to the PEDOT:PSS/PEO electrodes, both electrodes with EMImTFSI as a second additive exhibit a progressive shift during cycling, corresponding to a creep behavior. This phenomenon was not observed for the PEDOT:PSS/PEO electrodes and highlights the fact that introduction of EMImTFSI to the starting solution significantly changes the morphology of the resulting electrodes due to higher dilution and induces plasticizing effect. Both samples present higher strains compared to the PEDOT:PSS electrodes without a second additive. Taking into account the creep, the average strain of oxidized and reduced state is -1.00 % for the PEDOT:PSS/PEO(20%)/EMImTFSI electrode and -1.07 % for the PEDOT:PSS/PEO(40%)/EMImTFSI electrode. For comparison, these experimental results of linear free strain are compared with the free strains calculated from

bending deformation (Chapter 3, section 3.3.4) are presented in Appendix 3, section A.3.1 and demonstrate good agreement.

The characterized parameters ( $\rho$  and  $\varepsilon_0$ ) allow the calculation of the strain-to-charge ratio  $\alpha$ , required for the theoretical model. The volumetric charge densities ( $\rho$ ) and free strains ( $\varepsilon_0$ ) of the characterized PEDOT:PSS electrodes are summarized in **Table 6**, with the calculated strain-to-charge ratios ( $\alpha$ ), according to the equation 16. Since oxidation ( $\rho > 0$ ) is leading to a negative strain  $\varepsilon_0$ , negative  $\alpha$  values are obtained, as expected from cation mechanism.

**Table 6.** Characterized volumetric charge densities ( $\rho$ ) and free strains ( $\varepsilon_0$ ) of the PEDOT:PSS electrodes and calculated strain-to-charge ratios ( $\alpha$ ).

\* Measured in neat EMITFSI electrolyte

Additive of the electrode:	* $\rho$ C.m <sup>-3</sup>	* $\varepsilon_0$ %	$\alpha$ m <sup>3</sup> .C <sup>-1</sup>
PEDOT:PSS + 20% PEO	3.62 x 10 <sup>7</sup>	-0.73	-2.02 x 10 <sup>-10</sup>
PEDOT:PSS + 40% PEO	3.78 x 10 <sup>7</sup>	-0.93	-2.46 x 10 <sup>-10</sup>
PEDOT:PSS + 20% PEO + EMImTFSI	4.91 x 10 <sup>7</sup>	-1.00	-2.04 x 10 <sup>-10</sup>
PEDOT:PSS + 40% PEO + EMImTFSI	4.85 x 10 <sup>7</sup>	-1.07	-2.21 x 10 <sup>-10</sup>

The strain-to-charge ratios ( $\alpha$ ) of the PEDOT:PSS electrodes seem relatively constant, varying only between 2.02 x 10<sup>-10</sup> m<sup>3</sup>.C<sup>-1</sup> and 2.46 x 10<sup>-10</sup> m<sup>3</sup>.C<sup>-1</sup>, indicating that this coupling coefficient is mainly related to the nature of the electrolyte. These values are in the same range as found during the thesis of Fannir for PEDOT electrodes in EMImTFSI (2.10 x 10<sup>-10</sup> m<sup>3</sup>.C<sup>-1</sup>).

### 5.3.4 Conclusion

The section on synthesis and characterization of PEDOT:PSS/PEO composite electrodes helped to determine the Young's modulus of single electrodes in open-air and as a function of the redox level. The mechanical characterization demonstrated that the Young's modulus is higher in open-air compared to the measurements in EMImTFSI. It was also demonstrated that Young's modulus of the PEDOT:PSS electrodes is higher in oxidized state compared to the reduced state. Modifying the properties of the PEDOT:PSS electrodes by the use of additives allows to obtain electrodes with a Young's modulus between 321 – 1525 MPa in oxidized state and between 269 – 1388 MPa in reduced state. The electrochemomechanical experiments allowed to determine the experimental values of the volumetric charge density (3.62 – 4.91 x 10<sup>7</sup> C.m<sup>-3</sup>) and free linear strain (0.73 – 1.07 %) and to calculate the required parameter strain-to-charge ratio (2.02 – 2.46 x 10<sup>-10</sup> m<sup>3</sup>.C<sup>-1</sup>) for the electromechanical model.

All the characterized parameters of this section are summarized in **Table 7**, which will be later used to model the expected deformations, resulting from the combinations of the electrodes in the trilayer configuration. However, in order to complete the determination of the physical parameters, the characterization of the ionically conducting membrane (semi-IPN) will be described in the next section, to obtain all the required parameters for the theoretical model.

**Table 7.** Summarized parameters of PEDOT:PSS/PEO electrodes from mechanical and electrochemomechanical characterizations.

* Measured in neat EMITFSI electrolyte							
Additive of the electrode:	$h$ μm	$E^{open-air}$ MPa	$*E^{oxidized}$ MPa	$*E^{reduced}$ MPa	$*\rho$ C.m <sup>-3</sup>	$*\epsilon_0$ %	$\alpha$ m <sup>3</sup> .C <sup>-1</sup>
20% PEO	8.3	2270	1525	1388	$3.62 \times 10^7$	-0.73	$-2.02 \times 10^{-10}$
40% PEO	9.5	1538	735	663	$3.78 \times 10^7$	-0.93	$-2.46 \times 10^{-10}$
20% PEO + EMImTFSI	9.3	1004	682	527	$4.91 \times 10^7$	-1.00	$-2.04 \times 10^{-10}$
40% PEO + EMImTFSI	7.9	605	321	269	$4.85 \times 10^7$	-1.07	$-2.21 \times 10^{-10}$

#### 5.4 Semi-IPN with ionic liquid as a co-solvent

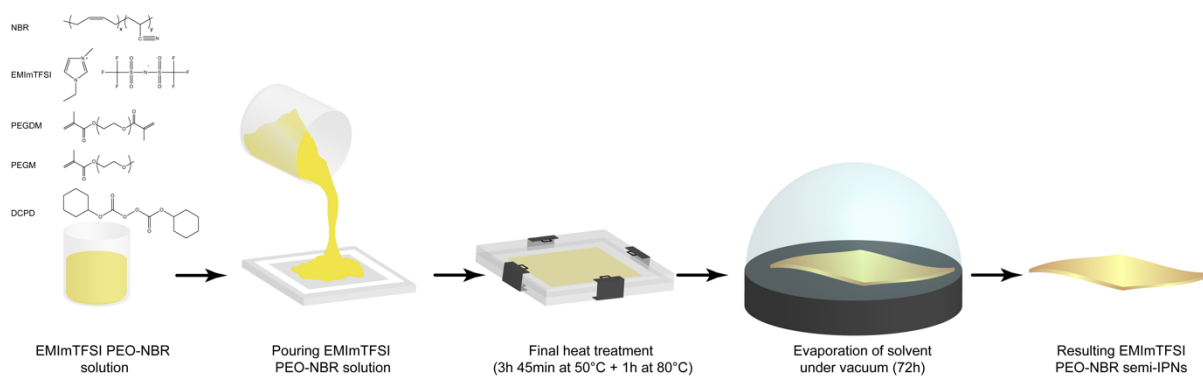
As said before, for an open-air actuation, the actuator needs the presence of two electroactive electrodes and a polymer membrane in between the two electrodes, containing ions, which are necessary for the redox process. Until now, the electroactive material is synthesized first, including the synthesis of the polymer membrane and the electrodes, and the device is finally swollen in the electrolyte by immersion in the ionic liquid (EMImTFSI). This method was necessary in the case of chemically polymerized electrodes because the washing step (to remove the oxidant and the residuals of the EDOT monomer) would have removed all the incorporated electrolyte. Therefore, the electrolyte was incorporated after the fabrication of the electroactive material through the swelling step. Unfortunately, the post swelling step is time consuming (from few days to several weeks) and not compatible with the microfabrication technologies. External swelling induces thickness changes of the actuator which can consequently cause delamination problems between the integrated electrical contacts and the device. In the present work, the use of PEDOT:PSS allows to avoid any washing step in the process and to consider the introduction of the electrolyte directly during

the synthesis of the semi-IPN. This would significantly decrease the fabrication time and would allow the characterization of the final devices in one day.

In this section, a semi-IPN fabrication method will be described to incorporate the ionic liquid (EMImTFSI) directly to the synthesis process. The fabrication and characterization have been carried out on thick samples (250  $\mu\text{m}$ ) to determine the properties of the PEO-NBR semi-IPNs with EMImTFSI directly incorporated during the synthesis, assuming that the thickness is not influencing the intrinsic properties of the resulting materials.

#### 5.4.1 Synthesis of PEO-NBR semi-IPN's with EMImTFSI as a co-solvent

The semi-IPN is synthesized with a weight ratio of 60-40 PEO-NBR and the synthesis is carried out according to the **Figure 78**. First, the NBR solution is prepared by dissolving the NBR (25 wt%) in cyclohexanone and stirred until complete dissolution. Then ionic liquid (EMImTFSI) is introduced to the solution and stirred until the homogenization of the solution (overnight). Three different ratios of EMImTFSI (100, 125 and 150 wt% vs PEO-NBR network) were used in order to compare the properties of the polymer membranes with different electrolyte contents. The PEO precursors (60 wt% vs NBR), consisting of PEGDM and PEGM, were introduced to the solution and stirred during 30 min. The mass ratio of PEGDM/PEGM is 25/75 in order to obtain a network containing high amount of dangling PEGM chains while presenting good mechanical properties.<sup>[103]</sup> The DCPD was used as a radical initiator for a PEO network and was added as a last component to the solution (3 wt% vs PEO precursors). The solution was stirred during 30 min and degassed. The reactive mixture was then poured into the molds (two glass plates separated by Teflon<sup>®</sup> frame with a thickness of 250  $\mu\text{m}$ ) and sealed by clamping all the edges. The molds were then placed into the oven for 3h45 min at 50°C, post-cured for 1h at 80°C and cooled for 30 min at room temperature before opening the molds. All the synthesized membranes were then placed into a sealed chamber to evaporate the solvent under vacuum during 72h.



**Figure 78.** Fabrication of 60-40 PEO-NBR semi-IPNs with EMImTFSI directly incorporated.

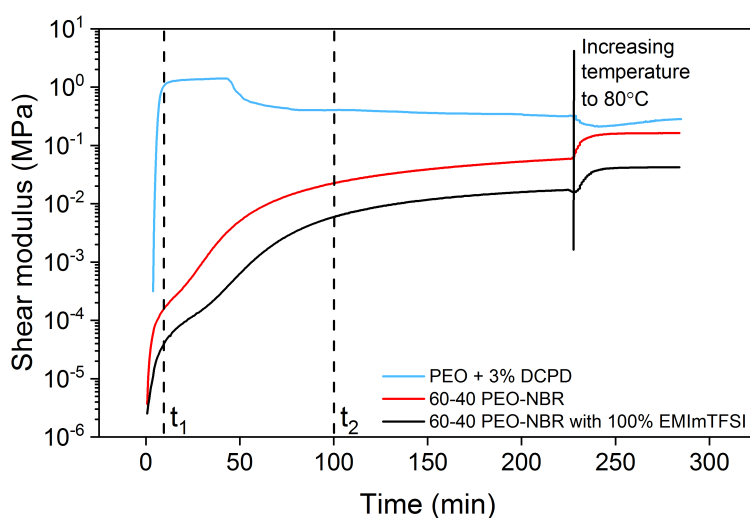
The semi-IPNs synthesized with EMImTFSI as a co-solvent are soft, flexible, stretchable and yellowish transparent. The characterization of mechanical and physicochemical properties will be described in the next subsections: polymerization kinetics (rheology), extractible content (Soxhlet extraction), ionic conductivity (electrochemical impedance spectroscopy) and mechanical properties. Finally, the elaboration of these membranes by spin-coating will be studied and the thickness as a function of the rotation speed will be characterized. Regular semi-IPNs without the presence of EMImTFSI were also synthesized for comparison through external swelling. Since the properties are often similar, most of the results concerning external swelling are reported in the appendix. If no specific indication in the following results is brought, the described materials are concerning the semi-IPNs synthesized with EMImTFSI as a co-solvent.

#### 5.4.2 Rheology

The rheology experiments were carried out to study the polymerization kinetics of the semi-IPNs synthesized with EMImTFSI as a co-solvent. The reaction mixtures were prepared and the polymerization during 3h45 min at 50°C and 1h at 80°C was monitored with Anton Paar rheometer MCR 301. The frequency sweep measurements were carried out at a constant oscillation amplitude of 1% and an oscillation frequency of 1 Hz. The polymerization kinetics can be followed by the dependence of the shear modulus  $G'$ .

**Figure 79** presents the results of the shear modulus  $G'$  as a function of polymerization time for different polymer networks i.e., the single PEO network, the PEO-NBR semi-IPN and the PEO-NBR semi-IPN with 100% EMITFSI directly included. The shear modulus is low in the beginning of the experiment due to the liquid nature of the starting mixture. A steady plateau in the shear modulus is reached when the polymerization reaches a maximum of conversion.

The steady state is dependent on the formation of the PEO network and evaporation of the solvent, indicating that the viscous solution has transformed into solid polymer film. The single PEO network in the presence of 3 wt% of DCPD is formed really fast and the plateau in the shear modulus is obtained approximately after 10min (black dashed line in the position  $t_1$ ). A decrease in the  $G'$  is observed after 45 min, corresponding to the solvent evaporation and loss of contact with the oscillating plate. The shear modulus of the 60-40 PEO-NBR semi-IPN mixtures synthesized in the presence or absence of EMImTFSI exhibit the same trend. A plateau in the shear modulus is obtained approximately after 100 min of polymerization at 50°C (black dashed line in the position  $t_2$ ), indicating the conversion of the PEO network during the polymerization at 50°C. Post-curing at 80°C during 1h is applied in order to ensure a complete conversion of the methacrylate functions of the PEG based monomers. This characterization is showing that the presence of EMImTFSI in the reactive mixture is not significantly modifying the polymerization kinetics of the PEO network. The semi-IPNs with higher content of EMImTFSI (125 % and 150 %) present the same trend and the results are brought in Appendix 3 section A.3.2.



**Figure 79.** Shear modulus ( $G'$ ) as a function of polymerization time for single PEO network, 60-40 PEO-NBR semi-IPN and 60-40 PEO-NBR semi-IPN with 100% EMImTFSI directly included.

### 5.4.3 Extractible content

To evaluate the extend of the cross-linking and the completion of the methacrylate derivatives polymerization, the semi-IPNs with a known weight ( $w_0$ ) were Soxhlet extracted during one week in dichloromethane. The extracted samples were dried under vacuum at



50°C during 4 days to obtain a constant weight ( $w_1$ ). The extractible content is obtained from a following equation:

$$EC (\%) = \frac{(w_0 - w_1)}{w_0} \times 100 \quad (18)$$

In the case of these semi-IPNs, the PEO network is crosslinked in the polymer matrix, NBR is linear and EMImTFSI as an additive. Linear NBR is not cross-linked in the system, but due to the high molecular weight ( $\approx 80\,000 \text{ g}\cdot\text{mol}^{-1}$ ), relatively hard to remove from the semi-IPN structure.<sup>[247]</sup> In order to evaluate the extractible content of PEO and NBR, the percentage of EMImTFSI was subtracted from the final extractible content and the results are presented in **Table 8**.

**Table 8.** Extractible content of the studied semi-IPNs.

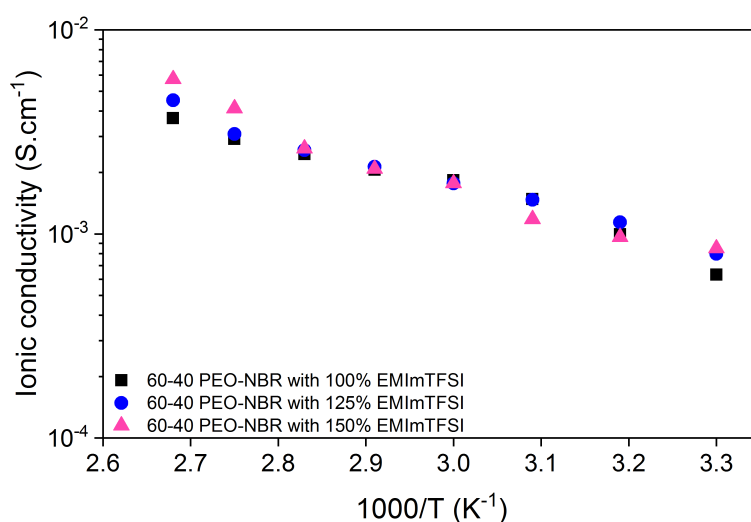
	Polymer content (%)	Total experimental extractible content (%)	EMImTFSI of total (%)	Extractible content without EMImTFSI (%)	Extractible content relative to polymer content (%)
60-40 PEO-NBR	100.0	12.1	0	12.1	12.1
60-40 PEO-NBR with 100% EMImTFSI	50.0	55.9	50.0	5.9	11.8
60-40 PEO-NBR with 125% EMImTFSI	44.4	60.4	55.6	4.9	11.0
60-40 PEO-NBR with 150% EMImTFSI	40.0	64.6	60.0	4.6	11.5

If NBR would be completely removed, the extractible content relative to polymer content should be 40 %. The extracted content of the regular 60-40 PEO-NBR semi-IPN is 12.1 %, indicating that PEO network is crosslinked correctly but also that NBR extraction is low either due to the high molecular weight or NBR grafting in the presence of DCPD during the polymerization. The extractible content of the semi-IPN with 100 % EMImTFSI is 55.9 %, from which 50.0 % is EMImTFSI and certainly removed during the extraction. Therefore, the extractible content without taking into account EMImTFSI is 5.9 %. This extractible value has to be examined relatively to the initial polymer content of the corresponding material. In the case of the semi-IPN with 100% EMImTFSI, PEO and NBR represent only half (50.0 %) of the synthesized membrane. As a consequence, it can be calculated that 11.8 % of the initial polymer content can be extracted after synthesis. Using the same method for the semi-IPNs with 125 % and 150 % EMImTFSI, similar extractible contents of 11.0 and 11.5 % are obtained, respectively. Altogether, these results present that the PEO network is well

crosslinked in all the studied semi-IPNs and the presence of EMImTFSI has no influence on the kinetics of PEO polymerization, even if the quantity is as high as 150 %.

#### 5.4.4 Ionic conductivity

Ionic conductivity of these materials is a critical parameter for actuator applications. The ionic liquid EMImTFSI has been used as an electrolyte for IPN based actuators during many years due to its good properties (high ionic conductivity, non-volatility, non-flammability and high thermal and chemical stability) and the compatibility with both, PEO and NBR phases.<sup>[96,112,248,249]</sup> The ionic conductivity was determined by electrochemical impedance spectroscopy as a function of temperature (30°C – 100°C) to evaluate the difference between the semi-IPNs synthesized in the presence of different contents of EMImTFSI. **Figure 80** presents the temperature dependence of the ionic conductivity and **Table 9** summarizes the ionic conductivity values at 30°C of the studied materials.



**Figure 80.** Ionic conductivity as a function of temperature for PEO-NBR semi-IPNs synthesized in the presence of EMImTFSI.

In the case of PEO-NBR IPNs, it is known that PEO network is much more ionically conductive than the NBR phase (almost 2 orders of magnitude). Festin *et al.* reported the values of ionic conductivities for single PEO and NBR networks swollen in EMImTFSI as  $2.0 \times 10^{-3}$  and  $2.8 \times 10^{-5}$  S.cm<sup>-1</sup>, respectively (not reported on the figure).<sup>[117]</sup> In the present work, all the semi-IPNs demonstrate the same behavior as a function of the temperature. Ionic conductivity is increasing when the temperature is increased because the mobility of ions being higher at higher temperatures. At 30°C, the ionic conductivity of all the semi-IPNs

with EMImTFSI directly included is in the range of  $6.3 - 8.9 \times 10^{-4} \text{ S.cm}^{-1}$ . The ionic conductivity increases from  $6.3 - 8.9 \times 10^{-4} \text{ S.cm}^{-1}$  when the content of EMImTFSI is increased to 150 %. These results are not surprising taking into account that the neat EMImTFSI has an ionic conductivity of  $8.9 \times 10^{-3} \text{ S.cm}^{-1}$ .<sup>[250]</sup> Therefore, the ionic conductivity is increasing when the amount of EMImTFSI in the semi-IPNs is increased. The overlay with externally swollen semi-IPNs is presented in Appendix 3 section A.3.3, presenting almost meaningless difference around half of magnitude and staying in the range of  $4.7 \times 10^{-4} - 1.0 \times 10^{-3} \text{ S.cm}^{-1}$  at 30°C. This highlights again the advantage of incorporation of EMImTFSI as a co-solvent during the synthesis of the semi-IPNs, removing one step from the fabrication process while keeping the same ionic conductivities.

**Table 9.** Ionic conductivity of neat EMImTFSI and PEO-NBR semi-IPNs synthesized in the presence of EMImTFSI.

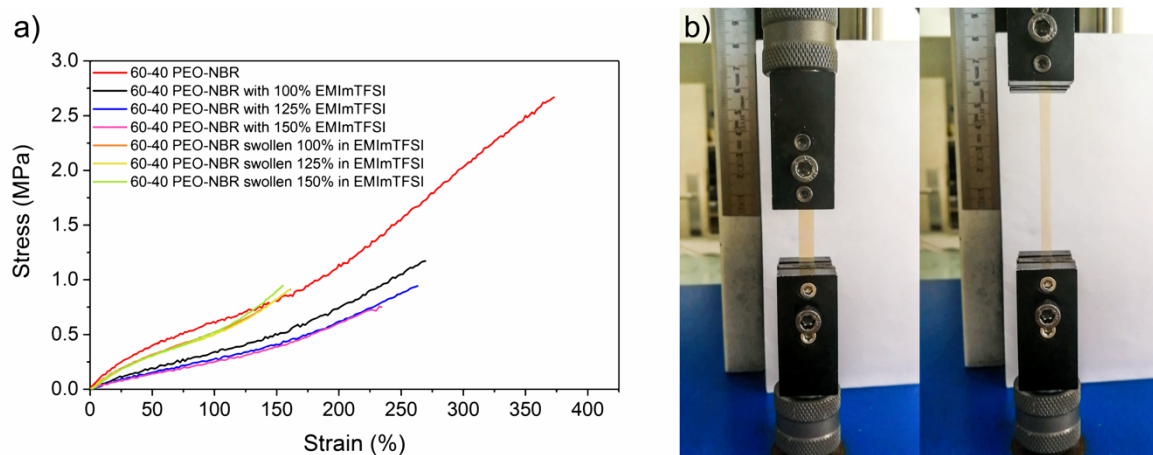
	Ionic conductivity at 30°C S.cm <sup>-1</sup>
neat EMImTFSI at 25°C <sup>[250]</sup>	$8.6 \times 10^{-3}$
60-40 PEO-NBR with 100% EMImTFSI	$6.3 \times 10^{-4}$
60-40 PEO-NBR with 125% EMImTFSI	$8.0 \times 10^{-4}$
60-40 PEO-NBR with 150% EMImTFSI	$8.9 \times 10^{-4}$

#### 5.4.5 Mechanical properties

Thermomechanical properties of the semi-IPNs were evaluated using Dynamic Mechanical Analysis (DMA) and the results are presented in Appendix 3 section A.3.4. Briefly, the general viscoelastic behavior of the materials is the same, the existence of two separate phases corresponding to NBR and PEO domains was observed for all the characterized semi-IPNs. Additionally, when comparing the semi-IPNs synthesized in the presence of EMImTFSI with the externally swollen semi-IPNs, the viscoelastic properties are almost identical.

This section is devoted more specifically to tensile strength experiments (stress as a function of strain). Tensile strength experiments of the resulting semi-IPNs were carried out in order to determine the Young's modulus and strain at break of these materials. Experiments were performed on samples ( $L \times w \times t = 20\text{mm} \times 5\text{mm} \times 0.25\text{mm}$ ) at a speed rate of  $1000 \text{ \%}.\text{min}^{-1}$ . The Young's modulus of the resulting semi-IPNs is obtained from the linear part of the stress-strain curve according to the equation (15) in the section 5.3.2.2 of this chapter.

**Figure 81a** presents the evolution of stress as a function of strain for all the characterized samples. The single PEO network and NBR networks (not reported on the figure) have been studied previously during the theses of Festin and Maziz.<sup>[173,247]</sup> It has been found that PEO single network is really brittle with extremely low values of strain at break (less than 10%) and Young's modulus between 4-11 MPa. On the contrary, the single NBR presents high strain at break (430 %) with a Young's modulus of 1.15 MPa. It was found in the present work that the 60-40 PEO-NBR semi-IPN without any EMImTFSI presents really high strain at break (373 %) with a Young's modulus of 0.86 MPa, indicating that the mechanical properties are mostly governed by the continuous NBR phase and making it attractive for actuator fabrication. The externally swollen semi-IPNs present notably lower strain at break (155 – 161 %) and result in Young's modulus between 0.64 – 0.69 MPa. Lower strain at break can be explained by the fact that external addition of ionic liquid is inducing some inner pre-stretching of the network chains and as a consequence, the swollen and pre-stretched semi-IPNs break at lower strain. On the contrary, including EMImTFSI as a co-solvent during the synthesis allows to fabricate semi-IPNs with higher strain at break and lower Young's modulus compared to the externally swollen semi-IPNs. The strain at break values for materials synthesized with EMImTFSI as a co-solvent are 270%, 263% and 234% for the samples with 100%, 125% and 150% EMImTFSI, respectively and the Young's modulus between 0.29 and 0.41 MPa. Higher strain at break and slightly lower Young's modulus compared to the externally swollen semi-IPNs might be due to the dilution effect. The externally swollen semi-IPNs are synthesized with just cyclohexanone as a solvent, but the new samples with cyclohexanone and EMImTFSI. Adding higher amount of solvent leads to less entangled networks, resulting in softer but also more stretchable materials. The good mechanical properties of the semi-IPN synthesized with 100 % EMImTFSI as a co-solvent are illustrated in **Figure 81b** and **Table 10** summarizes the values of strain at break and Young's modulus of different resulting semi-IPNs.



**Figure 81.** a) stress as a function of strain of different PEO-NBR semi-IPNs and b) illustration of 100% EMImTFSI PEO-NBR semi-IPN stretching at 200% strain.

**Table 10.** Strain at break and Young's modulus of PEO-NBR semi-IPN, PEO-NBR semi-IPNs synthesized in the presence of EMImTFSI and PEO-NBR semi-IPNs swollen in EMImTFSI.

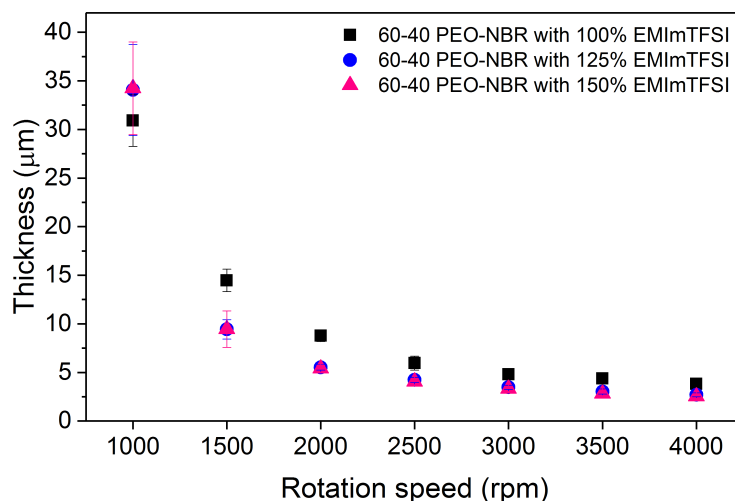
	Strain at break %	$E$ MPa
60-40 PEO-NBR	373	$0.86 \pm 0.03$
60-40 PEO-NBR with 100% EMImTFSI	270	$0.41 \pm 0.01$
60-40 PEO-NBR with 125% EMImTFSI	263	$0.33 \pm 0.01$
60-40 PEO-NBR with 150% EMImTFSI	234	$0.29 \pm 0.01$
60-40 PEO-NBR swollen 100% in EMImTFSI	161	$0.69 \pm 0.07$
60-40 PEO-NBR swollen 125% in EMImTFSI	160	$0.64 \pm 0.02$
60-40 PEO-NBR swollen 150% in EMImTFSI	155	$0.68 \pm 0.01$

#### 5.4.6 Thickness of spin-coated semi-IPNs

The previous studies were carried out on macroscale samples with a thickness of 250  $\mu\text{m}$ . In order to integrate these materials into microscale devices and to fabricate the actuators with layer stacking method, the possibility to synthesize thin membrane layers and to precisely control their thickness must be investigated.

The thickness can be controlled using the spin coating technique. **Figure 82** exhibits the thickness results of the spin-coated (acceleration 1000  $\text{rpm}\cdot\text{s}^{-1}$ ; duration 30s) semi-IPNs synthesized with EMImTFSI as a co-solvent. As expected, higher rotation speed leads to thinner semi-IPN layers. The thickness of the layers can be tuned between 2.5 and 34  $\mu\text{m}$  depending on the chosen rotation speed. The content of ionic liquid has bigger influence at lower rotation speeds ( $<3000$  rpm), where the semi-IPN with 100% EMImTFSI presents higher thickness compared to the 125% and 150% semi-IPNs. This can be explained by the higher viscosity of the starting mixture, when lower content of EMImTFSI has been added. The values obtained at 1000 rpm demonstrate contrary results, but due to the high roughness

and uneven surface, this rotation speed was not considered suitable to fabricate smooth and flat semi-IPN layer in the actuator fabrication process. At higher rotation speeds ( $>3000$  rpm) the difference in thickness is almost meaningless regardless the content of EMImTFSI in the polymer mixture.



**Figure 82.** Thickness as a function of rotation speed of spin-coated semi-IPNs synthesized in the presence of EMImTFSI.

#### 5.4.7 Conclusion

The study on semi-IPN synthesis with three different contents of EMImTFSI as a co-solvent presented good results. It was demonstrated that the incorporation of EMImTFSI does not influence the polymerization route or time, neither the morphology. The ionic conductivity measurements demonstrated high ionic conductivity for all the studied semi-IPNs and presented meaningless difference in comparison with externally swollen semi-IPNs. The characterization of mechanical properties showed an improvement when EMImTFSI was used as a co-solvent during the synthesis and resulted in more soft and stretchable materials, which is important for actuator application but also for many other devices. More importantly, incorporation of EMImTFSI directly into the polymer mixture has the advantage of removing the swelling step from the fabrication process and allowing the fabrication and characterization in the same day. It is also beneficial for microsystems to prevent the delamination problems between the electrical connections and the actuator during external swelling. All these advantageous properties make them attractive for actuator fabrication and the semi-IPN synthesized with 100% EMImTFSI as a co-solvent with high ionic conductivity

and highest mechanical properties is considered as the composition for further linear actuator fabrication.

## 5.5 Trilayer linear actuators

In this section, the determined parameters from the electrode and semi-IPN sections are used to predict the linear deformations of the trilayer linear actuators and to choose the optimized combinations based on these parameters. The second part describes the fabrication process based on the selected parameters and using the layer stacking method. The last part deals with mechanical and electrochemical characterizations of the resulting linear actuators.

### 5.5.1 Modeling: prediction of linear deformation

The obtained parameters of the different PEDOT:PSS/PEO electrodes and the semi-IPN with 100 % EMImTFSI as a co-solvent allow the use of the electromechanical model to predict the linear deformations and to choose the optimized combinations of the electrodes. The electromechanical model (section 5.2, equation 14) is re-written as follows:

$$\varepsilon = \rho_1 h_1 \frac{E_1 \alpha_1 - E_2 \alpha_2}{h_1 E_1 + h_2 E_2 + h_{SIPN} E_{SIPN}} \quad (19)$$

From this model, it was demonstrated previously that the deformation of the actuator was always governed by the stiffer electrode.<sup>[118]</sup> Considering this knowledge, the predictions on linear deformations are calculated in the case where the working electrode (W.E) is referred as the stiffer electrode and is named as electrode 1 and the counter electrode (C.E) as the softer electrode is named as electrode 2.

Charge is not appearing directly in the electromechanical model, but is involved in the product  $\rho_1 h_1$ , ( $\rho_x$  volumetric charge density and  $h_x$  thickness) brought in equation (20). The total charge of the actuator will be ruled by the electrode presenting the limiting electrochemical charge. Knowing that the length and the width of the electrodes are identical in the final actuator configuration, the product  $\rho h$  can be used to compare the charge for every type of electrodes considered for the combinations and to determine the charge limiting ones. For this, the length  $L$  and the width  $w$  were used as constant values ( $L \times w = 50 \text{ mm} \times 2 \text{ mm}$ ). The volumetric charge density  $\rho_x$  and thickness  $h_x$  were used as the corresponding



values of each electrode (obtained in section 5.3.3, **Table 11**) to calculate the product  $\rho h$ , which is also presented in the table.

$$q_x = \rho_x V_x = \rho_x h_x L W \quad (20)$$

**Table 11.** Summarized parameters of PEDOT:PSS/PEO electrodes from mechanical and electrochemomechanical characterizations of section 5.3 and calculated product  $\rho t$ .

\* Measured in neat EMITFSI electrolyte

Additive of the electrode:	$h$ $\mu\text{m}$	$E^{\text{open-air}}$ MPa	* $\rho$ $\text{C.m}^{-3}$	$\rho h$ $\text{C.m}^{-2}$
20% PEO	8.3	2270	$3.62 \times 10^7$	301
40% PEO	9.5	1538	$3.78 \times 10^7$	358
20% PEO + EMImTFSI	9.3	1004	$4.91 \times 10^7$	455
40% PEO + EMImTFSI	7.9	605	$4.85 \times 10^7$	384

All the 6 possible combinations where electrode 1 is stiffer compared to electrode 2 are summarized in **Table 12** with the comparison of product  $\rho h$  to determine the charge limiting electrode of these combinations.

**Table 12.** Comparison of charge limiting electrodes when electrode 1 is stiffer compared to electrode 2.

Electrode 2 \ Electrode 1	40% PEO + EMImTFSI	20% PEO + EMImTFSI	40% PEO	20% PEO
40% PEO + EMImTFSI	$E_1 = E_2$ $\rho_1 h_1 = \rho_2 h_2$	$E_1 > E_2$ $\rho_1 h_1 > \rho_2 h_2$	$E_1 > E_2$ $\rho_1 h_1 < \rho_2 h_2$	$E_1 > E_2$ $\rho_1 h_1 < \rho_2 h_2$
20% PEO + EMImTFSI		$E_1 = E_2$ $\rho_1 h_1 = \rho_2 h_2$	$E_1 > E_2$ $\rho_1 h_1 < \rho_2 h_2$	$E_1 > E_2$ $\rho_1 h_1 < \rho_2 h_2$
40% PEO			$E_1 = E_2$ $\rho_1 h_1 = \rho_2 h_2$	$E_1 > E_2$ $\rho_1 h_1 < \rho_2 h_2$

Among the 6 different possible combinations it was found that in 5 cases, the W.E (stiffer) is also the charge limiting electrode but in one combination (20% PEO + EMImTFSI and 40% PEO + EMImTFSI) the charge is limited by the counter electrode (C.E) (**Table 12**). For this last combination, the actuating electrode will be electrochemically limited by the counter electrode and only part of the deformation will be available. In other words, the maximum deformation of the electrode 1 cannot be obtained due to the limiting electrochemical charge of the electrode 2. In the case of the 5 other combinations (marked in green), all the electrochemical charge of the W.E can be used to maximize the available deformation and it is not limited by the electrode 2. These results on charge limiting electrodes have to be considered in the electromechanical model to predict the available deformations.

The required parameters of the PEDOT:PSS/PEO electrodes (thickness, Young's modulus, volumetric charge density and strain-to-charge ratio) for electromechanical model are summarized in **Table 13**. The thickness of the semi-IPN with 100% EMImTFSI is 14.5  $\mu\text{m}$  and the Young's modulus 0.41 MPa.

**Table 13.** Summarized parameters of PEDOT:PSS/PEO electrodes from mechanical and electrochemomechanical characterizations of section 3.

\* Measured in neat EMITFSI electrolyte

Additive of the electrode:	$h$ $\mu\text{m}$	$E^{\text{open-air}}$ MPa	$^*\rho$ $\text{C}\cdot\text{m}^{-3}$	$\alpha$ $\text{m}^3\cdot\text{C}^{-1}$
20% PEO	8.3	2270	$3.62 \times 10^7$	$-2.02 \times 10^{-10}$
40% PEO	9.5	1538	$3.78 \times 10^7$	$-2.46 \times 10^{-10}$
20% PEO + EMImTFSI	9.3	1004	$4.91 \times 10^7$	$-2.04 \times 10^{-10}$
40% PEO + EMImTFSI	7.9	605	$4.85 \times 10^7$	$-2.21 \times 10^{-10}$

These parameters are used in equation 19 to predict the linear deformation of the trilayer actuators, using different electrode combinations. The predicted linear strains of different PEDOT:PSS/PEO electrode combinations for the open-air Young's modules are brought in **Table 14**.

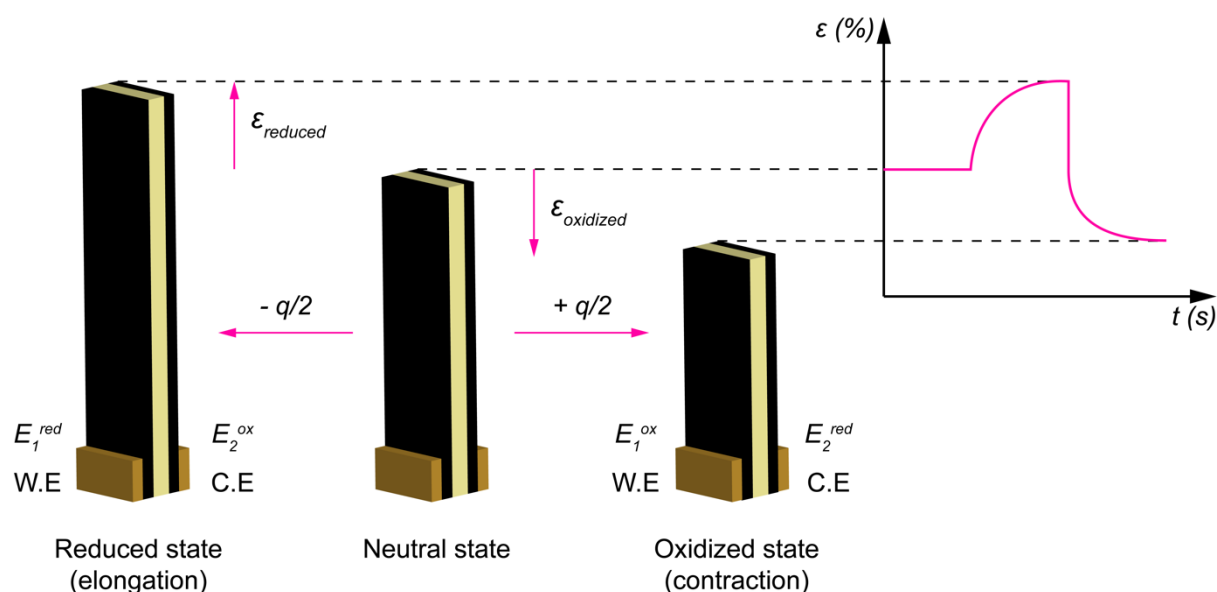
**Table 14.** Predicted linear strain  $\varepsilon$  based on electromechanical model for different PEDOT:PSS/PEO electrode combinations with the Young's modulus values in open air.

Electrode 1 \ Electrode 2	40% PEO + EMImTFSI	20% PEO + EMImTFSI	40% PEO	20% PEO
40% PEO + EMImTFSI	0	-0.33 %	-0.43 %	-0.40%
20% PEO + EMImTFSI		0	-0.23 %	-0.25 %
40% PEO			0	-0.07 %

The predicted linear strains in **Table 14** demonstrate that the combination of identical electrodes leads to a linear deformation theoretically equal to zero. However, as soon as non-identical electrodes are combined, a linear deformation is predicted. The maximum predicted deformation varies from -0.07 % to -0.43 %, depending on the combination of the electrodes. The maximum strain -0.43 % is predicted for the electrode combination of 40% PEO and 40% PEO + EMImTFSI. Interestingly, all the predicted values demonstrate negative strain, corresponding to a contraction of the actuator when electrode 1 is oxidized and electrode 2 reduced. This result is consistent with the work of Fannir, where the model predicted that stiffer electrode deformation will rule the total deformation of the device. In the case of EMImTFSI and the related cation mechanism, oxidation of the electrode leads to its

contraction and concomitantly, the reduction of the second electrode leads to its elongation. Based on the chosen configuration (electrode 1 is always the stiffer electrode), application of positive bias voltage will induce linear contraction of the electrode 1 and consequently the linear contraction of the actuator.

During the redox process of the actuators, one electrode is oxidized at the same time when the second electrode is reduced. It was demonstrated in the section 5.3.2.3 of this chapter, that the Young's modulus of the PEDOT:PSS electrodes is dependent on the redox level. In order to use the theoretical model even more accurately, the mechanical properties of the electrode layers should be considered as in oxidized and reduced state. The Young's modulus variation as a function of the redox level is not equivalent, i.e. the ratio between electrode 1 oxidized state and electrode 2 reduced state is not equal to the electrode 1 reduced state and electrode 2 oxidized state. Therefore, this change has to be taken into account and the maximum strain calculation has to be done according to the **Figure 83**. As said before, the W.E as electrode 1 is always the stiffer electrode and will rule the deformation of the actuator and C.E as electrode 2 is the softer electrode.



**Figure 83.** Schematic representation for the linear strain predictions considering the maximum obtainable strain in two extreme points, when the actuator is elongated and contracted.

Following the figure, the electromechanical model is written separately to predict the strain at two extreme points and the total predicted strain is the difference between those two extremums:

$$\varepsilon_{reduced} = -\frac{\rho_1}{2} h_1 \frac{E_1^{red} \alpha_1 - E_2^{ox} \alpha_2}{h_1 E_1^{red} + h_2 E_2^{ox} + h_{SIPN} E_{SIPN}} \quad (21)$$

$$\varepsilon_{oxidized} = \frac{\rho_1}{2} h_1 \frac{E_1^{ox} \alpha_1 - E_2^{red} \alpha_2}{h_1 E_1^{ox} + h_2 E_2^{red} + h_{SIPN} E_{SIPN}} \quad (22)$$

$$\varepsilon_{total} = \varepsilon_{oxidized} - \varepsilon_{reduced} \quad (23)$$

As shown in the **Figure 83**, the maximum obtainable strain can be calculated from the difference between the actuators oxidized and reduced state. The full electrochemical charge of the charge limiting electrode is divided by two and the Young's modulus in oxidized and reduced state are considered in the two extremums. The determined parameters from section 5.3 as a function of the redox level are summarized in **Table 15**.

**Table 15.** Summarized parameters of PEDOT:PSS/PEO electrodes from mechanical and electrochemomechanical characterizations of section 3.

\* Measured in neat EMITFSI electrolyte

Additive of the electrode:	$h$ μm	* $E^{oxidized}$ MPa	* $E^{reduced}$ MPa	* $\rho$ C.m <sup>-3</sup>	* $\varepsilon_0$ %	$\alpha$ m <sup>3</sup> .C <sup>-1</sup>
20% PEO	8.3	1525	1388	3.62 x 10 <sup>7</sup>	-0.73	-2.02 x 10 <sup>-10</sup>
40% PEO	9.5	735	663	3.78 x 10 <sup>7</sup>	-0.93	-2.46 x 10 <sup>-10</sup>
20% PEO + EMImTFSI	9.3	682	527	4.91 x 10 <sup>7</sup>	-1.00	-2.04 x 10 <sup>-10</sup>
40% PEO + EMImTFSI	7.9	321	269	4.85 x 10 <sup>7</sup>	-1.07	-2.21 x 10 <sup>-10</sup>

The parameters from **Table 15** are used in equations 21-23 to predict the linear deformation of the trilayer actuators based on different electrode combinations. The resulting predicted linear strains ( $\varepsilon_{total}$ ), considering the change in the modulus as a function of the redox level are brought in **Table 16**.

**Table 16.** Predicted linear strain  $\varepsilon_{total}$  based on electromechanical model from equations 21-23 for different PEDOT:PSS/PEO electrode combinations with the experimental Young's modulus values as a function of the redox level.

Electrode 1 \ Electrode 2	40% PEO + EMImTFSI	20% PEO + EMImTFSI	40% PEO	20% PEO
40% PEO + EMImTFSI	0	-0.35 %	-0.40 %	-0.46 %
20% PEO + EMImTFSI		0	-0.11 %	-0.27 %
40% PEO			0	-0.20 %

The predicted maximum linear strains ( $\varepsilon_{total}$ ) in **Table 16** demonstrate the same behavior with the previous obtained values, indicating that two identical electrodes lead to a linear

deformation equal to zero. In the same way with the previous model, the sign of the total predicted strain is negative, corresponding to the contraction of the actuator when electrode 1 is oxidized and electrode 2 reduced. The maximum obtainable strain (between the oxidized and reduced state) varies from -0.11 to -0.46 %. The highest strain -0.46 % is predicted for the electrode combination of 20% PEO and 40% PEO + EMImTFSI.

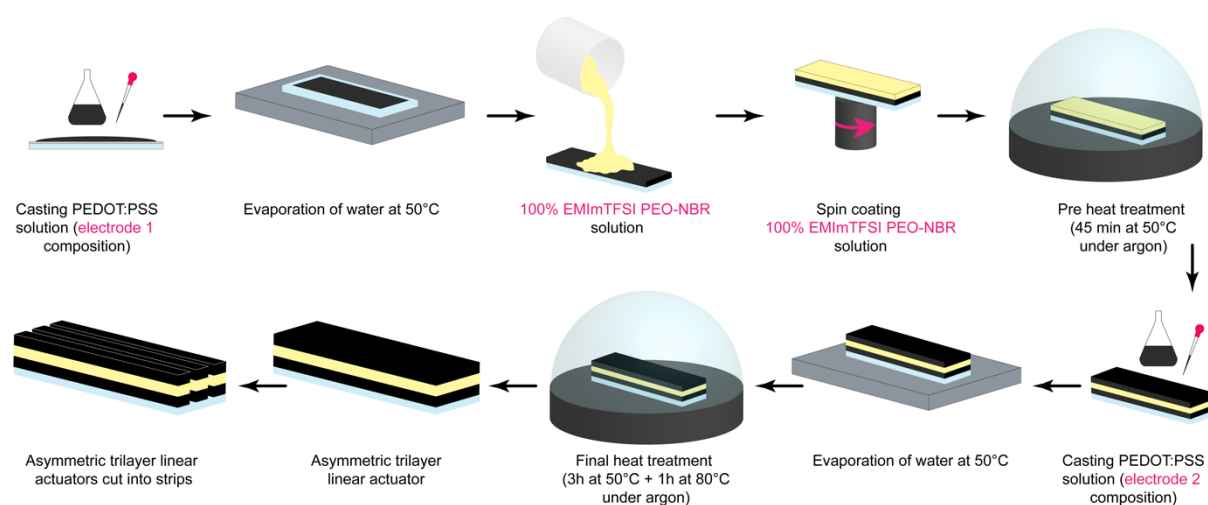
It is noteworthy to mention here that probably the real predicted linear strain value is somewhere in-between of those two different predictions. The final actuator is characterized in open-air, not immersed in ionic liquid. The Young's modulus in open-air is notably higher compared to the in-solution experiments, which makes the predicted values different between these two models. The real Young's modulus values as a function of the redox level in open-air cannot be measured due to the freestanding electrode configuration and therefore these values are not accessible.

The highest strains between these 2 tables were predicted either for the electrode combination of 20% PEO and 40% PEO + EMImTFSI or for the electrode combination of 40% PEO and 40% PEO + EMImTFSI. Due to the controversial results depending on the different Young's modulus values (open air or as a function of the redox level in solution) and relatively small difference in predicted strain, both of these combinations were chosen for asymmetric trilayer linear actuator fabrication.

### 5.5.2 Fabrication of asymmetric trilayer linear actuators

The fabrication of asymmetric trilayer actuators has been performed according to layer stacking method, described in Chapter 3. This process allows the control in thickness of each layer by modifying the volume of the casted solution and the rotation speed of spin-coater. The schematic view is brought in **Figure 84** for a reminder of the fabrication process. The actuators are obtained by fabricating each layer separately on top of the previous layer. The PEDOT:PSS/PEO electrodes are obtained through the casting process and the semi-IPN with EMImTFSI layer is deposited by spin-coating. First, the PEDOT:PSS solution according to electrode 1 composition is prepared and casted ( $0.08 \text{ ml.cm}^{-2}$ ) into previously prepared microscope slide molds. The substrate is then placed onto the heating plate at  $50^\circ\text{C}$  to evaporate the water and to form free-standing films. In the next step, the 100% EMImTFSI PEO-NBR solution is spin-coated ( $1500\text{rpm}-1000\text{rpm.s}^{-1}-30\text{s}$ ) on top of the first PEDOT:PSS/PEO electrode and pre-treated at  $50^\circ\text{C}$  during 45 min under argon. The second

PEDOT:PSS/PEO layer is obtained on top of the semi-IPN layer according to the composition of the electrode 2. The substrate is again placed on a heating plate to evaporate the water and to form the second PEDOT:PSS/PEO electrode. The final heat treatment is carried out during 3h at 50°C and post-cured during 1h at 80°C under argon. The resulting asymmetric trilayers are then cut into strips ( $L \times w = 50 \text{ mm} \times 2 \text{ mm}$ ) and are ready for characterizations. The incorporation of EMImTFSI directly into the PEO-NBR solution decreases significantly the fabrication time by removing the external swelling step from the process. As a result, the asymmetric linear actuators can be fabricated and characterized during the same day.



**Figure 84.** Fabrication process of asymmetric trilayer linear actuators based on layer stacking method.

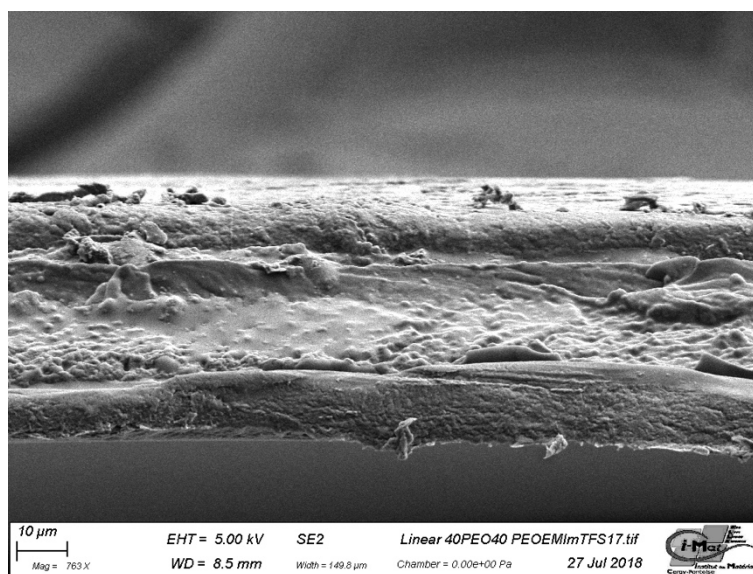
One of two electrode compositions resulted in adhesion problems between the substrate and the trilayer actuator. Therefore, the trilayer linear actuators characterized and described in the next sections are fabricated with composition PEDOT:PSS/PEO(40%) (electrode 1)//100% EMImTFSI PEO-NBR semi-IPN//PEDOT:PSS/PEO(40%)/EMImTFSI (electrode 2).

### 5.5.3 Characterization of asymmetric trilayer linear actuators

All the characterization results will be presented in the configuration as depicted in **Figure 86**, where charge limiting and stiffer electrode 1 (40% PEO) is connected to the working electrode (W.E) and softer electrode 2 (40% PEO + EMImTFSI) is connected to the counter electrode (C.E).

### 5.5.3.1 Trilayer configuration

The scanning electron microscopy (SEM) was performed in order to confirm the presence of three layers in the final configuration and to affirm the suitability of the layer stacking method for trilayer linear actuator fabrication. **Figure 85** presents the SEM image of the resulting linear actuator with a configuration of PEDOT:PSS/PEO(40%)/100% EMImTFSI PEO-NBR//PEDOT:PSS/PEO(40%)/EMImTFSI. The upper layer is corresponding to the electrode 1 (40% PEO) and the bottom layer to the electrode 2 (40% PEO + EMImTFSI).



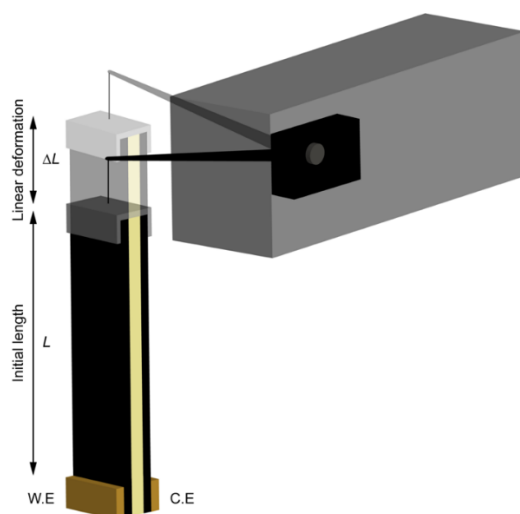
**Figure 85.** SEM image of the asymmetric trilayer linear actuator. Upper layer is corresponding to the 40% PEO electrode and bottom layer to the 40% PEO + EMImTFSI electrode.

The thickness of the final configuration (47  $\mu\text{m}$ ) is higher compared to the study on separate layers. The thickness of the 40% PEO electrode corresponds to the thickness of the electrode study, found previously. The thickness of the PEO-NBR layer with 100% EMImTFSI as a co-solvent is 24.5  $\mu\text{m}$ , which is 10  $\mu\text{m}$  higher compared to the thickness found in the previous study. The 40% PEO + EMImTFSI has also higher thickness compared to the electrode study (12.5  $\mu\text{m}$  instead of 7.9  $\mu\text{m}$ ). Higher thicknesses of the second and third layer can be explained by different substrates and wettability. The study on separate layers was performed using smooth microscope slides as substrates, but in trilayer configuration the next layers are synthesized on top of the previous layers. Overall, the SEM analysis proves the existence of three separate layers and confirms that layer stacking method is suitable to obtain asymmetrical linear actuators.



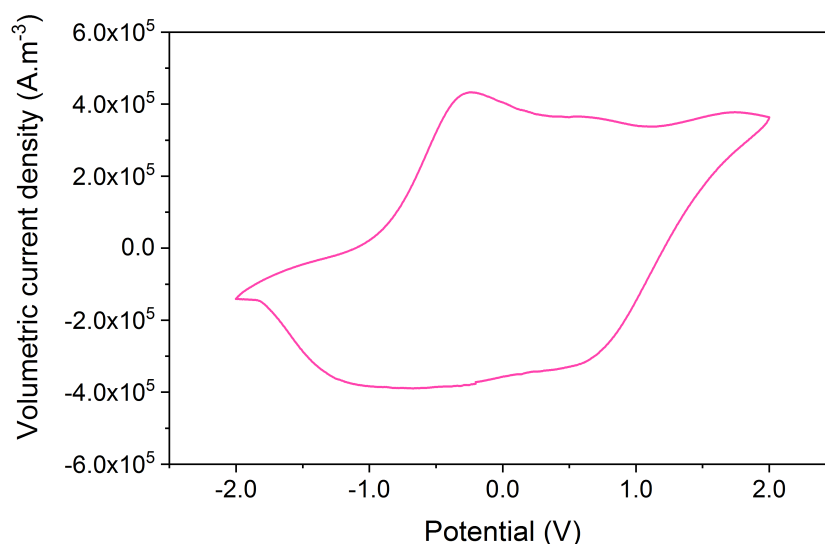
### 5.5.3.2 Electrochemical properties

The electrochemical properties were determined using cyclic voltammetry in open-air in a 2-electrode configuration ( $\pm 2.0$  V,  $20 \text{ mV}\cdot\text{s}^{-1}$ ). The measurements were performed as depicted in **Figure 86**, by connecting one end of the actuator to the potentiostat and the other end to the Aurora Muscle Lever Arm System (300 C) with a pre-stress of 0.4 MPa. The W.E was connected to electrode 1 (40% PEO) and the C.E to electrode 2 (40% PEO + EMImTFSI). Cyclic voltammograms were also used to calculate the charge and finally to evaluate the volumetric charge density of the trilayer device.



**Figure 86.** Experimental setup for asymmetric trilayer linear actuator characterizations.

The cyclic voltammogram of the asymmetric trilayer linear actuator in **Figure 87** presents high electroactivity with reversible oxidation and reduction process. The resulting calculated volumetric charge density of the asymmetrical trilayer linear actuator is  $7.1 \pm 3.1 \times 10^7 \text{ C}\cdot\text{m}^{-3}$ . These results are indicating good electrochemical properties and that the fabrication process of the trilayer does not alter the electroactivity of the 2 PEDOT:PSS/PEO electrodes.



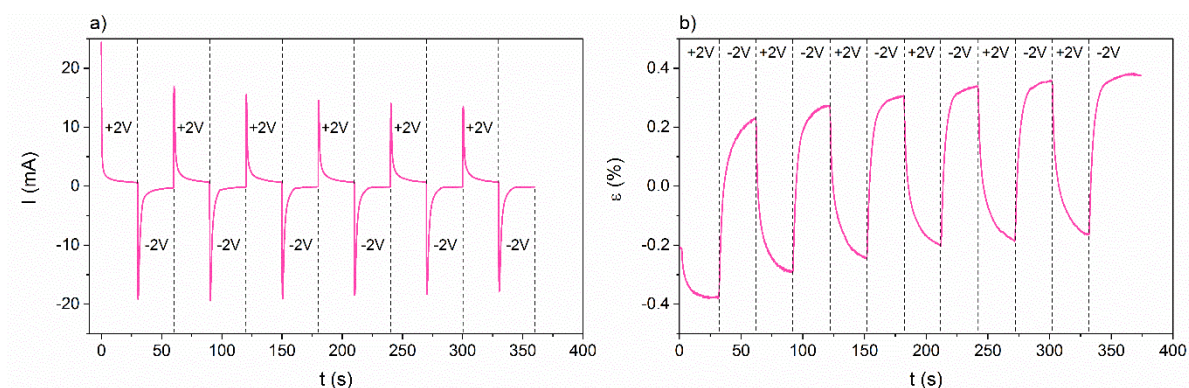
**Figure 87.** Cyclic voltammetry of the asymmetrical trilayer linear actuator with a configuration of PEDOT:PSS/PEO(40%)(electrode 1)//100% EMImTFSI PEO-NBR//PEDOT:PSS/PEO(40%)/EMImTFSI (electrode 2) at a scan rate of  $20 \text{ mV}\cdot\text{s}^{-1}$  and a voltage window of  $\pm 2.0 \text{ V}$  in open air.

### 5.5.3.3 Linear actuation in open-air

The actuation measurements were performed as depicted in **Figure 86**. Chronoamperometry (CA) ( $\pm 0.5 \text{ V}$ ;  $\pm 1.0 \text{ V}$ ,  $\pm 1.5 \text{ V}$ ,  $\pm 2.0 \text{ V}$ , step duration 30 s) was used to electrically stimulate the PEDOT:PSS trilayer linear actuators in isotonic mode with a pre-stress of 0.4 MPa.

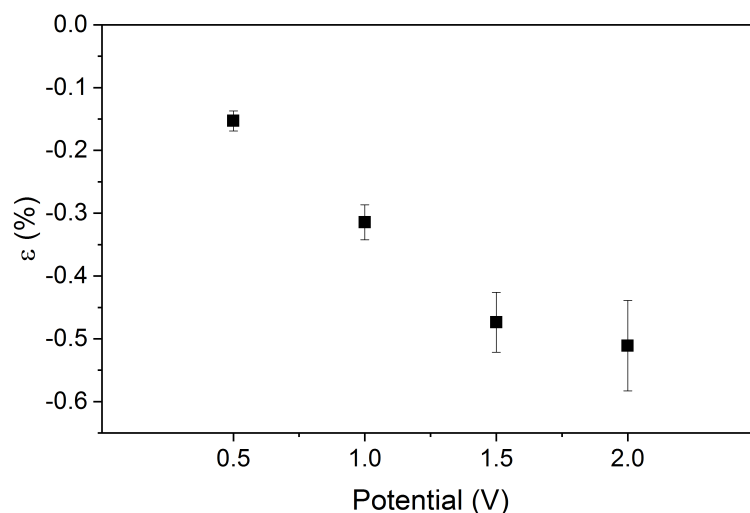
**Figure 88a** depicts the current response as a function of time during 30 s step at  $\pm 2.0 \text{ V}$  of the trilayer linear actuator. The electrical response under electrical stimulation demonstrates typical response of the trilayer device with current peak and decay. This behavior is similar to the supercapacitors with charging/discharging behavior. The current response demonstrates almost no leakage current, indicating that there are no significant short circuits between the two electrodes and demonstrating once again that elaboration process is well controlled. During electrochemical stimulation, the resulting mechanical response is recorded and is brought in **Figure 88b**. Following the direction of the deformation it can be seen that it follows the trend of the prediction. During positive potential bias, the contraction of the stiffer working electrode (1), due to cation expulsion during oxidation, leads to overall contraction (negative deformation) of the actuator. The resulting linear actuator is also demonstrating a creep behavior. The same phenomenon was observed during the free strain experiments of the freestanding ECP films with EMImTFSI as a second additive in section 5.3.3. These electrodes presented higher electromechanical relaxation probably due to the

morphological changes inducing plasticization and could be also the reason for a creep behavior in trilayer configuration.



**Figure 88.** Linear actuation characterization: a) current response as a function of time at  $\pm 2.0V$ ; b) corresponding strain as a function of time at  $\pm 2.0V$ .

**Figure 89** demonstrates the effect of the applied potential on the linear deformation during 30 s steps of all the studied samples. The contraction amplitude is varying from -0.15 to -0.51 %, when the potential is increased from 0.5 to 2.0 V. It can be seen also that kind of a plateau is obtained (**Figure 88**), indicating that the linear deformation wouldn't improve so much above 2.0 V which would also increase the risk of overoxidation and bad stability of the device.

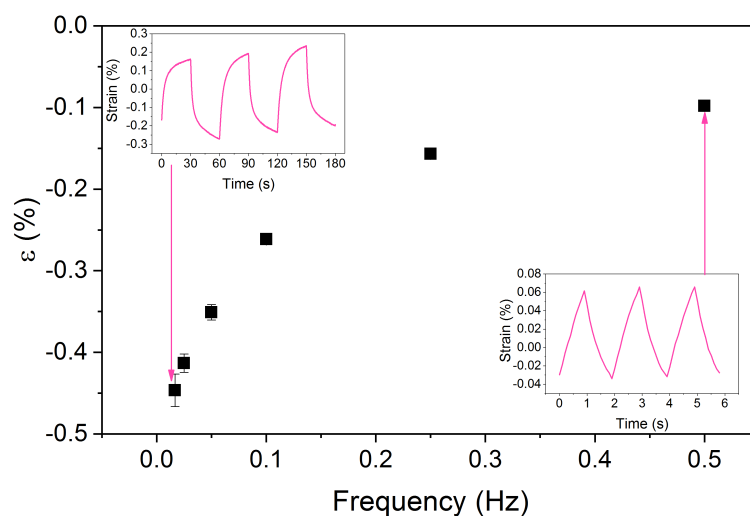


**Figure 89.** Linear actuation strain as a function of applied potential during electrical stimulation of 30 s steps. Negative linear strain corresponds to the contraction of the actuator during positive potential bias.

The electromechanical model predicted a linear deformation of -0.40 % with the Young's modulus values as a function of the redox level and -0.43 % with open-air Young's modules. The average experimental value is slightly higher (-0.51 %) but when comparing to the

previous two models, it is closer to the model where open-air Young's modulus was used (-0.43 %). While the experimental value is slightly higher, then the predicted -0.43 is close to the experimental error bar range of all the studied linear actuators ( $-0.51 \pm 0.07$  %). Given these results, it can be concluded that the open-air linear actuator was developed successfully, whose compositions can be chosen according to the electromechanical model to predict the linear deformation of the PEDOT:PSS linear actuators. Moreover, the correspondence with the predicted linear strain demonstrates that the stiffer and charge limiting electrode (working electrode) allow to maximize the resulting linear strain and the performances of the actuator are not limited by the counter electrode.

The linear strain of the asymmetrical trilayer actuator as a function of the frequency at an applied potential of  $\pm 2.0$  V is brought in **Figure 90**. The linear deformation of the actuator is decreasing when higher frequencies are applied. This is due to the charging of the electrodes. At lower frequency (0.02 Hz), the electrodes have enough time to fully charge and to reach the maximum available deformation (illustrated in the first inset of strain as a function of time). When the frequency is increased, the electrodes do not have enough time to fully charge and to reach the maximum available deformation, therefore the resulting linear deformation is decreasing (second inset of strain as a function of time). The response time of the resulting PEDOT:PSS linear actuator is not really high (which is expected in the case of ionic EAPs) but it is much faster compared to the previous macroscale linear actuator, where the deformation was not fully reached even after 600 second step ( $8 \times 10^{-4}$  Hz).<sup>[118]</sup> This result shows the huge benefit of the decreased thickness of the device which is allowed by the choice of these materials (PEDOT:PSS and ionic liquid containing semi-IPN) and the choice of the elaboration process.

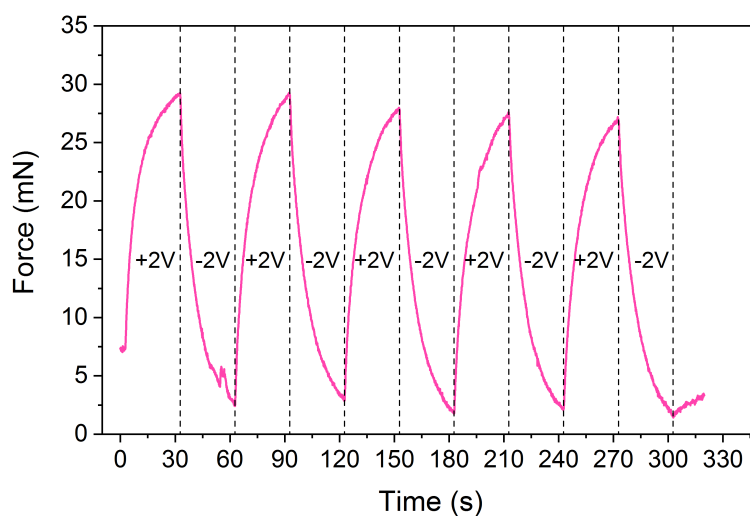


**Figure 90.** Linear strain as a function of the frequency of the asymmetrical trilayer linear actuator at an applied potential of  $\pm 2.0$  V. Negative linear strain corresponds to the contraction of the actuator during positive potential bias.

Finally, the obtained linear strain and volumetric charge density (in the previous subsection) were used to calculate the strain-to-charge ratio of the linear actuator. The resulting strain-to-charge ratio of the asymmetrical trilayer linear actuator is  $8.7 \pm 3.6 \times 10^{-11} \text{ m}^3 \cdot \text{C}^{-1}$ . This result is lower than for the separate electrodes ( $2.6 \times 10^{-10} \text{ m}^3 \cdot \text{C}^{-1}$  for the 40% PEO electrode and  $2.2 \times 10^{-10} \text{ m}^3 \cdot \text{C}^{-1}$  for the 40% PEO + EMImTFSI electrode), but can be explained by the fact that the electrodes are working against each other. As a consequence, it is not the free strain of the electrodes, but just the difference in the actuator configuration.

#### 5.5.3.4 Blocking force in open-air

The blocking force measurements were carried out using the same setup as for the linear strain experiments (**Figure 86**). The sample was stimulated by chronoamperometry ( $\pm 2.0$  V, step duration 30 s) in isometric mode and the resulting change in force was recorded by the Lever Arm System. The resulting blocking force is presented in **Figure 91**.



**Figure 91.** Blocking force as a function of time during  $\pm 2.0$  V stimulation of PEDOT:PSS/PEO(40%) (electrode 1)/100% EMIImTFSI PEO-NBR semi-IPN//PEDOT:PSS/PEO(40%)/EMIImTFSI (electrode 2) asymmetrical linear actuator.

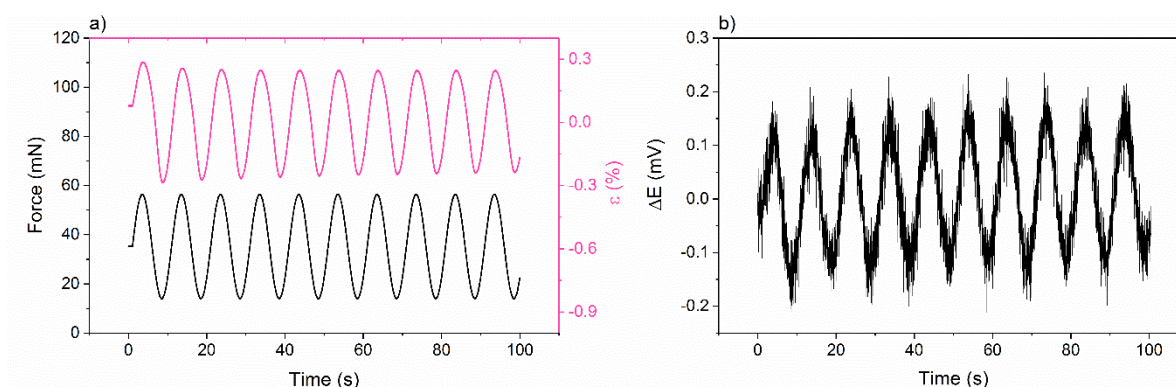
During redox process, when a positive potential is applied, the working electrode is oxidized, which results in contraction of the device and consequently in increase of the generated forces. On the opposite, when negative potential is applied, the working electrode expands and the generated forces decrease. The measured blocking force value of the asymmetric trilayer linear actuator is 0.3 MPa, corresponding to 25.8 mN. Additionally, a model was used to predict the theoretical blocking force value and to compare the result with the experimental value. The model and the predictions with comparison are presented in the Appendix 3, section A.3.5.

### 5.5.3.5 Sensing behavior of the linear electroactive materials

#### 5.5.3.5.1 Experiments & results

The skeletal muscles present also sensing feature, allowing them to sense every moment their own position and to develop work. This feature is called proprioception. The skeletal muscles are composed of bundles of fibers, where the functional unit of contraction is myofibril which in turn is composed of hundreds of protein filaments, responsible for the signal transduction. As an inspiration of the skeletal muscles, it appears interesting to evaluate if the materials developed in this chapter can also behave as linear strain sensors. This behavior would open promising perspective in the development of biomimetic artificial muscles. For this purpose, the sensing experiments of the linear actuators were performed.

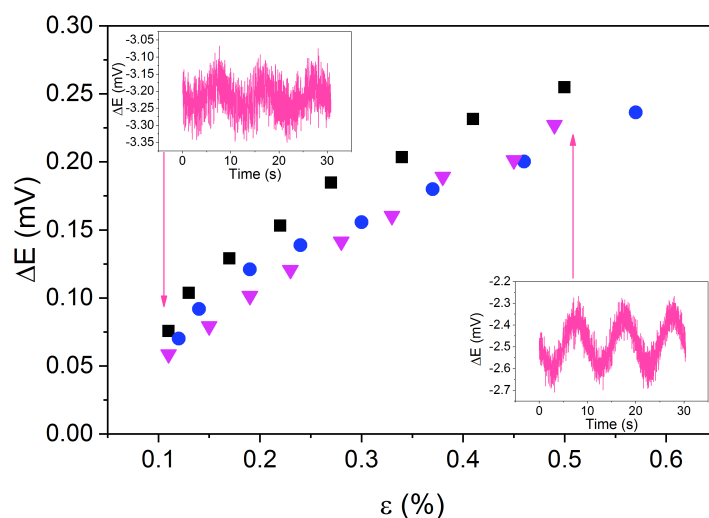
The experimental setup was used as for all the other characterizations, demonstrated in **Figure 86**. One end of the actuator was connected to the potentiostat and the other end to the Aurora Muscle Lever Arm System (300 C) with a pre-stress of 0.4 MPa. For sensor experiments, the linear device was mechanically stimulated (force controlled sinusoidal displacement at a frequency of 0.1 Hz) by the Lever Arm System and the resulting open circuit voltage (OCV) was recorded. The applied force with corresponding strain and resulting OCV response are brought in **Figure 92**. When the load is increased, the sample is elongating producing positive deformation and strain. On the opposite, when the load is decreased, the sample is shortening and resulting in negative deformation and strain. The external mechanical stimulation is resulting in electrical energy output, proving the possibility to detect linear stress/deformation and the existence of the sensing properties of these type linear actuators. The mechanical stimulation with approximately 0.5 % strain resulted in OCV response of 0.26 mV of this sample.



**Figure 92.** a) Applied force (mN) with corresponding strain (%) and b) resulting OCV response of the sensing experiments for linear actuators.

The response of the output voltage of the asymmetrical trilayer linear sensors as a function of the applied strain at a frequency of 0.1 Hz is brought in **Figure 93**. With lower applied strain (0.11 %), the signal of the output voltage is lower (0.07 mV) and noisier (illustrated in the first inset of  $\Delta E$  as a function of time). When the mechanical strain is increased then also the output voltage is increasing and the signal becomes smoother (the second inset of  $\Delta E$  as a function of time). The maximum value of  $0.23 \pm 0.03$  mV is obtained at an applied strain of approximately 0.5%. The values of linear sensing are in the same range (mV) with the results from the bending sensors in Chapter 3. These results demonstrate the possibility to detect and quantify the mechanical strain of the asymmetrical trilayer linear actuators.



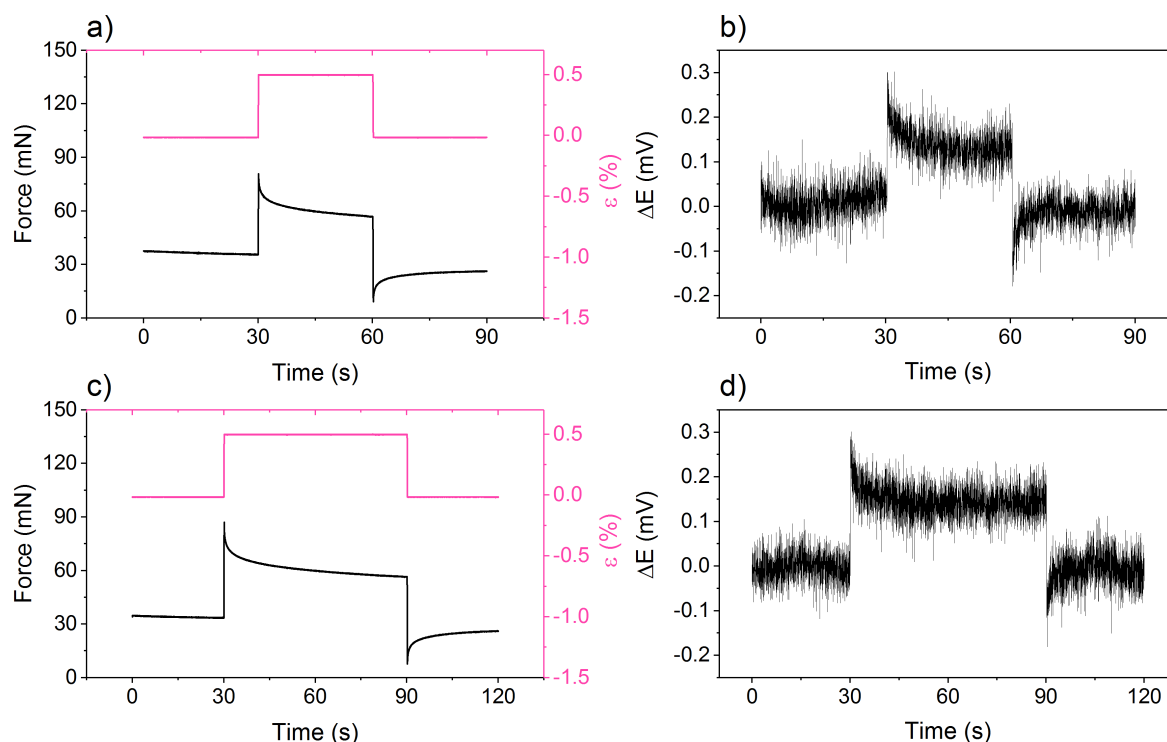


**Figure 93.** Open circuit voltage response to the sinusoidal mechanical stimulation as a function of applied strain at 0.1 Hz of three PEDOT:PSS asymmetrical trilayer linear sensors.

### 5.5.3.5.2 Discussion about the sensing mechanism

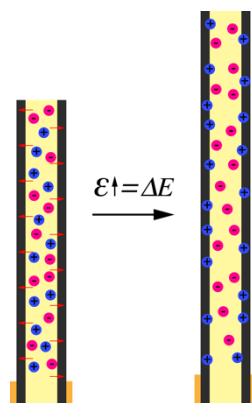
This section presents the asymmetric trilayer linear sensor output voltage signal as a function of given strain and discussion of possible sensing mechanism. Moreover, a model is used to predict the theoretical value of sensing. The sensing models for bending devices cannot be considered here, therefore a model dealing with linear deformation is used.

In order to evaluate the stability of the output signal for a given strain, the experiments were carried out by applying a step displacement and recording the OCV response. **Figure 94a** and **c** interpret the applied strain and measured force during 30 s and 1 min steps. Corresponding open circuit voltage responses are brought in **Figure 94b** and **d**. A voltage signal of approximately 0.15 mV is obtained with a small relaxation in the beginning, but afterwards the potential is relatively constant and reaching a plateau (figures **b** and **d**). The same behavior was observed by Shoa *et al.* with PPy freestanding films (immersed in 1 M sodium hexafluorophosphate aqueous solution), where the generated voltage did not decay significantly and remained quite constant during the square wave stress controlled mechanical stimulation.<sup>[207]</sup> It can be seen that the small relaxation in the beginning of the OCV measurement seems related the change in the force, when mechanical stimulation is applied.



**Figure 94.** Asymmetrical trilayer linear sensor output voltage response to the square wave mechanical stimulation with an applied step displacement (0.5 % strain corresponding to 43 mN) during 30 s and 1 min.

The same author proposed a model, explaining that the change in the potential is related to the insertion and expulsion of ions when stretching or compressing the polymer film. When external stress is applied, the polymer film is expanding and producing strain, consequently facilitating the access of ions. The energy of the ions inside the polymer film drops, because more ions flow in than leave. If the polymer is at open circuit potential, no net charge can enter or leave and the polymer becomes more positive if cations are mobile. The net insertion of the positive charge continues until the energy of both sides are equal. In other words, if the polymer film is stretched and the polymer chains expanded, it favors the presence of more ions, which in turn leads to the change in the voltage. As an example of this work, the sensors are composed of three layers and the presence of EMImTFSI is favoring the cation mechanism. Two different PEDOT:PSS/PEO electrodes are mechanically stretched at the same time, favoring the flow of cations into both electrodes and presenting positive voltage output (illustrated in **Figure 95**). If the trilayer linear actuator would have two identical electrodes, the output potential should be 0 mV.



**Figure 95.** Schematic illustration of the sensing mechanism based on external applied strain and ion movement.

The model of Shoa *et al.*, developed for immersed PPy freestanding films, was also used in this work to predict the theoretical value of the sensor voltage output according to the equation below:

$$V = -\sigma\alpha = -E\varepsilon\alpha \quad (24)$$

Where  $E$  and  $\alpha$  are the Young's modulus and the strain-to-charge ratio of the electrodes, respectively (determined previously) and  $\varepsilon$  is the applied mechanical strain (0.5 %). The output voltage was calculated for the two electrodes separately and the total output voltage value is considered as the difference between the values of both electrodes ( $V_{total} = V_1 - V_2$ ). During the sensor experiments, the Young's modulus of the electrodes should be at intermediate redox level, not fully oxidized nor fully reduced, making quite difficult to estimate the corresponding values. For that reason, the calculations were performed with three different sets of Young's modules:

1. Electrode 1 in oxidized state and electrode 2 in reduced state;
2. Electrode 1 in reduced state and electrode 2 in oxidized state;
3. Both electrodes in open-air

The resulting output voltage value  $V_{total}$  for the first, second and third combinations are 0.61 mV, 0.46 mV and 1.23 mV, respectively. While the linear strain prediction with the open-air Young's modules was closer to the experimental values, it can be seen that the output voltage prediction is closer to the experimental values with the Young's modules as a function of the redox level. Nevertheless, it is unfortunately difficult to make a conclusion which is the most accurate value for the prediction, due to the unknown Young's modulus of different electrodes during the sensor experiments. Regardless the predictions, the experimental value

of 0.23 mV (with an applied strain of approximately 0.5 %) is notably lower compared to these different predictions. However, the sign of the prediction is corresponding to the experiments. Positive applied mechanical strain results in positive voltage variation and on the opposite, negative applied mechanical strain results in negative voltage variation. The existence of two electrodes and stretching them at the same time, causing cation insertion into both electrodes simultaneously might affect the final output voltage due to the counteraction of the electrodes.

The sensing experiments of the asymmetric linear actuators demonstrated the possibility to detect and quantify linear deformation and proving the existence of the sensing properties. The maximum value of 0.23 mV was obtained when with an applied strain of approximately 0.5 %. The sensing ability of these materials could make them interesting for the development of biomimetic artificial muscles.

## 5.6 Conclusion

This chapter described efficient and simple process to fabricate linear actuators. The electromechanical model of Fannir was used to predict the linear deformation and to choose the best combination of electrodes for the asymmetrical trilayer linear actuator fabrication. The first part described the synthesis and characterization of the PEDOT:PSS/PEO composite electrodes to obtain all the necessary parameters for the model. The second part introduced the possibility to integrate ionic liquid directly into the ion reservoir membrane (semi-IPN) as a co-solvent and presented the fabrication method and characterization results. Moreover, the electromechanical model was adjusted in order to consider the Young's modulus values of the electrodes as a function of the redox level to predict the corresponding linear deformations in elongated and contracted state. The trilayer linear actuator PEDOT:PSS/PEO(40%) (electrode 1)//100% EMImTFSI PEO-NBR semi-IPN//PEDOT:PSS/PEO(40%)/EMImTFSI (electrode 2) was successfully fabricated using layer stacking method which does not require any manual handling compared to the previous method (masking, washing, external swelling). As synthesized, these linear actuators resulted in 0.51 % deformation, 25.8 mN generated forces and demonstrated improvement in response time, especially compared to the previous generation linear actuators. More interestingly, the sensing ability of these linear actuators was demonstrated on devices with a thickness less than 50  $\mu\text{m}$ , resulting in maximum generated voltages of 0.23 mV, making them attractive for biomimetic artificial muscles. The layer stacking method and chosen materials

(PEDOT:PSS and semi-IPN with EMImTFSI directly included) allow the fabrication and characterization of the devices in one day, also being compatible with microfabrication technologies. These thin linear actuators could be even parallelized and combined with sensing fibers in order to increase the generated forces and to develop proprioceptive artificial muscles based on fiber bundles.

## Conclusions and perspectives

## Conclusions

The work of this thesis was focused on the design, characterization and integration of microactuators based on electronically conductive polymers (ECPs). The goal of the thesis was to obtain efficient microactuators with simple, reproducible and microfabrication compatible method in order to integrate them into soft microsystems. To the best of our knowledge, this is the first time that the development of ECP based microactuators and microsensors was demonstrated with two integrated bottom and top electrical contacts on a flexible substrate, making them attractive for the development of efficient soft Micro-Electro-Mechanical Systems (MEMS).

The first experimental part of this work was focused on improving the recently developed microactuators fabricated with layer stacking method. This process demonstrated a promising method to fabricate microactuators directly on a flexible substrate with one electrical contact and without any manual handling, which is a necessary requirement for microfabrication. However, the resulting microactuators resulted in low performances (maximum strain 0.13 % and maximum output force 0.75  $\mu\text{N}$  under  $\pm 4.0$  V) which could be improved. For that reason, a study as a function of different parameters of vapor phase polymerized (VPP) poly(3,4-ethylenedioxythiophene) (PEDOT) electrodes was performed. Thus, the effect of iron(III)tosylate content in butanol, EMImTFSI content, mPEG content, polymerization time and temperature and rotation speed of spin-coating was investigated to enhance the electrical and electrochemical properties of the PEDOT electrodes. The microactuators were fabricated in collaboration with Tan N. Nguyen (ESR in MICACT project, IEMN) with optimized electrode parameters. These microactuators presented improvement in performances (maximum strain 0.5 % and maximum output force 11  $\mu\text{N}$  under  $\pm 1.5$  V) compared to the previous layer stacked fabricated microactuators. These results were published in *Electrochimica Acta* in 2018.

The second part of this work was dedicated to further improve the fabrication of layer stacked microactuators. The previous method and the use of VPP PEDOT electrodes require washing step to remove the oxidant and the residuals of the EDOT monomer, which is poorly compatible with microfabrication process and limiting the integration of these materials into microsystems. For that reason, already synthesized electroactive material as poly(3,4-ethylenedioxythiophene):poly(styrene sulfonate) (PEDOT:PSS) commercial dispersion was



chosen as a new electrode material for the fabrication of microactuators. Polar reactive additives based on poly(ethylene oxide) (PEO) were chosen to improve the poor electrical, electrochemical and mechanical properties, common for pristine PEDOT:PSS. The incorporation of PEO was expected to improve the electronic conductivity of the resulting electrodes. More importantly, due to the well-known ionic transport properties of PEO it was expected to facilitate the ion exchanges between the PEDOT and the electrolyte and consequently to increase the electroactivity of the resulting electrodes. Moreover, the incorporation of PEO reactive additives was expected to give a rise for the PEO network formation within the PEDOT:PSS electrodes and to improve the mechanical properties of the resulting electrodes. The electrical and electrochemical properties of the PEDOT:PSS electrodes were studied as a function of the PEO content to find the optimum content for microactuator fabrication. The electrode containing 40% PEO (vs final mass of the electrode) was chosen as the composite electrode for the microactuator fabrication. The synthesis of trilayer actuators was performed with modified layer stacking method, followed by laser patterning to obtain PEDOT:PSS based microactuators. These PEDOT:PSS/PEO microactuators presented even further improvement of layer stacked fabricated microactuators (maximum strain 0.82 % and maximum output force 472  $\mu\text{N}$  under  $\pm 2.2$  V). More importantly, the mechanical sensing behavior was demonstrated for the first time at microscale and presented enhancement of the sensitivity compared to the macroscale ECP based actuators (maximum output voltage 0.42 mV at 0.5 % strain). Additionally, the use of PEDOT:PSS allows to remove the washing step from the layer stacking fabrication process, making it fully compatible for the microfabrication process. The work of this chapter is submitted for a publication.

The next part of this manuscript demonstrated full microsystem process to integrate previously elaborated PEDOT:PSS based microactuators into microsystems with two electrical contacts directly on a flexible substrate without any manual handling during the process. The microfabrication process was realized by combining different microfabrication technologies (photolithography, etching, metal evaporation) and the microsystems were developed by reversing the steps, i.e. fabricating the microactuators first and finally encapsulating them into SU-8 to obtain the flexible support. The resulting process allows the fabrication of microsystems with different configurations and designs, for example, the realization of actuator-sensor microsystem with two separate pairs of electrical contacts. The resulting microsystems demonstrated maximum strain of 0.66 % and maximum output force

of 105  $\mu\text{N}$  under  $\pm 3.0$  V. Additionally, the mechanical sensing behavior was demonstrated for the first time for microsystems with integrated electrical contacts, resulting in maximum output voltage of 0.35 mV at 0.34 % strain. The work of this chapter will be the focus of another publication which is under preparation.

The last part of this manuscript described the development of PEDOT:PSS based linear actuators. First, the study on PEDOT:PSS based electrodes was performed to determine the electromechanical properties as a function of the redox level. Based on previously described electromechanical model, PEDOT:PSS electrodes with different mechanical and electrochemical properties were combined in order to develop open-air linear actuators. The use of PEDOT:PSS does not require washing step which allowed the introduction of the electrolyte (EMImTFSI) directly either in the electrode fabrication or during the synthesis of ionically conducting membrane. The linear actuators were successfully fabricated using layer stacking method and presented maximum strain of 0.5 % and maximum output force of 25.8 mN. Additionally, linear strain sensing of these materials was demonstrated (maximum output voltage 0.23 mV at a strain of 0.5 %) making them attractive for the development of multifiber artificial muscles. The work of this chapter will be the focus of another publication.

The performances of these microactuators are gathered and summarized in the following table.

Type of actuator	Strain (%)	Output force ( $\mu\text{N}$ )	Sensing abilities (OCV - corresponding strain)	Process facility
Previously described layer stacking method <sup>[139]</sup> VPP based PEDOT microactuator	0.13	0.75	Not determined	-
This work VPP based PEDOT microactuator	0.5	11	Not determined	-
This work PEDOT:PSS based microactuator	0.82	475	0.42 mV – 0.5%	++
This work Integrated PEDOT:PSS based micractuator	0.66	105	0.37 mV – 0.34%	+
Previously described fabrication method <sup>[118]</sup> Linear actuator	0.55 (600 s)	40 000	Not determined	-
This work Linear actuator	0.5 (30 s)	25 800	0.23mV – 0.5%	+++

Additionally, to the work described in this manuscript, I had the opportunity to collaborate on side projects which resulted in 2 publications:

1. Inga Põldsalu, Kätlin Rohtlaid, Tran Minh Giao Nguyen, Cedric Plesse, Frédéric Vidal, Mahdi Safaei Khorram, Anna-Liisa Peikolainen, Tarmo Tamm, Rudolf Kiefer, “Thin ink-jet printed trilayer actuators composed of PEDOT:PSS on interpenetrating polymer networks”, *Sensors and Actuators B: Chemical*, 2018
2. Tien Anh Nguyen, Chia-Ju Peng, Katlin Rohtlaid, Cedric Plesse, Tran-Minh Giao Nguyen, Frederic Vidal, Shih-Jui Chen, Luc Chassagne, Barthelemy Cagneau , “Conducting interpenetrating Polymer Network to Sense and Actuate: Measurements and Modeling” *Sensors and Actuators A: physical*, 2018

## Perspectives

The use of PEDOT:PSS as an electrode material is relatively new in the field of ECP based microactuators. This commercial dispersion allows simple and reproducible way of microactuator fabrication, making them more attractive for different applications. However, there are still some challenges and possible improvements for obtaining efficient microsystems:

- The use of PEDOT:PSS allows wide range of possibilities to tune the electrical, electrochemical and mechanical properties of the electrodes. High electrical and electrochemical properties of the PEDOT:PSS electrodes are the key factors for obtaining efficient microactuators. The study on electrical and electrochemical properties of the PEDOT:PSS electrodes with different additives could allow to improve the performances even further, resulting in improved performances of the bending and linear type actuators.
- The sensing property of the microactuators was demonstrated but further investigation is required in order to allow better understanding of the sensing mechanism. PEDOT and PPy based actuators have been investigated more thoroughly, but in general, there is no common accepted mechanism considering ECP based devices even at macroscale. The study in this manuscript demonstrated that PEDOT:PSS based devices produced different sensing signal compared to the PEDOT and PPy related

devices. Therefore, more thorough investigation is needed to understand better these effects.

- The developed microfabrication process allowed the fabrication of microactuators with integrated electrical contacts on a flexible substrate. The first characterization of the microsystems was performed in order to demonstrate that the microfabrication process does not damage the resulting microbeams extensively. Different microsystems with different beam dimensions (length and width) were characterized, but overall in-depth characterization is needed for these microsystems to conclude the results on the strain, blocking force and sensing, based on the device geometries.
- It was demonstrated that these microdevices can behave as microactuators or microsensors. The microdevice with combined actuator + sensor system requires further investigation in order to conclude the proprioception ability. First, the electrical connections should be tested to verify if some shielding or electrical ground could solve the problem. Another way would be the optimization of the geometry and to increase the distance between the electrical contacts or the overall size of the microdevice to overcome these challenges.
- The possibility of the development of PEDOT:PSS based linear actuators was performed but the next step would be to decrease the dimensions of the actuators and to evaluate the performances at microscale. The thickness of the resulting actuators (~ 50  $\mu\text{m}$ ) can be decreased easily by adjusting the volume of the casted solution and increasing the rotation speed of the spin-coater. Other dimensions (length and width) can be decreased using laser patterning for obtaining linear microactuators. As mentioned before, a study on different PEDOT:PSS electrode compositions could allow also to improve the performances of the resulting linear actuators. These linear actuators demonstrated sensing properties, but also proprioception should be studied. Further assembly of these devices can be one step closer for the development of multifiber artificial muscles.
- In the framework of this thesis, ionic liquid (EMImTFSI) was used as an electrolyte for all the actuators. The last chapter demonstrated the possibility of including the electrolyte directly during the synthesis, but in general, external swelling was used. External swelling can induce volume changes of the microactuators and consequently cause delamination of the electrical contacts of the microsystems. The membrane with EMImTFSI directly included could possibly overcome this issue, but all the

microfabrication process steps could partially remove the included EMImTFSI due to different development steps. As a consequence, the ions necessary for the redox process, could be removed during processing steps. Ideally, true solid polymer electrolyte (SPE) based on poly(ionic liquid), containing necessary ions and being resistant for all the microfabrication process steps is required to develop fully dry-state efficient microsystems.



## References

- [1] Y. Bar-Cohen, *19th AIAA Appl. Aerodyn. Conf.* **2001**.
- [2] Y. Bar-Cohen, *Electroactive Polymer (EAP) Actuators as Artificial Muscles: Reality, Potential, and Challenges. Second Edition*, **2004**.
- [3] R. Pelrine, R. Kornbluh, Q. Pei, J. Joseph, *Science (80- )*. **2000**, 287, 836.
- [4] H. S. Nalwa, *Ferroelectric Polymers - Chemistry, Physics and Applications*, **1995**.
- [5] V. D. Kugel, B. Xu, Q. M. Zhang, L. E. Cross, *Sensors Actuators, A Phys.* **1998**, 69, 234.
- [6] J. Y. Li, N. Rao, *J. Mech. Phys. Solids* **2004**, 52, 591.
- [7] R. H. Baughman, *Makromol. Chem., Mocomol. Symp.* **1991**, 51, 193.
- [8] Y. Osada, J. Gong, *Prog. Polym. Sci.* **1993**, 18, 187.
- [9] P. Calvert, J. O'Kelly, C. Souvignier, *Mater. Sci. Eng. C* **1998**, 6, 167.
- [10] R. H. Baughman, *Synth. Met.* **1996**, 78, 339.
- [11] E. W. H. Jager, E. Smela, O. Inganäs, *Science* **2000**, 290, 1540.
- [12] M. Shahinpoor, Y. Bar-Cohen, O. J. Simpson, J. Smith, *Smart Mater. Struct.* **1998**, 7.
- [13] R. H. Baughman, C. Cui, A. A. Zakhidov, Z. Iqbal, J. N. Barisci, G. M. Spinks, G. G. Wallace, A. Mazzoldi, D. De Rossi, A. G. Rinzler, O. Jaschinski, S. Roth, M. Kertesz, *Science (80- )*. **1999**, 284, 1340.
- [14] T. Sugino, K. Kiyohara, I. Takeuchi, K. Mukai, K. Asaka, *Sensors Actuators, B Chem.* **2009**, 141, 179.
- [15] I. Takeuchi, K. Asaka, K. Kiyohara, T. Sugino, N. Terasawa, K. Mukai, T. Fukushima, T. Aida, *Electrochim. Acta* **2009**, 54, 1762.
- [16] R. Dash, J. Chmiola, G. Yushin, Y. Gogotsi, G. Laudisio, J. Singer, J. Fischer, S. Kucheyev, *Carbon N. Y.* **2006**, 44, 2489.
- [17] J. Torop, M. Arulepp, J. Leis, A. Punning, U. Johanson, V. Palmre, A. Aabloo, *Materials (Basel)*. **2010**, 3, 9.
- [18] H. Shirakawa, E. J. Louis, S. C. Gau, A. G. MacDiarmid, C. K. Chiang, C. R. Fincher, Y. W. Park, A. J. Heeger, *Phys. Rev. Lett.* **1977**, 39, 1098.
- [19] A. J. Heeger, A. G. MacDiarmid, H. Shirakawa, *Stock. Sweden R. Swedish Acad. Sci.* **2000**.
- [20] A. G. MacDiarmid, *Synth. Met.* **2002**, 125, 11.
- [21] J. L. Brédas, J. C. Scott, K. Yakushi, G. B. Street, **1984**, 30, 1023.
- [22] J. L. Brédas, G. B. Street, *Acc. Chem. Res.* **1985**, 18, 309.
- [23] T. C. Chung, J. H. Kaufman, A. J. Heeger, F. Wudl, *Phys. Rev. B* **1984**, 30, 702.
- [24] H. Naarmann, N. Theophilou, *Synth. Met.* **1987**, 22, 1.
- [25] P. N. Adams, P. Devasagayam, S. J. Pomfret, L. Abell, A. P. Monkman, *J. Phys. Condens. Matter* **1998**,

- 10, 8293.
- [26] Y. Nogami, J. P. Pouget, T. Ishiguro, *Synth. Met.* **1994**, *62*, 257.
- [27] R. D. McCullough, S. P. Williams, R. D. Lowe, M. Jayaraman, S. Tristram-Nagle, *J. Am. Chem. Soc.* **1993**, *115*, 4910.
- [28] B. Winther-Jensen, D. W. Breiby, K. West, *Synth. Met.* **2005**, *152*, 1.
- [29] M. R. Gandhi, P. Murray, G. M. Spinks, G. G. Wallace, *Synth. Met.* **1995**, *73*, 247.
- [30] Q. Pei, O. Inganäs, *Solid State Ionics* **1993**, *60*, 161.
- [31] T. F. Otero, H. Grande, J. Rodriguez, *J. Phys. Org. Chem.* **1996**, *9*, 381.
- [32] Y. Qiu, J. R. Reynolds, *Polym. Eng. Sci.* **1991**, *31*, 417.
- [33] C. Lopez, M. F. M. Viegas, G. Bidan, E. Vieil, *Synth. Met.* **1994**, *63*, 73.
- [34] Q. Pei, O. Inganäs, *J. Phys. Chem.* **1992**, *96*, 10507.
- [35] T. Matencio, M. A. De Paoli, R. C. D. Peres, R. M. Torresi, S. I. Cordoba de Torresi, *Synth. Met.* **1995**, *72*, 59.
- [36] R. Temmer, A. Maziz, C. Plesse, A. Aabloo, F. Vidal, T. Tamm, *Smart Mater. Struct.* **2013**, *22*.
- [37] Y. Sonoda, W. Takashima, K. Kaneto, *Synth. Met.* **2001**, *119*, 267.
- [38] B. Qi, W. Lu, B. R. Mattes, *J. Phys. Chem. B* **2004**, *108*, 6222.
- [39] H. Okuzaki, T. Kondo, T. Kunugi, *Polymer (Guildf)*. **1999**, *40*, 995.
- [40] J. D. W. Madden, *Massachusetts Inst. Technol.* **1991**.
- [41] A. Elschner, S. Kirchmeyer, W. Lövenich, U. Merker, K. Reuter, *PEDOT - Principles and Applications of an Intrinsically Conductive Polymer*, **2011**.
- [42] R. Temmer, I. Must, F. Kaasik, A. Aabloo, T. Tamm, *Sensors Actuators B Chem.* **2012**, *166–167*, 411.
- [43] F. Vidal, J. F. Popp, C. Chevrot, D. Teyssié, *Smart Struct. Mater. 2002 Electroact. Polym. Actuators Devices* **2002**, *4695*, 95.
- [44] A. Mohammadi, M. A. Hasan, B. Liedberg, I. Lundström, W. R. Salaneck, *Synth. Met.* **1986**, *14*, 189.
- [45] L. Groenendaal, F. Jonas, D. Freitag, H. Pielartzik, J. R. Reynolds, *Adv. Funct. Mater.* **2000**, *12*, 481.
- [46] Y. Wang, C. Zhu, R. Pfattner, H. Yan, L. Jin, S. Chen, F. Molina-Lopez, F. Lissel, J. Liu, N. I. Rabiah, Z. Chen, J. W. Chung, C. Linder, M. F. Toney, B. Murmann, Z. Bao, *Sci. Adv.* **2017**, *3*, e1602076.
- [47] T. A. Skotheim, J. R. Reynolds, *Handbook of Conducting Polymers, Third Edition*, **2007**.
- [48] F. Louwet, L. Groenendaal, J. Dhaen, J. Manca, J. Van Luppen, E. Verdonck, L. Leenders, *Synth. Met.* **2003**, *135–136*, 115.
- [49] N. Kim, S. Kee, S. H. Lee, B. H. Lee, Y. H. Kahng, Y. R. Jo, B. J. Kim, K. Lee, *Adv. Mater.* **2014**, *26*, 2268.
- [50] Y. Xia, K. Sun, J. Ouyang, *Adv. Mater.* **2012**, *24*, 2436.



- [51] M. Cai, Z. Ye, T. Xiao, R. Liu, Y. Chen, R. W. Mayer, R. Biswas, K. M. Ho, R. Shinar, J. Shinar, *Adv. Mater.* **2012**, *24*, 4337.
- [52] Z. Zhao, G. F. Richardson, Q. Meng, S. Zhu, H. C. Kuan, J. Ma, *Nanotechnology* **2016**, *27*, 42001.
- [53] H. Yan, T. Jo, H. Okuzaki, *Polym. J.* **2009**, *41*, 1028.
- [54] H. Okuzaki, H. Suzuki, T. Ito, *Synth. Met.* **2009**, *159*, 2233.
- [55] A. Simate, B. Tondou, P. Souères, C. Bergaud, *ACS Appl. Mater. Interfaces* **2015**, *7*, 19966.
- [56] A. Simate, F. Mesnilgrente, B. Tondou, P. Souères, C. Bergaud, *Sensors Actuators, B Chem.* **2016**, *229*, 425.
- [57] I. Põldsalu, K. Rohtlaid, T. Minh, G. Nguyen, C. Plesse, F. Vidal, M. S. Khorram, A. Peikolainen, T. Tamm, R. Kiefer, *Sensors Actuators B. Chem.* **2017**.
- [58] J. Huang, P. F. Miller, J. C. De Mello, A. J. De Mello, D. D. C. Bradley, *Synth. Met.* **2003**, *139*, 569.
- [59] A. Moujoud, S. H. Oh, H. S. Shin, H. J. Kim, *Phys. Status Solidi Appl. Mater. Sci.* **2010**, *207*, 1704.
- [60] J. Y. Kim, J. H. Jung, D. E. Lee, J. Joo, *Synth. Met.* **2002**, *126*, 311.
- [61] C. Badre, L. Marquant, A. M. Alsayed, L. A. Hough, *Adv. Funct. Mater.* **2012**, *22*, 2723.
- [62] B. Fan, X. Mei, J. Ouyang, *Macromolecules* **2008**, *41*, 5971.
- [63] Y. Xia, J. Ouyang, *Org. Electron. physics, Mater. Appl.* **2010**, *11*, 1129.
- [64] Y. Xia, H. Zhang, J. Ouyang, *J. Mater. Chem.* **2010**, *20*, 9740.
- [65] Y. Xia, J. Ouyang, *ACS Appl. Mater. Interfaces* **2010**, *2*, 474.
- [66] U. Lang, E. Muller, N. Naujoks, J. Dual, *Adv. Funct. Mater.* **2009**, *19*, 1215.
- [67] R. H. Baughman, L. W. Shacklette, R. L. Elsenbaumer, E. J. Plichta, C. Becht, *Conjugated Polymeric Materials: Opportunities in Electronics, Optoelectronics, and Molecular Electronics*, **1990**.
- [68] P. Chiarelli, D. De Rossi, A. Della Santa, A. Mazzoldi, *Polym. Gels Networks* **1994**, *2*, 289.
- [69] M. Kaneko, M. Fukui, W. Takashima, K. Kaneto, *Synth. Met.* **1997**, *84*, 795.
- [70] E. Smela, O. Inganäs, Q. Pei, I. Lundström, *Adv. Mater.* **1993**, *5*, 630.
- [71] E. W. H. Jager, O. Inganäs, I. Lundström, *Science (80-. )*. **2000**, *288*, 2335.
- [72] T. F. Otero, J. Rodríguez, *Intrinsically Conducting Polymers: An Emerging Technology*, **1992**.
- [73] S. J. Higgins, K. V. Lovell, R. M. Gamini Rajapakse, N. M. Walsby, *J. Mater. Chem.* **2003**, *13*, 2485.
- [74] S. D. Deshpande, J. Kim, S. R. Yun, *Synth. Met.* **2005**, *149*, 53.
- [75] S. D. Deshpande, J. Kim, S. R. Yun, *Smart Mater. Struct.* **2005**, *14*, 876.
- [76] G. Alici, A. Punning, H. R. Shea, *Sensors Actuators B Chem.* **2011**, *151*, 72.
- [77] T. F. Otero, E. Angulo, J. Rodríguez, C. Santamaría, *J. Electroanal. Chem.* **1992**, *341*, 369.
- [78] Q. Pei, O. Inganas, *Adv. Mater.* **1992**, *4*, 227.

- [79] T. F. Otero, J. M. Sansinena, J. M. Sansiñena, *Bioelectrochemistry Bioenerg.* **1995**, 38, 411.
- [80] M. Kaneko, K. Kaneto, *React. Funct. Polym.* **1998**, 37, 155.
- [81] E. Smela, O. Inganäs, I. Lundström, *Science (80- )*. **1995**, 268, 1735.
- [82] E. Smela, *J. micromechanics microengineering* **1999**, 9, 1.
- [83] M. Fuchiwaki, T. F. Otero, *J. Mater. Chem. B* **2014**, 2, 1954.
- [84] T. F. Otero, J. G. Martinez, *Sensors Actuators, B Chem.* **2014**, 199, 27.
- [85] Q. Pei, O. Inganäs, G. Gustafsson, M. Granström, *Synth. Met.* **1993**, 55, 1221.
- [86] J. M. Sansinena, V. Olazabal, T. F. Otero, C. N. Polo da Fonseca, M. A. De Paoli, *Chem. Commun.* **1997**, 2217.
- [87] T. W. Lewis, L. A. P. Kane-Maguire, A. S. Hutchison, G. M. Spinks, G. G. Wallace, *Synth. Met.* **1999**, 102, 1317.
- [88] W. Lu, A. G. Fadeev, B. Qi, E. Smela, B. R. Mattes, J. Ding, G. M. Spinks, J. Mazurkiewicz, D. Zhou, G. G. Wallace, D. R. MacFarlane, S. A. Forsyth, M. Forsyth, *Science (80- )*. **2002**, 297, 983.
- [89] D. Zhou, G. M. Spinks, G. G. Wallace, C. Tiypiboonchaiya, D. R. MacFarlane, M. Forsyth, J. Sun, *Electrochim. Acta* **2003**, 48, 2355.
- [90] F. Vidal, J. F. Popp, C. Plesse, C. Chevrot, D. Teyssié, *J. Appl. Polym. Sci.* **2003**, 90, 3569.
- [91] M. Khayet, T. Matsuura, *Ind. Eng. Chem. Res.* **2001**, 40, 5710.
- [92] X. Wang, C. Xiao, H. Liu, Q. Huang, H. Fu, *J. Appl. Polym. Sci.* **2018**, 135.
- [93] M. Qtaishat, T. Matsuura, B. Kruczek, M. Khayet, *Desalination* **2008**, 219, 272.
- [94] G. Li, Z. Li, P. Zhang, H. Zhang, Y. Wu, *Pure Appl. Chem.* **2008**, 80, 2553.
- [95] X. Tang, R. Muchakayala, S. Song, Z. Zhang, A. R. Polu, *J. Ind. Eng. Chem.* **2016**, 37, 67.
- [96] M. S. Cho, H. J. Seo, J. D. Nam, H. R. Choi, J. C. Koo, K. G. Song, Y. Lee, *Sensors Actuators, B Chem.* **2006**, 119, 621.
- [97] M. S. Cho, H. J. Seo, J. D. Nam, H. R. Choi, J. C. Koo, Y. Lee, *Smart Mater. Struct.* **2007**, 16.
- [98] H. J. Choi, Y. M. Song, I. Chung, K. S. Ryu, N. J. Jo, *Smart Mater. Struct.* **2009**, 18.
- [99] Y. Li, R. Tanigawa, H. Okuzaki, *Smart Mater. Struct.* **2014**, 23.
- [100] H. Okuzaki, S. Takagi, F. Hishiki, R. Tanigawa, *Sensors Actuators, B Chem.* **2014**, 194, 59.
- [101] D. Klempner, L. H. Sperling, L. . Utracki, in *Adv. Chem. Ser.*, **1994**.
- [102] A. D. Jenkins, P. Kratochvíl, R. F. T. Stepto, U. W. Suter, *Pure Appl. Chem.* **1996**, 68.
- [103] C. Plesse, F. Vidal, C. Gauthier, J. M. Pelletier, C. Chevrot, D. Teyssié, *Polymer (Guildf)*. **2007**, 48, 696.
- [104] C. Gauthier, C. Plesse, F. Vidal, J. M. Pelletier, C. Chevrot, D. Teyssié, *Polymer (Guildf)*. **2007**, 48, 7476.

- [105] C. Plesse, A. Khaldi, Q. Wang, E. Cattan, D. Teyssié, C. Chevrot, F. Vidal, *Smart Mater. Struct.* **2011**, *20*.
- [106] N. Festin, C. Plesse, P. Pirim, C. Chevrot, F. Vidal, *Sensors Actuators, B Chem.* **2014**, *193*, 82.
- [107] K. Kaneto, H. Saito, Y. Min, A. G. MacDiarmid, *Polym. Mater. Sci. Eng.* **1994**, 713.
- [108] K. Kaneto, M. Kaneko, Y. Min, A. G. MacDiarmid, *Synth. Met.* **1995**, *71*, 2211.
- [109] P. Bonhôte, A.-P. Dias, N. Papageorgiou, K. Kalyanasundaram, M. Grätzel, *Inorg. Chem.* **1996**, *35*, 1168.
- [110] M. Galiński, A. Lewandowski, I. Stepniak, *Electrochim. Acta* **2006**, *51*, 5567.
- [111] J. Ding, D. Zhou, G. Spinks, G. Wallace, S. Forsyth, M. Forsyth, D. MacFarlane, *Chem. Mater.* **2003**, *15*, 2392.
- [112] F. Vidal, C. Plesse, D. Teyssié, C. Chevrot, *Synth. Met.* **2004**, *142*, 287.
- [113] B. Gaihre, G. Alici, G. M. Spinks, J. M. Cairney, *Sensors Actuators, B Chem.* **2011**, *155*, 810.
- [114] F. Vidal, C. Plesse, H. Randriamahazaka, D. Teyssie, C. Chevrot, *Mol. Cryst. Liq. Cryst.* **2006**, *448*.
- [115] H. Randriamahazaka, C. Plesse, F. Vidal, C. Gauthier, C. Chevrot, D. Teyssie, *Smart Struct. Mater. 2004 Electroact. Polym. Actuators Devices* **2004**, 5385, 294.
- [116] C. Plesse, F. Vidal, D. Teyssie, C. Chevrot, *Adv. Sci. Technol.* **2008**, *61*, 53.
- [117] N. Festin, A. Maziz, C. Plesse, D. Teyssié, C. Chevrot, F. Vidal, *Smart Mater. Struct.* **2013**, *22*, 104005.
- [118] A. Fannir, R. Temmer, G. T. M. Nguyen, L. Cadiegues, E. Laurent, J. D. W. Madden, F. Vidal, C. Plesse, *Adv. Mater. Technol.* **2018**, *1800519*, 1800519.
- [119] V. Woehling, G. T. M. Nguyen, C. Plesse, S. Cantin, J. D. W. Madden, F. Vidal, *Sensors Actuators B Chem.* **2017**.
- [120] R. H. Baughman, L. W. Shacklette, R. L. Elsenbaumer, E. J. Plichta, C. Becht, *Mol. Electron.* **1991**, 267.
- [121] E. Smela, M. Kallenbach, J. Holdenried, *J. Microelectromechanical Syst.* **1999**, *8*, 373.
- [122] E. W. H. Jager, E. Smela, O. Inganäs, *Sensors Actuators, B Chem.* **1999**, *56*, 73.
- [123] P. F. Pettersson, E. W. H. Jager, O. Inganäs, *1st Annu. Int. IEEE-EMBS Spec. Top. Conf. Microtechnologies Med. Biol. Proc. (Cat. No.00EX451)* **2000**, *56*, 1999.
- [124] E. W. H. Jager, C. Immerstrand, K. H. Peterson, K. E. Magnusson, I. Lundström, O. Inganäs, *Biomed. Microdevices* **2002**, *4*, 177.
- [125] C. Immerstrand, E. W. H. Jager, K.-E. Magnusson, T. Sundqvist, I. Lundström, O. Inganäs, K. H. Peterson, *Med. Biol. Eng. Comput.* **2003**, *41*, 357.
- [126] S. Taccola, F. Greco, B. Mazzolai, V. Mattoli, E. W. H. Jager, *J. Micromechanics Microengineering* **2013**, 23.
- [127] G. Alici, M. J. Higgins, *Smart Mater. Struct.* **2009**, *18*, 065013.
- [128] B. Gaihre, G. Alici, G. M. Spinks, J. M. Cairney, *Sensors Actuators, A Phys.* **2010**, *165*, 321.

- [129] B. Gaihre, G. Alici, G. M. Spinks, J. M. Cairney, *J. Microelectromechanical Syst.* **2012**, *21*, 574.
- [130] E. W. H. Jager, N. Masurkar, N. F. Nworah, B. Gaihre, G. Alici, G. M. Spinks, *Sensors Actuators, B Chem.* **2013**, *183*, 283.
- [131] A. Khaldi, C. Plesse, C. Soyer, E. Cattan, F. Vidal, C. Legrand, D. Teyssié, *Appl. Phys. Lett.* **2011**, *98*.
- [132] A. Khaldi, C. Plesse, C. Soyer, C. Chevrot, D. Teyssié, F. Vidal, E. Cattan, *Proc. SPIE - Smart Mater. Struct.* **2012**, *8340*, 83400J.
- [133] A. Khaldi, C. Plesse, C. Soyer, E. Cattan, F. Vidal, C. Chevrot, D. Teyssié, *Proc. ASME 2011 Int. Mech. Eng. Congr. Expo.* **2011**, *1*.
- [134] A. Maziz, C. Plesse, C. Soyer, C. Chevrot, D. Teyssié, E. Cattan, F. Vidal, *Adv. Funct. Mater.* **2014**, *24*, 4851.
- [135] A. Maziz, C. Plesse, C. Soyer, E. Cattan, F. Vidal, *Proc. SPIE* **2015**, *9430*.
- [136] A. Khaldi, D. Falk, K. Bengtsson, A. Maziz, D. Filippini, N. D. Robinson, E. W. H. Jager, *ACS Appl. Mater. Interfaces* **2018**, *10*, 14978.
- [137] A. Khaldi, A. Maziz, G. Alici, G. M. Spinks, E. W. H. Jager, *SPIE Smart Struct. Mater. Nondestruct. Eval. Heal. Monit.* **2015**, *9430*, 94301R.
- [138] A. Khaldi, A. Maziz, G. Alici, G. M. Spinks, E. W. H. Jager, *Sensors Actuators, B Chem.* **2016**, *230*, 818.
- [139] A. Maziz, C. Plesse, C. Soyer, E. Cattan, F. Vidal, *ACS Appl. Mater. Interfaces* **2016**, *8*, 1559.
- [140] Y. Zhong, S. Lundemo, E. W. H. Jager, *Smart Mater. Struct.* **2018**, *27*.
- [141] P. A. Levermore, L. Chen, X. Wang, R. Das, D. D. C. Bradley, *Adv. Mater.* **2007**, *19*, 2379.
- [142] P. A. Levermore, R. Jin, X. Wang, L. Chen, D. D. C. Bradley, J. C. De Mello, *J. Mater. Chem.* **2008**, *18*, 4414.
- [143] P. Talemi, M. Delaigue, P. Murphy, M. Fabretto, *ACS Appl. Mater. Interfaces* **2015**, *7*, 8465.
- [144] S. Admassie, F. Zhang, A. G. Manoj, M. Svensson, M. R. Andersson, O. Inganäs, *Sol. Energy Mater. Sol. Cells* **2006**, *90*, 133.
- [145] M. A. Rahman, A. Rahim, M. Maniruzzaman, K. Yang, C. Lee, H. Nam, H. Soh, J. Lee, *Sol. Energy Mater. Sol. Cells* **2011**, *95*, 3573.
- [146] J. M. D'Arcy, M. F. El-Kady, P. P. Khine, L. Zhang, S. H. Lee, N. R. Davis, D. S. Liu, M. T. Yeung, S. Y. Kim, C. L. Turner, A. T. Lech, P. T. Hammond, R. B. Kaner, *ACS Nano* **2014**, *8*, 1500.
- [147] C. Karlsson, J. Nicholas, D. Evans, M. Forsyth, M. Strømme, M. Sjödin, P. C. Howlett, C. Pozo-Gonzalo, *ChemSusChem* **2016**, *9*, 2112.
- [148] K. G. Padmalekha, S. Admassie, *Synth. Met.* **2009**, *159*, 1885.
- [149] A. S. Shaplov, D. O. Ponkratov, P. H. Aubert, E. I. Lozinskaya, C. Plesse, A. Maziz, P. S. Vlasov, F. Vidal, Y. S. Vygodskii, *Polym. (United Kingdom)* **2014**, *55*, 3385.
- [150] T. A. Ho, T. S. Jun, Y. S. Kim, *Sensors Actuators, B Chem.* **2013**, *185*, 523.
- [151] E. Spain, T. E. Keyes, R. J. Forster, *Biosens. Bioelectron.* **2013**, *41*, 65.

- [152] E. M. Stewart, M. Fabretto, M. Mueller, P. J. Molino, H. J. Griesser, R. D. Short, G. G. Wallace, *Biomater. Sci.* **2013**, *1*, 368.
- [153] A. Mohammadi, I. Lundström, W. R. Salaneck, O. Inganäs, *Synth. Met.* **1987**, *21*, 169.
- [154] C. Xu, P. Wang, X. Bi, *J. Appl. Polym. Sci.* **1995**, *58*, 2155.
- [155] J. Kim, E. Kim, Y. Won, H. Lee, K. Suh, *Synth. Met.* **2003**, *139*, 485.
- [156] B. Winther-Jensen, K. West, *Macromolecules* **2004**, *37*, 4538.
- [157] M. V Fabretto, D. R. Evans, M. Mueller, K. Zuber, R. D. Short, G. G. Wallace, P. J. Murphy, *Chem. Mater.* **2012**, *24*, 1.
- [158] B. Winther-Jensen, J. Chen, K. West, G. Wallace, *Macromolecules* **2004**, *37*, 5930.
- [159] P. Subramanian, N. B. Clark, L. Spiccia, D. R. MacFarlane, B. Winther-Jensen, C. Forsyth, *Synth. Met.* **2008**, *158*, 704.
- [160] P. Subramanian, N. Clark, B. Winther-Jensen, D. MacFarlane, L. Spiccia, *Aust. J. Chem.* **2009**, 133.
- [161] K. Hong, S. H. Kim, C. Yang, T. K. An, H. Cha, C. Park, C. E. Park, *Org. Electron. physics, Mater. Appl.* **2011**, *12*, 516.
- [162] B. Winther-Jensen, M. Forsyth, K. West, J. W. Andreasen, P. Bayley, S. Pas, D. R. MacFarlane, *Polymer (Guildf)*. **2008**, *49*, 481.
- [163] M. A. Ali, H. H. Kim, C. Y. Lee, H. S. Soh, J. G. Lee, *Met. Mater. Int.* **2009**, *15*, 977.
- [164] M. A. Ali, H. Kim, C. Lee, H. Nam, J. Lee, *Synth. Met.* **2011**, *161*, 1347.
- [165] H. Chelawat, S. Vaddiraju, K. Gleason, *Chem. Mater.* **2010**, *22*, 2864.
- [166] A. Laforgue, *J. Mater. Chem.* **2010**, *20*, 8233.
- [167] C. M. Madl, P. N. Kariuki, J. Gendron, L. F. J. Piper, W. E. Jones, *Synth. Met.* **2011**, *161*, 1159.
- [168] T. Y. Truong, N. D. Luong, J. Nam, *Macromol. Res.* **2007**, *15*, 465.
- [169] M. Fabretto, K. Zuber, C. Hall, P. Murphy, *Macromol. Rapid Commun.* **2008**, *29*, 1403.
- [170] K. Zuber, M. Fabretto, C. Hall, P. Murphy, *Macromol. Rapid Commun.* **2008**, *29*, 1503.
- [171] M. Fabretto, M. Müller, K. Zuber, P. Murphy, *Macromol. Rapid Commun.* **2009**, *30*, 1846.
- [172] B. Gaihre, S. Ashraf, G. M. Spinks, P. C. Innis, G. G. Wallace, *Sensors Actuators, A Phys.* **2013**, *193*, 48.
- [173] A. Maziz, *Univ. Cergy-Pontoise* **2014**.
- [174] Y. Wu, G. Alici, J. D. W. Madden, G. M. Spinks, G. G. Wallace, *Adv. Funct. Mater.* **2007**, *17*, 3216.
- [175] M. Döbbelin, R. Marcilla, M. Salsamendi, C. Pozo-Gonzalo, P. M. Carrasco, J. A. Pomposo, D. Mecerreyes, *Chem. Mater.* **2007**, *19*, 2147.
- [176] M. Y. Teo, N. Kim, S. Kee, B. S. Kim, G. Kim, S. Hong, S. Jung, K. Lee, *ACS Appl. Mater. Interfaces* **2017**, *9*, 819.
- [177] A. De Izarra, S. Park, J. Lee, Y. Lansac, Y. H. Jang, *J. Am. Chem. Soc.* **2018**, *140*, 5375.

- [178] Y. Jia, X. Li, F. Jiang, C. Li, T. Wang, Q. Jiang, J. Hou, J. Xu, *J. Polym. Sci. Part B Polym. Phys.* **2017**, *55*, 1738.
- [179] J. F. Perez-Benito, *J. Phys. Chem. A* **2004**, *108*, 4853.
- [180] H. Kim, K. Jeong, C. J. Yu, H. S. Nam, H. Soh, J. Lee, *Solid. State. Electron.* **2012**, *67*, 70.
- [181] A. Ugur, F. Katmis, M. Li, L. Wu, Y. Zhu, K. K. Varanasi, K. K. Gleason, *Adv. Mater.* **2015**, *27*, 4604.
- [182] D. Wu, J. Zhang, W. Dong, H. Chen, X. Huang, B. Sun, L. Chen, *Synth. Met.* **2013**, *176*, 86.
- [183] T. N. Nguyen, K. Rohtlaid, C. Plesse, G. T. M. Nguyen, C. Soyer, S. Grondel, E. Cattan, J. D. W. Madden, F. Vidal, *Electrochim. Acta* **2018**, *265*, 670.
- [184] E. Smela, *MRS Bull.* **2008**, *33*, 197.
- [185] Y. Xia, J. Ouyang, *ACS Appl. Mater. Interfaces* **2012**, *4*, 4131.
- [186] P. R. Das, L. Komsiyaska, O. Osters, G. Wittstock, *ECS Trans.* **2015**, *68*, 45.
- [187] R. V. Apraksin, A. I. Volkov, S. N. Eliseeva, V. V. Kondratiev, *J. Solid State Electrochem.* **2017**, *21*, 3487.
- [188] K. Ikushima, S. John, A. Ono, S. Nagamitsu, *Synth. Met.* **2010**, *160*, 1877.
- [189] A. Simate, B. Tondou, F. Mathieu, P. Souères, C. Bergaud, *Electroact. Polym. Actuators Devices* **2015**, *9430*, 94301E.
- [190] N. Terasawa, K. Asaka, *Langmuir* **2016**, *32*, 7210.
- [191] N. Terasawa, K. Asaka, *Sensors Actuators, B Chem.* **2017**, *248*, 273.
- [192] D. Wang, C. Lu, J. Zhao, S. Han, M. Wu, W. Chen, *RSC Adv.* **2017**, *7*, 31264.
- [193] A. Simate, A. Delagarde, B. Tondou, P. Souères, E. Flahaut, C. Bergaud, *Nanotechnology* **2017**, *28*.
- [194] A. M. Nardes, R. A. J. Janssen, M. Kemerink, *Adv. Funct. Mater.* **2008**, *18*, 865.
- [195] P. G. Raj, V. S. Rani, A. Kanwat, J. Jang, *Mater. Res. Bull.* **2016**, *74*, 346.
- [196] B. J. Worfolk, S. C. Andrews, S. Park, J. Reinspach, N. Liu, M. F. Toney, S. C. B. Mannsfeld, Z. Bao, *Proc. Natl. Acad. Sci.* **2015**, *112*, 14138.
- [197] M. B. McDonald, P. T. Hammond, *ACS Appl. Mater. Interfaces* **2018**, *10*, 15681.
- [198] B. R. Saunders, B. Vincent, *Adv. Colloid Interface Sci.* **1999**, *1*.
- [199] T. M. Huang, S. Batra, J. Hu, T. Miyoshi, M. Cakmak, *Polym. (United Kingdom)* **2013**, *54*, 6455.
- [200] S. Zhang, E. Hubis, C. Girard, P. Kumar, J. DeFranco, F. Cicoira, *J. Mater. Chem. C* **2016**, *4*, 1382.
- [201] D. Mantione, I. Del Agua, W. Schaafsma, M. Elmahmoudy, I. Uguz, A. Sanchez-Sanchez, H. Sardon, B. Castro, G. G. Malliaras, D. Mecerreyes, *ACS Appl. Mater. Interfaces* **2017**, *9*, 18254.
- [202] I. del Agua, D. Mantione, U. Ismailov, A. Sanchez-Sanchez, N. Aramburu, G. G. Malliaras, D. Mecerreyes, E. Ismailova, *Adv. Mater. Technol.* **2018**, *1700322*, 1700322.
- [203] U. Lang, J. Dual, *Key Eng. Mater.* **2007**, *345–346*, 1189.

- [204] D. Tank, H. H. Lee, D. Y. Khang, *Macromolecules* **2009**, *42*, 7079.
- [205] G. Alici, N. N. Huynh, *Sensors Actuators, A Phys.* **2006**, *132*, 616.
- [206] N. T. Nguyen, Y. Dobashi, C. Soyer, C. Plesse, G. T. M. Nguyen, F. Vidal, E. Cattan, S. Grondel, J. D. W. Madden, *Smart Mater. Struct.* **2018**, *27*.
- [207] T. Shoa, J. D. W. Madden, T. Mirfakhrai, G. Alici, G. M. Spinks, G. G. Wallace, *Sensors Actuators, A Phys.* **2010**, *161*, 127.
- [208] M. S. Sarwar, Y. Dobashi, E. F. Scabeni Glitz, M. Farajollahi, S. Mirabbasi, S. Naficy, G. M. Spinks, J. D. W. Madden, *SPIE Smart Struct. Mater. + Nondestruct. Eval. Heal. Monit.* **2015**, *9430*, 943026.
- [209] Y. Liu, Y. Hu, J. Zhao, G. Wu, X. Tao, W. Chen, *Small* **2016**, *12*, 5074.
- [210] A. Khaldi, A. Maziz, C. Plesse, C. Soyer, F. Vidal, E. Cattan, *Sensors Actuators, B Chem.* **2016**, *229*, 635.
- [211] P. G. A. Madden, *Massachusetts Inst. Technol.* **2003**.
- [212] A. Punning, M. Kruusmaa, A. Aabloo, *Sensors Actuators, A Phys.* **2007**, *136*, 656.
- [213] K. Kruusamäe, P. Brunetto, S. Graziani, A. Punning, G. Di Pasquale, A. Aabloo, *Polym. Int.* **2010**, *59*, 300.
- [214] J. D. Madden, R. A. Cush, T. S. Kanigan, I. W. Hunter, *Synth. Met.* **2000**, *113*, 185.
- [215] W. Takashima, M. Fukui, M. Kaneko, K. Kaneto, *Japanese J. Appl. Phys. Part 1-Regular Pap. Short Notes Rev. Pap.* **1995**, *34*, 3786.
- [216] A. Della Santa, D. De Rossi, A. Mazzoldi, *Synth. Met.* **1997**, *90*, 93.
- [217] A. Della Santa, D. De Rossi, A. Mazzoldi, *Smart Mater. Struct.* **1997**, *6*, 23.
- [218] E. Smela, W. Lu, B. R. Mattes, *Synth. Met.* **2005**, *151*, 25.
- [219] J. Ding, L. Liu, G. M. Spinks, D. Zhou, G. G. Wallace, J. Gillespie, *Synth. Met.* **2003**, *138*, 391.
- [220] S. Hara, T. Zama, W. Takashima, K. Kaneto, *Synth. Met.* **2004**, *146*, 47.
- [221] S. Hara, T. Zama, A. Ametani, W. Takashima, K. Kaneto, *J. Mater. Chem.* **2004**, *14*, 2724.
- [222] K. Yamato, K. Kaneto, *Anal. Chim. Acta* **2006**, *568*, 133.
- [223] J. G. Martinez, T. F. Otero, E. W. H. Jager, *Langmuir* **2014**, *30*, 3894.
- [224] R. Kiefer, N. Aydemir, J. Torop, T. Tamm, R. Temmer, J. Travas-Sejdic, I. Must, F. Kaasik, A. Aabloo, *Sensors Actuators, B Chem.* **2014**, *201*, 100.
- [225] Z. Zondaka, A. Kivilo, S. Nakshatharan, K.-A. Küppar, U. Johanson, T. Tamm, R. Kiefer, *Synth. Met.* **2018**, *245*, 67.
- [226] T. F. Otero, M. Broschart, *J. Appl. Electrochem.* **2006**, *36*, 205.
- [227] T. F. Otero, M. T. Cortés, G. V. Arenas, *Electrochim. Acta* **2007**, *53*, 1253.
- [228] F. Vidal, C. Plesse, G. Palaprat, A. Kheddar, J. Citerin, D. Teyssié, C. Chevrot, *Synth. Met.* **2006**, *156*, 1299.

- [229] K. Ikushima, S. John, K. Yokoyama, S. Nagamitsu, *Smart Mater. Struct.* **2009**, *18*.
- [230] A. Mazzoldi, C. Degl'Innocenti, M. Michelucci, D. De Rossi, *Mater. Sci. Eng. C* **1998**, *6*, 65.
- [231] J. D. Madden, R. A. Cush, T. S. Kanigan, C. J. Brennan, I. W. Hunter, *Synth. Met.* **1999**, *105*, 61.
- [232] W. Lu, E. Smela, P. Adams, G. Zuccarello, B. R. Mattes, *Chem. Mater.* **2004**, *16*, 1615.
- [233] C. Plesse, F. Vidal, D. Teyssié, C. Chevrot, *Chem. Commun. (Camb)*. **2010**, *46*, 2910.
- [234] H. Okuzaki, K. Hosaka, H. Suzuki, T. Ito, *React. Funct. Polym.* **2013**, *73*, 986.
- [235] A. Khaldi, C. Plesse, F. Vidal, S. K. Smoukov, *Adv. Mater.* **2015**, *27*, 4418.
- [236] J. D. W. Madden, P. G. A. Madden, I. W. Hunter, *Smart Struct. Mater. 2001 Electroact. Polym. Actuators Devices* **2001**, *4329*, 72.
- [237] P. Metz, G. Alici, G. M. Spinks, *Sensors Actuators, A Phys.* **2006**, *130–131*, 1.
- [238] T. Shoa, J. D. Madden, N. R. Munce, V. Yang, *Polym. Int.* **2010**, *59*, 343.
- [239] H. Yan, S. Arima, Y. Mori, T. Kagata, H. Sato, H. Okuzaki, *Thin Solid Films* **2009**, *517*, 3299.
- [240] G. M. Spinks, L. Liu, G. G. Wallace, D. Zhou, *Adv. Funct. Mater.* **2002**, *12*, 437.
- [241] R. Z. Pytel, E. L. Thomas, I. W. Hunter, *Polymer (Guildf)*. **2008**, *49*, 2008.
- [242] T. Shoa, T. Mirfakhrai, J. D. W. Madden, *Synth. Met.* **2010**, *160*, 1280.
- [243] M. Farajollahi, F. Sassani, N. Naserifar, A. Fannir, C. Plesse, G. T. M. Nguyen, F. Vidal, J. D. W. Madden, *Smart Mater. Struct.* **2016**, *25*, 115044.
- [244] T. Sendai, H. Suematsu, K. Kaneto, *Jpn. J. Appl. Phys.* **2009**, *48*, 0515061.
- [245] M. Bahrami-Samani, C. D. Cook, J. D. Madden, G. M. Spinks, P. G. Whitten, *Thin Solid Films* **2008**, *516*, 2800.
- [246] H. Randriamahazaka, C. Plesse, D. Teyssié, C. Chevrot, *Electrochim. Acta* **2005**, *50*, 4222.
- [247] N. Festin, *Univ. Cergy-Pontoise* **2012**.
- [248] E. Marwanta, T. Mizumo, N. Nakamura, H. Ohno, *Polymer (Guildf)*. **2005**, *46*, 3795.
- [249] L. J. Goujon, A. Khaldi, A. Maziz, C. Plesse, G. T. M. Nguyen, P.-H. Aubert, F. Vidal, C. Chevrot, D. Teyssié, *Macromolecules* **2011**, *44*, 9683.
- [250] G. Wang, S. Fang, Y. Liu, D. Luo, L. Yang, S. I. Hirano, *RSC Adv.* **2016**, *6*, 66650.
- [251] SU-8 Permanent Epoxy Negative Photoresist, <http://www.microchem.com> (accessed 30.12.2018) **2018**.
- [252] P. Du, X. Lin, X. Zhang, *Sensors Actuators, A Phys.* **2010**, *163*, 240.



# Appendix

## Appendix 1. Materials and experimental methods

### A.1.1. Materials

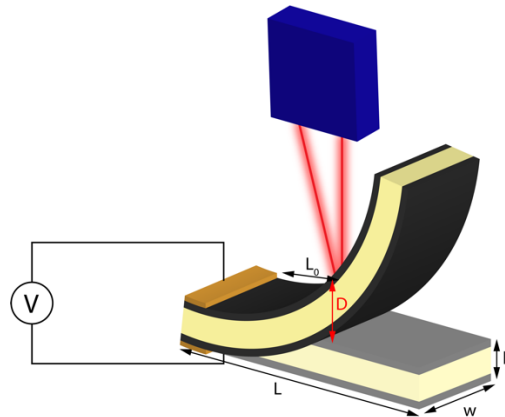
Name	Abbreviation	Provider
1) 3,4-ethylenedioxythiophene	EDOT (distilled under reduced pressure)	Bayer
2) Iron (III) tosylate	Fe(OTs) <sub>3</sub> (Clevios CB 55 V2)	Heraeus Group
3) Poly(3,4-ethylenedioxythiophene):poly(styrene sulfonate)	PEDOT:PSS (Clevios PH1000)	Heraeus Group
4) Poly(ethylene glycol) dimethacrylate	PEGDM	Sigma Aldrich
5) Poly(ethylene glycol) methyl ether methacrylate	PEGM	Sigma Aldrich
6) Nitrile butadiene rubber	NBR	Lanxess
7) 1-ethyl-3-methylimidazolium bis(trifluoromethanesulfonyl)imide	EMImTFSI	Solvionic
8) Dicyclohexyl peroxydicarbonate	DCPD	Groupe Arnaud
9) Ammonium persulfate	APS	Sigma Aldrich
10) Methanol	MeOH	VWR
11) Butanol	BuOH	Alfa Aesar
12) Cyclohexanone		TCI Chemicals
13) S1828 photoresist		Microchem
14) SU-8 2000 photoresist series		Microchem
15) MF-319		Microchem
16) SU-8 developer		Microchem

### A.1.2. Strain difference

The strain difference ( $\varepsilon$ ) of the actuators between two electroactive electrodes was calculated according to Sugino, using the equation below:<sup>[14]</sup>

$$\Delta\varepsilon = \frac{2Dh}{L_0^2 + D^2}$$

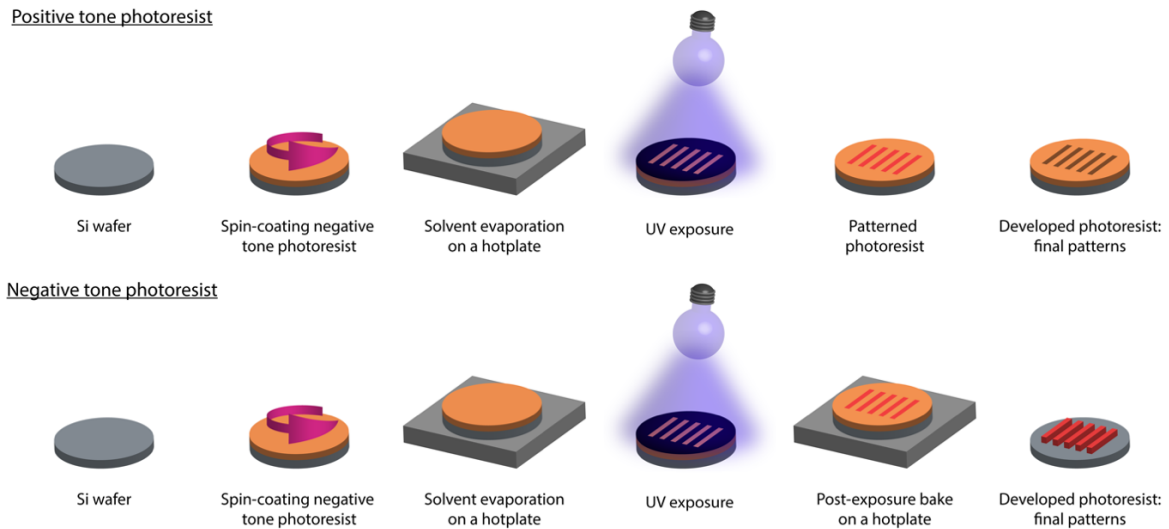
where  $D$  is the displacement of the actuator from neutral to actuated state,  $h$  is the thickness of the actuator and  $L_0$  is the distance between the clamped end of the actuator and the measurement point on the beam (Figure A. 1).



**Figure A. 1. Schematic representation of the actuation measurement for strain difference calculation.**

### A.1.3. Photolithography steps and SU-8 photoresist

Photolithography is used in order to fabricate the devices with desired shape or geometry. This method allows to use the photoresist as a mask for different etching methods, in order to create the wanted design. The first step of this method is the design of the device by making a photomask. When the goal is to pattern already fabricated device, then only one mask can be used but in most cases the fabrication processes are more complex and require many photomasks for different layers. Photomask is the master pattern which allows fabricating/replicating thousands of complicated components directly on a substrate (wafer), using a photoresist (negative or positive tone). Once the photomasks have been made, the standard photolithography of positive photoresist consists of four different steps: 1) deposition of a photoresist; 2) softbaking; 3) exposure to the UV and 4) development. The standard photolithography of negative photoresist involves the same steps with one additional step: 1) deposition of a photoresist; 2) softbaking; 3) exposure to the UV; 4) post-exposure bake and 5) development. In the case of positive tone photoresists, the UV exposed area will be removed and in the case of negative photoresist, the UV exposed area will be thermally crosslinked to form patterns. The photolithography steps for both photoresists are illustrated in Figure A. 2.



**Figure A. 2. Photolithography steps for positive and negative tone photoresists.**

Deposition of the photoresist is usually obtained through spin-coating to form a smooth and homogeneous layer. In the next step, the substrate is placed on a hotplate to remove residual solvent from the photoresist. Subsequently, the substrate and the photomask are aligned with a mask aligner and the photoresist covered substrate is exposed to the UV-light to pattern the desired shapes. In the case of negative tone photoresist, a post-exposure bake is required in order to thermally crosslink the exposed area and to form the patterns. Both, positive and negative tone photoresists have special developers in order to remove non-crosslinked areas and to form 3D structures of the photoresist. The duration and the temperatures of different steps depend on the used photoresist and final thickness of the layers.

SU-8 is an epoxy based negative tone photoresist. Negative refers to a photoresist where the UV exposed parts become crosslinked and the rest of the film remains soluble and can be removed during the development step. In this work, the SU-8 2000 series photoresists are used. The series number refers to SU-8 resists with different viscosities, allowing to tune the thickness of the layers between 0.5 to  $> 200 \mu\text{m}$ . The manufacturer (Microchem) has provided a recommended program for the deposition of SU-8 resist, composed of two segments of spin-coating. The first segment ( $500\text{rpm}-100\text{rpm}\cdot\text{s}^{-1}$  during 5-10s) is carried out with an open-lid at low speed to well cover the substrate with SU-8 and let the solvent evaporate. The second segment is carried out at adapted speed to obtain the desired thickness of the layer. The properties of the SU-8 2000 series used photoresists are brought in Table A. 1.

**Table A. 1. Properties of the used SU-8 2000 series photoresists.**<sup>[251]</sup>

<b>SU-8 2000</b>	<b>Solids (%)</b>	<b>Viscosity (cSt)</b>	<b>Density (g/ml)</b>
2002	29	7.5	1.123
2010	58	380	1.187
2035	69.95	7000	1.227
2075	73.45	22000	1.236

## Appendix 2. Additional results of chapter 3

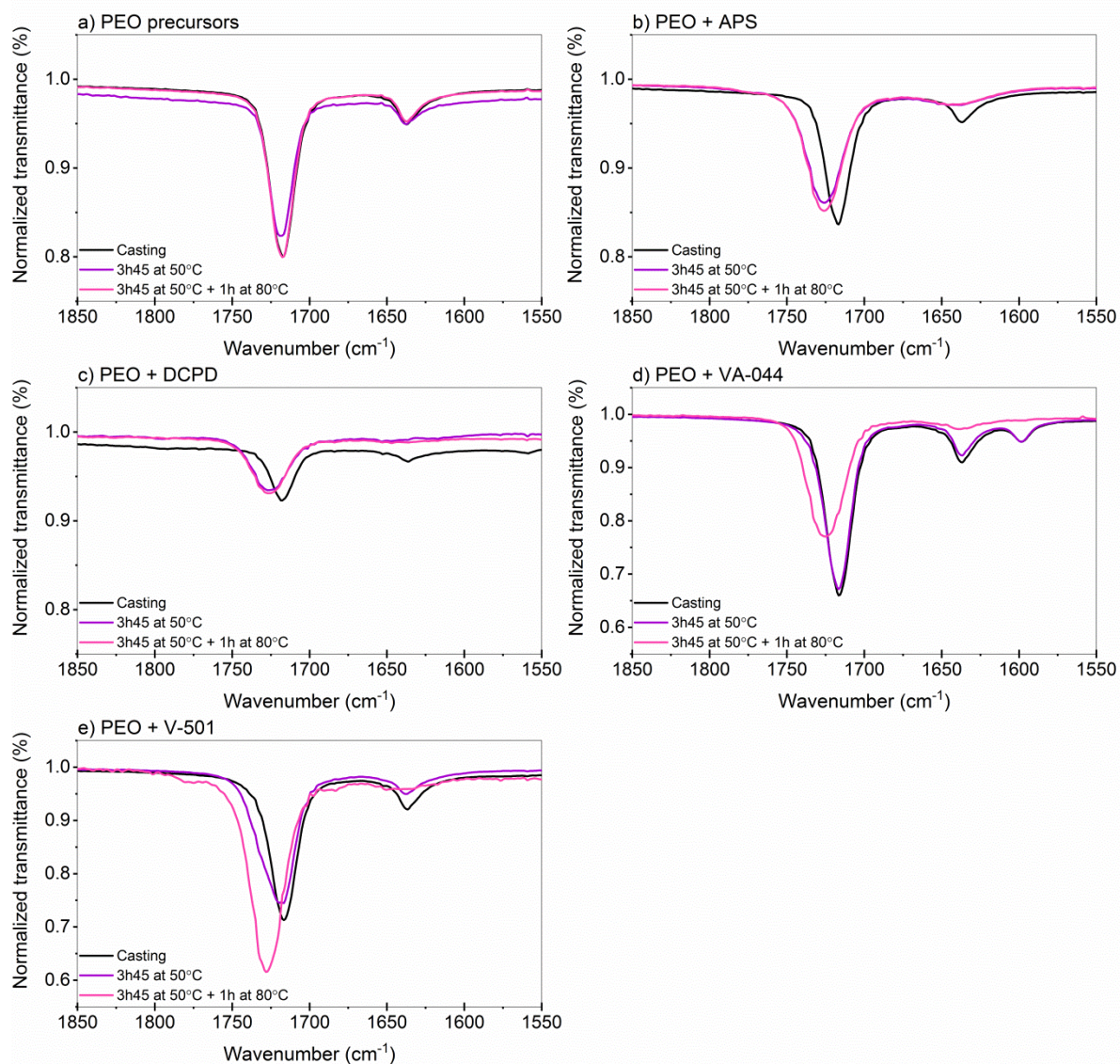
### A.2.1. ATR-FT-IR

Different type of radical initiators (**Table A. 2**) were studied in order to investigate the reaction kinetics of PEO precursors by attenuated total reflection (ATR) infrared spectroscopy (FT-IR). A persulfate, peroxide and two different azo radical initiators were chosen for the polymerization.

**Table A. 2.** List of radical initiators used for PEO polymerization.

Nature of the initiator	Name of the initiator	Abbreviation
Persulfate	Ammonium persulfate	APS
Peroxide	Dicyclohexyl Peroxydicarbonate	DCPD
Azo	2,2'-Azobis[2-(2-imidazolin-2-yl)propane]dihydrochloride	VA-044
Azo	4,4'-azobis(4-cyanovaleric acid)	V-501

**Figure A. 3. a** demonstrates that the bands corresponding to C=O and C=C stretching vibrations at  $1717\text{ cm}^{-1}$  and  $1637\text{ cm}^{-1}$ , respectively, remain unchanged after heat treatment. This confirms that no polymerization occurs without initiator. The presence of peroxide initiators (APS and DCPD) allows the polymerization of methacrylate function (**Figure A. 3. b-c**). We can see that in both cases, the C=O vibration band at  $1717\text{ cm}^{-1}$  is totally shifted to  $1726\text{ cm}^{-1}$  after the heat treatment at  $50^\circ\text{C}$ . Also, the methacrylic carbon double bond peak at  $1637\text{ cm}^{-1}$  is disappeared, which proves the crosslinking of PEO network in the presence of APS or DCPD already after the heat treatment at  $50^\circ\text{C}$ . **Figure A. 3. d-e** reveal the results of PEO precursors polymerization in the presence of two azo polymerization initiators. VA-044 is known to be a low-temperature radical initiator and surprisingly the polymerization occurs only after the heat treatment at  $80^\circ\text{C}$ . In this initiator, an additional absorbance at  $1597\text{ cm}^{-1}$  is observed which can belong to imidazolin-2-yl function in VA-044 initiator. The second azo initiator V-501 follows the same trend indicating that PEO polymerization appears after the final heat treatment. The ATR-FT-IR spectroscopy proves that all the initiators are initiating the polymerization and PEO network could be formed after the heat treatment at  $50^\circ\text{C}$  or after the final heat treatment at  $80^\circ\text{C}$ , depending on the nature of the radical initiator.



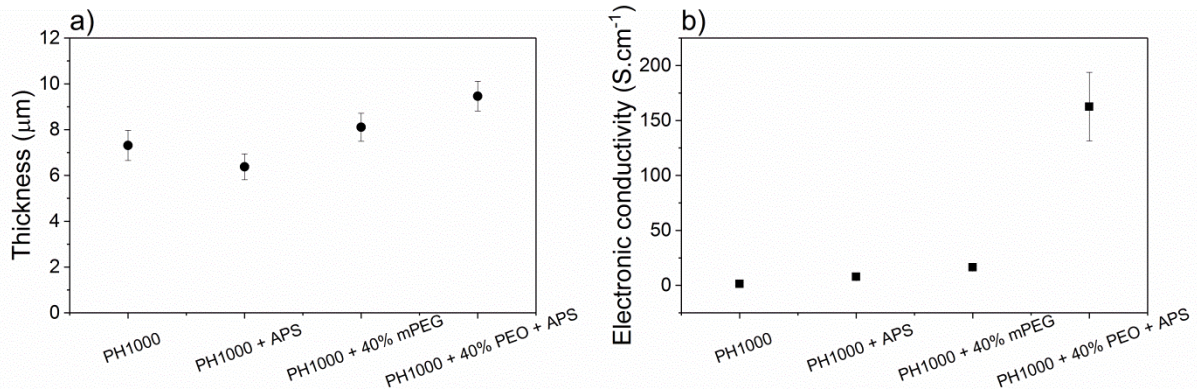
**Figure A. 3.** Normalized transmittance of ATR-FT-IR spectrums of the mixture of PEO precursors and different initiators after different steps in the fabrication process: a) PEO precursors; b) PEO + APS; c) PEO + DCPD; d) PEO + VA-044; e) PEO + V-501.

### A.2.2. PEDOT:PSS/PEO(40%) + different initiators (electrical and electrochemical properties)

First, the effect of the additives was studied on PEDOT:PSS electrode properties separately. Four different electrodes were compared: PH1000; PH1000 + APS; PH1000 + 40% mPEG and PH1000 + 40% PEO + APS to study the effect of each additive. The thickness of the resulting PEDOT:PSS electrodes is brought in **Figure A. 4. a**. Adding APS or PEO precursors (mPEG) into the PEDOT:PSS solution has almost no effect on electrodes thickness, ranging between 6.4 – 8.1  $\mu\text{m}$ . The presence of both additives is increasing the thickness from 7.3  $\mu\text{m}$  (PH1000) to 9.5  $\mu\text{m}$  (PH1000 + 40% PEO + APS). As a second



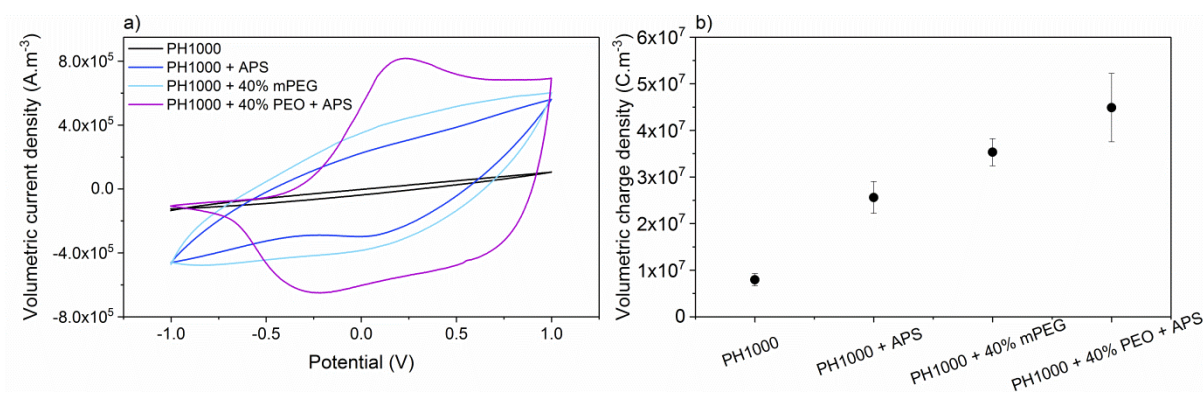
parameter, the electronic conductivity of the PEDOT:PSS electrodes with different additives was studied **Figure A. 4. b**. The pristine PEDOT:PSS electrode has relatively low electronic conductivity  $1 \text{ S.cm}^{-1}$ . Slight increase in electronic conductivity is observed with the addition of APS ( $8 \text{ S.cm}^{-1}$ ) and 40% mPEG ( $16 \text{ S.cm}^{-1}$ ). However, the combination of two additives has a major impact and the resulting electronic conductivity of the PH1000 + 40% PEO + APS electrode is  $163 \text{ S.cm}^{-1}$ .



**Figure A. 4.** Thickness (a) and electronic conductivity (b) of different PEDOT:PSS electrodes in swollen state (EMImTFSI): PH1000, PH1000 + APS, PH1000 + 40% mPEG and PH1000 + 40% PEO + APS

**Figure A. 5. a.** demonstrates the cyclic voltammetry (CV, normalized as a function of the electrode volume) with an inset of volumetric charge density ( $\rho$ ). It can be seen that the pristine PEDOT:PSS electrode (PH1000) presents really low current with non-existent electroactivity. The PEDOT:PSS electrodes start to be electroactive with the presence of additives (APS or mPEG), presenting higher current and some definition in redox process. However, the highest current with clearly defined oxidation and reduction peaks is obtained for the PEDOT:PSS electrode with the combination of two additives (PH1000 + 40% PEO + APS). The volumetric charge density results confirm the increase in the electroactivity, when different additives are incorporated to the PEDOT:PSS casting solution (**Figure A. 5. b.**). As in the case of electronic conductivity, then also  $\rho$  of the pristine PEDOT:PSS electrode remains low ( $8.0 \times 10^6 \text{ C.m}^{-3}$ ). The  $\rho$  increases with the addition of APS ( $2.6 \times 10^7 \text{ C.m}^{-3}$ ) and 40% mPEG ( $3.5 \times 10^7 \text{ C.m}^{-3}$ ). The maximum value  $4.5 \times 10^7 \text{ C.m}^{-3}$  is obtained for the PEDOT:PSS electrode with the combination of two additives. All three parameters, electronic conductivity, cyclic voltammetry and volumetric charge density present the highest obtained values for the PH1000 + 40% PEO + APS electrode.

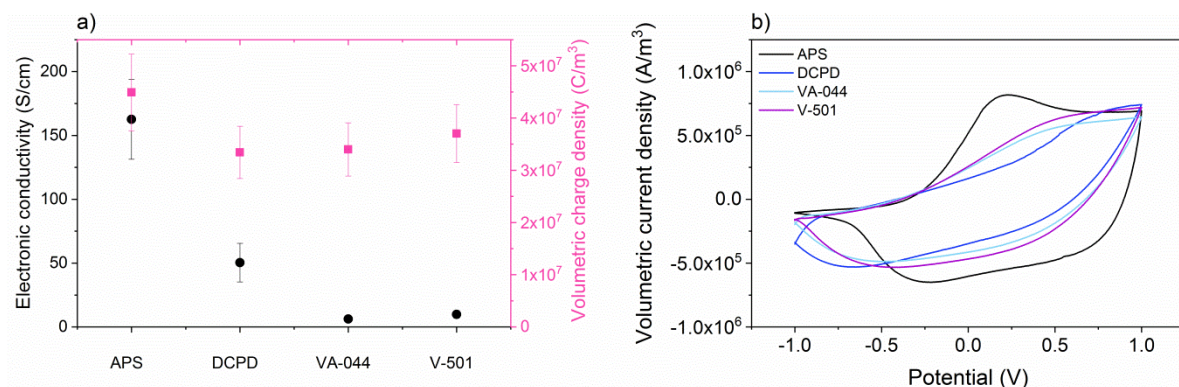




**Figure A. 5.** a) Cyclic voltammetry and b) volumetric charge density of PEDOT:PSS electrodes with different additives at a scan rate of 20 mV.s<sup>-1</sup> and a voltage window of  $\pm 1.0$  V in EMImTFSI.

### A.2.3. PH1000 + 40% PEO + different initiators

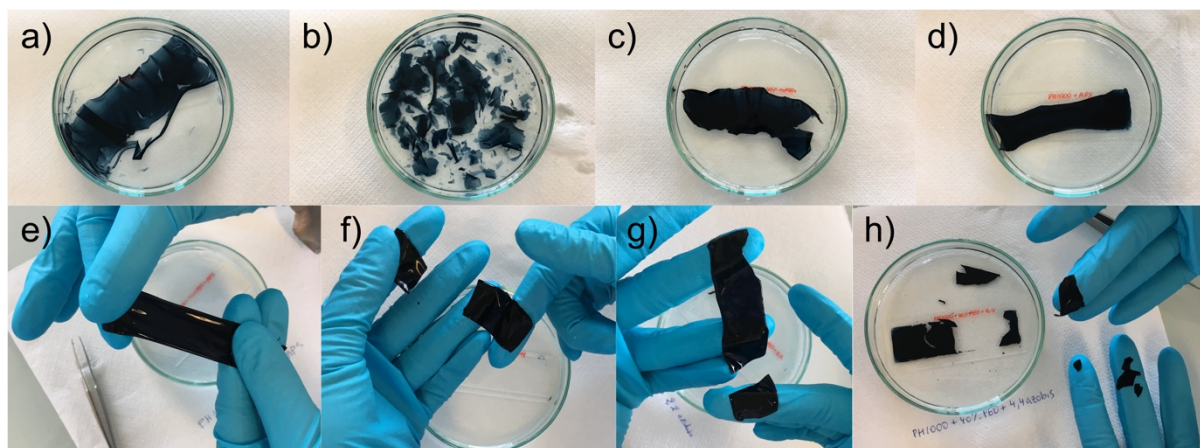
The electrical and electrochemical properties of the PEDOT:PSS electrodes with 40% PEO and different initiators were studied. As can be seen from **Figure A. 6. a**, the electrode with 40% PEO and APS has the highest electronic conductivity and also volumetric charge density. Both values are high (144 S.cm<sup>-1</sup> and 4.7 x 10<sup>7</sup> C.m<sup>-3</sup>) and in the range as found in the previous section. Interestingly, the azo based initiators seem to eliminate the positive effect of PEO addition on electronic conductivity (VA-044 6 S.cm<sup>-1</sup> and V-501 10 S.cm<sup>-1</sup>) although reaching high volumetric charge densities. On the contrary, the electrode with 40% PEO and DCPD has higher electronic conductivity (50 S.cm<sup>-1</sup>) but the volumetric charge density is in the same range as for two azo based initiators (3.3 x 10<sup>7</sup> C.m<sup>-3</sup>). It can be expected that the bending amplitude would be in the same range for the microactuators with those 3 initiators (DCPD, VA-044 and V-501) depending on the volumetric charge density, but faster for the microactuator with DCPD relying on the result of electronic conductivity. **Figure A. 6. b** demonstrates the difference in electroactivity between the electrodes with 40% PEO and different initiators. The electrode with APS has evidently higher current with more clearly defined oxidation and reduction peaks. The electroactivities of the other electrodes with DCPD, VA-044 and V-501 have also improved compared to the pristine PEDOT:PSS electrode, but not as much as the electrode with APS.



**Figure A. 6.** Electrical and electrochemical properties of PEDOT:PSS electrodes with 40% PEO and different initiators: a) electronic conductivity (●) and volumetric charge density (■); b) cyclic voltammetry at a scan rate of 20 mV.s<sup>-1</sup> and a voltage window of ±1.0 V in EMImTFSI.

#### A.2.4. Dimensional stability by water immersion

The pristine PEDOT:PSS film, PEDOT:PSS film with 40% mPEG and PEDOT:PSS film with APS deformed directly when immersed into the water. PEDOT:PSS electrodes with 40% PEO and different initiators (**Table A. 2**) remained films after immersing into the water (**Figure A. 7. e-h**). The PEDOT:PSS electrode with 40% PEO + APS was really stable and remained as a strong film even while removing from the water. It was still possible to handle and to stretch the electrode without breaking it into pieces. The PEDOT:PSS electrodes with 40% PEO + DCPD and 40% PEO + VA-044 lasted as films in the water but broke into pieces while removing from the water. This result shows that even if some crosslinking effect occurred, the films were still softer compared to the PEDOT:PSS electrode with 40% PEO + APS. The PEDOT:PSS electrode with 40% PEO and V-501 broke already into pieces while trying to handle it in the water, indicating that the crosslinking effect was the weakest for this electrode.



**Figure A. 7.** PEDOT:PSS films after water immersion during 10 minutes. a) PH1000 (directly when immersed into water); b) PH1000; c) PH1000 + 40% mPEG; d) PH1000 + APS; e) PH1000 + 40% PEO + APS; f) PH1000 + 40% PEO + DCPD; g) PH1000 + 40% PEO + VA-044; h) PH1000 + 40% PEO + V-501.

## Appendix 3. Additional results of chapter 5

### A.3.1. Model to predict the free strain of the electrodes based on bending deformations

The strain difference of the bending measurements is usually calculated through the curvature  $K$  of the bending or through the displacement  $D$  from neutral to actuated state at a fixed-point  $L$  on the actuator. Both of these methods are quite general for calculating the strain difference of the actuators during bending deformations. The strain difference values are usually lower compared to the free strain, which is the strain of the ECP layer, where no external forces are restraining the deformation (necessary work to bend the semi-IPN or two electrodes working against each other). In other words, free strain is the strain of the electrodes which could be produced if there were no constraints. In order to determine the free strain of the electrodes based on bending experiments, models have been developed while taking into account the thickness and Young's modulus of each layer. The calculation of the free strain based on the model and bending experiments is carried out in order to compare the experimental free strain values to the ones obtained from bending measurements.

Du has proposed a multilayer bending model for conducting polymer actuators from a classical beam bending theory.<sup>[252]</sup> This model includes the thickness and the Young's modulus of each layer to estimate the free strain of the trilayer bending actuator. In order to solve the final equation it has to be known that  $K$  is the curvature of the actuator, the symbols  $m_2$ ,  $m_3$ ,  $n_2$  and  $n_3$  are the ratios in the thickness and Young's modulus between different layers:  $m_2 = \frac{h_{sIPN}}{h_E}$ ,  $m_3 = \frac{h_E}{h_E}$ ,  $n_2 = \frac{E_{sIPN}}{E_E}$  and  $n_3 = \frac{E_E}{E_E}$ . Subscript *sIPN* stands for the semi-IPN layer and subscript *E* for the electrode layer. Also, the symbols  $Y_2$ ,  $Y_3$  and  $Y_{23}$  stand for different equations considering the relations between different layers and can be calculated according to the following equations:

$$Y_2 = 4m_2n_2 + 6m_2^2n_2 + 4m_2^3n_2 + m_2^4n_2^2 \quad (25)$$

$$Y_3 = 4m_3n_3 + 6m_3^2n_3 + 4m_3^3n_3 + m_3^4n_3^2 \quad (26)$$

$$Y_{23} = m_2m_3n_3[(4m_2^2 + 6m_2m_3 + 4m_3^2)n_2 + 12(1 + m_2 + m_3)] \quad (27)$$

Taking into account all the previous equations, the free strain of the PEDOT:PSS layers based on the bending strain can be estimated from the following equation:

$$\varepsilon = \frac{Kh_E[1 + Y_2 + Y_3 + Y_{23}]}{-6m_3n_3[1 + 2m_2 + m_3 + m_2n_2(m_2 + m_3)]} \quad (28)$$

Based on the bending deformation results of Chapter 3, section 3.3.4, the resulting values for PEDOT:PSS electrodes with 20% and 40% PEO are summarized in **Table A. 3** with the experimental free strain values from Chapter 5, section 5.3.3. The Young's modulus of the PEO-NBR membrane is approximately 1 MPa and the thickness 15  $\mu\text{m}$ .

**Table A. 3.** Parameters of PEDOT:PSS/PEO electrodes.

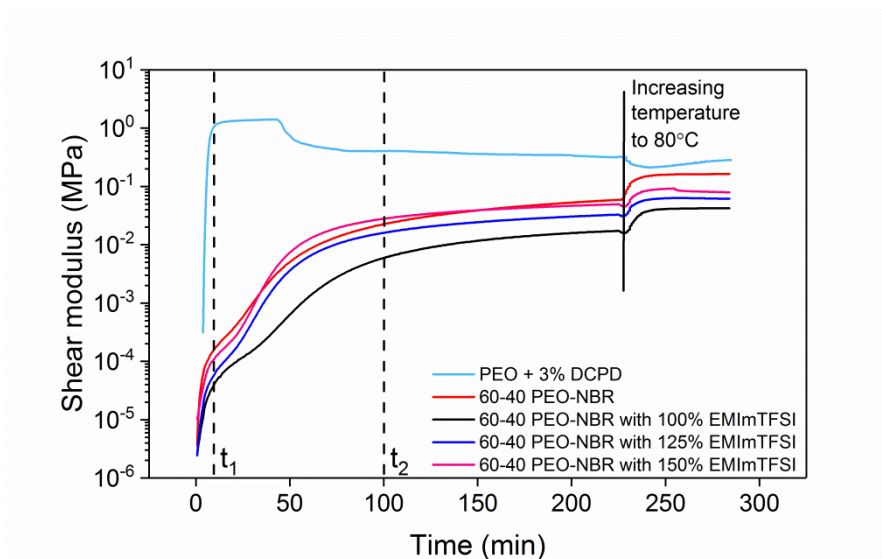
	PEDOT:PSS + 20% PEO	PEDOT:PSS + 40% PEO
Thickness ( $\mu\text{m}$ )	*8.2	*9.2
Young's modulus (MPa)	*3840	* 1600
Volumetric charge density ( $\text{C}\cdot\text{m}^{-3}$ )	* $2.8 \times 10^7$	* $4.5 \times 10^7$
Experimental free strain (%)	0.73	0.93

\*Values from Chapter 3.

Employing the obtained values from **Table A. 3** into the equation (28), the resulting free strain values are 0.76 % and 1.07 % for the PEDOT:PSS electrodes with 20% and 40% PEO, respectively. The free strain values are slightly higher compared to the strain difference (0.68 % for 20% PEO and 0.82 % for 40% PEO). This is due to the trilayer configuration and mechanical interface between the layers, resulting in decreased properties compared to the capability of the single electrode layer. Comparing the free strain experimental values to the extrapolated values, it can be seen that the experimental value of the free strain (0.73 %) for PEDOT:PSS electrode with 20% PEO is almost the same with the calculated value (0.76 %). The difference between the experimental (0.93 %) and calculated (1.07 %) values for the PEDOT:PSS + 40% PEO electrode is slightly higher, but still relatively close.

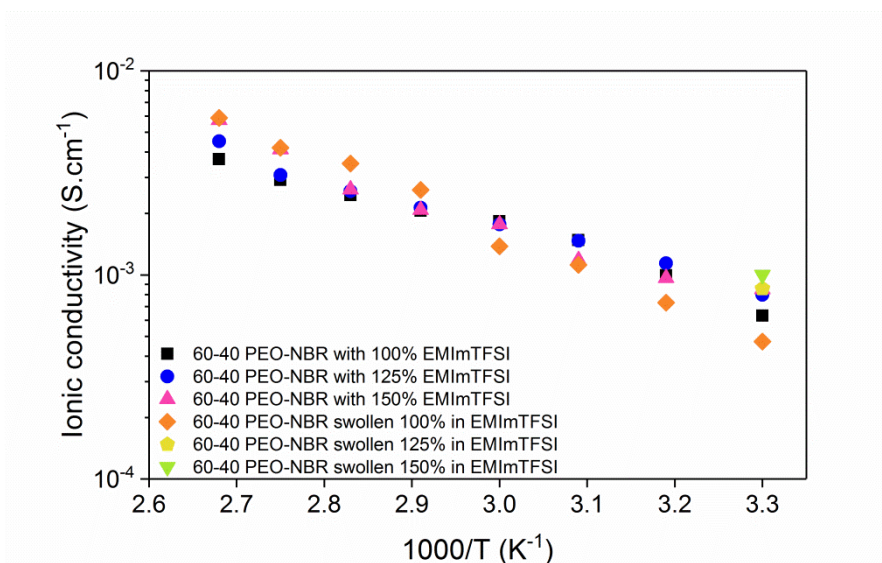
This multilayer bending model helped to calculate the free strain of the single PEDOT:PSS electrodes based on bending measurements and to compare the results to the experimental free strain values. The comparison demonstrated a good correspondence, where the value for the PEDOT:PSS + 20% PEO electrode was almost the same and for the PEDOT:PSS + 40% PEO electrode the calculated value was slightly higher.

## A.3.2. Rheology



**Figure A. 8.** Shear modulus ( $G'$ ) as a function of polymerization time for single PEO network, 60-40 PEO-NBR semi-IPN and 60-40 PEO-NBR semi-IPN with 100, 125 and 150 % EMImTFSI directly included.

## A.3.3. Ionic conductivity



**Figure A. 9.** Ionic conductivity as a function of temperature for PEO-NBR semi-IPNs synthesized in the presence of EMImTFSI and for PEO-NBR semi-IPNs swollen in EMImTFSI.



**Table A. 4.** Ionic conductivity of neat EMImTFSI, PEO-NBR semi-IPNs synthesized in the presence of EMImTFSI and for PEO-NBR semi-IPNs swollen in EMImTFSI.

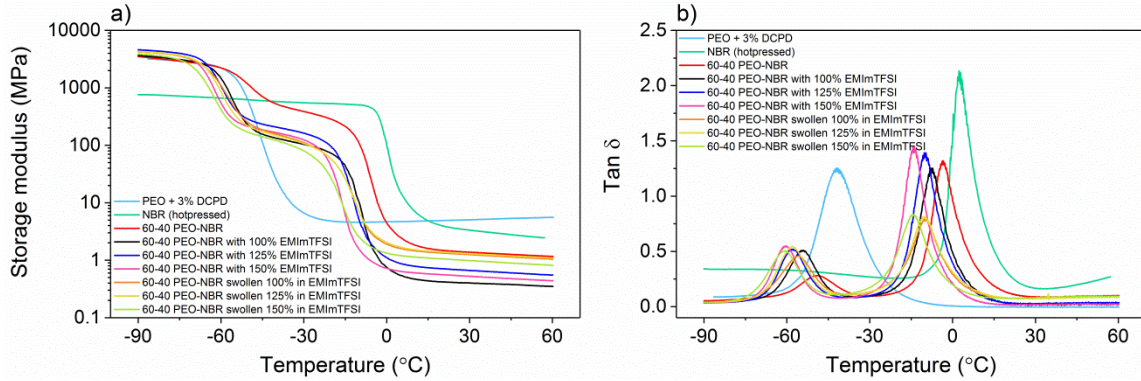
	Ionic conductivity at 30°C S.cm <sup>-1</sup>
neat EMImTFSI at 25°C [250]	8.8 x 10 <sup>-3</sup>
60-40 PEO-NBR with 100% EMImTFSI	6.3 x 10 <sup>-4</sup>
60-40 PEO-NBR with 125% EMImTFSI	8.0 x 10 <sup>-4</sup>
60-40 PEO-NBR with 150% EMImTFSI	8.9 x 10 <sup>-4</sup>
60-40 PEO-NBR swollen 100% in EMImTFSI	4.7 x 10 <sup>-4</sup>
60-40 PEO-NBR swollen 125% in EMImTFSI	8.6 x 10 <sup>-4</sup>
60-40 PEO-NBR swollen 150% in EMImTFSI	1.0 x 10 <sup>-3</sup>

#### A.3.4. Thermomechanical properties

Dynamic mechanical analysis (DMA) allows the study of the viscoelastic behavior of the semi-IPNs. The experiments were carried out in tensile mode at a frequency of 1 Hz from -90°C to 60°C with a heating rate of 3°C.min<sup>-1</sup>. The storage modulus  $E'$  and the loss factor  $\tan \delta$  for single PEO network and hotpressed NBR, for PEO-NBR semi-IPNs synthesized with EMImTFSI as a co-solvent and for PEO-NBR semi-IPNs swollen externally in EMImTFSI are brought in **Figure A. 10. a** and **b**. The values of the storage modulus  $E'$  at 25°C and mechanical relaxation temperatures  $T_\alpha$  of PEO and NBR peaks of corresponding materials are summarized in **Table A. 5**.

In general, there are three temperature regions, corresponding to the glass state, viscoelastic transition and rubber state (**Figure A. 10. a**). These materials are in a glassy state at low temperatures and their storage modulus stay between 0.8 and 4.6 GPa. During viscoelastic transition at intermediate temperatures, a drop of the storage modulus is observed. At higher temperatures, after viscoelastic transition, these materials reach a rubbery plateau. The PEO network and the hotpressed NBR present one viscoelastic transition at intermediate temperatures and their storage modulus at 25°C are 5.0 and 3.6 MPa, respectively. All the different PEO-NBR semi-IPNs demonstrate two viscoelastic transitions at intermediate temperatures, corresponding to dual phase morphology and presenting two distinct phases i.e. the PEO and NBR phases. Comparing the semi-IPNs synthesized with EMImTFSI as a co-solvent with the semi-IPNs externally swollen in EMImTFSI, it can be seen that the general viscoelastic behavior is similar and the storage modulus at 25°C are lower than 1.5 MPa for all the synthesized semi-IPNs without any significant flow of the material and confirming the crosslinking nature of the synthesized materials. The semi-IPNs that are synthesized with EMImTFSI as a co-solvent demonstrate slightly lower storage modulus at 25°C. This can be

explained by the dilution effect. Addition of EMImTFSI is diluting the viscous PEO-NBR solution and forms less entangled networks, resulting in softer materials and therefore lower storage modulus.



**Figure A. 10.** The storage modulus  $E'$  (a) and the loss factor  $\tan \delta$  (b) for PEO and NBR single networks, for PEO-NBR semi-IPN, for PEO-NBR semi-IPNs synthesized with EMImTFSI as a co-solvent and for PEO-NBR semi-IPNs swollen in EMImTFSI.

The loss factor  $\tan \delta$  is brought in **Figure A. 10. b**. The PEO network and hotpressed NBR present one maximum peak of  $\tan \delta$  at  $-42^\circ\text{C}$  and at  $2^\circ\text{C}$ , respectively. The different PEO-NBR semi-IPNs demonstrate two mechanical relaxation peaks, corresponding either to the PEO rich phase or NBR rich phase. All the semi-IPNs present shift of the mechanical relaxation temperature in both of the phases. The shift in these phases can be explained by the presence of EMImTFSI either as a co-solvent or through the swelling step. The corresponding PEO and NBR phase peaks of the 60-40 PEO-NBR semi-IPN are at  $-49^\circ\text{C}$  and at  $-4^\circ\text{C}$ . When EMImTFSI is introduced to the starting mixture or incorporated through the swelling step and the content is further increased, the corresponding PEO and NBR phase peaks are shifting to lower temperatures. The total shift in the NBR phase is from  $2^\circ\text{C}$  to  $-14^\circ\text{C}$  and the total PEO transition temperature peak shift is from  $-42^\circ\text{C}$  to  $-60^\circ\text{C}$ . The PEO peak shift is following the same trend as in the case of NBR peak shift and presenting decrease in the relaxation temperatures if the content of EMImTFSI is increased. It can be assumed that the presence of EMImTFSI is plasticizing the resulting materials and causing a decrease in the relaxation temperatures. The loss factor of the NBR relaxation temperatures is notably higher for the semi-IPNs synthesized with EMImTFSI as a co-solvent. This means that the mechanical damping or also called dissipation of energy in the materials is higher in the semi-IPNs synthesized directly with EMImTFSI as a co-solvent. The intensity of the PEO relaxation temperatures is similar in both cases, either if the semi-IPNs are synthesized with EMImTFSI as a co-solvent or externally swollen. When comparing the relaxation



temperature values (**Table A. 5**) of the semi-IPNs with 100%, 125% and 150% EMImTFSI as a co-solvent with the externally swollen semi-IPNs, it can be seen that the values for the semi-IPNs with 100% EMImTFSI are really similar and the values for 125% and 150% EMImTFSI semi-IPNs are exactly the same.

**Table A. 5.** Storage modulus  $E'$  at 25°C and mechanical relaxation temperatures  $T_\alpha$  of PEO and NBR peaks.

	$E'$ at 25°C MPa	$T_\alpha$ of PEO °C	$T_\alpha$ of NBR °C
PEO + 3% DCPD	5.0	-42	
NBR (hotpressed)	3.6		2
60-40 PEO-NBR	1.4	-49	-4
60-40 PEO-NBR with 100% EMImTFSI	0.4	-54	-8
60-40 PEO-NBR with 125% EMImTFSI	0.7	-58	-10
60-40 PEO-NBR with 150% EMImTFSI	0.5	-60	-14
60-40 PEO-NBR swollen 100% in EMImTFSI	1.3	-56	-10
60-40 PEO-NBR swollen 125% in EMImTFSI	1.3	-58	-10
60-40 PEO-NBR swollen 150% in EMImTFSI	1.0	-60	-14

The characterization of thermomechanical properties demonstrates the existence of two separate phases for all the characterized semi-IPNs. The general viscoelastic behavior of the materials is the same when comparing the semi-IPNs synthesized with EMImTFSI as a co-solvent with the externally swollen semi-IPNs. The peak shift in relaxation temperatures is most likely due to the presence and further increase in the amount of EMImTFSI. The loss factor of the NBR phase in the semi-IPNs synthesized with EMImTFSI directly as a co-solvent is higher compared to the externally swollen ones indicating higher damping factor and energy absorbance.

### A.3.5. Model to predict the blocking force

A model was used to predict the theoretical blocking force value and to compare the result to the experimental value. For developing the model for blocking force, the same assumptions are used as brought in Chapter 5, section 5.2, equations (9, 10 and 11). That means, that inner stresses of each layer in trilayer configuration are defined separately.

The theoretical value of the stress can be calculated at the equilibrium when the strain is equal to zero:

$$\sigma_B = \frac{A_1 E_1 \alpha_1 \frac{q_1}{V_1} - A_2 E_2 \alpha_2 \frac{q_2}{V_2}}{A_1 + A_2 + A_{SIPN}} \quad (29)$$

With  $\alpha$  the average strain-to-charge ratio and  $q$  the limiting charge of the electrode 1, the equation becomes:

$$\sigma_B = \frac{-\alpha q}{V_{total}} (E_1 - E_2) \quad (30)$$

Substituting the average value of the strain-to-charge ratio of two different PEDOT:PSS electrodes, the limiting charge of the electrode 1 and calculating the stress during contraction ( $E_1^{ox}-E_2^{red}$ ) and elongation ( $E_1^{red}-E_2^{ox}$ ), the total theoretical value is 0.8 MPa corresponding to 66.2 mN.

The experimental value (0.3 MPa corresponding to 25.8 mN) is more than 2 times lower compared to the theoretical value (0.8 MPa corresponding to 66.2 mN). This could be related to error on mechanical properties and some ion exchange mechanism that can change during isometric experiments. For example, if the sample cannot contract, some expansion can occur with anions coming into the electrode.

## Abstract

Electroactive polymers (EAPs) are able to change their shape and/or size in response to electrical stimulation, but also to generate electrical signal in response to mechanical stimulation. As flexible, and lightweight materials, they arise as promising candidates for the development of soft Micro-Electro-Mechanical Systems (MEMS) to move towards soft electronics. The goal of this thesis is the fabrication and characterization of microactuators and microsensors based on electronically conductive polymers (ECPs) to obtain efficient devices for further integration into microsystems.

The recently elaborated layer stacking method for fabricating ECP based microactuators was taken as a starting point of this thesis. The optimization of vapor phase polymerization of 3,4-ethylenedioxythiophene (EDOT) was studied in order to improve the electrical and electrochemical properties of the electrodes and as a result, the microactuators performances.

As a next step, poly(3,4-ethylenedioxythiophene):poly(styrene sulfonate) (PEDOT:PSS) was chosen as a new electrode material to develop more simple and reproducible layer stacking method. Polar reactive additives based on poly(ethylene oxide) (PEO) were incorporated to the PEDOT:PSS commercial dispersion to elaborate electrodes with improved electrical, mechanical and electrochemical properties. These PEDOT:PSS composite electrodes were then used to fabricate efficient trilayer microactuators. Additionally, the mechanical strain sensing of these trilayers was demonstrated for the first time on microscale.

The integration of these PEDOT:PSS based microactuators was then performed according to a process fully compatible with microsystems. The process describes for the first time the complete elaboration of the trilayer microdevices, their full integration with electrical connections and subsequent operation on a flexible substrate without any manual handling, allowing the design of microsystems with complex configurations. The resulting microsystems were successfully characterized as microactuators and as microsensors.

Finally, air-operating linear actuators have been developed by the combination of PEDOT:PSS based electrodes with different physical properties as predicted by a theoretical model. The electrochemical and mechanical properties of PEDOT:PSS based electrodes were first studied as a function of their composition but also of their the redox level. Best combination of electrodes was used to develop asymmetrical trilayer devices with simple layer stacking method. The resulting devices presented linear actuation with performances in the range of predicted values. Linear strain sensing ability of these materials was also demonstrated.

The work of this thesis demonstrated a simple and reproducible elaboration method for fabricating PEDOT:PSS based microactuators and microsensors with high performances. The developed microfabrication process allows their full integration into microsystems and brings them closer to the development of soft and efficient ECP-MEMS.



## Résumé

Les polymères électroactifs (EAPs) sont capables de changer de forme et/ou de dimension en réponse à une stimulation électrique, mais aussi de générer un signal électrique en réponse à une stimulation mécanique. Ces matériaux flexibles et légers apparaissent comme des candidats prometteurs pour le développement de systèmes micro-électro-mécaniques (MEMS en anglais « Micro-Electro-Mechanical Systems»). Le but de cette thèse est la fabrication et la caractérisation de microactionneurs et de microcapteurs à base de polymères conducteurs électroniques (PCEs) afin d'obtenir des dispositifs performants pour une intégration dans les microsystèmes.

Premièrement, un procédé d'élaboration par empilement de couches récemment décrit pour les microactionneurs à base de PCEs, a été pris comme point de départ de cette thèse. L'optimisation de la polymérisation en phase vapeur du 3,4-éthylènedioxythiophène (EDOT) a ainsi été réalisée afin d'améliorer les propriétés électriques et électrochimiques des électrodes obtenues et ainsi d'améliorer les performances des microactionneurs résultants.

Dans une deuxième partie, le poly(3,4-éthylènedioxythiophène):poly(styrène sulfonate) (PEDOT:PSS) a été choisi comme nouveau matériau d'électrode afin de rendre le procédé d'empilement de couches plus simple et reproductible. Des additifs réactifs polaires à base de poly(oxyde d'éthylène) (PEO) ont été incorporés à une dispersion commerciale de PEDOT:PSS pour élaborer des électrodes aux propriétés électriques, mécaniques et électrochimiques améliorées. Ces électrodes composites à base de PEDOT:PSS ont ensuite été utilisées pour fabriquer des microactionneurs tricouches performants. De plus, les propriétés de capteur de déformation mécanique de ces tricouches ont été démontrées pour la première fois à l'échelle microscopique.

La troisième partie de ce travail décrit l'intégration complète de ces dispositifs électrostimulables à base de PEDOT:PSS selon des procédés totalement compatibles aux microsystèmes. Ce travail décrit pour la première fois l'élaboration des microdispositifs tricouches, leur intégration complète avec contacts électriques et leur fonctionnement sur substrat flexible sans aucun maniement manuel, permettant ainsi la conception de microsystèmes avec des configurations complexes. Les microsystèmes obtenus ont été caractérisés avec succès en tant que microactionneurs et microcapteurs.

Enfin, des actionneurs linéaires et fonctionnant à l'air libre ont été développés par la combinaison d'électrodes à base de PEDOT:PSS présentant différentes propriétés physiques. Les propriétés électrochimiques et mécaniques de ces électrodes ont tout d'abord été étudiées en fonction de leur composition et leur niveau d'oxydation. A partir d'un modèle théorique, la meilleure combinaison d'électrodes a été utilisée pour l'élaboration de dispositifs tricouches asymétriques. Les systèmes résultants ont présenté des déformations linéaires cohérentes avec la prédiction du modèle électromécanique. Par ailleurs la capacité de ces matériaux à détecter et quantifier une déformation linéaire a également été démontrée.

Les travaux de cette thèse ont démontré une méthode d'élaboration simple et reproductible pour la fabrication de microactionneurs et de microcapteurs à base de PEDOT:PSS avec des performances élevées. Le procédé de microfabrication développé permet leur intégration complète dans les microsystèmes et ouvre des perspectives prometteuses pour le développement de PCE-MEMS flexibles et efficaces.



